

# Flamelet modelling for partially premixed turbulent jet diffusion flames

**Citation for published version (APA):**

Ovink, R. (1999). *Flamelet modelling for partially premixed turbulent jet diffusion flames*. [Phd Thesis 1 (Research TU/e / Graduation TU/e), Mechanical Engineering]. Technische Universiteit Eindhoven.  
<https://doi.org/10.6100/IR527800>

**DOI:**

[10.6100/IR527800](https://doi.org/10.6100/IR527800)

**Document status and date:**

Published: 01/01/1999

**Document Version:**

Publisher's PDF, also known as Version of Record (includes final page, issue and volume numbers)

**Please check the document version of this publication:**

- A submitted manuscript is the version of the article upon submission and before peer-review. There can be important differences between the submitted version and the official published version of record. People interested in the research are advised to contact the author for the final version of the publication, or visit the DOI to the publisher's website.
- The final author version and the galley proof are versions of the publication after peer review.
- The final published version features the final layout of the paper including the volume, issue and page numbers.

[Link to publication](#)

**General rights**

Copyright and moral rights for the publications made accessible in the public portal are retained by the authors and/or other copyright owners and it is a condition of accessing publications that users recognise and abide by the legal requirements associated with these rights.

- Users may download and print one copy of any publication from the public portal for the purpose of private study or research.
- You may not further distribute the material or use it for any profit-making activity or commercial gain
- You may freely distribute the URL identifying the publication in the public portal.

If the publication is distributed under the terms of Article 25fa of the Dutch Copyright Act, indicated by the "Taverne" license above, please follow below link for the End User Agreement:

[www.tue.nl/taverne](http://www.tue.nl/taverne)

**Take down policy**

If you believe that this document breaches copyright please contact us at:

[openaccess@tue.nl](mailto:openaccess@tue.nl)

providing details and we will investigate your claim.

**Flamelet Modelling for Partially Premixed  
Turbulent Jet Diffusion Flames**

**CIP-DATA LIBRARY TECHNISCHE UNIVERSITEIT EINDHOVEN**

Ovink, Roy

Flamelet modelling for partially premixed turbulent jet diffusion flames /  
by Roy Ovink. -Eindhoven : Technische Universiteit Eindhoven,  
1999. -Proefschrift. -ISBN 90-386-2761-0

NUGI 834

Trefwoorden: verbranding / turbulente vrijstralen / numerieke stromingsleer ; CFD /  
hittedraad anemometrie

Subject headings: combustion / turbulent free jets / computational fluid dynamics ; CFD /  
hot-wire anemometry

Druk: Universiteitsdrukkerij TU Eindhoven

# **Flamelet Modelling for Partially Premixed Turbulent Jet Diffusion Flames**

PROEFSCHRIFT

ter verkrijging van de graad van doctor aan de  
Technische Universiteit Eindhoven, op gezag van de  
Rector Magnificus, prof.dr. M. Rem, voor een  
commissie aangewezen door het College voor  
Promoties in het openbaar te verdedigen  
op maandag 20 december 1999 om 16.00 uur

door

Roy Ovink

geboren te Hengelo (Ov)



Dit proefschrift is goedgekeurd door de promotoren:

prof.dr.ir. H.W.M. Hoeijmakers  
en  
prof.dr.ir. A.A. van Steenhoven

This research was supported by STW.

*Voor mijn ouders*



# Contents

<b>1 Introduction</b> . . . . .	<b>5</b>
1.1 Turbulence . . . . .	6
1.2 Turbulent combustion models . . . . .	7
1.3 Outline of this thesis . . . . .	9
<b>2 Governing equations for chemically reacting flow</b> . . . . .	<b>11</b>
2.1 Conservation equations . . . . .	11
2.2 Equation of state . . . . .	13
2.3 Constitutive equations . . . . .	14
2.4 Simplifying assumptions . . . . .	16
2.4.1 Conserved scalar approach . . . . .	16
2.4.2 Conservation equation of energy . . . . .	17
2.4.3 Equation of state . . . . .	18
<b>3 Turbulent flows</b> . . . . .	<b>19</b>
3.1 Turbulent length, time and velocity scales . . . . .	19
3.2 Averaged equations . . . . .	23
3.3 Turbulence closure model . . . . .	26
3.3.1 $k$ - $\epsilon$ turbulence model . . . . .	26
3.3.2 Presumed PDF method . . . . .	28
3.4 Numerical solution algorithm . . . . .	30
<b>4 Axi-symmetrical turbulent jets</b> . . . . .	<b>39</b>
4.1 Mathematical model . . . . .	39
4.2 Hot-wire anemometry in an isothermal turbulent jet . . . . .	44
4.2.1 Experimental set-up . . . . .	45
4.2.2 Frequency response and spatial resolution . . . . .	46
4.2.3 Look-up inversion method for HWA . . . . .	48
4.2.4 Forward-reverse ambiguity effects . . . . .	50
4.2.5 Effect of the fluctuating binormal velocity component . . . . .	51
4.2.6 Incorporating an equation for the fluctuating tangential velocity component . . . . .	56
4.2.7 Results . . . . .	59
4.3 Thermocouple measurements in a heated jet . . . . .	66
4.3.1 Results . . . . .	67
4.4 Modifications to the $k$ - $\epsilon$ model . . . . .	70
4.5 Conclusions . . . . .	73

<b>5 Turbulent diffusion flames</b> . . . . .	<b>75</b>
5.1 One-dimensional scalar dissipation layers . . . . .	75
5.2 Regimes diagram for non-premixed turbulent combustion . . . . .	78
5.3 Laminar diffusion flamelet model . . . . .	81
5.4 One-dimensional laminar counterflow diffusion flames . . . . .	86
5.4.1 Definition of the mixture fraction . . . . .	88
5.4.2 The relation between the strain rate and the scalar dissipation rate . . . . .	89
5.5 Averaged scalar quantities . . . . .	91
5.6 A stabilized natural gas flame . . . . .	92
5.7 Conclusions . . . . .	97
<b>6 Turbulent premixed flames</b> . . . . .	<b>99</b>
6.1 Regimes diagram for premixed turbulent combustion . . . . .	99
6.2 Flamelet modelling . . . . .	104
6.3 One-dimensional laminar premixed flames . . . . .	107
6.4 Averaged equations . . . . .	108
6.5 Results . . . . .	113
6.6 Conclusions . . . . .	121
<b>7 Lifted turbulent jet diffusion flames</b> . . . . .	<b>123</b>
7.1 Lifted-flame stabilization mechanism . . . . .	123
7.2 Turbulent burning velocity in a non-homogeneous mixture fraction field . . . . .	124
7.3 Results . . . . .	125
7.4 Conclusions . . . . .	129
<b>8 Concluding discussion</b> . . . . .	<b>131</b>
8.1 Turbulence measurements and modelling . . . . .	131
8.2 Turbulent combustion modelling . . . . .	132
8.3 Future directions . . . . .	134
<b>References</b> . . . . .	<b>137</b>
<b>Appendices</b>	
<b>A Measured mean velocity and temperature distributions in a turbulent jet</b> . . . . .	<b>149</b>
<b>B Reaction mechanism</b> . . . . .	<b>151</b>
<b>C Diffusion flamelet results</b> . . . . .	<b>155</b>
<b>D Premixed flamelet results</b> . . . . .	<b>159</b>
<b>E Equation for the flame surface area ratio</b> . . . . .	<b>163</b>
<b>F Equation for the variance in <math>G</math></b> . . . . .	<b>165</b>

<b>Summary</b> .....	<b>167</b>
<b>Samenvatting</b> .....	<b>169</b>
<b>Nawoord</b> .....	<b>171</b>
<b>Curriculum Vitae</b> .....	<b>172</b>



# Chapter 1

## Introduction

Turbulent flames form an important phenomenon from a scientific as well as from a practical point of view. Turbulent combustion is generally subdivided into two classes: premixed and non-premixed combustion. In systems with extensive premixing, such that the mixture is flammable everywhere, burning can occur through both a combination of laminar premixed flames and laminar diffusion flames. This is known as partially premixed combustion. Important applications of partially premixed combustion may for example be found in Diesel engines, gas turbines and combustion in furnaces. Fuel rich regions are used for flame stabilization but, in order to minimize  $\text{NO}_x$  formation, most of the combustion occurs under premixed fuel lean conditions.

Figure 1.1 gives a schematic drawing of a burner. The function of a burner is to bring together the fuel with the air such that a desirable flame is obtained. Burners like used in the glass industry are usually made up out of a metal tube through which the premixed mixture of fuel and oxygen is injected into the furnace. Besides requirements with respect to the efficiency, the length of the flame is about the most important consideration in the operation of furnaces. It is important that the flame length is such that a wall situated opposite to the injection is not heated too much. A too long flame may destroy this wall by corrosion. Conversely, a flame which is too short generally produces low quality glass by spot heating and non-uniform heating of the surface of the melt.

In the case of gas-burners, primary air is often supplied to realize a stable burning of the flame. Without premixing with primary air, the gas flame is long, radiating (luminous) and unstable. Such a flame is called a diffusion flame because oxygen has to be supplied by diffusion from the surrounding secondary air. By premixing the fuel with primary air the flame will become shorter, more stable and less radiating. The length of the flame is also influenced by the type of fuel used and the burner exit diameter. The flame length does not depend very much on the fuel mass flow. The reason for this is that at a higher burner exit velocity the mixing with the combustion air will also be stronger, causing the flame length to remain almost constant.

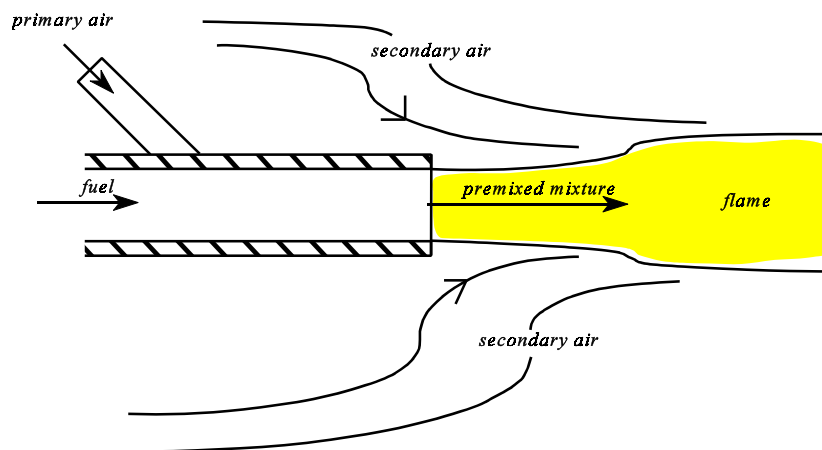


Figure 1.1 Schematic drawing of a burner.



## 1.1 TURBULENCE

Like the burners used in the glass-melting furnace, most industrial burners are operating on a high power level. This implies high flow velocities. Therefore generally the flames are turbulent. Turbulence increases the efficiency of the mixing process by a factor of thousand and more. A principal difficulty in the modelling of turbulent flames is the adequate modelling of turbulence itself.

In jets, turbulence is initiated by the flow being subject to so-called Kelvin-Helmholtz instabilities (Lesieur, 1990). These instabilities are generated by large velocity gradients in the flow. Molecular viscosity is responsible for the exchange of momentum in the flow, thereby diminishing these velocity gradients. As a result of the Kelvin-Helmholtz instabilities, vortices start to develop in the flow. The vortical structure increases the length of the interface between two layers with different velocities. Therefore, they most effectively transport momentum.

In a turbulent flow the velocity fluctuates both in space and time. Certain patterns repeat themselves at irregular intervals, there is never exact repetition, and the motion is truly non-periodic. When two identical systems are started at nearly identical conditions, the two motions diverge from each other at an exponential rate. Of course, if the starting conditions were precisely the same, then the deterministic nature of the equations (Chapter 2) guarantees that the motions are identical for all time. But since some uncertainty in the starting conditions is inevitable in real physical systems, in the turbulent flow regime the divergence of nominally identical motions cannot be avoided.

The procedures involved in computational turbulence may be divided in two global categories: (1) deterministic methods, and (2) probabilistic methods

### (i) Deterministic methods

The most straightforward way of finding a solution to the Navier-Stokes equations is by solving them directly, this is called a Direct Numerical Simulation (DNS). These simulations have a rather limited range of applicability. A turbulent flow shows fluctuations on small as well as on large scales. Even in a constant density environment this makes obtaining the numerical solution of the governing equations, i.e. the Navier-Stokes equations, not feasible for the high Reynolds numbers of interest in the present study. To resolve the small scales, a very fine grid, and consequently a large computer memory, is needed. The required time resolution makes these calculations also very time consuming. Capabilities of current computers limit DNS calculations (without combustion) to low Reynolds numbers. Nevertheless, solving the complete set of equations for reacting flows subjected to turbulent fluctuations may be very useful. DNS produces simplified but realistic realizations of a small part of a turbulent flame. This may help us to understand real flames and to model them using a necessarily less complete mathematical flow model.

### (ii) Probabilistic methods

Even if it would be possible to perform a DNS for a practical system one may well ask whether there is any sense in finding numerical solutions to the Navier-Stokes equations, since two solutions from identical initial conditions using slightly different approximations would also diverge. However, these different solutions represent the same statistical behaviour, i.e. the probability of finding a certain state in space and time is equal for both solutions. Thus, in implementing the approach of the first category, it is sufficient to know the behaviour of the flow variables in a statistical sense.

Probabilistic methods attempt to directly solve equations for these statistical quantities. Therefore, all statistical methods apply some kind of averaging technique to the Navier-Stokes equations (Chapter 3). The drawback of these statistical methods is that, due to the averaging process, the nonlinear terms in the Navier-Stokes equations give rise to correlation terms of fluctuating variables that have to be modelled. Finding an appropriate model for these correlations is known as the turbulence closure problem. A major difficulty with turbulence models is their lack of universality. A turbulence closure optimized for a particular type of turbulent flame may not be adequate to predict the flame behaviour in other configurations. To model the correlation terms and thereby close the flow model, in the present study, use is made of the standard  $k$ - $\epsilon$  turbulence model. The  $k$ - $\epsilon$  model has been used in a majority of turbulent jet calculations reported in literature. In spite of its lack of universality and the many specific assumptions made in its derivation, the  $k$ - $\epsilon$  model offers an adequate way of simulating turbulent jet flames.

## 1.2 TURBULENT COMBUSTION MODELS

Discussion of the chemical aspects of turbulent combustion is facilitated if we deal with non-premixed (Chapter 5) and premixed systems (Chapter 6) separately. However, there are several points of similarity in the description of the chemical behaviour of these two systems. When an averaging technique is applied to the conservation equation for species  $Y_i$ , an averaged chemical source term  $\overline{\dot{w}_i}$  for species  $Y_i$  appears. When reactions are assumed to be fast, chemical reaction is confined to thin surfaces, e.g. laminar flamelets. For both systems, the mean rate of creation of species, e.g.  $\overline{\dot{w}_i}$ , may then be expressed as

$$\overline{\dot{w}_i} = \overline{\dot{w}_{i,f}} \overline{\Sigma} \quad (1.1)$$

where  $\overline{\dot{w}_{i,f}}$  [kg/m<sup>2</sup>s] is the rate of creation of species  $i$  per unit area of flamelet surface, and  $\overline{\Sigma}$  [m<sup>-1</sup>] is the flame surface area of flamelet per unit volume. In non-premixed systems  $\overline{\dot{w}_{i,f}}$  depends on the molecular transport of reactants from each side of the reaction zone while in premixed systems  $\overline{\dot{w}_{i,f}}$  depends on the speed at which a premixed flamelet propagates into reactants. Another shared point is that both systems may in first approximation be described by a single scalar variable. In non-premixed systems that variable is the so-called *mixture fraction*  $Z$ , while in premixed systems it is the *progress variable*  $c$ . Although the meaning of these scalars is quite different, each plays a decisive role in determining the instantaneous and statistical state of the fluid. By introduction of the scalar quantities  $Z$  and  $c$ , the emphasis is put on finding a solution for these two quantities rather than on finding a solution of the averaged transport equations for all species and the temperature.

### (i) Non-premixed combustion

For non-premixed combustion, the mixture fraction  $Z$  obeys a source free convection-diffusion equation that is relatively easy to solve. The mixture fraction may be defined as a scaled element mass fraction. It is therefore a conserved scalar which is invariant under combustion. Strictly, the mixture fraction  $Z$  can be introduced only if diffusivities of all species are equal. The simplest model based on the conserved scalar  $Z$  is obtained if one assumes that fuel and oxidizer react in a one-step, irreversible, infinitely fast reaction. This is the so-called flame sheet approximation, introduced by Burke and Schumann (1928). Another model based on the mixture fraction  $Z$  is the chemical equilibrium model. Given the pressure and the enthalpy, the equilibrium

composition can be determined as a function of the instantaneous mixture fraction  $Z$  by making use of standard techniques (e.g. Williams, 1985b).

In the laminar flamelet model, a turbulent diffusion flame is assumed to be an ensemble of laminar diffusion flames. For this model to be valid, the Damköhler number (defined as the ratio of the Kolmogorov time to the chemical time) must be high, and the diffusion flame must be thin in mixture-fraction-space. If this is the case, then the local structure in a turbulent diffusion flame may be regarded to be one-dimensional. The local instantaneous scalar flame structure may then be described by a set of equations in one dimension, the so-called flamelet equations. With these flamelet equations, all scalar quantities may be solved as a function of two parameters; the mixture fraction  $Z$  and the scalar dissipation rate at the point of stoichiometric mixture, i.e.  $\chi_{st}$ . Numerical data obtained from flamelet calculations is stored into a so-called flamelet library which may be incorporated directly into the turbulent flame calculations if they are averaged appropriately. With  $\chi_{st}$  as the chemical non-equilibrium parameter, the flamelet method makes it possible to model chemical non-equilibrium effects like flame quenching.

In the averaging procedure, use is made of presumed probability density functions (PDF's). The shape of a presumed PDF is determined by two moments alone; the mean and the variance of the concerning quantity.

#### (ii) Premixed combustion

In premixed combustion, the scalar field may be described by a progress variable  $c$  which equals 0 in the unburnt mixture and 1 in the burnt gas. In the simplest approach, the premixed flame is regarded as infinitely thin and the progress of the species mass fractions within the premixed flame front is left unresolved. The progress variable may be interpreted as a non-dimensional product mass fraction and therefore it obeys a transport equation similar to that for a species mass fraction. By time-averaging this equation, a time averaged chemical source term appears. A first model for this time averaged chemical source term was given by Spalding (1977) and it is called the ‘‘Eddy-Break-Up’’ model (EBU model). A drawback of the EBU model is that the mean chemical source term is only controlled by the turbulent flow field, and that there is no influence of chemistry on the mean chemical source term. In the Bray-Moss-Libby model (BML model) (Bray *et al.*, 1994b), the mean chemical source term is given by

$$\overline{\dot{w}} = \rho_u s_L^0 I_0 \Sigma \quad (1.2)$$

and it depends on the density of the unburnt mixture  $\rho_u$  and the laminar burning velocity  $s_L^0$  which in turn depends on the local mixture composition. The empirical factor  $I_0$ , called the mean stretch factor, accounts for the influence of flame stretch and flame curvature on the laminar burning velocity. As in Equation (1.1),  $\Sigma$  is the local flamelet surface-to-volume ratio. It may for example be given as a function of the mean progress variable, making the model very similar to the EBU model. Also a transport equation may be solved for  $\Sigma$  (Cant *et al.*, 1990). However, many unknown correlations appear that have to be modelled. Models like the EBU model and the BML model, are often not sufficiently accurate to predict the correct turbulent burning velocity and turbulent flame brush thickness.

Alternatively, the solution for the progress variable may be found by solving a kinematic equation for the so-called level set function  $G$ . In this model, the mean turbulent flame front is found as the zero level set of the level set function  $G$ . The propagation speed of the turbulent flame front is prescribed by a model equation for the turbulent burning velocity (see Chapter 6).

### (iii) Partially premixed combustion

Partially premixed combustion is found in the stabilization mechanism of lifted turbulent diffusion flames that will be treated in Chapter 7. Because the flame is lifted, the fuel emanating from the burner is subjected to partial premixing. Besides the development of a diffusion flame the mixed reactants can ignite and burn in a premixed fashion. In such lifted flames, flame propagation generates a flame structure that is called a triple flame. Triple flames may be described by a combination of a laminar premixed flame and a laminar diffusion flame (Müller *et al.*, 1994a).

## **1.3 OUTLINE OF THIS THESIS**

The model geometry to be studied in this thesis is that of an axi-symmetric burner. This geometry is much simpler than that found in practical systems, but it allows to incorporate all the important basic ingredients we want to study. The boundary conditions for such an axi-symmetric jet are also rather easy to implement into a numerical method. In this thesis, models for both premixed and diffusion flamelets will be used in combination with a  $k$ - $\epsilon$  turbulence model to numerically simulate diffusion flames, premixed flames and partially premixed flames.

Chapter two starts with a description of the full set of macroscopic equations to be solved. Chapter three deals with the averaging process and the turbulence closure problem. Chapter four focusses on the numerical simulation of a turbulent jet without chemical reactions. Calculated results will be compared to measurements employing hot-wire anemometry (HWA). A special method of treating the hot-wire anemometry signals has been developed and will be explained. Mean temperature measurements have been carried out using a thermocouple. The mixing process will be described by the temperature measurements in a heated jet. Chapter five focusses on the numerical simulation of turbulent diffusion flames. It is shown how the mixture fraction equation can be used in numerically simulating these flames. Chapter six treats the turbulent premixed flames where an equation for the scalar  $G$  is used to describe the premixed flame. Chapter seven treats the combined problem, where the diffusion flamelet model and the premixed flamelet model have been used in combination to numerically simulate a lifted turbulent jet diffusion flame. Chapter eight gives some final remarks and recommendations for future research.



## Chapter 2

### Governing equations for chemically reacting flow

For studying turbulent partially premixed diffusion flames a number of theoretical models have been developed. Each of them has its advantages and disadvantages. At first the governing equations may be divided into two groups according to the condition of whether or not the flow may be considered as a continuum.

In this thesis, the flow will be considered to be a continuum. The conditions for the validity of equations describing continuum flows may be found from the criterion that the characteristic interaction length and time of interaction of the particles composing the flow are both small compared to the characteristic macroscopic dimensions of the flow. At relatively low temperatures, the characteristic interaction length is the mean free path of the molecules. At normal temperature and atmospheric pressure it is in the order of  $0.1\mu\text{m}$ .

Continuum or macroscopic equations are extremely useful in solving a large number of practical problems connected with chemically reacting flows. It is well known that a macroscopic description of fluid flow may be derived from the postulation of a number of conservation laws such as conservation of mass, momentum and energy. The general equations of conservation are not sufficient to describe a chemically reacting flow. Additional equations giving more information about the nature of the fluid and the flow should be introduced. These relations may be expressed in the form of equations of state, in the form of constitutive relations connecting stresses with velocity gradients, viscosity coefficients, etc.

#### 2.1 CONSERVATION EQUATIONS

##### (i) Conservation of mass

From the mass balance of an arbitrary control volume it follows, in conservation form, that:

$$\frac{\partial \rho}{\partial t} + \frac{\partial \rho u_j}{\partial x_j} = 0 \quad (2.1)$$

where  $t = \text{time [s]}$

$x_j = \text{Cartesian coordinate in } j\text{th direction [m]}$

$\rho = \text{mass density [kg/m}^3\text{]}$

$u_j = \text{component of the velocity vector } \underline{u} \text{ [m/s] in a Cartesian coordinate system.}$

The second term in Equation (2.1) indicates a summation over the index  $j$  ( $j=1,2,3$ ) according to Einstein's convention.

For a mixture with  $N$  species, the mixture density  $\rho$  is the sum of the species mass densities  $\rho_k$ :

$$\rho = \sum_{k=1}^N \rho_k \quad (2.2)$$

The velocity vector  $\underline{u}$  of the mixture is the mass-weighted sum of species velocities  $\underline{v}_k$ :

$$\rho \underline{u} = \sum_k (\rho_k \underline{v}_k) \quad (2.3)$$

The mass conservation Equation (2.1) may also be written as:

$$\frac{D\rho}{Dt} + \rho \frac{\partial u_j}{\partial x_j} = 0 \quad (2.4)$$

In this equation  $D/Dt$  denotes the material derivative:

$$\frac{D}{Dt} = \frac{\partial}{\partial t} + u_j \frac{\partial}{\partial x_j} \quad (2.5)$$

### (ii) Conservation of species

By considering the conservation of species for an arbitrary control volume it follows, in conservation form, that:

$$\frac{\partial}{\partial t} \rho Y_i + \frac{\partial}{\partial x_k} \rho u_k Y_i = - \frac{\partial}{\partial x_k} J_{ik} + \dot{w}_i \quad (i=1, \dots, N) \quad (2.6)$$

where the mass fraction  $Y_i$  is defined by

$$Y_i = \frac{\rho_i}{\rho} \quad (2.7)$$

$J_{ij}$  is the mass molecular diffusion flux of species  $i$  in the  $j$ -th coordinate direction and  $\dot{w}_i$  is the rate of mass generation of species  $i$ , i.e. the chemical source term with unit  $\text{kg m}^{-3} \text{s}^{-1}$ .

### (iii) Conservation of momentum

By considering the change of momentum for an arbitrary control volume and equating this to the imposed force it follows, in conservation form, that:

$$\frac{\partial \rho u_i}{\partial t} + \frac{\partial \rho u_i u_j}{\partial x_j} = \frac{\partial \sigma_{ji}}{\partial x_j} + \rho \sum_{k=1}^N (Y_k f_{ki}) \quad (i=1,2,3) \quad (2.8)$$

where  $\sigma_{ji}$  is the stress tensor:

$$\sigma_{ji} = -p \delta_{ji} + \tau_{ji} \quad (2.9)$$

with  $p$  [ $\text{N/m}^2$ ] as the pressure.  $\delta_{ji}$  denotes the Kronecker delta which is equal to zero unless  $j=i$  for which it is equal to one.  $\rho Y_k f_{ki}$  is the body force acting on the  $k$ -th species in the  $x_i$ -direction. Examples of body forces are the gravity force and the Lorentz force for electromagnetic influences.

### (iv) Conservation of energy

From the energy balance for an arbitrary control volume it follows that:

$$\begin{aligned} \frac{\partial}{\partial t} (\rho [U + \frac{1}{2} u_i u_i]) + \frac{\partial}{\partial x_j} (\rho u_j [U + \frac{1}{2} u_i u_i]) = \\ \sum_{k=1}^N f_{ki} (\rho Y_k u_i + J_{ki}) + \frac{\partial}{\partial x_j} (\sigma_{ji} u_i) - \frac{\partial q_j}{\partial x_j} + \dot{Q} \end{aligned} \quad (2.10)$$

Here  $U$  [J/kg] is the internal energy per unit mass.  $q_j$  [J/m<sup>2</sup>s] is the component in  $x_j$ -direction of the heatflux vector  $\underline{q}$ , i.e.  $-\partial q_j / \partial x_j$  [J/m<sup>3</sup>s] is the heat locally added through conduction and diffusion processes (see Section 2.3).  $\dot{Q}$  [J/m<sup>3</sup>s] is the amount of heat added volumetrically per unit of time and volume due to radiative exchange and electrical currents (Joule heat).

Using Equation (2.1) it follows that Equation (2.10) may also be written as:

$$\rho \frac{D}{Dt} \left( U + \frac{1}{2} u_i u_i \right) = \sum_{k=1}^N f_{ki} (\rho Y_k u_i + J_{ki}) + \frac{\partial}{\partial x_j} (\sigma_{ji} u_i) - \frac{\partial q_j}{\partial x_j} + \dot{Q} \quad (2.11)$$

The energy equation may also be written in terms of the so-called enthalpy  $h$  [J/kg] which is introduced by the definition:

$$h = U + \frac{p}{\rho} \quad (2.12)$$

With Equation (2.9) it is found that:

$$\frac{\partial}{\partial x_j} (\sigma_{ji} u_i) = \frac{\partial}{\partial x_j} [(-p \delta_{ji} + \tau_{ji}) u_i] = -\frac{\partial}{\partial x_j} (p u_j) + \frac{\partial}{\partial x_j} (\tau_{ji} u_i) \quad (2.13)$$

Using the continuity Equation (2.4), the first term on the right hand side of Equation (2.13) can be rewritten as:

$$\begin{aligned} -\frac{\partial}{\partial x_j} (p u_j) &= -p \frac{\partial u_j}{\partial x_j} - u_j \frac{\partial p}{\partial x_j} = \frac{p}{\rho} \frac{D\rho}{Dt} - u_j \frac{\partial p}{\partial x_j} \\ &= -\rho p \frac{D}{Dt} \left( \frac{1}{\rho} \right) - u_j \frac{\partial p}{\partial x_j} = -\rho \frac{D}{Dt} \left( \frac{p}{\rho} \right) + \frac{Dp}{Dt} - u_j \frac{\partial p}{\partial x_j} \\ &= -\rho \frac{D}{Dt} \left( \frac{p}{\rho} \right) + \frac{\partial p}{\partial t} \end{aligned} \quad (2.14)$$

So that Equation (2.13) can be rewritten as:

$$\frac{\partial}{\partial x_j} (\sigma_{ji} u_i) = -\rho \frac{D}{Dt} \left( \frac{p}{\rho} \right) + \frac{\partial p}{\partial t} + \frac{\partial}{\partial x_j} (\tau_{ji} u_i) \quad (2.15)$$

Substitution of this equation into Equation (2.11) yields:

$$\rho \frac{D}{Dt} \left( U + \frac{p}{\rho} + \frac{1}{2} u_i u_i \right) = \frac{\partial p}{\partial t} + \sum_{k=1}^N f_{ki} (\rho Y_k u_i + J_{ki}) + \frac{\partial}{\partial x_j} (u_i \tau_{ji}) - \frac{\partial q_j}{\partial x_j} + \dot{Q} \quad (2.16)$$

So the energy equation in terms of the enthalpy  $h$  is:

$$\rho \frac{D}{Dt} \left( h + \frac{1}{2} u_i u_i \right) = \frac{\partial p}{\partial t} + \sum_{k=1}^N f_{ki} (\rho Y_k u_i + J_{ki}) + \frac{\partial}{\partial x_j} (u_i \tau_{ji}) - \frac{\partial q_j}{\partial x_j} + \dot{Q} \quad (2.17)$$

## 2.2 EQUATIONS OF STATE

From thermodynamics it is known that two relationships exist between the macroscopic characteristics of the fluid, namely, density, pressure, internal energy, and temperature. One of these functional relationships is usually called the thermal equation of state. In the specific case of a gaseous medium, some more or less simple relationships for the equation of state have been



adopted. We will assume that we are dealing with a perfect gas for which the thermal equation of state reads:

$$p = \rho RT = \frac{\rho R_0 T}{W} = \rho R_0 T \sum_{k=1}^N \frac{Y_k}{W_k} \quad (2.18)$$

where  $R$  = specific gas constant [J/kg K]  
 $R_0$  = universal gas constant = 8.3144 J/mol K  
 $T$  = temperature [K]  
 $W$  = mixture molecular weight [kg/mol]  
 $W_i$  = molecular weight of species  $i$  [kg/mol]

Also needed is a relation between the enthalpy  $h$  and the temperature  $T$ . The enthalpy  $h$  is the mass-weighted sum of the specific enthalpy of all species:

$$h = \sum_{i=1}^n Y_i h_i \quad (2.19)$$

The specific enthalpy  $h_i$  of species  $i$  is a function of the temperature given by:

$$h_i = h_i^0 + \int_{T_0}^T c_{p_i}(T) dT \quad (2.20)$$

where  $h_i^0$  is the heat of formation per unit mass at reference temperature  $T_0$  and  $c_{p_i}$  [J/kg K] is the specific heat at constant pressure per unit mass of species  $i$ . The mass weighted specific heat is introduced by:

$$c_p = \sum_{i=1}^N Y_i c_{p_i} \quad (2.21)$$

Using Equations (2.19), (2.20) and (2.21) we may write:

$$dh = c_p dT + \sum_{i=1}^N h_i dY_i \quad (2.22)$$

## 2.3 CONSTITUTIVE EQUATIONS

### (i) Diffusion flux

The diffusion flux may be modelled as:

$$J_{ij} = -\rho D_i \frac{\partial Y_i}{\partial x_j} - \frac{D_i^T}{\rho T} \frac{\partial T}{\partial x_j} \quad (2.23)$$

where the first term on the right hand side represents Fick's law with a single diffusion coefficient  $D_i$  for diffusion of species  $i$  in the mixture.  $D_i^T$  is the thermal diffusion coefficient of species  $i$  in the mixture. Transport properties are often simplified by neglecting thermal diffusion.

### (ii) Heat-flux vector

Conduction and diffusion processes yield the heat-flux vector as:

$$q_j = -\lambda \frac{\partial T}{\partial x_j} + \sum_{i=1}^N h_i J_{ij} \quad (2.24)$$

where Fourier's law of thermal conductivity states that the heat flux is proportional to the temperature gradient (first term on the right hand side). The quantity  $\lambda$  (J/K m s) denotes the thermal conductivity. Furthermore, the heat flux vector includes the transport of specific species enthalpy ( $h_i$ ) by diffusion (second term on the right hand side).

From Equation (2.22) It follows that:

$$\frac{\partial h}{\partial x_j} = c_p \frac{\partial T}{\partial x_j} + \sum_{i=1}^N h_i \frac{\partial Y_i}{\partial x_j} \quad (2.25)$$

so that for the conduction term can be written:

$$\lambda \frac{\partial T}{\partial x_j} = \frac{\lambda}{c_p} \frac{\partial h}{\partial x_j} - \frac{\lambda}{c_p} \sum_{i=1}^N h_i \frac{\partial Y_i}{\partial x_j} \quad (2.26)$$

and by substitution of this equation into Equation (2.24) it follows that:

$$q_j = -\frac{\lambda}{c_p} \frac{\partial h}{\partial x_j} + \sum_{i=1}^N h_i \left( \frac{\lambda}{c_p} \frac{\partial Y_i}{\partial x_j} + J_{ij} \right) \quad (2.27)$$

### (iii) Shear stress tensor

For a Newtonian fluid the shear stress tensor  $\tau_{ij}$ , also called the deviatoric stress tensor, reads:

$$\tau_{ji} = \mu \left( \frac{\partial u_j}{\partial x_i} + \frac{\partial u_i}{\partial x_j} \right) + \left( \mu' - \frac{2}{3} \mu \right) \delta_{ji} \frac{\partial u_k}{\partial x_k} \quad (2.28)$$

where  $\mu$  [Ns/m<sup>2</sup>] is the dynamic viscosity. The viscosity coefficient  $\mu'$  is the so-called bulk viscosity. For monatomic gas mixtures, kinetic theory shows that  $\mu'=0$ . The nonzero values of  $\mu'$  for polyatomic gases are, as explained by Williams (1965), caused by the relaxation effects between the translational motion and the various internal degrees of freedom. These effects lead to a positive value for  $\mu'$ . However, in studies of combustion processes  $\mu'$  is usually taken to be negligible.

### (iv) Chemical source term

A chemical reaction mechanism of  $M$  elementary reaction steps, involving  $N$  species, can be represented by the following set of equations:

$$\sum_{i=1}^N \nu_{i,k}' M_i \rightarrow \sum_{i=1}^N \nu_{i,k}'' M_i \quad k=1, \dots, M \quad (2.29)$$

where  $\nu_{i,k}'$  are the stoichiometric coefficients of the reactants,  $\nu_{i,k}''$  the stoichiometric coefficients of the products and  $M_i$  identifies the chemical symbol for species  $i$ . The production rate of species  $i$  is equal to

$$\dot{w}_i = W_i \sum_{k=1}^M (\nu_{i,k}'' - \nu_{i,k}') RR_k \quad (2.30)$$

where  $W_i$  is the molecular weight of species  $i$  and  $RR_k$  is the reaction rate for the  $k$ -th reaction. According to the law of mass action this reaction rate is given by

$$RR_k = k_k \prod_{i=1}^N (C_{M_i})^{v_{i,k}} \quad (2.31)$$

where  $k_k$  is the specific reaction-rate constant for the  $k$ -th reaction.  $C_{M_i}$  is the molar concentration of species  $M_i$ , which is the number of moles of species  $i$  per unit volume,

$$C_{M_i} = \frac{\rho_i}{W_i} \quad (2.32)$$

For a given chemical reaction,  $k_k$  is independent of the concentrations  $C_{M_i}$  and depends only on the temperature. In general,  $k_k$  is modelled according to the empirical Arrhenius expression:

$$k_k = A_k e^{-E_k/R_u T} \quad (2.33)$$

where  $E_k$  is the activation energy for reaction  $k$ .  $A_k$  represents the collision frequency, or frequency factor, for reaction  $k$ . This collision frequency is approximated by

$$A_k = B_k T^{\alpha_k} \quad (2.34)$$

A table of values for these reaction constants that are used in the present study is given in Appendix B.

## 2.4 SIMPLIFYING ASSUMPTIONS

### 2.4.1 Conserved scalar approach

Transport properties are often simplified by neglecting thermal-diffusion in Equation (2.23) and by modelling the diffusion flux by Fick's law:

$$J_{ij} = -\rho D_i \frac{\partial Y_i}{\partial x_j} \quad (2.35)$$

It has to be mentioned here that severe temperature gradients may occur in flows with combustion with the consequence that thermal-diffusion effects may be significant. However, when the conservation equation of species (2.6) is to be applied to turbulent flows, there are compelling reasons to simplify the treatment of molecular diffusion. Apart from a detailed analysis of laminar diffusion there are already sufficient complexities in turbulent reacting flows to justify the simplification associated with Fick's law. Besides, in most turbulent reacting flows of practical interest, the turbulence Reynolds number is sufficiently high so that molecular transport is of secondary importance.

The conservation equation of species (2.6) can now be written as:

$$\frac{\partial}{\partial t} \rho Y_j + \frac{\partial}{\partial x_k} \rho u_k Y_j = \frac{\partial}{\partial x_k} \rho D_j \frac{\partial Y_j}{\partial x_k} + \dot{w}_j \quad (j=1, \dots, N) \quad (2.36)$$

Since in chemical reactions elements are conserved, we have for each element  $i$

$$\sum_{j=1}^N \mu_{ij} \dot{w}_j = 0 \quad (2.37)$$

where  $\mu_{ij}$  is the number of kilograms of the element  $i$  in a kilogram of species  $j$  and  $\dot{w}_j$  is the mass rate of creation of species  $j$ . We can thus develop from Equation (2.36) the conservation

equations for elements  $Z_i = \sum_{j=1}^N \mu_{ij} Y_j$ , namely

$$\frac{\partial}{\partial t} \rho Z_i + \frac{\partial}{\partial x_k} \rho u_k Z_i = \frac{\partial}{\partial x_k} \sum_{l=1}^N \rho \mu_{il} D_l \frac{\partial Y_l}{\partial x_k} \quad (2.38)$$

Under the assumption of one single diffusion coefficient, i.e. if  $D_j = D$ , Equation (2.38) reduces to

$$\frac{\partial}{\partial t} \rho Z_i + \frac{\partial}{\partial x_k} \rho u_k Z_i = \frac{\partial}{\partial x_k} \rho D \frac{\partial Z_i}{\partial x_k} \quad (2.39)$$

Such an approximation may lead to considerable errors in case the diffusion coefficients are not all equal. However, for turbulent flows (Chapter 3), the arbitrariness of the choice of  $D$  has little influence on the mean equations for the mass fractions  $Z_i$ , since the molecular diffusivity  $D$  is much smaller than the turbulent diffusivity  $D_t$  (see Section 3.3.1). Because the turbulent diffusivity  $D_t$  is equal for all elements, the averaged Equation (2.39) becomes identical for all elements.

Despite the reservations concerning its accuracy, the assumption of equal diffusion coefficients is often applied because it leads to a considerable simplification. An important observation is that the partial differential Equations (2.39) now have become identical for all  $Z_i$ . The implication is that under appropriate initial and boundary conditions, conditions which prevail in many circumstances of practical interest, the solution of all these equations can be obtained from that of a single partial differential equation for a conserved scalar  $Z(\underline{x}, t)$ , the so-called mixture fraction,

$$\frac{\partial}{\partial t} \rho Z + \frac{\partial}{\partial x_k} \rho u_k Z = \frac{\partial}{\partial x_k} \rho D \frac{\partial Z}{\partial x_k} \quad (2.40)$$

$Z$  may be defined as a linear combination of element mass fractions, and it is generally convenient to scale  $Z$  to be in the range  $[0, 1]$  with the value zero in one stream and the value unity in a second stream. An appropriate definition of the mixture fraction for complete combustion of a hydrocarbon fuel is given in Section 5.4.1.

In the limit of fast chemistry, i.e. fast relative to the time scales of the flow, the problem of determining the chemical composition is drastically simplified. For example, if the *static pressure*  $p$  and the *enthalpy*  $h$  are known, the equilibrium composition can be determined if the *mixture fraction*  $Z$  and thereby the element mass fractions of all elements present are known. This chemical equilibrium composition may then be determined a priori and therefore the need to evaluate the reaction rates during the actual flow calculation is removed.

#### 2.4.2 Conservation equation of energy

A further simplification may be made in the conservation equation of energy. The conservation equation of energy may be written in various forms. In low-speed turbulent flows, i.e. flows in which a characteristic Mach number is small compared with unity, it is customary to adopt the static enthalpy as the variable characterizing the energy content of the fluid and thus to make the following assumptions:

- the kinetic energy of the fluid can be neglected in comparison with the enthalpy,  $u_i u_i / 2 \ll h$
- changes in the enthalpy due to pressure fluctuations  $\partial p / \partial t$  are assumed to be small, but this only

holds if pressure waves are not too strong and if the flow is free to expand.

- the change of enthalpy due to work done by the body forces can be neglected.
- the change of enthalpy due to work done by viscous stresses can be neglected.
- the change of enthalpy due to radiation can be neglected.

The conservation equation of energy (2.17) can then be written as:

$$\rho \frac{Dh}{Dt} = -\frac{\partial q_j}{\partial x_j} \quad (2.41)$$

By substitution of Equation (2.27) for the heat flux vector into Equation (2.41) and making use of Equation (2.35) for the diffusion flux, the final conservation equation, the conservation equation of energy, can be written as:

$$\frac{\partial}{\partial t} \rho h + \frac{\partial}{\partial x_k} \rho u_k h = \frac{\partial}{\partial x_j} \left[ \frac{\lambda}{c_p} \frac{\partial h}{\partial x_j} + \sum_{i=1}^N \left( \rho D - \frac{\lambda}{c_p} \right) h_i \frac{\partial Y_i}{\partial x_j} \right] \quad (2.42)$$

This equation is significantly simplified under the assumption that  $\rho D = \lambda/c_p$ , that is, the Lewis number ( $Le$ ) defined as

$$Le = \frac{\lambda/c_p}{\rho D} = \frac{\alpha}{D} = \frac{\text{rate of energy transport}}{\text{rate of mass transport}} \quad (2.43)$$

equals 1. Thus we see that if the Lewis number is unity, then the energy equation in terms of the static enthalpy takes on a standard convection-diffusion form:

$$\frac{\partial}{\partial t} \rho h + \frac{\partial}{\partial x_k} \rho u_k h = \frac{\partial}{\partial x_j} \rho D \frac{\partial h}{\partial x_j} \quad (2.44)$$

The implication of the assumption  $Le=1$  is that, subjected to appropriate boundary and initial conditions, also the solution of the energy equation can be obtained from the solution for the conserved scalar  $Z$ . Therefore, if the energy Equation (2.44) is applied, the calculation of the state variables in a reacting flow is greatly simplified. For example, if chemical equilibrium prevails, the solution for the *static pressure*  $p$  and the *mixture fraction*  $Z$  yield the entire state of the fluid. In the case of large flames, change of enthalpy due to radiation cannot be neglected and  $h$  is independent of  $Z$ .

#### 2.4.3 Equation of state

The last assumption is that the density is not influenced by the static pressure, i.e. the medium is basically regarded to be incompressible. If pressure fluctuations are not too large, like in a free jet, it may be assumed that the density is only influenced by temperature changes, non-uniform density mixing and chemical reactions. The density may then be calculated from the equation of state (2.18) by inserting a characteristic value  $p_c$  for the static pressure  $p$ :

$$\rho = \frac{p_c}{R_0 T \sum_{k=1}^N \frac{Y_k}{W_k}} \quad (2.45)$$

The result of this last assumption is that, if chemical equilibrium prevails, the density has become a function of the *mixture fraction*  $Z$  only.

## Chapter 3

### Turbulent Flows

In this chapter, an averaging technique will be applied to the Navier-Stokes equations. Hence, a feasible system of equations will be obtained for the high Reynolds number regime that is of interest in the present study. The averaging technique is based on the so-called Reynolds decomposition in which a variable is split into a time-averaged part and a fluctuation. Correlation coefficients and standard deviations of the fluctuating variables may be used to define the turbulent length, time and velocity scales that characterize the turbulent flow field.

The  $k$ - $\varepsilon$  model will be used as a turbulence closure model, i.e. for modelling the correlation terms. The Favre-averaging technique will be used to avoid modelling of the density-velocity correlation terms. A presumed PDF method, in which the shape of the probability density function for the mixture fraction is prescribed, is used for obtaining the averaged scalar quantities like the time-averaged density.

In Section 3.4, the numerical solution algorithm will be described for an axi-symmetrical jet configuration. Use is made of a rectangular computational domain.

#### 3.1 TURBULENT LENGTH, TIME AND VELOCITY SCALES

A turbulent flow field may be characterized by several length, time and velocity scales. These scales are based on time-averaged (mean) properties of the flow field. A time-averaged quantity may be defined as follows. By taking samples of a certain quantity  $\phi$  in a turbulent flow at a certain time interval  $\Delta t$ , the mean value for  $\phi$  may be determined from

$$\bar{\phi} = \frac{1}{N} \sum_{k=1}^N \phi_k \quad (3.1)$$

where  $N$  is the total number of samples taken. This equation may also be written as

$$\bar{\phi} = \frac{1}{T} \sum_{k=1}^N \phi_k \Delta t \quad (3.2)$$

where  $T$  is the total measuring (or averaging) time,  $T = N\Delta t$ . By letting the time interval  $\Delta t$  approach zero a time-averaged value for  $\phi$  is defined by

$$\bar{\phi}(\underline{x}, t) = \frac{1}{T} \int_{\tau = -\frac{1}{2}T}^{\frac{1}{2}T} \phi(\underline{x}, t + \tau) d\tau \quad (3.3)$$

where  $T$  must be long enough to smooth out the turbulent fluctuations but short enough not to average out any imposed time dependence. However, in this thesis, only flows will be considered in which the mean quantities are constant in time. Equation (3.3) may then be replaced by an equation with  $T \rightarrow \infty$ .

Applying the so-called Reynolds decomposition, a variable  $\phi$  may be split into a time-averaged part  $\bar{\phi}$  and a fluctuation  $\phi'$ ,

$$\phi(\underline{x}, t) = \overline{\phi(\underline{x})} + \phi'(\underline{x}, t) \quad (3.4)$$

A general spatial correlation coefficient function  $\rho_{ij}$  may then be defined as

$$\rho_{ij}(x_1, x_2, x_3) = \frac{(\overline{\phi'_i})_A (\overline{\phi'_j})_B}{\sqrt{(\overline{\phi_i^2})_A} \sqrt{(\overline{\phi_j^2})_B}} \quad (3.5)$$

where  $\phi_i$  and  $\phi_j$  may be different scalar quantities or velocity components. For homogeneous isotropic turbulence, the general spatial velocity correlation coefficient function can be described in terms of the longitudinal and lateral correlation coefficients  $f(x_1)$  and  $g(x_2)$  (Hinze, 1959), respectively. The longitudinal velocity correlation coefficient is defined as

$$f(x_1) = \frac{\overline{u'_1(0)u'_1(x_1)}}{\sqrt{\overline{u_1^2(0)}} \sqrt{\overline{u_1^2(x_1)}}} \quad (3.6)$$

where  $x_1$  is in the mean-flow direction. The lateral correlation coefficient is defined as

$$g(x_2) = \frac{\overline{u'_1(0)u'_1(x_2)}}{\sqrt{\overline{u_1^2(0)}} \sqrt{\overline{u_1^2(x_2)}}} \quad (3.7)$$

where  $x_2$  is perpendicular to the mean-flow direction. For homogeneous isotropic turbulence,  $f$  and  $g$  may be expanded into Taylor series (Hinze, 1959) like

$$\begin{aligned} f(x_1) &= 1 - \frac{x_1^2}{2!} \frac{1}{\overline{u_1^2}} \left( \frac{\partial u'_1}{\partial x_1} \right)_{x_1=0}^2 + \frac{x_1^4}{4!} \frac{1}{\overline{u_1^2}} \left( \frac{\partial^2 u'_1}{\partial x_1^2} \right)_{x_1=0}^2 - \dots \\ g(x_2) &= 1 - \frac{x_2^2}{2!} \frac{1}{\overline{u_1^2}} \left( \frac{\partial u'_1}{\partial x_2} \right)_{x_2=0}^2 + \frac{x_2^4}{4!} \frac{1}{\overline{u_1^2}} \left( \frac{\partial^2 u'_1}{\partial x_2^2} \right)_{x_2=0}^2 - \dots \end{aligned} \quad (3.8)$$

Furthermore, for isotropic turbulence it holds that (Batchelor, 1956):

$$\frac{\overline{\partial u'_1 \partial u'_1}}{\partial x_1 \partial x_1} = \frac{\overline{\partial u'_2 \partial u'_2}}{\partial x_2 \partial x_2} = \frac{1}{2} \frac{\overline{\partial u'_1 \partial u'_1}}{\partial x_2 \partial x_2} \quad (3.9)$$

Therefore, for small values of  $x_1$  and  $x_2$ , Equation (3.8) may be written as

$$f(x_1) = 1 - \frac{x_1^2}{2\lambda^2}, \quad g(x_2) = 1 - \frac{x_2^2}{\lambda^2} \quad (3.10)$$

where  $\lambda$  is the so-called Taylor microscale:

$$\lambda = \sqrt{\frac{\overline{u_1^2}}{(\overline{\partial u'_1 / \partial x_1})^2}} \quad (3.11)$$

The Taylor microscale may also be expressed in terms of the turbulence kinetic energy  $k$  defined by

$$k = \frac{1}{2} \overline{u_i^2} \quad (3.12)$$

and its dissipation  $\varepsilon$  (see Section 3.2) which is for isotropic turbulence equal to

$$\varepsilon = \frac{\mu}{\rho} \overline{\frac{\partial u_i'}{\partial x_k} \frac{\partial u_i'}{\partial x_k}} \quad (3.13)$$

For isotropic turbulence it holds that  $\overline{u_1'^2} = \overline{u_2'^2} = \overline{u_3'^2}$  and therefore

$$k = \frac{1}{2} \overline{u_i'^2} = \frac{3}{2} \overline{u_1'^2} \quad (3.14)$$

and with Equation (3.9), the dissipation rate may be written as

$$\varepsilon = 15 \frac{\mu}{\rho} \overline{(\partial u_1' / \partial x_1)^2} \quad (3.15)$$

With Equation (3.14) and Equation (3.15) the Taylor microscale may then be written as

$$\lambda = \sqrt{10 \frac{\mu}{\rho} \frac{k}{\varepsilon}} \quad (3.16)$$

Turbulent flows consist of eddies of different sizes. The energy exchange between the mean flow and the turbulence is governed by the dynamics of the large eddies. The size of the largest energy containing eddies is usually described by the longitudinal integral length scale  $L_f$  defined by

$$L_f = \int_0^{\infty} f(x_1) dx_1 \quad (3.17)$$

This length scale tells us how far we would have to go from a point in the flow for the velocity fluctuations to become uncorrelated. The integral length scale is mainly determined by the burner geometry and it is of the order of the burner exit diameter. The lateral integral length scale  $L_g$  is defined by

$$L_g = \int_0^{\infty} g(x_2) dx_2 \quad (3.18)$$

For isotropic turbulence, the lateral integral length scale is equal to one-half times the longitudinal integral length scale (Batchelor, 1956). In this study, the integral length scale denoted by  $l_t$  refers to the longitudinal integral length scale  $L_f$ . Based on the calculated quantities  $k$  and  $\varepsilon$  (see Section 3.3.1), it may be approximated by (Peters, 1997)

$$l_t = L_f = 2L_g = 0.20 \frac{k^{3/2}}{\varepsilon} \quad (3.19)$$

A turbulent flow field may locally be characterized by a root-mean-square velocity fluctuation  $v' = \sqrt{u_i'^2}/3$ . In terms of the turbulence kinetic energy, the root-mean-square velocity fluctuation is given by:

$$v' = \sqrt{\frac{2}{3} k} \quad (3.20)$$

The turbulent time scale  $t_t$  is then given by



$$t_t = \frac{l_t}{v'} \quad (3.21)$$

Based on these integral scales, the turbulence Reynolds number is defined as

$$Re_t = \frac{\bar{\rho} v' l_t}{\mu} \quad (3.22)$$

The Kolmogorov length scale,  $\eta$ , is defined as the size of the smallest eddies in a turbulent flow, and can be estimated to be

$$\eta = \left( \frac{\mu^3}{\rho^3 \varepsilon} \right)^{1/4} \quad (3.23)$$

These eddies are also called the dissipating eddies because in these eddies the kinetic energy is dissipated by viscous action. Near to the burner exit, the Kolmogorov length scale can be as small as 0.1 mm. The Kolmogorov time scale is given by

$$t_\eta = \left( \frac{\mu}{\rho \varepsilon} \right)^{1/2} \quad (3.24)$$

Therefore, the Taylor microscale may also be expressed as

$$\lambda = \sqrt{15 \frac{\mu v'^2}{\rho \varepsilon}} = \sqrt{15} v' t_\eta \quad (3.25)$$

The Taylor microscale is not a direct measure of either the large energy-containing eddies nor of the smallest dissipating eddies. Equation (3.25) indicates that it may be interpreted as  $\sqrt{15}$  times the distance that a large eddy with velocity  $v'$  convects a Kolmogorov eddy during its turnover time  $t_\eta$ .

Another length scale frequently used in turbulence modelling is the so-called mixing length  $l_m$  introduced by Prandtl (1925). The mixing length may be compared to the integral length scale by considering an equilibrium, near-wall boundary layer. The 'law of the wall' (Hinze, 1959) states that the velocity distribution in the turbulent part of the boundary layer can be expressed as

$$\bar{u}(y) = \frac{u_\tau}{\kappa} \ln \left( \frac{u_\tau y}{\mu/\rho} \right) + A \quad (3.26)$$

where  $u_\tau = \sqrt{\tau_w/\rho}$  is the friction velocity, with  $\tau_w$  the mean wall shear stress and  $y$  is the distance normal to the wall. From Equation (3.26) it is obtained that

$$\frac{d\bar{u}}{dy} = \frac{u_\tau}{\kappa y} \quad (3.27)$$

The mixing length in the boundary layer is introduced as

$$l_m = \kappa y \quad (3.28)$$

with  $\kappa=0.40$  the universal von Kármán constant.

With the  $k$ - $\varepsilon$  turbulence model, the mean wall shear stress may be evaluated as

$$\tau_w = \mu_t \frac{d\bar{u}}{dy} \quad (3.29)$$

and Equation (3.27) may then be written as

$$\frac{d\bar{u}}{dy} = \frac{\mu_t}{\rho l_m^2} \quad (3.30)$$

For equilibrium conditions (production equals dissipation) Equation (3.55) reduces to

$$-\overline{u'v'} \frac{d\bar{u}}{dy} = \varepsilon \quad (3.31)$$

Furthermore, as we shall see from Equation (3.50) for the Reynolds stress tensor, it may be evaluated that

$$-\overline{\rho u'v'} = \mu_t \frac{d\bar{u}}{dy} \quad (3.32)$$

Combining Equation (3.30), (3.31) and (3.32) and solving for  $l_m$  leads with  $\mu_t = C_\mu \rho k^2 / \varepsilon$  to

$$l_m = C_\mu^{3/4} \frac{k^{3/2}}{\varepsilon} \quad (3.33)$$

Comparing Equation (3.33) for the mixing length to Equation (3.19) for the integral length scale it follows with  $C_\mu = 0.09$  that the mixing length is just slightly smaller than the integral length scale. It is noticed here that also other definitions and notations are used in literature. For example the notation  $l_t$  is often used to refer to the eddy length scale, i.e.  $l_t = k^{3/2} / \varepsilon$ . Such a definition would have a large influence on the other model constants in this thesis, for example the model constants in the expression for the turbulent burning velocity in Chapter 6. It is therefore important to mention that the definitions given in this section are used consistently throughout this study.

## 3.2 AVERAGED EQUATIONS

### (i) Continuity equation

Let us first consider the continuity equation as given by Equation (2.1). Time averaging according to Equation (3.3) leads to

$$\frac{\partial \overline{\rho u_j}}{\partial x_j} = 0 \quad (3.34)$$

Applying the Reynolds decomposition of Equation (3.4) we obtain

$$\frac{\partial \overline{\rho} \bar{u}_j}{\partial x_j} + \frac{\partial \overline{\rho' u_j'}}{\partial x_j} = 0 \quad (3.35)$$

where correlations  $\overline{\rho' u_j'}$  appear. These correlations are non-zero in flows with large density fluctuations like in a flame. Therefore they have to be modelled. Also in the averaged momentum equations these density-velocity correlation terms appear. To circumvent the modelling of these terms the Favre-averaging technique is now introduced. A mass-weighted or Favre-averaged quantity is defined as

$$\tilde{\phi} = \frac{\overline{\rho\phi}}{\bar{\rho}} \quad (3.36)$$

Substituting this into Equation (3.34) the time-averaged continuity equation reads

$$\frac{\partial \bar{\rho} \tilde{u}_j}{\partial x_j} = 0 \quad (3.37)$$

and we now want to find a solution for the time-averaged density  $\bar{\rho}$  and the Favre-averaged velocity components  $\tilde{u}_j$ .

### (ii) Momentum equations

With Favre-averaging, a quantity  $\phi$  may be decomposed into a Favre-averaged quantity  $\tilde{\phi}$  and a fluctuation  $\phi''$ ,

$$\phi(\underline{x}, t) = \tilde{\phi}(\underline{x}) + \phi''(\underline{x}, t) \quad (3.38)$$

By substituting this into the momentum equations (2.8) except for density and pressure, and applying time-averaging, the time-averaged momentum equations read, for steady flow

$$\frac{\partial}{\partial x_j} (\bar{\rho} \tilde{u}_i \tilde{u}_j) = -\frac{\partial \bar{p}}{\partial x_i} + \frac{\partial}{\partial x_j} (\bar{\tau}_{ij} + R_{ij}) + \bar{\rho} g_i \quad (i=1,2,3) \quad (3.39)$$

where  $\bar{\tau}_{ij}$  is the time-averaged shear stress tensor and  $R_{ij}$  is an element of the Reynolds-stress tensor,

$$R_{ij} = -\bar{\rho} \overline{u_i'' u_j''} \quad (3.40)$$

### (iii) Reynolds-stress transport equations

The Reynolds-stress transport equations may be obtained by multiplying the momentum equation for  $u_i$  with  $u_j''$ , time averaging and adding the same equation with  $i$  and  $j$  interchanged:

$$\begin{aligned} \bar{\rho} \tilde{u}_k \frac{\partial}{\partial x_k} \left( -\frac{R_{ij}}{\bar{\rho}} \right) - R_{jk} \frac{\partial \tilde{u}_i}{\partial x_k} - R_{ik} \frac{\partial \tilde{u}_j}{\partial x_k} + \frac{\partial}{\partial x_k} \left( \bar{\rho} \overline{u_i'' u_j'' u_k''} \right) = \\ -\overline{u_j'' \frac{\partial p}{\partial x_i}} - \overline{u_i'' \frac{\partial p}{\partial x_j}} + \frac{\partial}{\partial x_k} \left( -\mu \frac{\partial R_{ij}}{\partial x_k} \right) - \bar{\rho} \tilde{\epsilon}_{ij} \end{aligned} \quad (3.41)$$

where  $\tilde{\epsilon}_{ij}$  is an element of the dissipation rate tensor representing the work of viscous stresses due to fluctuation motion,

$$\tilde{\epsilon}_{ij} = \frac{\mu}{\bar{\rho}} \left\{ 2 \frac{\partial u_i''}{\partial x_k} \frac{\partial u_j''}{\partial x_k} - \overline{u_j'' \frac{\partial}{\partial x_i} \left( \frac{\partial u_k''}{\partial x_k} \right)} - \overline{u_i'' \frac{\partial}{\partial x_j} \left( \frac{\partial u_k''}{\partial x_k} \right)} \right\} \quad (3.42)$$

The second and third term between brackets are called dilatation dissipation and are usually neglected. Clearly the Reynolds-stress transport equations contain new cross-correlations, for which equations may be derived, which however will again contain unknown correlations.

(iv) Turbulence kinetic-energy equation

For  $i=j$ , Equation (3.41) becomes the turbulence-kinetic-energy equation:

$$\frac{\partial}{\partial x_k}(\bar{\rho}\tilde{u}_k\tilde{k}) = R_{ik}\frac{\partial\tilde{u}_i}{\partial x_k} - \overline{u_k''\frac{\partial p}{\partial x_k}} - \frac{1}{2}\frac{\partial}{\partial x_k}(\bar{\rho}\overline{u_k''\tilde{u}_i''u_i''}) + \frac{\partial}{\partial x_k}\left(\mu\frac{\partial\tilde{k}}{\partial x_k}\right) - \bar{\rho}\tilde{\epsilon} \quad (3.43)$$

where  $\tilde{k} = \frac{1}{2}\overline{u_i''u_i''}$  is called the turbulence kinetic energy, and  $\tilde{\epsilon}$  represents dissipation of turbulent energy by viscous motion,

$$\tilde{\epsilon} = \frac{\mu}{\bar{\rho}}\frac{\partial u_i''}{\partial x_k}\frac{\partial u_i''}{\partial x_k} \quad (3.44)$$

(v) Mixture fraction equation

Time-averaging of Equation (2.40) gives the equation for the Favre-averaged mixture fraction, for steady flow

$$\frac{\partial}{\partial x_k}(\bar{\rho}\tilde{u}_k\tilde{Z}) = \frac{\partial}{\partial x_k}\left(\overline{\rho D\frac{\partial Z}{\partial x_k}} - \bar{\rho}\overline{u_k''\tilde{Z}''}\right) \quad (3.45)$$

(vi) Mixture fraction variance equation

Multiplying the mixture fraction Equation (2.40) by its fluctuation  $Z''$ , and applying time averaging gives the equation for the mixture fraction variance, for steady flow

$$\frac{\partial}{\partial x_k}(\bar{\rho}\tilde{u}_k\tilde{Z}''^2) = \frac{\partial}{\partial x_k}\left(\overline{\rho D\frac{\partial Z''^2}{\partial x_k}} - \bar{\rho}\overline{u_k''(Z''^2)''}\right) + P_{Z''^2} - \bar{\rho}\epsilon_{Z''^2} \quad (3.46)$$

where  $P_{Z''^2}$  represents the production of mixture fraction fluctuations,

$$P_{Z''^2} = -2\bar{\rho}\overline{u_k''Z''}\frac{\partial\tilde{Z}}{\partial x_k} \quad (3.47)$$

and  $\epsilon_{Z''^2}$  represents dissipation by molecular diffusion,

$$\epsilon_{Z''^2} = 2D\frac{\partial Z''}{\partial x_k}\frac{\partial Z''}{\partial x_k} \quad (3.48)$$

(v) Equation of state

If the given system of equations can be solved for the Favre-averaged velocities,  $\bar{p}$ ,  $\tilde{k}$ ,  $\tilde{\epsilon}$ ,  $\tilde{Z}$  and  $\tilde{Z}''^2$ , then the time-averaged density is obtained by time-averaging the equation of state (2.45):

$$\bar{\rho} = p_c / \left( R_0 T \sum_{k=1}^N \frac{Y_k}{W_k} \right) \quad (3.49)$$

How to obtain this time-averaged density and all other scalar quantities like the species mass fractions and the temperature will be treated in Section 3.3.2.

### 3.3 TURBULENCE CLOSURE MODEL

In the preceding section a set of equations has been derived for the Favre-averaged velocities, turbulence kinetic energy, Favre-averaged mixture fraction, mixture fraction variance, and time-averaged density. However, due to the averaging process, correlation terms of fluctuating variables were introduced. In order to close the given set of equations, a turbulence model has to be used that relates these correlation terms to the quantities for which the equations are being solved.

Various models have been proposed to achieve closure of the equations for turbulence in reacting flow systems. The model used in this study is the so-called  $k$ - $\varepsilon$  two-equation model that was introduced by Jones and Launder (1972) for recirculating flows.

#### 3.3.1 $k$ - $\varepsilon$ turbulence model

##### (i) Momentum equations

A linear relationship is assumed between Reynolds stress and the rate of strain:

$$R_{ij} = \mu_t \left( \frac{\partial \tilde{u}_i}{\partial x_j} + \frac{\partial \tilde{u}_j}{\partial x_i} \right) - \frac{2}{3} \delta_{ij} \left( \bar{\rho} k + \mu_t \frac{\partial \tilde{u}_j}{\partial x_j} \right) \quad (3.50)$$

The time-averaged viscous shear stress tensor is approximated by

$$\bar{\tau}_{ij} = \mu \left( \frac{\partial \tilde{u}_i}{\partial x_j} + \frac{\partial \tilde{u}_j}{\partial x_i} \right) - \frac{2}{3} \mu \frac{\partial \tilde{u}_i}{\partial x_i} \delta_{ij} \quad (3.51)$$

The time-averaged shear stress tensor and the Reynolds stress tensor are often combined by replacing the turbulent viscosity in Equation (3.50) by the effective viscosity  $\mu_{eff} = \mu_t + \mu$ , i.e. like

$$\bar{\tau}_{ij} + R_{ij} = \mu_{eff} \left( \frac{\partial \tilde{u}_i}{\partial x_j} + \frac{\partial \tilde{u}_j}{\partial x_i} \right) - \frac{2}{3} \delta_{ij} \left( \bar{\rho} k + \mu_{eff} \frac{\partial \tilde{u}_j}{\partial x_j} \right) \quad (3.52)$$

The turbulent viscosity is often much larger than the molecular viscosity. In analogy with the constant density model, the turbulent viscosity is modelled as

$$\mu_t = C_\mu \bar{\rho} \frac{\tilde{k}^2}{\varepsilon} \quad (3.53)$$

where the turbulence constant  $C_\mu = 0.09$ . Equation (3.53) makes the turbulent viscosity proportional to the mean density. However, that dependency is uncertain. In fact, Equation (3.53) may lead to unrealistic results in stagnating turbulence with significant density fluctuations (Bray *et al.*, 1991). Although in future research additional attention should be given to the influence of

density fluctuations on the turbulent viscosity, at present, Equation (3.53) is used without modification.

(ii) Turbulence kinetic-energy equation

In Equation (3.43), the pressure gradient term has been neglected because in the type of flows considered in the present study this term is sufficiently small to neglect it. The turbulent diffusion term has been modelled by using a Boussinesq-type hypothesis and a fixed Prandtl number  $\sigma_k$ :

$$-\overline{\rho} \frac{\partial \tilde{u}_i \tilde{u}_i}{\partial x_k} = \frac{\mu_t}{\sigma_k} \frac{\partial \tilde{u}_i \tilde{u}_i}{\partial x_k} \quad (3.54)$$

This leads to the following equation for  $\tilde{k}$ :

$$\frac{\partial}{\partial x_k} \overline{\rho} \tilde{u}_k \tilde{k} = \frac{\partial}{\partial x_k} \left[ \left( \frac{\mu_t}{\sigma_k} + \mu \right) \frac{\partial \tilde{k}}{\partial x_k} \right] + P_k - \overline{\rho} \tilde{\epsilon} \quad (3.55)$$

where  $P_k = R_{ik} \frac{\partial \tilde{u}_i}{\partial x_k}$  represents the production of turbulence kinetic energy in which the Reynolds stress term is modelled by Equation (3.50).

(iii) Equation for the dissipation rate

The turbulence dissipation rate  $\tilde{\epsilon}$  is found from the following transport equation (Hanjalic *et al.*, 1972):

$$\frac{\partial}{\partial x_k} \overline{\rho} \tilde{u}_k \tilde{\epsilon} = \frac{\partial}{\partial x_k} \left[ \left( \frac{\mu_t}{\sigma_\epsilon} + \mu \right) \frac{\partial \tilde{\epsilon}}{\partial x_k} \right] + \frac{\tilde{\epsilon}}{\tilde{k}} (C_1 P_k - C_2 \overline{\rho} \tilde{\epsilon}) \quad (3.56)$$

which is very similar to the equation for the turbulent kinetic energy. The large-eddy frequency  $\tilde{\epsilon}/\tilde{k}$  has been used to model the production and dissipation terms. A Boussinesq-type hypothesis is employed with the Prandtl number  $\sigma_\epsilon$ . The constants in the  $k$ - $\epsilon$  model are determined empirically (Jones *et al.*, 1972) by considering various equilibrium turbulent flows. The constants are given in Table 3.1

$C_\mu$	$C_1$	$C_2$	$\sigma_k$	$\sigma_\epsilon$
0.09	1.44	1.92	1	1.3

Table 3.1 Standard model coefficients in the  $k$ - $\epsilon$  model

(v) Mixture fraction equation

A Boussinesq approximation is adopted for the turbulent flux of scalar quantities, namely

$$-\overline{\rho} \frac{\partial \tilde{u}_j \tilde{\phi}}{\partial x_j} = \frac{\mu_t}{\sigma_{t,\phi}} \frac{\partial \tilde{\phi}}{\partial x_j} \quad (3.57)$$

where  $\sigma_{t,\phi}$  is a fixed turbulent Schmidt number.

The mean molecular fluxes are relatively unimportant compared to the turbulent fluxes and are (with  $Le=1$ ) modelled by

$$\overline{\rho D \frac{\partial \Phi}{\partial x_k}} = \frac{\mu}{\sigma} \frac{\partial \tilde{\Phi}}{\partial x_k} \quad (3.58)$$

For the mixture fraction Equation (3.45) this leads to

$$\frac{\partial}{\partial x_k} \overline{\rho \tilde{u}_k \tilde{Z}} = \frac{\partial}{\partial x_k} \left[ \left( \frac{\mu_t}{\sigma_{t,Z}} + \frac{\mu}{\sigma} \right) \frac{\partial \tilde{Z}}{\partial x_k} \right] \quad (3.59)$$

It is common practice to take the Schmidt number  $\sigma_{t,Z}$  equal to 0.7 for free shear flows.

#### (vi) Mixture fraction variance equation

Applying the Boussinesq approximation to the mixture fraction variance Equation (3.46) leads to

$$\frac{\partial}{\partial x_k} (\overline{\rho \tilde{u}_k \tilde{Z}''^2}) = \frac{\partial}{\partial x_k} \left[ \left( \frac{\mu_t}{\sigma_{t,Z}''^2} + \frac{\mu}{\sigma} \right) \frac{\partial \tilde{Z}''^2}{\partial x_k} \right] + P_{Z''^2} - \overline{\rho \epsilon_{Z''^2}} \quad (3.60)$$

where the Schmidt number  $\sigma_{t,Z}''^2$  is equal to 0.7. The production of mixture fraction fluctuations is modelled as

$$P_{Z''^2} = \frac{\mu_t}{\sigma_{t,Z}} \left( \frac{\partial \tilde{Z}}{\partial x_k} \right)^2 \quad (3.61)$$

For modelling the scalar dissipation rate  $\epsilon_{Z''^2}$ , a classical model has been used based on the assumption of proportionality of time scales for mechanical and scalar turbulence,  $\tilde{k}/\epsilon - \tilde{Z}''^2/\epsilon_{Z''^2}$ , with a constant of proportionality close to 2 (Beguier *et al.*, 1978),

$$\epsilon_{Z''^2} = 2 \frac{\tilde{\epsilon}}{\tilde{k}} \tilde{Z}''^2 \quad (3.62)$$

### 3.3.2 Presumed PDF method

The system of equations given in the preceding section is closed by solving the equation of state (3.49) for the time-averaged density. Here it is assumed that the mixture is in chemical equilibrium. How to treat non-equilibrium chemistry will be outlined in Chapter 5. For equilibrium chemistry all scalar quantities, except for the pressure, are functions of the mixture fraction  $Z$  only:

$$\phi = \phi(Z) \quad (3.63)$$

Similar to Section 3.1 for time, now the domain for  $Z$  is split into a number of intervals  $\Delta Z_j$  ( $j=1, \dots, N_{\text{intervals}}$ ) with a discrete value  $Z_j$  being within the interval  $\Delta Z_j$ . A discrete probability density function  $P(Z_j)$  may then be defined in such a way that  $P(Z_j)$  times the width of the interval  $\Delta Z_j$  gives the probability of  $Z$  being within that interval. Therefore, when measuring,  $P(Z_j)$  may be determined from

$$P(Z_j)\Delta Z_j = \frac{N_{\Delta Z_j}}{N} \quad (3.64)$$

where  $N_{\Delta Z_j}$  is the number of samples within interval  $\Delta Z_j$  and  $N$  the total number of samples taken. Constructing a PDF in this way from measurements often reveals a remarkable and almost universal structure. This is, like in this study, often taken advantage of in combustion modelling.

If the PDF for  $Z$  is known, then a time-averaged value for the scalar  $\phi$  may be approximated by

$$\bar{\phi} \approx \sum_{j=1}^{N_{intervals}} \frac{\phi(Z_j) N_{\Delta Z_j}}{N} = \sum_{j=1}^{N_{intervals}} \phi(Z_j) P(Z_j) \Delta Z_j \quad (3.65)$$

By letting the interval widths  $\Delta Z_j$  approach zero, one obtains (with  $Z$  scaled between 0 and 1):

$$\bar{\phi} = \int_{Z=0}^1 \phi(Z) P(Z) dZ \quad (3.66)$$

A Favre-averaged scalar quantity may be calculated by

$$\bar{\phi} = \frac{\overline{\rho\phi}}{\bar{\rho}} = \int_{Z=0}^1 \phi(Z) \frac{\rho(Z)P(Z)}{\bar{\rho}} dZ = \int_{Z=0}^1 \phi(Z) \tilde{P}(Z) dZ \quad (3.67)$$

where  $\tilde{P}(Z)$  is the so-called Favre PDF for  $Z$ ,

$$\tilde{P}(Z) = \frac{\rho(Z)P(Z)}{\bar{\rho}} \quad (3.68)$$

Making use of the presumed PDF method, it is assumed that the shape of the PDF for  $Z$  may be prescribed by the Favre-averaged mixture fraction and its variance. It is often approximated by a beta-function distribution,

$$\tilde{P}(Z) = \frac{Z^{a-1}(1-Z)^{b-1}}{\beta(a,b)} \quad (3.69)$$

where  $\beta(a,b)$  is the beta-function,

$$\beta(a,b) = \int_0^1 Z^{a-1}(1-Z)^{b-1} dZ \quad (3.70)$$

with

$$\begin{aligned} a &= \gamma \tilde{Z} \\ b &= \gamma(1-\tilde{Z}) \\ \gamma &= \frac{\tilde{Z}(1-\tilde{Z})}{\tilde{Z}^2} - 1 \end{aligned} \quad (3.71)$$

Aside from the mathematical convenience, prescribing the shape of the Favre PDF instead of that for the conventional PDF is justified because the conventional PDF's in a mixing layer are influenced by the density ratio (Roshko, 1976). The PDF in a constant-density layer tends to show more symmetry than the PDF in a layer with large differences in density. However, when measurement data are reworked in terms of the Favre probability density function, it is very similar to that found in uniform density flow (Kennedy *et al.*, 1979). Favre quantities behave like conventional quantities in isothermal flows, and therefore the PDF is prescribed as a Favre PDF.



The time-averaged density may be obtained by making use of the fact that

$$\int_{Z=0}^1 P(Z) dZ = 1 \quad (3.72)$$

and replacing the conventional PDF in Equation (3.72) by the Favre PDF according to Equation (3.68) then leads to

$$\bar{\rho} = \left[ \int_{Z=0}^1 \frac{\tilde{P}(Z)}{\rho(Z)} dZ \right]^{-1} \quad (3.73)$$

All other time-averaged scalar quantities may then be obtained by replacing the conventional PDF in Equation (3.66) by the Favre PDF according to Equation (3.68):

$$\bar{\phi} = \int_{Z=0}^1 \phi(Z) \frac{\bar{\rho} \tilde{P}(Z)}{\rho(Z)} dZ \quad (3.74)$$

### 3.4 NUMERICAL SOLUTION ALGORITHM

In the present investigation of axi-symmetrical turbulent jet flows, first a cylindrical system of coordinates with the  $x_1$ -axis coinciding with the centerline of the jet (Figure 3.1) is introduced. The transformation reads:

$$\begin{aligned} x &= x_1 \\ r &= \sqrt{x_2^2 + x_3^2} \\ \theta &= \arctan(x_3/x_2) \end{aligned} \quad (3.75)$$

and cylindrical velocity components are introduced according to

$$\begin{aligned} u &= u_1 \\ v &= u_2 \cos \theta + u_3 \sin \theta \\ w &= u_3 \cos \theta - u_2 \sin \theta \end{aligned} \quad (3.76)$$

where  $u$ ,  $v$  and  $w$  are the axial, radial and tangential velocity components, respectively. The tangential velocity component  $w$  is also called the azimuthal or swirl velocity component.

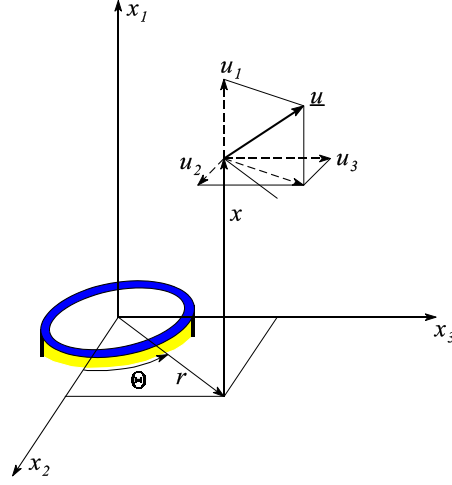


Figure 3.1 Cylindrical coordinate system.

Because of axial-symmetry the gradients in  $\theta$  direction are zero, i.e.  $\partial./\partial\theta=0$ . In this study, swirling flows will not be considered. Therefore the mean tangential velocity component equals zero, i.e.  $\tilde{w}=0$ . In cylindrical coordinates the equations read:

(i) Continuity

$$\frac{\partial}{\partial x}(\bar{\rho}\tilde{u}) + \frac{1}{r} \frac{\partial}{\partial r}(r\bar{\rho}\tilde{v}) = 0 \quad (3.77)$$

(ii) Momentum

$x$ -component,

$$\frac{\partial}{\partial x}(\bar{\rho}\tilde{u}\tilde{u}) + \frac{1}{r} \frac{\partial}{\partial r}(r\bar{\rho}\tilde{u}\tilde{v}) = -\frac{\partial \bar{p}}{\partial x} + \frac{\partial}{\partial x} \left[ \frac{4}{3} \mu_{eff} \frac{\partial \tilde{u}}{\partial x} - \frac{2}{3} \bar{\rho} \tilde{k} \right] + \frac{1}{r} \frac{\partial}{\partial r} \left[ r \mu_{eff} \left( \frac{\partial \tilde{u}}{\partial r} + \frac{\partial \tilde{v}}{\partial x} \right) \right] - \bar{\rho} g \quad (3.78)$$

$r$ -component,

$$\frac{\partial}{\partial x}(\bar{\rho}\tilde{u}\tilde{v}) + \frac{1}{r} \frac{\partial}{\partial r}(r\bar{\rho}\tilde{v}\tilde{v}) = -\frac{\partial \bar{p}}{\partial r} + \frac{\partial}{\partial x} \left[ \mu_{eff} \left( \frac{\partial \tilde{v}}{\partial x} + \frac{\partial \tilde{u}}{\partial r} \right) \right] + \frac{1}{r} \frac{\partial}{\partial r} \left[ r \left( \frac{4}{3} \mu_{eff} \frac{\partial \tilde{v}}{\partial r} - \frac{2}{3} \bar{\rho} \tilde{k} \right) \right] - \frac{1}{r} \left( 2\mu_r \frac{\tilde{v}}{r} - \frac{2}{3} \bar{\rho} \tilde{k} \right) \quad (3.79)$$

(iii) Turbulence kinetic energy

$$\frac{\partial}{\partial x}(\bar{\rho}\tilde{u}\tilde{k}) + \frac{1}{r} \frac{\partial}{\partial r}(r\bar{\rho}\tilde{v}\tilde{k}) = \frac{\partial}{\partial x} \left[ \left( \frac{\mu_t}{\sigma_k} + \mu \right) \frac{\partial \tilde{k}}{\partial x} \right] + \frac{1}{r} \frac{\partial}{\partial r} \left[ r \left( \frac{\mu_t}{\sigma_k} + \mu \right) \frac{\partial \tilde{k}}{\partial r} \right] + P_k - \bar{\rho} \tilde{\epsilon} \quad (3.80)$$

where

$$P_k = \mu_t \left[ 2 \left\{ \left( \frac{\partial \tilde{u}}{\partial x} \right)^2 + \left( \frac{\partial \tilde{v}}{\partial r} \right)^2 + \left( \frac{\tilde{v}}{r} \right)^2 \right\} + \left( \frac{\partial \tilde{u}}{\partial r} + \frac{\partial \tilde{v}}{\partial x} \right)^2 \right] \quad (3.81)$$

(iv) Dissipation rate

$$\frac{\partial}{\partial x}(\bar{\rho}\tilde{u}\tilde{\epsilon}) + \frac{1}{r} \frac{\partial}{\partial r}(r\bar{\rho}\tilde{v}\tilde{\epsilon}) = \frac{\partial}{\partial x} \left[ \left( \frac{\mu_t}{\sigma_\epsilon} + \mu \right) \frac{\partial \tilde{\epsilon}}{\partial x} \right] + \frac{1}{r} \frac{\partial}{\partial r} \left[ r \left( \frac{\mu_t}{\sigma_\epsilon} + \mu \right) \frac{\partial \tilde{\epsilon}}{\partial r} \right] + \frac{\tilde{\epsilon}}{\tilde{k}} (C_1 P_k - C_2 \bar{\rho}\tilde{\epsilon}) \quad (3.82)$$

(v) Mixture fraction

$$\frac{\partial}{\partial x}(\bar{\rho}\tilde{u}\tilde{Z}) + \frac{1}{r} \frac{\partial}{\partial r}(r\bar{\rho}\tilde{v}\tilde{Z}) = \frac{\partial}{\partial x} \left[ \left( \frac{\mu_t}{\sigma_{t,Z}} + \mu \right) \frac{\partial \tilde{Z}}{\partial x} \right] + \frac{1}{r} \frac{\partial}{\partial r} \left[ r \left( \frac{\mu_t}{\sigma_{t,Z}} + \mu \right) \frac{\partial \tilde{Z}}{\partial r} \right] \quad (3.83)$$

(vi) Mixture fraction variance

$$\frac{\partial}{\partial x}(\bar{\rho}\tilde{u}\tilde{Z}^{\prime 2}) + \frac{1}{r} \frac{\partial}{\partial r}(r\bar{\rho}\tilde{v}\tilde{Z}^{\prime 2}) = \frac{\partial}{\partial x} \left[ \left( \frac{\mu_t}{\sigma_{t,Z}} + \mu \right) \frac{\partial \tilde{Z}^{\prime 2}}{\partial x} \right] + \frac{1}{r} \frac{\partial}{\partial r} \left[ r \left( \frac{\mu_t}{\sigma_{t,Z}} + \mu \right) \frac{\partial \tilde{Z}^{\prime 2}}{\partial r} \right] + P_{\tilde{Z}^{\prime 2}} - \bar{\rho}\epsilon_{\tilde{Z}^{\prime 2}} \quad (3.84)$$

where

$$P_{\tilde{Z}^{\prime 2}} = \frac{\mu_t}{\sigma_{t,Z}} \left[ \left( \frac{\partial \tilde{Z}}{\partial x} \right)^2 + \left( \frac{\partial \tilde{Z}}{\partial r} \right)^2 \right] \quad (3.85)$$

Each of the derived transport equations may be written in a general form,

$$\frac{\partial}{\partial x}(\rho u \phi) + \frac{1}{r} \frac{\partial}{\partial r}(r \rho v \phi) = \frac{\partial}{\partial x} \left( \Gamma \frac{\partial \phi}{\partial x} \right) + \frac{1}{r} \frac{\partial}{\partial r} \left( r \Gamma \frac{\partial \phi}{\partial r} \right) + S \quad (3.86)$$

where  $\phi$  is equal to 1 for conservation of mass,  $u$  and  $v$  for conservation of momentum,  $Z$  for conservation of elements,  $\tilde{Z}^{\prime 2}$ ,  $\tilde{k}$  or  $\tilde{\epsilon}$ .  $\Gamma$  is a generalized exchange coefficient and  $S$  is the so-called source term.

Equations of the type of Equation (3.86) may be solved numerically by dividing the flow domain into control volumes. The calculation domain used for calculating the turbulent jets is rectangular and the grid is as indicated in Figure 3.2. The grid is most dense near the nozzle. In the core region of the jet ( $x/D \leq 5$ ) the grid spacing is kept constant. Outside the core region, the grid spacing in  $x$ - and  $r$ -direction increases linearly with  $x$  and  $r$ , respectively. To ensure that the boundary of the computational domain is sufficiently far away from the jet, the width of the computational domain is about 2.5 times the half-width of the jet (see Section 4) at its most downstream position. This results in a width to length ratio of about 0.25.

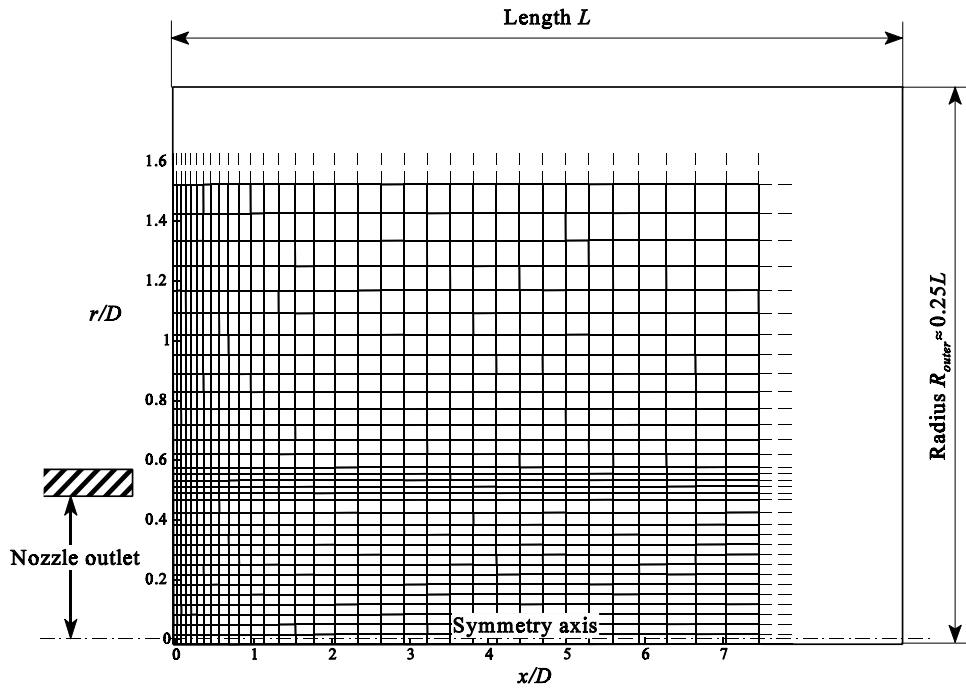


Figure 3.2 Computational domain and grid.

The grid is staggered for the axial and radial velocity components, i.e. velocity components are computed in different control volumes than the scalar variables. The control volumes are as indicated in Figure 3.3. The velocity components are computed on the control volume-faces associated with the scalar variables because the velocity components are needed there to evaluate the convective fluxes of the scalar quantities. The velocity gridpoints are located midway between the scalar-quantity gridpoints. The velocity control-volume faces are midway between the velocity gridpoints. By this well known procedure, so-called checker board oscillations in the predicted pressure field are avoided.

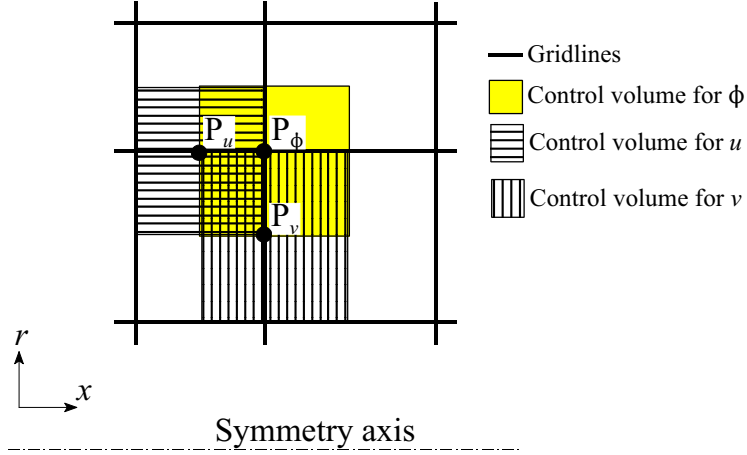


Figure 3.3 Control volumes.

By integration of Equation (3.86) over the control volume of Figure (3.4), the following balance equation is obtained:

$$(\rho_e u_e \phi_e - \rho_w u_w \phi_w) r \delta r \delta \theta + (r_n \rho_n v_n \phi_n - r_s \rho_s v_s \phi_s) \delta x \delta \theta = \left( \Gamma_e \frac{\partial \phi}{\partial x} \Big|_e - \Gamma_w \frac{\partial \phi}{\partial x} \Big|_w \right) r \delta r \delta \theta + \left( r_n \Gamma_n \frac{\partial \phi}{\partial x} \Big|_n - r_s \Gamma_s \frac{\partial \phi}{\partial x} \Big|_s \right) \delta x \delta \theta + S r \delta x \delta r \delta \theta \quad (3.87)$$

The lower-case subscripts  $e$ ,  $w$ ,  $n$  and  $s$  denote evaluation at the control volume faces. The quantities are evaluated at the control faces employing linear interpolation, for example

$$\phi_n = \frac{\phi_P + \phi_N}{2} \quad (3.88)$$

The gradients in the diffusive terms are discretized by a second-order scheme:

$$\begin{aligned} \frac{\partial \phi}{\partial x} \Big|_e &= \frac{\phi_E - \phi_P}{\delta x_e}, & \frac{\partial \phi}{\partial x} \Big|_w &= \frac{\phi_P - \phi_W}{\delta x_w} \\ \frac{\partial \phi}{\partial x} \Big|_n &= \frac{\phi_N - \phi_P}{\delta r_n}, & \frac{\partial \phi}{\partial r} \Big|_s &= \frac{\phi_P - \phi_S}{\delta r_s} \end{aligned} \quad (3.89)$$

The discretized equation, as described extensively by Patankar (1980), may then be written as:

$$A_P \phi_P = A_E \phi_E + A_W \phi_W + A_N \phi_N + A_S \phi_S + S r \delta x \delta r \quad (3.90)$$

with  $A_P = A_E + A_W + A_N + A_S$

The coefficients  $A_k$  represent the influence of the value of  $\phi_k$  on the corresponding gridpoint through convective and diffusive effects. The source term  $S$  in general is a non-linear function of  $\phi$  and it is linearized as  $S = S_C + S_P \phi_P$ . Incorporation of linear dependence is better than treating  $S$  as a constant because proper linearization of the source term frequently is the key to obtaining a converging solution procedure (Patankar, 1980). With this procedure Equation (3.90) becomes:

$$(A_P - S_P r \delta x \delta r) \phi_P = A_E \phi_E + A_W \phi_W + A_N \phi_N + A_S \phi_S + S_C r \delta x \delta r \quad (3.91)$$

In the present study the so-called ‘hybrid-scheme’ is used for the coefficients  $A_k$ ,

$$\begin{aligned} A_E &= \max\left(\frac{1}{2}|C_e|, D_e\right) - \frac{1}{2}C_e, & A_W &= \max\left(\frac{1}{2}|C_w|, D_w\right) + \frac{1}{2}C_w \\ A_N &= \max\left(\frac{1}{2}|C_n|, D_n\right) - \frac{1}{2}C_n, & A_S &= \max\left(\frac{1}{2}|C_s|, D_s\right) + \frac{1}{2}C_s \end{aligned} \quad (3.92)$$

where the convection and diffusion coefficients are given by  $C_e = \rho_e u_e r \delta r$  and  $D_e = (\Gamma_e / \delta x_e) r \delta r$  and similar expressions for the other coefficients. When the local Peclet number ( $P_k = C_k / D_k$ ) is larger than 2, diffusive fluxes are neglected. This procedure is known as ‘upwind’ differencing and it is used to stabilize the numerical algorithm. The resulting first-order accuracy presents no problem when the grid spacing is small enough. Stabilization is also enhanced when all coefficients  $A_k$  are positive, and therefore the coefficient  $S_p$  should always be negative.

The equations of the type of Equation (3.91) are solved by the Tri-Diagonal-Matrix-Algorithm (TDMA) (Press *et al.*, 1992). To prevent divergence of the procedure to solve the coupled set of equations, an under-relaxation method is employed.

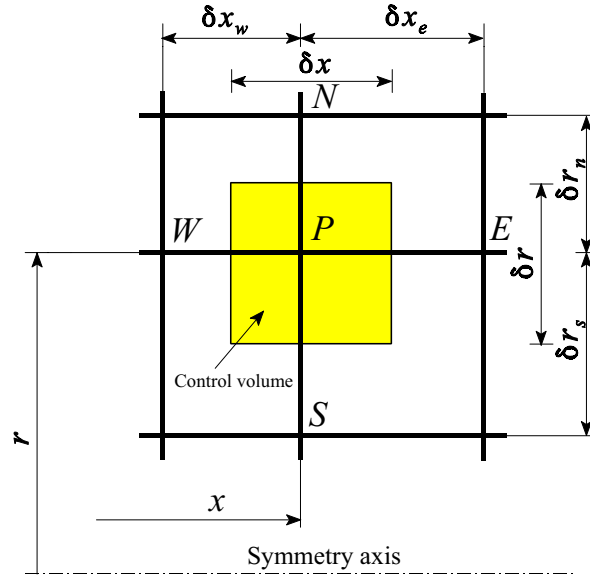


Figure 3.4 Control volume.

Boundary conditions can be implemented as either Dirichlet or Neumann boundary conditions. Dirichlet, or fixed-value, boundary conditions are implemented by setting the quantity at boundary gridpoints to a certain fixed value and applying a sufficient strong convective flux. Neumann, or zero-gradient, boundary conditions are implemented by setting the corresponding coefficient  $A_k$  to zero, thereby breaking the connection between the boundary gridpoint and the ‘live’ gridpoint where the solution is computed. For example for a turbulent jet diffusion flame without a co-flow and a uniform outlet profile with outlet velocity  $U_{outlet}$  and turbulence intensity  $I$ , boundary conditions for the different variables may be implemented as indicated in Figure 3.5.

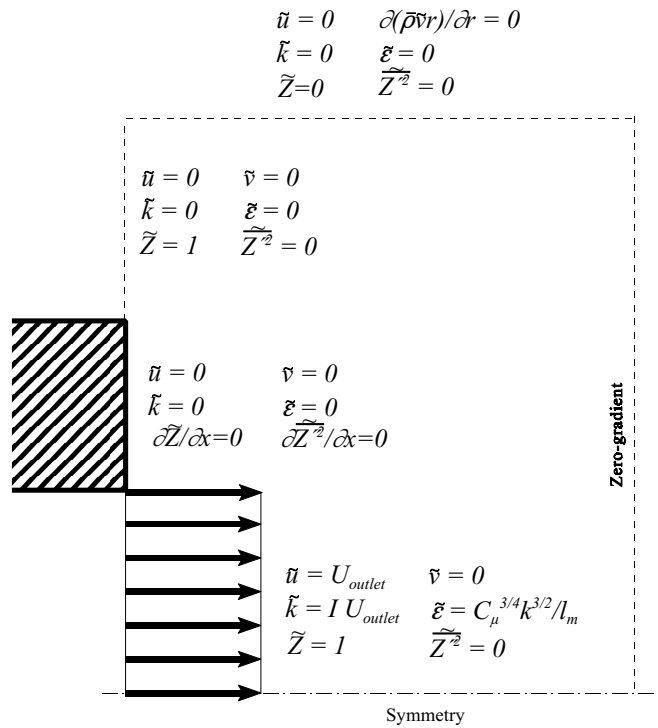


Figure 3.5 Boundary conditions.

The procedure employed for the numerical simulation of the flow field is the so-called SIMPLE algorithm. The name SIMPLE stands for Semi-Implicit Method for Pressure-Linked Equations. In this method the continuity equation is used to obtain a so-called pressure correction equation. This is arrived at by decomposing  $u$  and  $v$  into the computed velocities,  $u^*$  and  $v^*$ , and velocity corrections,  $u'$  and  $v'$ . That is  $u = u^* + u'$  and  $v = v^* + v'$ . Similarly the pressure is written as  $p = p^* + p'$ . From the discretized momentum equations, equations relating  $u'$  to  $p'$  and  $v'$  to  $p'$  can be found. Finally, by using the continuity equation, a pressure correction for  $p'$  is obtained.

The order in which the equations in the SIMPLE algorithm are solved is:

1. Compute  $u^*$  and  $v^*$  from the momentum equations with the guessed pressure and density field.
2. Compute  $p'$  from the pressure-correction equation.
3. Update the pressure with  $p'$ .
4. Update the velocity with the velocity-corrections  $u'$  and  $v'$ .
5. Compute scalar variables such as  $\tilde{k}$ ,  $\tilde{\varepsilon}$ ,  $\tilde{Z}$ ,  $\tilde{Z}^2$ , and  $\tilde{\rho}$ .
6. Return to 1, until convergence is achieved.

Figure 3.6 shows the result of a simulation of a high Reynolds number ( $Re = 16500$ ) turbulent air jet to be discussed in Section 4.2.7. The simulation has been performed on a computational domain with a length of 50 nozzle diameters and a width of 12.5 nozzle diameters. The computation involved 50 radial grid nodes while the number of grid points in axial directions was varied from 50 to 80 and 100 nodes. The results show hardly any difference between the computations with 80 and 100 nodes in axial direction. Therefore, for the computation with 80 nodes in axial direction the numerical accuracy is expected to exceed the uncertainties of other aspects of the predictions. For this prediction, the grid expands in axial direction with an expansion factor of 1.05. A number of 15 nodes was used for the nozzle outlet profile, and 3 nodes at the nozzle wall. In the co-flow, the expansion factor in radial direction was equal to 1.1. Increasing the number of grid points in radial direction had no significant effect on the outcome of the computations.

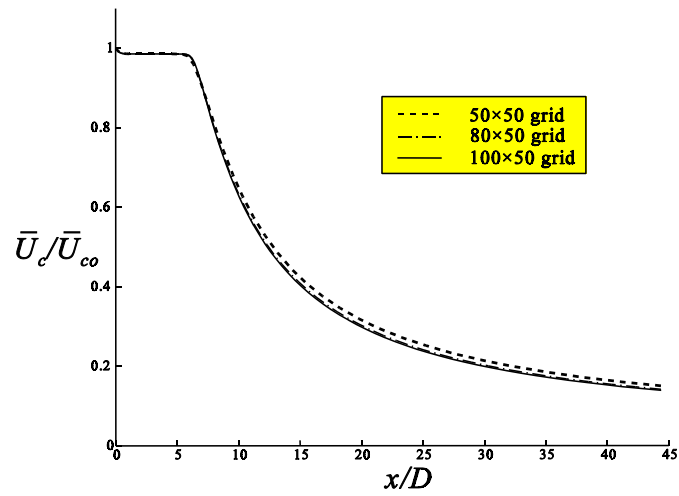


Figure 3.6 Varying the number of grid points in axial direction.





## Chapter 4

### Axi-symmetrical turbulent jets

Axi-symmetric turbulent jet flows belong to the family of free turbulent flows. Free turbulence is encountered in a flow field where there is no direct effect of any fixed boundary on the turbulence in the flow. Also the plane jet and the mixing layer between two parallel flows with different mean velocities (which is often called the half jet) are examples of free turbulent flows. Another group of free turbulent flows is given by the wake flows behind obstacles, like the plane wake behind a cylindrical rod or the circular wake behind a sphere. These examples may also be categorized into plane mean flows and rotationally symmetric (axi-symmetrical) mean flows.

In Section 4.1, a mathematical model will be used for introducing some important characteristics of an axi-symmetric turbulent jet flows. Important parameters describing an axi-symmetrical turbulent jet flow will be introduced like the so-called entrainment rate, the decay constants and the half-width spreading rates.

The hot-wire anemometry method will be used for performing measurements in a turbulent jet. Some of the important jet-characteristics will be measured and compared to results obtained with the standard  $k$ - $\epsilon$  model. Section 4.2 is concerned with the interpretation of the time averaged signals from an X hot-wire probe and the development of a related look-up inversion method. In the present study, a correction method has been developed that accounts for the effect of the fluctuating binormal velocity component. It is demonstrated that the influence of the fluctuating binormal velocity component cannot be neglected if accurate flow measurements are required. In Section 4.3, a thermocouple will be used for temperature measurements in a heated jet. The mixture fraction field predicted with the standard  $k$ - $\epsilon$  model will be compared to the measured temperature field.

In literature, many modifications have been used to the standard  $k$ - $\epsilon$  model in order to find a better agreement between measurements and predictions in a turbulent jet. Some of these modifications to the standard  $k$ - $\epsilon$  model will be discussed in Section 4.4.

#### 4.1 MATHEMATICAL MODEL

To get some insight into the qualitative behaviour of a turbulent jet, in this section some further simplifications will be adopted. In this way it is possible to find an analytical solution to these simplified equations.

In many examples of free turbulence it is possible to distinguish one main flow direction in which the velocity is substantially larger than in any other direction. This circumstance considerably simplifies the theoretical investigation of these flows because changes of quantities in the direction of the main flow are slow compared to those in the transverse direction. Also the mean-pressure variation is small in the transverse direction. In the main-flow direction the pressure varies mainly according to the pressure distribution in the undisturbed flow. Usually the pressure distribution in the main-flow direction is uniform. Therefore, the assumption may be made that the pressure is uniform throughout the whole flow region.

With the present mathematical model, solutions are obtained with the property of similarity. The term "similarity" is used when a length scale and a velocity scale alone are assumed to be sufficient to determine the structure of any field of turbulence. For turbulent jet flows, the more

or less bell-shaped curves are seen to be geometrically similar when the velocities at any section are made non-dimensional with the mean centerline-velocity as a velocity scale and when the radial distances are made non-dimensional with the so-called “half-value” distance. This “half-value” distance is the distance from the centerline to the point at which the mean velocity is half the value on the centerline.

The assumptions read:

- buoyancy is absent
- the pressure in the fluid is uniform
- in the axial direction ( $x$ ), diffusion, heat conduction and viscous action are negligible

With these assumptions the equations for conservation of mass (3.77), momentum in axial direction (3.78) and mixture fraction (3.83) read for  $\mu \ll \mu_t$ :

(i) Continuity equation:

$$\frac{\partial}{\partial x}(\bar{\rho}\tilde{u}) + \frac{1}{r} \frac{\partial}{\partial r}(r\bar{\rho}\tilde{v}) = 0 \quad (4.1)$$

(ii) Conservation of momentum in axial direction:

$$\frac{\partial}{\partial x}(\bar{\rho}\tilde{u}\tilde{u}) + \frac{1}{r} \frac{\partial}{\partial r}(r\bar{\rho}\tilde{v}\tilde{v}) = \frac{1}{r} \frac{\partial}{\partial r} \left[ r \mu_t \frac{\partial \tilde{u}}{\partial r} \right] \quad (4.2)$$

(iii) Mixture fraction equation:

$$\frac{\partial}{\partial x}(\bar{\rho}\tilde{u}\tilde{Z}) + \frac{1}{r} \frac{\partial}{\partial r}(r\bar{\rho}\tilde{v}\tilde{Z}) = \frac{1}{r} \frac{\partial}{\partial r} \left[ r \frac{\mu_t}{\sigma_{t,Z}} \frac{\partial \tilde{Z}}{\partial r} \right] \quad (4.3)$$

#### Jet invariants

Because of conservation of momentum,

$$I_u = 2\pi \int_0^{\infty} \bar{\rho}\tilde{u}^2 r dr \quad (4.4)$$

is independent of  $x$ , i.e.  $\partial I_u / \partial x = 0$  as follows directly from Equation (4.2).

Because  $Z$  is a conserved scalar,

$$I_Z = 2\pi \int_0^{\infty} \bar{\rho}\tilde{u}\tilde{Z} r dr \quad (4.5)$$

is independent of  $x$ , i.e.  $\partial I_Z / \partial x = 0$  as follows from Equation (4.3).

These quantities are equal to the rates of flow of axial momentum and of jet medium (for example fuel), respectively. Because  $I_u$  and  $I_Z$  are independent of  $x$ , their values are equal to their values at the injection plane, where  $x=0$ . Assuming a uniform profile at the injection plane, i.e.  $\tilde{u}=u_0$  and  $\tilde{Z}=1$ :

$$I_u = \frac{1}{4} \pi \bar{\rho} u_0^2 D^2 \quad (4.6)$$

$$I_Z = \frac{1}{4} \pi \bar{\rho} u_0 D^2 \quad (4.7)$$

where  $D$  is the nozzle diameter.

### Analytical solution

Assuming a constant turbulent viscosity  $\mu_t$  and constant density, the following relations satisfy the differential Equations (4.1), (4.2) and (4.3) (Schlichting *et al.*, 1997):

$$\tilde{u} = \frac{1}{8\alpha} \sqrt{\frac{3I_u}{\pi\bar{\rho}}} \frac{1}{x+a} \frac{1}{(1+\eta^2)^2} \quad (4.8)$$

$$\tilde{v} = \frac{1}{2} \sqrt{\frac{3I_u}{\pi\bar{\rho}}} \frac{1}{x+a} \frac{\eta(1-\eta^2)}{(1+\eta^2)^2} \quad (4.9)$$

$$\tilde{Z} = \frac{(2\sigma_{t,z}+1)I_z/\bar{\rho}}{8\alpha\sqrt{3\pi I_u/\bar{\rho}}} \frac{1}{x+a} \frac{1}{(1+\eta^2)^{2\sigma_{t,z}}} \quad (4.10)$$

where the non-dimensional space variable  $\eta$  is defined by

$$\eta = \frac{1}{8\alpha} \frac{r}{x+a} \quad (4.11)$$

and  $\alpha$  is a constant. This solution does not satisfy the boundary conditions for the injection plane ( $x=-a$ ) in detail, but it agrees with the integral relations (4.4) and (4.5). They can therefore be accepted as solutions which are valid for large values of  $x$ , at which the effects of the details of the profiles of  $u$  and  $Z$  at  $x=-a$  have become insignificant.

On dimensional arguments the turbulent viscosity has been modelled by

$$\mu_t = \alpha \sqrt{\frac{3\bar{\rho}I_u}{\pi}} \quad (4.12)$$

where the empirical constant  $\alpha$  has to be determined from measurements. Notice that  $\mu_t$  is constant throughout the whole flowfield, which is unrealistic in the outer flow region where  $\mu_t$  falls to the laminar value.

### Stream function

The stream function  $\psi$  may be defined as

$$\psi = 2\pi \int_0^r \bar{\rho} \tilde{u} r dr = 8\alpha \sqrt{3\pi\bar{\rho}I_u} \frac{x+a}{1+64\alpha^2 \left(\frac{x+a}{r}\right)^2} \quad (4.13)$$

The physical significance of the stream function is that lines of  $\psi=\text{constant}$  are streamlines; in steady flow these are curves actually traced out by the particles in the flow. Figure 4.1 shows the streamlines of the averaged velocity field and the contour lines of the mean mixture fraction for  $\alpha=0.017$  and  $\sigma_{t,z}=0.5$ . It will be shown later that these values for  $\alpha$  and  $\sigma$  correspond to the values found in practice.

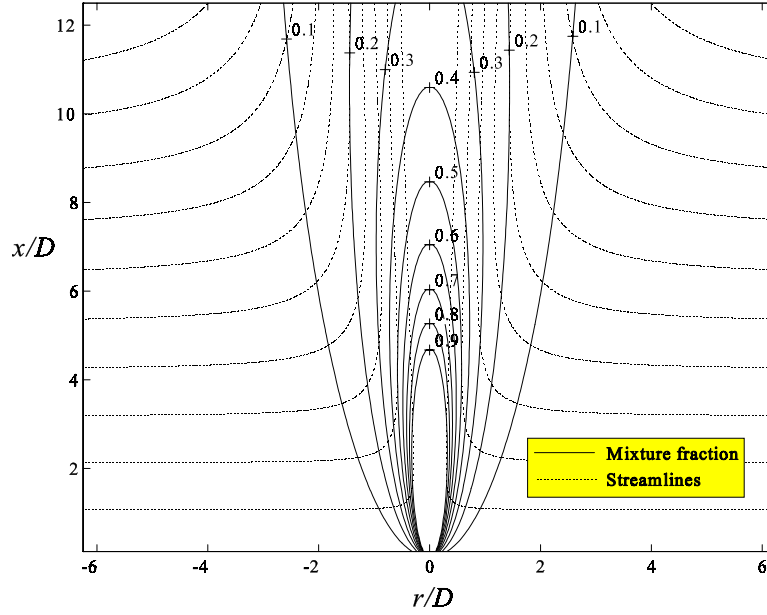


Figure 4.1 Mixture fraction and streamlines.

#### Entrainment rate

The total mass rate of flow in the jet,  $M$ , can be obtained by integration, as follows:

$$M = 2\pi \int_{r=0}^{\infty} \bar{\rho} \bar{u} r dr = 8\alpha \sqrt{3\pi \bar{\rho} I_u} (x+a) \quad (4.14)$$

The entrainment rate, i.e. the rate of increase of  $M$  with  $x$ , is obtained by differentiation of (4.14); the result is:

$$\frac{dM}{dx} = 8\alpha \sqrt{3\pi \bar{\rho} I_u} \quad (4.15)$$

#### Decay constants

The values of  $u$  and  $Z$  on the axis vary reciprocally with axial distance  $x$ , in accordance with

$$\frac{u_0}{\tilde{u}_c} = K_u \frac{x+a}{D} \quad (4.16)$$

$$\frac{1}{\tilde{Z}_c} = K_z \frac{x+a}{D} \quad (4.17)$$

where  $K_u$  and  $K_z$  are the velocity and mixture fraction decay constants, respectively. With Equations (4.6), (4.7), (4.8) and (4.10) it follows that

$$K_u = \alpha \frac{16\sqrt{3}}{3} \quad (4.18)$$

$$K_Z = \frac{\alpha 16\sqrt{3}}{2\sigma_{t,z} + 1} \quad (4.19)$$

If the flame length  $L$  of a turbulent diffusion flame is defined as the distance from the nozzle to the axial position on the centerline where the mixture fraction becomes equal to the stoichiometric value,  $L$  may be calculated from Equation (4.17) as  $L = D/(K_Z Z_{st}) - a$ . As already mentioned in Chapter 1, the length of a turbulent diffusion flame does not depend very much on the fuel mass flow. Notice that this simplified model also predicts that the length of a turbulent diffusion flame is independent of the nozzle outlet velocity.

Radial distributions of  $u$ ,  $v$  and  $Z$ , when normalized by the centerline values, are

$$\frac{\tilde{u}}{\tilde{u}_c} = \frac{1}{(1+\eta^2)^2} \quad (4.20)$$

$$\frac{\tilde{v}}{\tilde{u}_c} = 4\alpha \frac{\eta(1-\eta^2)}{(1+\eta^2)^2} \quad (4.21)$$

$$\frac{\tilde{Z}}{\tilde{Z}_c} = \frac{1}{(1+\eta^2)^{2\sigma_{t,z}}} \quad (4.22)$$

The velocity reaches half of its centerline value for  $\eta$  equal to  $\eta_{1/2}^u = \sqrt{2^{1/2} - 1}$  while the mixture fraction reaches half of its centerline value for  $\eta$  equal to  $\eta_{1/2}^Z = \sqrt{2^{1/2\sigma_{t,z}} - 1}$ . It is often useful to characterise the width of a jet by the half width  $r_{1/2}$ , i.e. the radius at which the axial velocity component equals one-half of its value on the centerline. From Equation (4.11) it follows that

$$r_{1/2}^u = S_{1/2}^u (x+a) \quad (4.23)$$

$$r_{1/2}^Z = S_{1/2}^Z (x+a) \quad (4.24)$$

where  $S_{1/2}^u$  and  $S_{1/2}^Z$  are the so-called half width spreading rates. They are equal to:

$$S_{1/2}^u = \frac{dr_{1/2}^u}{dx} = 8\alpha\eta_{1/2}^u \quad (4.25)$$

$$S_{1/2}^Z = \frac{dr_{1/2}^Z}{dx} = 8\alpha\eta_{1/2}^Z \quad (4.26)$$

From measurements (Wynanski *et al.*, 1969) the half width spreading rate for  $u$  is evaluated to be approximately equal to 0.086 and that for  $Z$  is equal to 0.13 (Keagy *et al.*, 1950). This implies  $\alpha$  to be approximately equal to 0.017 and the turbulent Prandtl number  $\sigma_{t,z}$  to be equal to 0.5. When the entrainment rate is calculated with these constants from Equation (4.15), it is evaluated to be equal to  $0.42\sqrt{\rho I_u}$ . From measurement (Ricou *et al.*, 1961) this entrainment rate is evaluated to be considerably less, i.e.  $0.28\sqrt{\rho I_u}$ . The reason for this is that the uniform- $\mu_t$  model is unrealistic in the outer region, where  $\mu_t$  reduces to the laminar value.

Other similarity features are:

$$\begin{aligned}\frac{\tilde{k}}{\tilde{u}_c^2(x)} &= f_1(\eta) \\ \frac{\tilde{Z}^2}{\tilde{Z}^2(x)} &= f_2(\eta)\end{aligned}\tag{4.27}$$

When the density varies, an analytical solution of the equations cannot be found, in general. However, for large  $x$  the density is approximately equal to the ambient air density and the jet invariants may be rewritten as

$$\begin{aligned}I_u &= \frac{1}{4}\pi\rho_1 u_0^2 D^2 = \frac{1}{4}\pi\rho_0 u_0^2 D_e^2 \\ I_Z &= \frac{1}{4}\pi\rho_1 u_0 D^2 = \frac{1}{4}\pi\rho_0 u_0 D_e^2\end{aligned}\tag{4.28}$$

where  $\rho_0$  the ambient air density and  $\rho_1$  the nozzle fluid density. Therefore, the velocity decay and mixture fraction decay scale in the same way as in the constant density case if  $D$  is replaced by the effective nozzle diameter  $D_e$ :

$$D_e = \omega^{-1/2} D\tag{4.29}$$

where  $\omega = \rho_0/\rho_1$ .

## 4.2 HOT-WIRE ANEMOMETRY IN AN ISOTHERMAL TURBULENT JET

In this section, the well known Hot-Wire Anemometry (HWA) method will be used for performing velocity measurements in an axial symmetric turbulent jet. HWA has a good frequency response, high accuracy, and it is rather easy to use. Therefore, HWA is the most widely used tool for turbulent flow studies. The principle of HWA is based on heat transfer of an electrically heated element to the flow, where the heat transfer to the flow depends on the fluid velocity. The heated element is cooled by the flow which results in a drop of the electrical resistance of the element. The hot-wire element is a short ( $\pm 1$  mm active length) and very thin ( $5\ \mu\text{m}$ ) wire fitted between prongs. The wires are made of tungsten or platinum.

For measurements in three dimensional (3D) turbulent flows many types of hot-wire probes may be used. Each type has its advantages and disadvantages. With four-wire probes an over-determined system of equations is obtained, the solution of which may cause many difficulties. Other probes including three-wire probes have a low spatial resolution. Regions near the wall, which are of great interest in many studies, are difficult to reach with this probe. The probe used by Müller (1982) consists of a single inclined wire. The probe is rotated around its axis. In spite of the simplicity of its principle it is rather complex in both its construction and calibration. It needs many measuring points and the accuracy is affected. These factors led to the decision to make use of the X-wire probe in the present study. Such a probe has a relatively small size giving a high spatial resolution. The separation between the wires is of the order of 1 mm. An extensive overview of HWA has been given by Bruun (1995).

#### 4.2.1 Experimental set-up

Figure 4.2 gives a sketch of the experimental set-up. The airflow out of the nozzle is generated with high-pressure air (6 bar). After opening the valve, the air is led into a buffer to attenuate the high frequency pressure variations. The air is filtered by an oil filter before it enters the mass flow controller (MFC). The MFC is used to regulate the mass flow and thereby indirectly the outlet velocity of the nozzle. From the MFC the air flows through a heater which is controlled by a regulator and a feed-back temperature indicator. For safety precautions the heater is equipped with a cut-off switch for situations where the temperature may rise too high. Finally the air reaches the nozzle.

The hot-wire probe may be positioned at every position along the centerline of the jet. The probe axis is placed in the main stream direction, thereby minimizing the influence of the probe on the flow.

The hot-wire signals of the anemometers, DISA type 55D00, produce a voltage between 0 and 10V, depending on the monitored velocity. A laboratory interface with 8 A/D inputs has been used to convert the hot-wire signals into a digital signal. The software used to control the sampling and conversion has been written in LABVIEW. For post-processing the calibration and measurement data, software has been written in MATLAB.

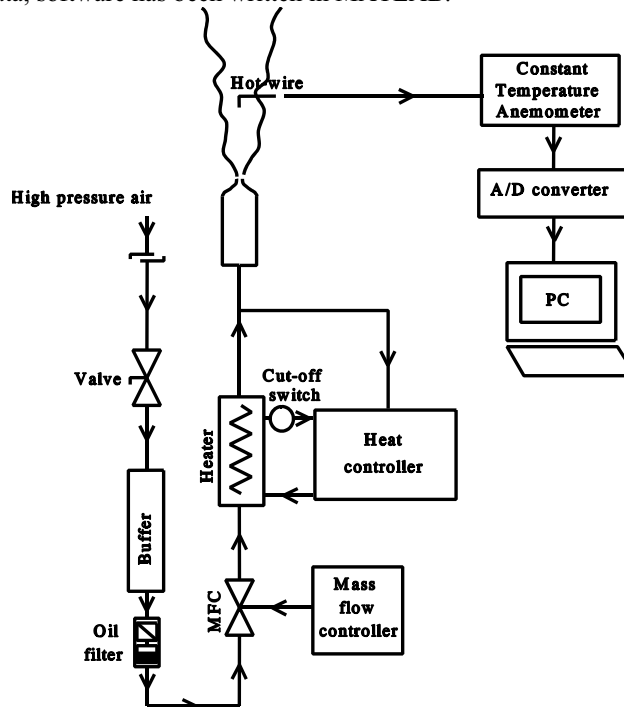


Figure 4.2 Experimental set-up.

To be able to perform a full calibration of a cross-wire at different temperatures the experimental set-up may also be used as a calibration set-up in which the wires are yawed with respect to the mean flow direction. In this way, data about sensitivity of the probe to the tangential velocity components is obtained. Before leaving the nozzle, the turbulence in the flow is suppressed by grids. Then the flow contracts and emanates from the nozzle. So the calibration



is performed in a low-turbulence-level jet flow. The velocity at the outlet is calculated from the pressure drop over the nozzle. A measurement of the velocity profile of the ejected jet flow shows that the profile is flat within a circle with a radius of 75% of the nozzle outlet radius. Within this region, the turbulence intensity  $I$  defined as

$$I = \frac{\sqrt{\overline{u'^2}}}{U} \quad (4.30)$$

is less than 0.5%. If the wire is placed in this region, the velocity at the position of the wire is accurately known and can be used for calibrating the hot-wire. With an outlet cross section of 120 mm<sup>2</sup>, a maximum velocity of 30 m/s can be reached.

#### 4.2.2 Frequency response and spatial resolution

Hot-wire anemometry can be carried out by two principles; the constant current method and the constant temperature method. Applying the constant current method, the current through the wire is kept constant, and the change of resistance due to cooling is measured. Applying the constant temperature method, the resistance is kept constant, and the voltage over the wire needed to achieve this is measured. Because of the limitation by heat transfer in the wire, the maximum frequency that can be followed in the constant current mode is in of the order of 100Hz, which is far too low for turbulence measurements. Therefore often use is made of the constant temperature method with which frequencies up to 100kHz can be monitored. This operation mode is very adequate for measuring turbulence, having typical frequencies up to 20kHz.

To achieve a good spatial resolution, a hot-wire probe should have a wire length,  $l$ , which is short compared to the smallest eddy size that occurs in the flow, i.e. the Kolmogorov length  $\eta$ . However, for standard hot-wire probes, with a length of 1.25mm and a diameter of 4-5 $\mu$ m, an imperfect spatial resolution of the fine scale turbulence is obtained because the Kolmogorov length scale may be as small as 0.1mm in the wall-region close to the nozzle. For a single normal hot-wire placed perpendicular to the mean flow, the measured fluctuating velocity  $u'_m$  will be:

$$u'_m = \frac{1}{l} \int_0^l u'(r) dr \quad (4.31)$$

where  $r$  is a coordinate along the wire, perpendicular to the mean flow direction. The measured normal Reynolds stress may be derived as

$$\overline{u_m'^2} = \frac{1}{l^2} \int_{r=0}^l \int_{r'=0}^l \overline{u'(r')u'(r)} dr' dr = \frac{1}{l^2} \int_{r=0}^l \int_{r'=0}^l \overline{u'^2(r')} \frac{\overline{u'(r')u'(r)}}{\overline{u'^2(r')}} dr' dr \quad (4.32)$$

For the case of homogeneous, isotropic turbulent flow, this equation may be written as

$$\overline{u_m'^2} = \frac{\overline{u'^2}}{l^2} \int_{r=0}^l \int_{r'=0}^l g(r-r') dr dr' \quad (4.33)$$

where  $g(r)$  is the transverse correlation coefficient defined by Equation (3.7). The relation between the measured and the real normal Reynolds stress depends very much on the shape of the correlation coefficient. For small values of  $r$  the correlation function may be approximated by Equation (3.10), i.e.  $g(r-r') = 1 - (r-r')^2/\lambda^2$ . By substitution of this relation into Equation (4.33) the following relation for the measured normal Reynolds stress may be derived:

$$\overline{u_m'^2} = \overline{u'^2} \left( 1 - \frac{l^2}{6\lambda^2} \right) \quad (4.34)$$

where  $\lambda$  is the Taylor microscale given by Equation (3.16). The spatial resolution error may be defined by

$$error = \frac{\overline{u_m^2} - \overline{u^2}}{\overline{u^2}} = -\frac{l^2}{6\lambda^2} = -\frac{l^2}{60} \frac{\rho \epsilon}{\mu k} \quad (4.35)$$

This relation is valid if the wire length  $l$  is small compared to the Taylor microscale  $\lambda$ . Therefore, it may be used for errors up to about 4% ( $l/\lambda=0.5$ ). For larger errors, the correlation coefficient may for example be approximated by

$$g(r) = \begin{cases} \cos(2r/l_t) & r \leq \pi l_t/4 \\ 0 & r \geq \pi l_t/4 \end{cases} \quad (4.36)$$

This relation satisfies  $g(0)=1$ ,  $g'(0)=0$  and the integral relation (3.18). Substitution of Equation (4.36) into Equation (4.33) leads for  $l \leq \pi l_t/4$  to

$$error = \frac{l_t^2}{2l^2} \left[ 1 - \cos\left(\frac{2l}{l_t}\right) \right] - 1 = \frac{0.1k^{3/2}}{l^2\epsilon} \left[ 1 - \cos\left(\frac{10l\epsilon}{k^{3/2}}\right) \right] - 1 \quad (4.37)$$

This expression may be used for errors up to about 19% ( $l/l_t=\pi/4$ ). Figure 4.3 shows the predicted spatial resolution error along the centerline of a turbulent jet to be discussed in Section 4.2.7. where  $l$  has been set to 1.25 mm, the density  $\rho$  to 1.15 kg/m<sup>3</sup> and the dynamic viscosity  $\mu$  to 17.1·10<sup>-6</sup> Pa s. Although there is a small region  $5 \leq x/D \leq 10$  where both predicted errors become large, the resolution error is believed not to exceed a value of about 4% throughout the entire flow field. This value has also been reported in the literature (Bruun, 1995).

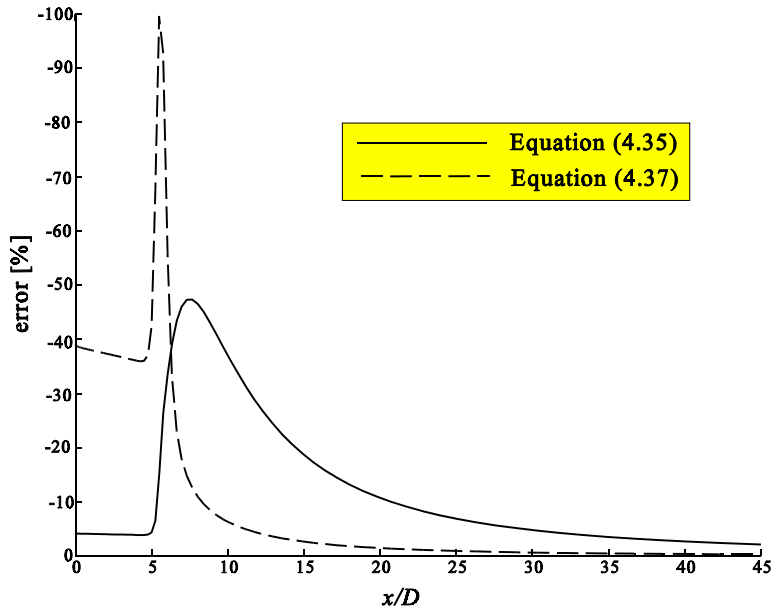


Figure 4.3 Predicted spatial resolution error in the measured normal Reynolds stress along the centerline of a turbulent jet (see Section 4.2.7).

#### 4.2.3 Look-up inversion method for HWA

The method of measurement used in this investigation is similar to the so-called look-up matrix methods. A first look-up matrix method was introduced by Cheesewright (1972). In his method a  $(U_0, \alpha)$  calibration was carried out using eight different velocities and fifteen angular positions. For each velocity/yaw-angle pair  $(U_0, \alpha)$  (Figure 4.4), a unique voltage pair  $(E_1, E_2)$  is obtained, provided that the velocity vector is within the approach-acceptance region. The probe is oriented such that the binormal velocity component ( $W$ ) equals zero. The angles  $\alpha_1$  and  $\alpha_2$  are both approximately equal to  $45^\circ$ . The calibration data were curve-fitted using separate fifth-order polynomials in  $E_1$  and  $E_2$  for the  $U$  and  $V$  velocity components. Then a look-up matrix was created containing values corresponding to all possible discrete values for  $E_1$  and  $E_2$ .

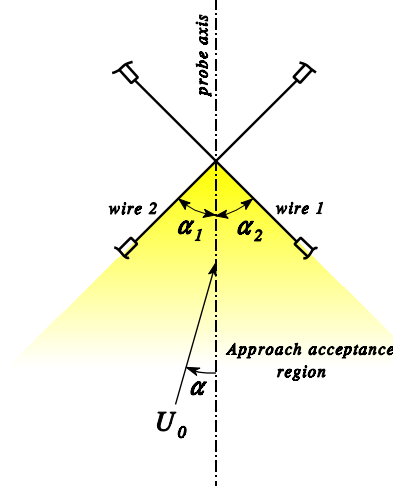


Figure 4.4 Definition of the yaw-angle in the prong plane.

The procedure used by Cheesewright is a rather cumbersome procedure, and later methods have used a matrix of much smaller dimension linked to an interpolation scheme. The first of these methods was introduced by Willmarth and Bogar (1977). Other look-up matrix methods have subsequently been presented by Zilberman (1981), Johnson and Eckelmann (1984), Lueptow *et al.* (1988), Browne *et al.* (1989), and Schewe and Ronneberger (1990).

In the present study use is made of an interpolation scheme also. First of all the relation between the velocity and the voltage output of the wire has to be calibrated in combination with the anemometer used in conjunction with this wire. In the calibration technique used, the cross-wire is exposed to four velocities evenly distributed in the expected velocity range, while the probe is yawed with respect to the velocity vector in the flow angle range  $-30^\circ \leq \alpha \leq 30^\circ$  ( $5^\circ$  increments).

A polynomial function of the form:

$$E^2(U_0, \alpha) = \sum_{n=0}^N c_n(\alpha) (U_0^{1/2})^n \quad (4.38)$$

is used to fit the data for each yaw-angle  $\alpha$ .

It was found that a first-order polynomial of the form

$$E^2 = c_0(\alpha) + c_1(\alpha) U_0^{1/2} \quad (4.39)$$

was accurate enough to keep the relative error within the 0.15% range (Figure 4.5).

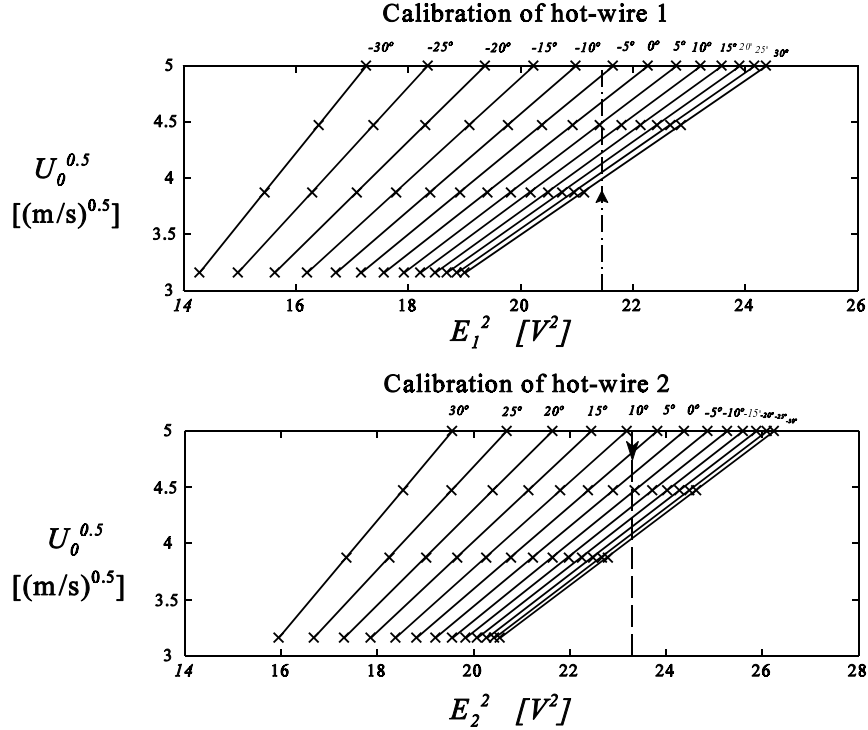


Figure 4.5 Calibration curves for the two hot-wires for different values of the yaw-angle  $\alpha$ .

Hot-wires have to be recalibrated on a regular basis due to changing environmental circumstances as well as ageing effects of the wires.

After the calibration has been performed, the measurement can be done. To obtain the velocity components  $U$  and  $V$  related to a pair of input voltages  $E_1$  and  $E_2$ , the following procedure is used. A line corresponding to  $E=E_1$  is drawn in Figure 4.5 and the intersection points with the individual calibration curves are determined. A similar procedure is applied to the value  $E_2$  for wire 2. Plotting these points on a  $\sqrt{U_0}, \alpha$  graph (Figure 4.6) identifies two curves corresponding to wires 1 and 2, respectively. The correct value of  $(U_0, \alpha)$  is obtained from the intersection of these two curves. The related values of  $U$  and  $V$  are calculated from:

$$\begin{aligned} U &= U_0 \cos \alpha \\ V &= U_0 \sin \alpha \end{aligned} \tag{4.40}$$

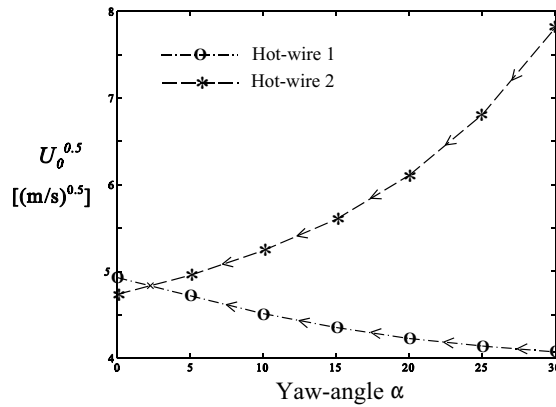


Figure 4.6  $U_0^{0.5}$  versus yaw-angle  $\alpha$  plots corresponding to  $E_1$  and  $E_2$  in Figure 4.5.

#### 4.2.4 Forward-reverse ambiguity effects

The signal ambiguity for an X-hot-wire probe is illustrated in Figure 4.7. Due to the rotational symmetry of the sensing elements the sign of the normal and tangential velocity components will not have any effect on the measured voltages  $E_1$  and  $E_2$ . Therefore, a velocity  $U_0$  that is outside the approach acceptance region will result in a measured velocity  $U_0^*$  with the same absolute value for the normal and tangential velocity components. In other words; the measured velocity  $U_0^*$  has the same cooling effect as the real velocity  $U_0$ . Due to this directional insensitivity the measured mean velocity  $\bar{U}$  will be too high and the measured mean velocity  $\bar{V}$  will be too low if situations like depicted in Figure 4.7 do occur. Also the measured variances will be too low. A solution for this problem may be found in using the flying hot-wire-anemometer technique (Payne *et al.*, 1966 and Sheih *et al.*, 1971), in which the probe is moved with a known velocity so that the resulting relative velocity will remain within the approach acceptance region. Such a method, however, has not been used in the present study and the effect of forward-reverse ambiguity has been neglected.

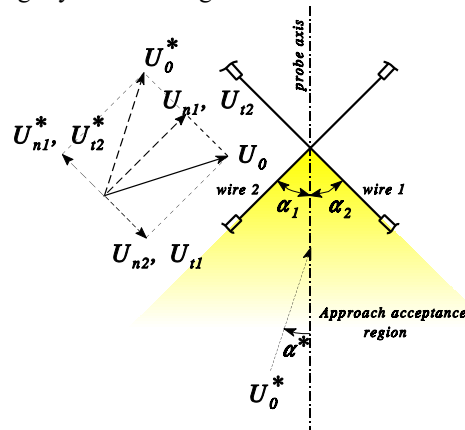


Figure 4.7 Forward-reverse ambiguity.

#### 4.2.5 Effect of the fluctuating binormal velocity component

The look-up inversion method described in Section 4.2.3 gives very accurate results for a pure two-dimensional flow situation. However, turbulent flows are never two-dimensional. In turbulent flows there is always a third velocity component, i.e. the binormal velocity component which is defined as the velocity component perpendicular to both wires. Although the mean binormal velocity component may be zero, the fluctuation in the binormal velocity component is not equal to zero in turbulent flows. It has been demonstrated by Tutu *et al.* (1975) that very large errors are made if the influence of the fluctuating binormal velocity component is neglected. They demonstrated that errors in the measured Reynolds stresses can be as high as 28% when the turbulence intensity is 35%. These errors were caused by the combined effect of forward-reverse ambiguity and sensitivity to the binormal velocity component. Tutu *et al.* (1975) demonstrated however that, especially at low turbulence intensity ( $I \leq 30\%$ ), the error due to the forward-reverse ambiguity effect is small compared to the error associated with neglecting the effect of the binormal velocity component. Therefore, special attention will be given here to the influence of the fluctuating binormal velocity component on the X hot-wire results.

#### Relation between measured and real velocity components

The positioning of the hot-wires is as depicted in Figure 4.8 with  $U$  as the axial velocity component,  $V$  as the radial velocity component and  $W$  as the tangential or binormal velocity component. From the measured voltages  $E_1$  and  $E_2$  the measured velocity components  $U_m$  and  $V_m$  in the prong plane are calculated as if the flow is two-dimensional, i.e. from Equations (4.40):

$$\begin{aligned} U_m &= U_0 \cos \alpha \\ V_m &= U_0 \sin \alpha \end{aligned} \quad (4.41)$$

However, the real velocity components  $U$ ,  $V$  and  $W$  are not in the prong plane (Figure 4.8).

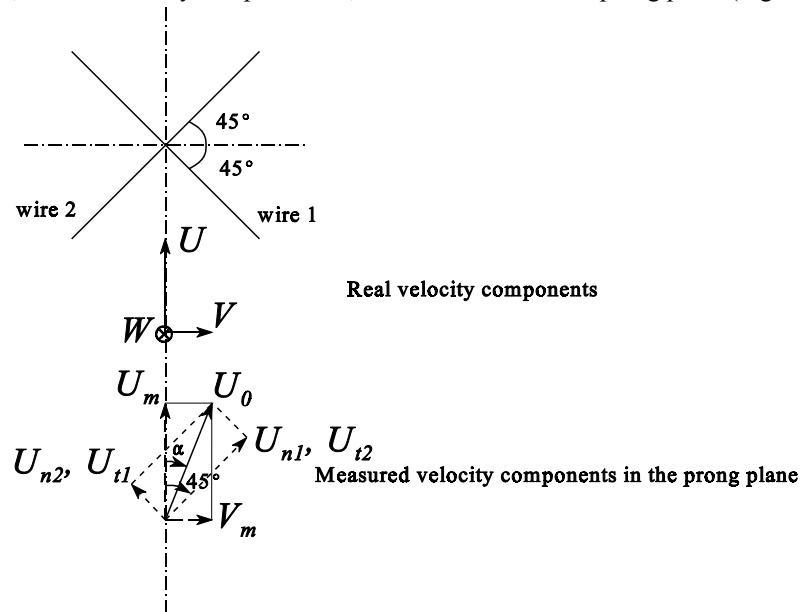


Fig 4.8 Real and measured velocity components.

To express the effect of the binormal velocity component, i.e.  $W$ , on the measured velocity components  $U_m$  and  $V_m$ , we have to make use of an additional relation for the angular sensitivity of an inclined hot-wire. Jörgenson (1971) and Champagne *et al.* (1982) established the following relationship for the effective cooling velocity  $U_{eff}$  of a wire:

$$U_{eff}^2 = U_n^2 + k^2 U_t^2 + h^2 U_b^2 \quad (4.42)$$

where  $U_n$ ,  $U_t$  and  $U_b$  are the normal, tangential and binormal (normal to the prong plane) velocity components, respectively. The effective cooling velocity is the velocity which, in normal direction, would give the same voltage difference over the wire as the real velocity. Therefore the voltage difference over the wire is only a function of this effective cooling velocity. The factors  $k$  and  $h$  account for the additional cooling due to the tangential and binormal velocity component, respectively. The factor  $k$  is called the ‘yaw factor’ and  $h$  the ‘pitch factor’. The factors  $k$  and  $h$  depend on the length to diameter ratio of the wire and the prong effects. Typical values for  $k$  and  $h$  for a standard plated hot-wire are 0.2 and 1.05 (Bruun, 1995), respectively.

The effective cooling velocity of the measured velocity components equals the effective cooling velocity of the real velocity components. Therefore:

$$\begin{aligned} U_{eff_1}^2 &= U_0^2 \cos^2(45^\circ - \alpha) + k^2 U_0^2 \sin^2(45^\circ - \alpha) = \frac{1}{2}(U+V)^2 + \frac{1}{2}k^2(U-V)^2 + h^2 W^2 \\ U_{eff_2}^2 &= U_0^2 \sin^2(45^\circ - \alpha) + k^2 U_0^2 \cos^2(45^\circ - \alpha) = \frac{1}{2}(U-V)^2 + \frac{1}{2}k^2(U+V)^2 + h^2 W^2 \end{aligned} \quad (4.43)$$

Summation and subtraction of the set of Equations (4.43) gives the following X-hot-wire response equations:

$$\begin{aligned} U_0^2 &= U^2 + V^2 + \frac{2h^2}{1+k^2} W^2 \\ U_0^2 \sin 2\alpha &= 2UV \end{aligned} \quad (4.44)$$

Equations (4.44) may be replaced by

$$\begin{aligned} U_0^2 &= U^2 + V^2 + 2h^2 W^2 \\ U_0^2 \sin 2\alpha &= 2UV \end{aligned} \quad (4.45)$$

where the influence of the yaw factor  $k$  has been taken into account by the redefined pitch factor  $h$ . A typical value for  $h$  is then given by  $h \approx \sqrt{1.05^2 / (1 + 0.2^2)} \approx 1.03$ . An appropriate value for the pitch factor  $h$  may also be found during the calibration in a turbulence free flow by adjusting certain values for  $U$ ,  $V$  and  $W$ . By adjusting  $V$  to 0,  $U$  to  $U_{cal} \cos \beta$  and  $W$  to  $U_{cal} \sin \beta$  it is found from Equations (4.45) that:

$$h = \sqrt{\frac{U_0^2 - U_{cal}^2 \cos^2 \beta}{2U_{cal}^2 \sin^2 \beta}} \quad (4.46)$$

where  $U_{cal}$  is an adjusted calibration velocity and  $\beta$  is an adjusted calibration angle. An experimental value of 1.0 has been found which compares well to the typical value found from literature.

Notice that Equations (4.41) may also be written as

$$\begin{aligned} U_0^2 &= U_m^2 + V_m^2 \\ U_0^2 \sin 2\alpha &= 2U_m V_m \end{aligned} \quad (4.47)$$

Therefore, Equations (4.45) may be interpreted as a corrected version of Equations (4.47) in which the influence of the binormal velocity component  $W$  has been taken into account. In the limit of a zero binormal velocity component, the corrected X-hot-wire response Equations (4.45) reduce to the uncorrected X-hot-wire response Equations (4.47). Therefore, the high accuracy of the look-up inversion method for real two-dimensional flow has been maintained.

A relation between the measured and real velocity components is obtained by equating the right hand side of Equations (4.45) to the right hand side of Equations (4.47):

$$U_m = \sqrt{\frac{1}{2}[U^2 + V^2 + 2h^2W^2 + \sqrt{(U^2 + V^2 + 2h^2W^2)^2 - 4U^2V^2}]} \quad (4.48)$$

$$V_m = \left(\frac{U}{U_m}\right)V$$

Equations (4.48) indicate that with  $W \neq 0$  the axial velocity component is always over-estimated, i.e.  $U_m \geq U$ , and thereby the radial velocity component  $V$  is always under-estimated.

#### Relation between measured and real Reynolds stresses

In order to find a relation between the measured Reynolds stresses  $\overline{u'^2}_m$ ,  $\overline{v'^2}_m$  and  $\overline{u'v'}_m$  and real Reynolds stresses  $\overline{u'^2}$ ,  $\overline{v'^2}$  and  $\overline{u'v'}$  the following procedure is used. First, the measured quantities  $A_1$  and  $A_2$  are introduced by:

$$A_1 = U_0^2$$

$$A_2 = U_0^2 \sin 2\alpha \quad (4.49)$$

the uncorrected X-hot-wire response Equations (4.47) are written like

$$A_1 = U_m^2 + V_m^2$$

$$A_2 = 2U_m V_m \quad (4.50)$$

and the corrected response Equations (4.45) are written like

$$A_1 = U^2 + V^2 + 2h^2W^2$$

$$A_2 = 2UV \quad (4.51)$$

A standard averaging technique is applied to the equations. One can decompose each velocity component and the variables  $A_i$  into a mean and fluctuating part like

$$U = \overline{U} + u' \quad (4.52)$$

Using standard averaging techniques, we get the following set of equations:

$$\overline{A}_1 = \overline{U^2} + \overline{V^2} + \overline{u'^2} + \overline{v'^2} + 2h^2\overline{w'^2}$$

$$\overline{A}_2 = 2(\overline{U}\overline{V} + \overline{u'v'}) \quad (4.53)$$

where it is assumed that the mean binormal velocity component equals zero, i.e.  $\overline{W} = 0$  for a turbulent jet flow without swirl. An identical set of equations is obtained for the measured quantities by setting  $w'$  to zero. A set of equations for the turbulent flow quantities may be obtained by subtracting Equations (4.53) from the instantaneous Equations (4.51),

$$a_1' = 2\overline{U}u' + (u'^2 - \overline{u'^2}) + 2\overline{V}v' + (v'^2 - \overline{v'^2}) + 2h^2(w'^2 - \overline{w'^2})$$

$$a_2' = 2\overline{U}v' + 2\overline{V}u' + 2(u'v' - \overline{u'v'}) \quad (4.54)$$

The following set of turbulence equations may be obtained:



$$\begin{aligned}
\overline{a_1'^2} &= 4\overline{U^2 u'^2} + 4\overline{V^2 v'^2} + 8\overline{U V u'v'} + \overline{g_1(u',v',w')} \\
\overline{a_2'^2} &= 4\overline{V^2 u'^2} + 4\overline{U^2 v'^2} + 8\overline{U V u'v'} + \overline{g_2(u',v',w')} \\
\overline{a_1' a_2'} &= 4\overline{U^2 u'v'} + 4\overline{U V u'^2} + 4\overline{V^2 u'v'} + 4\overline{U V v'^2} + \overline{g_3(u',v',w')}
\end{aligned} \tag{4.55}$$

where the functions  $\overline{g_1}$ ,  $\overline{g_2}$  and  $\overline{g_3}$  contain third and higher order correlation terms in  $u'$ ,  $v'$  and  $w'$ . The functions  $\overline{g_1}$ ,  $\overline{g_2}$  and  $\overline{g_3}$  may be evaluated as

$$\overline{g_i} = \int_{-\infty}^{\infty} \int_{-\infty}^{\infty} \int_{-\infty}^{\infty} g_i(u',v',w') P(u',v',w') du' dv' dw' \tag{4.56}$$

where the probability density function  $P(u',v',w')$  may be modelled for the specific flow conditions found in a turbulent jet flow without swirl. Statistical independence is assumed for the tangential velocity component,

$$P(u',v',w') = P(u',v')P(w') \tag{4.57}$$

and therefore

$$\begin{aligned}
\overline{u'w'} &= 0, \quad \overline{v'w'} = 0, \quad \overline{u'v'w'} = 0, \quad \overline{u'^2 w'} = 0, \\
\overline{u'w'^2} &= 0, \quad \overline{v'w'^2} = 0, \quad \overline{v'^2 w'} = 0 \\
\overline{u'^2 w'^2} &= \overline{u'^2} \overline{w'^2} \\
\overline{v'^2 w'^2} &= \overline{v'^2} \overline{w'^2}
\end{aligned} \tag{4.58}$$

A bivariate normal distribution is assumed over  $u'$  and  $v'$ ,

$$P(u',v') = \frac{1}{2\pi\sigma_u\sigma_v\sqrt{1-\rho^2}} \exp\left\{-\frac{1}{2}\left(\frac{1}{1-\rho^2}\right)\left[\frac{u'^2}{\sigma_u^2} - 2\rho\frac{u'v'}{\sigma_u\sigma_v} + \frac{v'^2}{\sigma_v^2}\right]\right\} \tag{4.59}$$

where  $\sigma_u$  and  $\sigma_v$  are the standard deviations of  $u$  and  $v$ , respectively, and  $\rho$  is the correlation coefficient of  $u$  and  $v$ ,

$$\rho = \frac{\overline{u'v'}}{\sigma_u\sigma_v} \tag{4.60}$$

Assuming this distribution leads to the following relations:

$$\begin{aligned}
\overline{u'^2 v'} &= 0, \quad \overline{u'v'^2} = 0, \quad \overline{u'^3} = 0 \quad \text{and} \quad \overline{v'^3} = 0 \\
\overline{u'^3 v'} &= 3\overline{u'^2} \overline{u'v'} \\
\overline{u'v'^3} &= 3\overline{v'^2} \overline{u'v'} \\
\overline{u'^2 v'^2} &= 2(\overline{u'v'})^2 + \overline{u'^2} \overline{v'^2} \\
\overline{u'^4} &= 3(\overline{u'^2})^2 \\
\overline{v'^4} &= 3(\overline{v'^2})^2
\end{aligned} \tag{4.61}$$

The distribution for  $w'$  is assumed to be normal:

$$P(w') = \frac{1}{\sqrt{2\pi}\sigma_w} \exp\left[-\frac{w'^2}{2\sigma_w^2}\right] \tag{4.62}$$

Therefore:

$$\overline{w'^3} = 0 \text{ and } \overline{w'^4} = 3(\overline{w'^2})^2 \quad (4.63)$$

The functions  $\overline{g_1}$ ,  $\overline{g_2}$  and  $\overline{g_3}$  may then be evaluated as

$$\begin{aligned} \overline{g_1} &= 2(\overline{u'^2})^2 + 2(\overline{v'^2})^2 + 8h^4(\overline{w'^2})^2 + 4(\overline{u'v'})^2 \\ \overline{g_2} &= 4\overline{u'^2} \overline{v'^2} + 4(\overline{u'v'})^2 \\ \overline{g_3} &= 4\overline{u'^2} \overline{u'v'} + 4\overline{v'^2} \overline{u'v'} \end{aligned} \quad (4.64)$$

The full set of Equations (4.53) and (4.55) now read:

$$\begin{aligned} \overline{A_1} &= \overline{U^2} + \overline{V^2} + \overline{u'^2} + \overline{v'^2} + 2h^2\overline{w'^2} \\ \overline{A_2} &= 2(\overline{U} \overline{V} + \overline{u'v'}) \\ \overline{a_1'^2} &= 4\overline{U^2} \overline{u'^2} + 4\overline{V^2} \overline{v'^2} + 8\overline{U} \overline{V} \overline{u'v'} + 2(\overline{u'^2})^2 + 2(\overline{v'^2})^2 + 8h^4(\overline{w'^2})^2 + 4(\overline{u'v'})^2 \\ \overline{a_2'^2} &= 4\overline{V^2} \overline{u'^2} + 4\overline{U^2} \overline{v'^2} + 8\overline{U} \overline{V} \overline{u'v'} + 4\overline{u'^2} \overline{v'^2} + 4(\overline{u'v'})^2 \\ \overline{a_1'a_2'} &= 4\overline{U^2} \overline{u'v'} + 4\overline{U} \overline{V} \overline{u'^2} + 4\overline{V^2} \overline{u'v'} + 4\overline{U} \overline{V} \overline{v'^2} + 4\overline{u'^2} \overline{u'v'} + 4\overline{v'^2} \overline{u'v'} \end{aligned} \quad (4.65)$$

Let us now look at the uncorrected response Equations (4.50). Under the assumption that the measured PDF  $P_m(U_m, V_m)$  may also be approximated by a bivariate normal distribution, an identical system of equations is obtained for the measured mean velocity components and measured Reynolds stresses, i.e.

$$\begin{aligned} \overline{A_1} &= \overline{U_m^2} + \overline{V_m^2} + \overline{u'_m{}^2} + \overline{v'_m{}^2} \\ \overline{A_2} &= 2(\overline{U_m} \overline{V_m} + \overline{u'_m v'_m}) \\ \overline{a_1'^2} &= 4\overline{U_m^2} \overline{u'_m{}^2} + 4\overline{V_m^2} \overline{v'_m{}^2} + 8\overline{U_m} \overline{V_m} \overline{u'_m v'_m} + 2(\overline{u'_m{}^2})^2 + 2(\overline{v'_m{}^2})^2 + 4(\overline{u'_m v'_m})^2 \\ \overline{a_2'^2} &= 4\overline{V_m^2} \overline{u'_m{}^2} + 4\overline{U_m^2} \overline{v'_m{}^2} + 8\overline{U_m} \overline{V_m} \overline{u'_m v'_m} + 4\overline{u'_m{}^2} \overline{v'_m{}^2} + 4(\overline{u'_m v'_m})^2 \\ \overline{a_1'a_2'} &= 4\overline{U_m^2} \overline{u'_m v'_m} + 4\overline{U_m} \overline{V_m} \overline{u'_m{}^2} + 4\overline{V_m^2} \overline{u'_m v'_m} + 4\overline{U_m} \overline{V_m} \overline{v'_m{}^2} + 4\overline{u'_m{}^2} \overline{u'_m v'_m} + 4\overline{v'_m{}^2} \overline{u'_m v'_m} \end{aligned} \quad (4.66)$$

The relation between measured Reynolds stresses and real Reynolds stresses is now given by equating the right hand side of Equation (4.65) to the right hand side of Equation (4.66).

#### Influence of the fluctuating binormal velocity component in jet flows

We are now able to give an estimate of the error associated with neglecting the influence of the fluctuating binormal velocity component. Here it will be carried out for a flow condition that is typical for jet flows, i.e.  $\overline{V}=0$ ,  $\sigma_v=0.8\sigma_u$ ,  $\sigma_w=0.8\sigma_u$  and  $\rho=0.3$ . The notation  $\sigma_\phi$  refers to the standard deviation of  $\phi$ , and  $\rho$  is the correlation coefficient of  $u'$  and  $v'$ , i.e.  $\rho = \overline{u'v'}/(\sigma_u\sigma_v)$ . For this flow condition, it may be obtained from Equations (4.65) that

$$\begin{aligned} \overline{A_1} &= (1+2.92I^2)\overline{U^2} \\ \overline{A_2} &= 0.48I^2\overline{U^2} \\ \overline{a_1'^2} &= (4I^2+6.33I^4)\overline{U^4} \\ \overline{a_2'^2} &= (2.56I^2+2.79I^4)\overline{U^4} \\ \overline{a_1'a_2'} &= (0.96I^2+1.57I^4)\overline{U^4} \end{aligned} \quad (4.67)$$

where  $I$  is the turbulence intensity defined as  $I = \sigma_u / \bar{U}$ . The pitch factor  $h$  has been set equal to 1. By equating the right hand side of Equations (4.66) to the right hand side of Equations (4.67), measurement errors, defined as

$$error = \frac{x_m - x}{x} \quad (4.68)$$

with  $x$  as the considered averaged quantity, may be evaluated as a function of the turbulence intensity  $I$ . Figure 4.9 shows the evaluated errors in the mean axial velocity component and Reynolds stresses associated with neglecting the influence of the binormal velocity component. It appears that the measured (interpreted) mean velocity is higher than the actual velocity. The contrary is true for the Reynolds stresses. Similar results have also been found by Tutu and Chevray (1975). Although the errors they found were slightly higher due to the combined effect of forward-reverse ambiguity and sensitivity to the binormal velocity component. Obviously, neglecting the influence of the binormal velocity component is responsible for making large errors in the data conversion. Therefore additional information has to be obtained about the magnitude of the fluctuating binormal velocity component. The procedure employed for obtaining information about this binormal velocity component will be described in the next section.

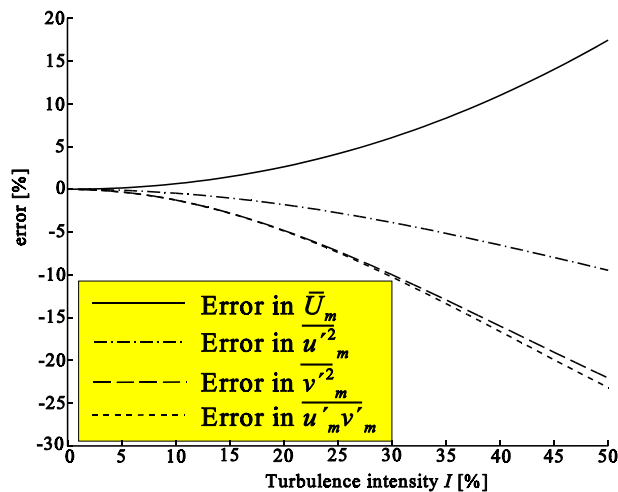


Figure 4.9 The relative error associated with neglecting the influence of the binormal velocity component as a function of the turbulence intensity  $I$ .

#### 4.2.6 Incorporating an equation for the fluctuating tangential velocity component

With Equations (4.65) we have a set of 5 equations with 6 unknowns, i.e.  $\bar{U}$ ,  $\bar{V}$ ,  $\overline{u'^2}$ ,  $\overline{v'^2}$ ,  $\overline{u'v'}$ , and  $\overline{w'^2}$ . Therefore an additional equation has to be obtained for the variance in the tangential velocity component. To obtain this equation, the wires will be placed in another attitude, i.e. attitude  $b$  in Figure 4.10. In prong attitude  $b$ , the tangential velocity component  $W$  is in the prong plane whereas the radial velocity component  $V$  has become the binormal velocity component.

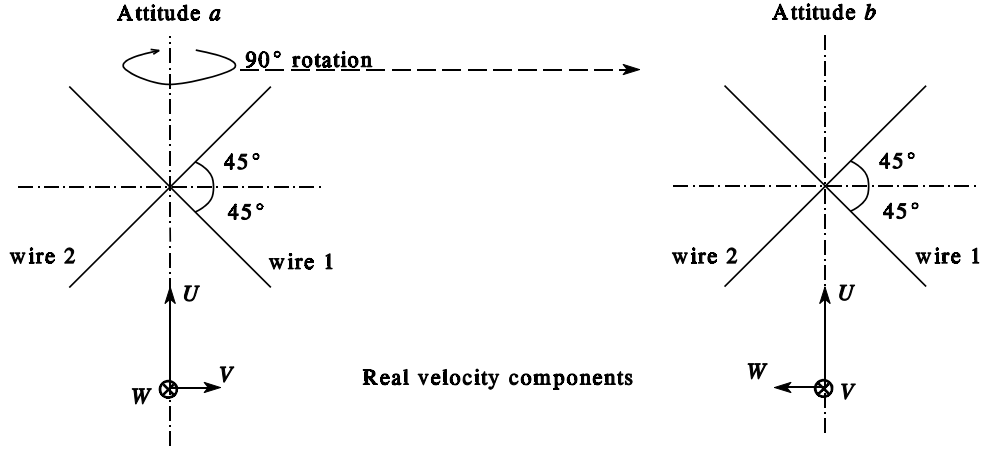


Figure 4.10 Different prong attitudes.

Similar to Equations (4.45) it is obtained for prong attitude  $b$  that

$$\begin{aligned} U_0^2 &= U^2 + 2h^2V^2 + W^2 \\ U_0^2 \sin 2\alpha &= -2UW \end{aligned} \quad (4.69)$$

Introducing the measured quantities  $A_3$  and  $A_4$  for this prong attitude as

$$\begin{aligned} A_3 &= U_0^2 \\ A_4 &= U_0^2 \sin 2\alpha \end{aligned} \quad (4.70)$$

leads with the assumption that  $\overline{W} = 0$  and the PDF described in the preceding section to the following averaged equations:

$$\begin{aligned} \overline{A_3} &= \overline{U^2 + 2h^2V^2 + u'^2 + 2h^2v'^2 + w'^2} \\ \overline{A_4} &= 0 \\ \overline{a_3'^2} &= 4\overline{U^2 u'^2} + 2\overline{(u')^2} + 16h^4\overline{V^2 v'^2} + 8h^4\overline{(v')^2} + 2\overline{(w')^2} + 16h^2\overline{U V u'v'} + 8h^2\overline{(u'v')^2} \\ \overline{a_4'^2} &= 4\overline{U^2 w'^2} + 4\overline{u'^2 w'^2} \\ \overline{a_3' a_4'} &= 0 \end{aligned} \quad (4.71)$$

If the influence of the binormal velocity component is neglected, then combining the equation for  $\overline{A_3}$  and that for  $\overline{a_4'^2}$  yields the variance in the tangential velocity component as:

$$\overline{w_m'^2} = 2\overline{A_3} - 2\sqrt{\overline{A_3^2} - \overline{a_4'^2}} \quad (4.72)$$

Therefore it seems appropriate to use a combination of these two equations as an additional equation for the variance in the tangential velocity component, i.e.

$$\overline{a_4'^2} = 4(\overline{A_3} - 2h^2\overline{V^2} - 2h^2\overline{v'^2} - \overline{w'^2})\overline{w'^2} \quad (4.73)$$

Now suppose that the variance in the tangential velocity component is equal to zero. In that case, the measured PDF  $P_m(U_m, V_m)$  is not necessarily equal to the bivariate normal distribution which was assumed in the preceding section. Therefore, correction constants may be added to

the Equations (4.64):

$$\begin{aligned}\overline{g}_1 &= 2(\overline{u'_m})^2 + 2(\overline{v'_m})^2 + 4(\overline{u'_m v'_m})^2 + c_1 \\ \overline{g}_2 &= 4\overline{u'_m}^2 \overline{v'_m}^2 + 4(\overline{u'_m v'_m})^2 + c_2 \\ \overline{g}_3 &= 4\overline{u'_m}^2 \overline{u'_m v'_m} + 4\overline{v'_m}^2 \overline{u'_m v'_m} + c_3\end{aligned}\quad (4.74)$$

In order to maintain the high accuracy of the look-up inversion method in case of  $\overline{w'^2}=0$ , the constants  $c_1$ ,  $c_2$  and  $c_3$  may be evaluated from Equations (4.55) as:

$$\begin{aligned}c_1 &= \overline{a_1'^2} - 4\overline{U_m}^2 \overline{u'_m}^2 - 4\overline{V_m}^2 \overline{v'_m}^2 - 8\overline{U_m} \overline{V_m} \overline{u'_m v'_m} - 2(\overline{u'_m})^2 - 2(\overline{v'_m})^2 - 4(\overline{u'_m v'_m})^2 \\ c_2 &= \overline{a_2'^2} - 4\overline{V_m}^2 \overline{u'_m}^2 - 4\overline{U_m}^2 \overline{v'_m}^2 - 8\overline{U_m} \overline{V_m} \overline{u'_m v'_m} - 4\overline{u'_m}^2 \overline{v'_m}^2 - 4(\overline{u'_m v'_m})^2 \\ c_3 &= \overline{a_1' a_2'} - 4\overline{U_m}^2 \overline{u'_m v'_m} - 4\overline{U_m} \overline{V_m} \overline{u'_m}^2 - 4\overline{V_m}^2 \overline{u'_m v'_m} \\ &\quad - 4\overline{U_m} \overline{V_m} \overline{v'_m}^2 - 4\overline{u'_m}^2 \overline{u'_m v'_m} - 4\overline{v'_m}^2 \overline{u'_m v'_m}\end{aligned}\quad (4.75)$$

and the adapted system of Equations (4.65) reads:

$$\begin{aligned}\overline{A}_1 &= \overline{U^2} + \overline{V^2} + \overline{u'^2} + \overline{v'^2} + 2h^2 \overline{w'^2} \\ \overline{A}_2 &= 2(\overline{U} \overline{V} + \overline{u' v'}) \\ \overline{a_1'^2} &= 4\overline{U}^2 \overline{u'^2} + 4\overline{V}^2 \overline{v'^2} + 8\overline{U} \overline{V} \overline{u' v'} + 2(\overline{u'^2})^2 + 2(\overline{v'^2})^2 + 8h^4 (\overline{w'^2})^2 + 4(\overline{u' v'})^2 + c_1 \\ \overline{a_2'^2} &= 4\overline{V}^2 \overline{u'^2} + 4\overline{U}^2 \overline{v'^2} + 8\overline{U} \overline{V} \overline{u' v'} + 4\overline{u'^2} \overline{v'^2} + 4(\overline{u' v'})^2 + c_2 \\ \overline{a_1' a_2'} &= 4\overline{U}^2 \overline{u' v'} + 4\overline{U} \overline{V} \overline{u'^2} + 4\overline{V}^2 \overline{u' v'} + 4\overline{U} \overline{V} \overline{v'^2} + 4\overline{u'^2} \overline{u' v'} + 4\overline{v'^2} \overline{u' v'} + c_3\end{aligned}\quad (4.76)$$

Following this procedure, it is ensured that for  $\overline{w'^2} \rightarrow 0$  the solution found from the adapted Equations (4.76) approaches the solution found by making use of the look-up inversion method.

The complete system of equations now reads:

$$E = \begin{pmatrix} F_1 \\ F_2 \\ F_3 \\ F_4 \\ F_5 \\ F_6 \end{pmatrix} = \begin{pmatrix} \overline{A}_1 - \overline{U}^2 - \overline{V}^2 - \overline{u'^2} - \overline{v'^2} - 2h^2 \overline{w'^2} \\ \overline{A}_2 - 2\overline{U} \overline{V} - 2\overline{u' v'} \\ \overline{a_1'^2} - 4\overline{U}^2 \overline{u'^2} - 2(\overline{u'^2})^2 - 4\overline{V}^2 \overline{v'^2} - 2(\overline{v'^2})^2 - 8h^4 (\overline{w'^2})^2 - 8\overline{U} \overline{V} \overline{u' v'} - 4(\overline{u' v'})^2 - c_1 \\ \overline{a_2'^2} - 4\overline{V}^2 \overline{u'^2} - 4\overline{U}^2 \overline{v'^2} - 8\overline{U} \overline{V} \overline{u' v'} - 4\overline{u'^2} \overline{v'^2} - 4(\overline{u' v'})^2 - c_2 \\ \overline{a_1' a_2'} - 4\overline{U}^2 \overline{u' v'} - 4\overline{U} \overline{V} \overline{u'^2} - 4\overline{u'^2} \overline{u' v'} - 4\overline{V}^2 \overline{u' v'} - 4\overline{U} \overline{V} \overline{v'^2} - 4\overline{v'^2} \overline{u' v'} - c_3 \\ \overline{a_4'^2} - 4\overline{A}_3 \overline{w'^2} + 8h^2 \overline{V}^2 \overline{w'^2} + 8h^2 \overline{v'^2} \overline{w'^2} + 4(\overline{w'^2})^2 \end{pmatrix} = \begin{pmatrix} 0 \\ 0 \\ 0 \\ 0 \\ 0 \\ 0 \end{pmatrix}\quad (4.77)$$

This set of six algebraic equations has to be solved for the six unknowns;  $\overline{U}$ ,  $\overline{V}$ ,  $\overline{u'^2}$ ,  $\overline{v'^2}$ ,  $\overline{u' v'}$ , and  $\overline{w'^2}$ .

So we have to solve  $F(\underline{u}) = \underline{Q}$ , for  $\underline{u} = [\overline{U}, \overline{V}, \overline{u'^2}, \overline{v'^2}, \overline{u' v'}, \overline{w'^2}]^T$

Using Newton's method we linearize around  $\underline{u}_{n-1}$  and solve

$$\underline{u}_n = \underline{u}_{n-1} - (F'(\underline{u}_{n-1}))^{-1} F(\underline{u}_{n-1})\quad (4.78)$$

where

$$F'(\underline{u}) = \begin{pmatrix} 2\bar{U} & 2\bar{V} & 1 & 1 & 0 & 2h^2 \\ 2\bar{V} & 2\bar{U} & 0 & 0 & 2 & 0 \\ 8\bar{U}\bar{u}'^2 + 8\bar{V}\bar{u}'\bar{v}' & 8\bar{V}\bar{v}'^2 + 8\bar{U}\bar{u}'\bar{v}' & 4\bar{U}^2 + 4\bar{u}'^2 & 4\bar{V}^2 + 4\bar{v}'^2 & 8\bar{U}\bar{V} + 8\bar{u}'\bar{v}' & 16h^4\bar{w}'^2 \\ 8\bar{U}\bar{v}'^2 + 8\bar{V}\bar{u}'\bar{v}' & 8\bar{V}\bar{u}'^2 + 8\bar{U}\bar{u}'\bar{v}' & 4\bar{V}^2 + 4\bar{v}'^2 & 4\bar{U}^2 + 4\bar{u}'^2 & 8\bar{U}\bar{V} + 8\bar{u}'\bar{v}' & 0 \\ 8\bar{U}\bar{u}'\bar{v}' + 4\bar{V}\bar{u}'^2 + 4\bar{V}\bar{v}'^2 & 8\bar{V}\bar{u}'\bar{v}' + 4\bar{U}\bar{u}'^2 + 4\bar{U}\bar{v}'^2 & 4\bar{U}\bar{V} + 4\bar{u}'\bar{v}' & 4\bar{U}\bar{V} + 4\bar{u}'\bar{v}' & 4\bar{U}^2 + 4\bar{u}'^2 + 4\bar{V}^2 + 4\bar{v}'^2 & 0 \\ 0 & -16h^2\bar{V}\bar{w}'^2 & 0 & -8h^2\bar{w}'^2 & 0 & 4\bar{A}_3 - 8h^2\bar{V}^2 - 8h^2\bar{v}'^2 - 8\bar{w}'^2 \end{pmatrix} \quad (4.79)$$

The solution obtained from the look-up inversion method, i.e. Equations (4.41) and Equation (4.72), may be used as an initial guess for  $\underline{u}$ .

#### 4.2.7 Results

Measurements have been carried out in a high Reynolds number turbulent air jet at an atmospheric pressure  $p$  of  $0.992 \cdot 10^5 \text{ Pa} \pm 1\%$ . The temperature  $T$  was kept constant at  $26.2^\circ\text{C}$ . The mass flow through the nozzle  $M$  was adjusted by the Mass Flow Controller (MFC) to  $2.74 \cdot 10^{-3} \text{ kg/s}$  with an error of 1%. With a nozzle diameter  $D$  of 12.36 mm and a density  $\rho$  of  $1.15 \text{ kg/m}^3$  this gives an average nozzle exit velocity  $\bar{U}_{avg}$  of  $19.8 \text{ m/s} \pm 1\%$ . The Reynolds number ( $Re = \rho \bar{U}_{avg} D / \mu$ ) may then be calculated to be equal to 16500.

Figure 4.11-12 show the conditions measured at a distance of 2.5 mm downstream of the nozzle exit. Figure 4.11 shows the mean axial velocity profile. The axial outlet velocity at the centerline,  $\bar{U}_{co}$ , was measured to be equal to 20.4 m/s. The profile is very flat and shows even a slight increase of the velocity close to the wall. At the wall there is a very steep gradient in the boundary layer. The curve-fitted line shown in Figure 4.11 has been used for prescribing the boundary condition in  $\bar{U}$  in the numerical simulation.

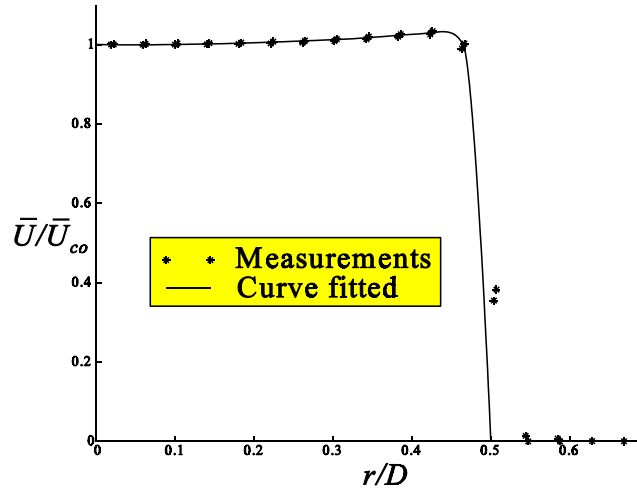


Figure 4.11 Mean axial velocity component at the nozzle exit.

Figure 4.12 shows the mean radial velocity component at the nozzle exit. The curve-fitted line shown in Figure 4.12 has been used for prescribing the boundary condition in the numerical simulation. Measurement results have been corrected such as to obtain a zero radial velocity component at the centerline. It is assumed that a measured non-zero mean radial velocity component at the centerline is caused by the fact that the probe axis makes a small angle  $\alpha$  with

the centerline of the jet. Therefore, the relation between the real velocity components and the measured velocity components is given by

$$\begin{aligned} U &= U_m \cos\alpha - V_m \sin\alpha \\ V &= U_m \sin\alpha + V_m \cos\alpha \end{aligned} \quad (4.80)$$

This leads to the following correction formula

$$\begin{aligned} \bar{U} &= \bar{U}_m \cos\alpha - \bar{V}_m \sin\alpha \\ \bar{V} &= \bar{U}_m \sin\alpha + \bar{V}_m \cos\alpha \\ \overline{u'^2} &= \overline{u'^2}_m \cos^2\alpha - 2\overline{u'v'}_m \sin\alpha \cos\alpha + \overline{v'^2}_m \sin^2\alpha \\ \overline{v'^2} &= \overline{u'^2}_m \sin^2\alpha + 2\overline{u'v'}_m \sin\alpha \cos\alpha + \overline{v'^2}_m \cos^2\alpha \\ \overline{u'v'} &= (\overline{u'^2}_m - \overline{v'^2}_m) \sin\alpha \cos\alpha + \overline{u'v'}_m (\cos^2\alpha - \sin^2\alpha) \end{aligned} \quad (4.81)$$

The angle  $\alpha$  is adjusted such that a zero mean radial velocity component is obtained at the centerline:

$$\alpha = -\arctan\left(\frac{\bar{V}_m}{\bar{U}_m}|_{r=0}\right) \quad (4.82)$$

Applied values for  $\alpha$  where small, up to about  $0.5^\circ$ .

A striking characteristic of Figure 4.12 is the constant gradient in  $\bar{V}$  close to the centerline of the nozzle, i.e.  $\bar{V}/\bar{U}_{co} \approx 2.5 \cdot 10^{-2} r/D$ . This will influence the gradient in axial direction of the axial velocity component close to the nozzle exit. From the continuity equation it follows that:

$$\frac{\partial(\bar{U}/\bar{U}_{co})}{\partial(x/D)} = -\frac{1}{r/D} \frac{\partial}{\partial(r/D)} \left( \frac{r}{D} \frac{\bar{V}}{\bar{U}_{co}} \right) \quad (4.83)$$

Therefore, the gradient in the axial velocity component at the centerline is linked to a gradient in the radial velocity component at the centerline. At the ejection plane, the radial velocity profile may be approximated by

$$\frac{\bar{V}}{\bar{U}_{co}} \Big|_{x=0} = c_0 + c_1 \left( \frac{r}{D} \right) + c_2 \left( \frac{r}{D} \right)^2 + c_3 \left( \frac{r}{D} \right)^3 + \dots \quad (4.84)$$

Because of symmetry,  $c_0$  should be equal to zero in order to avoid a jump in the radial velocity component at the centerline. The constant  $c_1$  is approximately equal to  $2.5 \cdot 10^{-2}$ . Substitution of Equation (4.84) into Equation (4.83) leads to

$$\frac{\partial(\bar{U}/\bar{U}_{co})}{\partial(x/D)} \Big|_{x=0} = -2c_1 - 3c_2 \left( \frac{r}{D} \right) - 4c_3 \left( \frac{r}{D} \right)^2 - \dots \quad (4.85)$$

and therefore, for  $r \rightarrow 0$

$$\frac{\partial(\bar{U}/\bar{U}_{co})}{\partial(x/D)} \Big|_{x=0} = -2c_1 \approx -5.0 \cdot 10^{-2} \quad (4.86)$$

This result differs largely from the zero gradient that would be found if the outlet profile would be that of a fully developed turbulent pipe flow. Therefore, a core region, in which the axial velocity component remains approximately constant, is not observed in the present measurements (Figure 4.13). The cause of the exit velocity profile distribution not being a fully-developed pipe

flow distribution is the geometry of the nozzle being too short, i.e. causing a too rapid contraction.

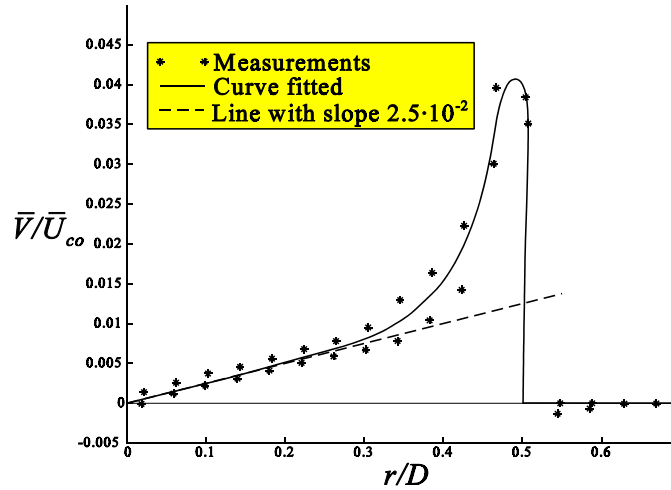


Figure 4.12 Mean radial velocity component at the nozzle exit.

Measured velocity fluctuation intensities at the burner exit were very low, i.e. less than 0.5% over the entire outlet. Boundary conditions for  $k$  and  $\epsilon$  have been set as in Figure 3.5 with a turbulence intensity  $I$  of 0.005 over the entire outlet and a constant mixing length  $l_m$  of 0.07 times the nozzle diameter  $D$ . Because the turbulence intensity at the nozzle outlet is very low compared to values of the turbulence intensity found downstream of the nozzle, the specific distributions of  $I$  and  $l_m$  over the nozzle outlet are expected to have just a small influence on the outcome of the numerical simulations. Measured mean velocity distributions in the jet are presented in Appendix A.

Figure 4.13 shows the centerline axial velocity component as a function of the axial distance from the nozzle exit. A true core region in which the mean velocity remains approximately constant is not identified. As explained at the beginning of this section, this is caused by the gradient in radial direction of the radial velocity component. The initial slope of the axial distribution of the centerline velocity agrees closely with the value estimated in Equation (4.86). The numerical simulation employing the standard  $k$ - $\epsilon$  model, using the values from Table 3.1, did not predict the same behaviour in the core region. This may be caused by setting an incorrect boundary condition for the radial velocity component at the inflow plane of the computational domain, especially in the co-flow. However, because of forward-reverse ambiguity effects, the experimental uncertainty in the value for the radial velocity component is very large in the co-flow region.

The velocity decay constant  $K_u$  varies experimentally with the axial location between 0.16 upstream and 0.19 downstream. For the numerical solution the velocity decay constant is approximately equal to 0.17. This agrees reasonably well with the experimental value of 0.165 found by Panchapakesan *et al.* (1993).



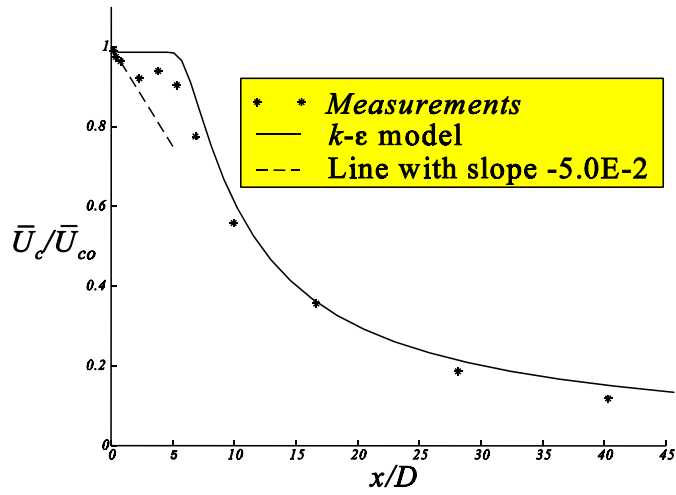


Figure 4.13 Centerline profile of the normalized axial velocity  $\bar{U}_c/\bar{U}_{co}$ .

Figure 4.14 shows the half-width of the jet as a function of the axial distance. In the far field, the half-width spreading rate has been determined to be equal to 0.083. This is lower than the values found in literature (Table 4.1) which may be caused by the used HWA correction method or by effects due to a different Reynolds number. From Figure 4.14 it can be seen that the virtual origin is at an axial position of  $x=-a=-0.9D$ . The half-width spreading rate predicted with the standard  $k-\epsilon$  model is approximately equal to 0.090. Compared to the present experimental result of  $s_{1/2}^u=0.083$ , the half-width spreading rate is over-estimated with about 8%.

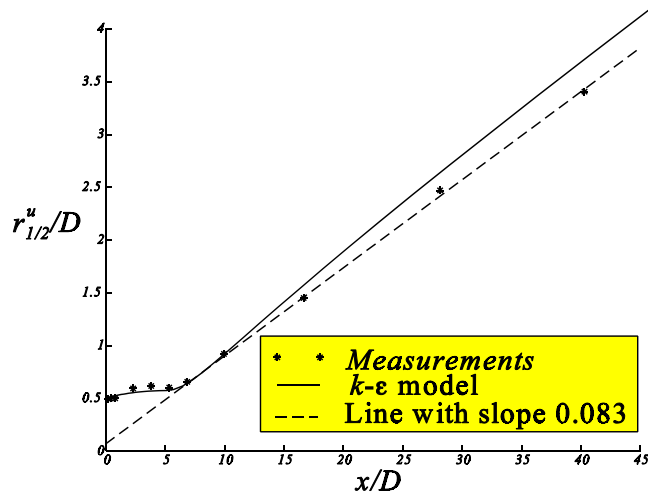


Figure 4.14 Variation of the halfwidth  $r_{1/2}^u/D$  with axial distance.

Author(s)	$S_{1/2}''$
Wyganski <i>et al.</i> (1969)	0.086
Rodi (1975)	0.086
Wittmer (1980)	0.088
George <i>et al.</i> (1988)	0.095
Capp <i>et al.</i> (1990)	0.094
Panchapakesan <i>et al.</i> (1993)	0.096
Present	0.083

Table 4.1 Measured halfwidth spreading rates for round jets.

Figure 4.15 shows the variation with axial distance of the total mass rate of flow in the jet. In the far field the entrainment rate has been determined to be equal to  $0.25\sqrt{\rho I_u}$ . Also this value is slightly lower than that found in literature, i.e.  $0.28\sqrt{\rho I_u}$  (Ricou *et al.* 1961). The entrainment rate that follows from the numerical simulation employing the  $k-\epsilon$  model agrees satisfactorily with the value obtained from the measurements.

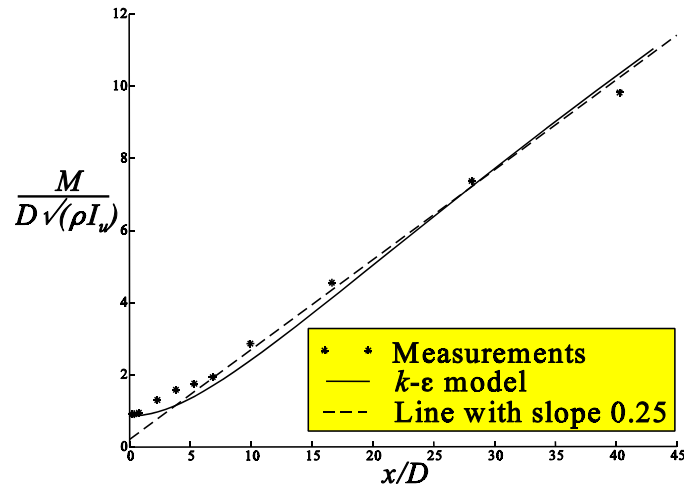


Figure 4.15 Normalized total mass rate of flow in the jet.

Figure 4.16 shows the radial profile of the normalized axial velocity  $\bar{U}/\bar{U}_c$  as a function of the normalized radial distance  $r/(x+a)$ . Also shown is the analytical relation according to Equation (4.20) and the solution given by the present computational method. The value for  $\alpha$  has been adjusted to 0.016 so that the analytical solution coincides with the measurements at the half-value point  $r_{1/2}=0.083(x+a)$ . Obviously the analytical solution predicts a too high value for the mean axial velocity component in the outer region. The reason for this is the inadequacy of the uniform- $\mu_t$  model in the outer region, where  $\mu_t$  falls to the laminar value. The  $k-\epsilon$  model also over-predicts the mean axial velocity component in the outer region. The turbulent viscosity  $\mu_t$  is over-predicted by the  $k-\epsilon$  model in the outer region. However, also the measurement results

ought to be treated with some suspicion in the outer region. Because of the absence of a dominant velocity in axial direction and the relative high turbulence intensities, forward-reverse ambiguity effects of the hot-wire (see Section 4.2.4) play an important role in that region. As a result of this, also the calculated total mass flow, i.e. Figure 4.15, must be treated carefully because the outer region has a large contribution to the integral of Equation (4.14).

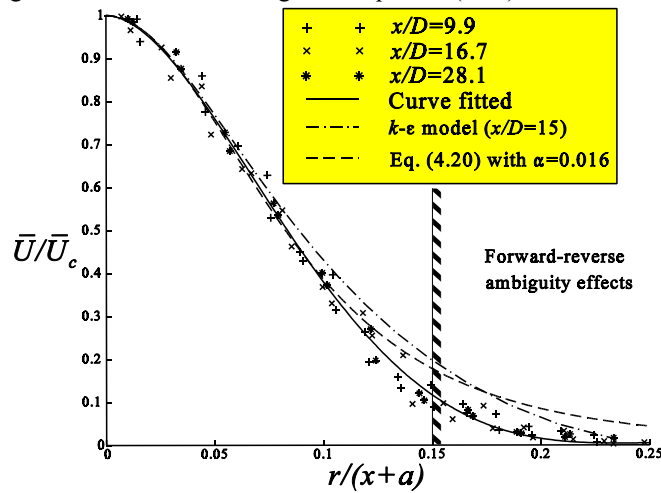


Figure 4.16 Radial profile of the normalized axial velocity  $\bar{U}/\bar{U}_c$  as a function of the normalized radial distance  $r/(x+a)$ .

Figure 4.17 shows the radial profile of the normalized radial velocity  $\bar{V}/\bar{U}_c$  as a function of the normalized radial distance  $r/(x+a)$ . This figure shows much scatter because the radial velocity component is very small compared to the axial velocity component. Remember that Equation (4.81) has been applied to obtain a zero mean radial velocity component at the centerline. However, a non-zero radial velocity component may also have been caused by an off-centerline position. This would lead to an error in the applied value for  $\alpha$ . A small error in the probe angle adjustment will lead to a large error in the measured radial velocity component.

Negative values for  $\bar{V}$  were observed in the outer region. The measured values for  $\bar{V}$  decrease however much faster to zero than the analytical solution given by Equation (4.32) or the values obtained from the numerical simulation employing the  $k-\epsilon$  model. This is probably caused by the forward-reverse ambiguity effect (Section 4.2.4), where a value for the radial velocity component  $\bar{V}$  higher than that for the axial velocity component  $\bar{U}$  is reflected into a higher value for the measured mean axial velocity component  $\bar{U}$ . An increase of the mean axial velocity component with just 1% is however within the error range of Figure 4.16 and therefore not detectable. In the outer region, the radial velocity component may however be expected to be smaller than that of the analytical solution because the entrainment rate of the measured jet is much smaller than that determined from the analytical solution.

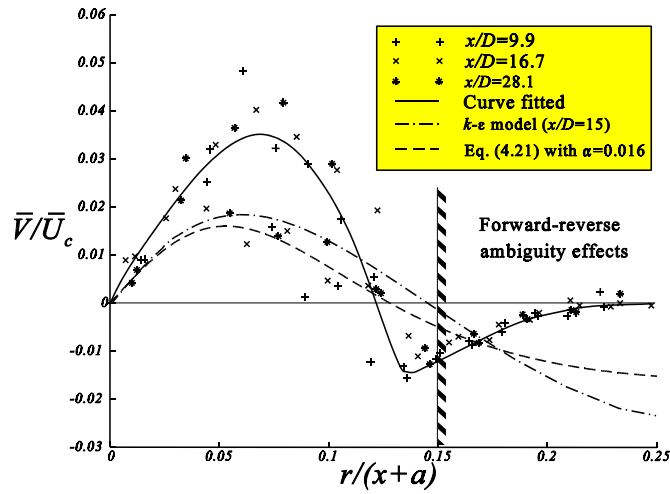


Figure 4.17 Radial profile of the normalized radial velocity  $\bar{V}/\bar{V}_c$  as a function of the normalized radial distance  $r/(x+a)$ .

Figure 4.18 shows the variation of the relative velocity fluctuation intensities along the centerline of the jet. Like for the mean axial velocity component, also for the relative velocity fluctuation intensities of the radial and tangential velocity components, similarity seems to be attained after about 10 nozzle diameters. For the relative velocity fluctuation intensity of the axial velocity component, however, similarity was not even attained at an axial distance of 40 nozzle outlet diameters.

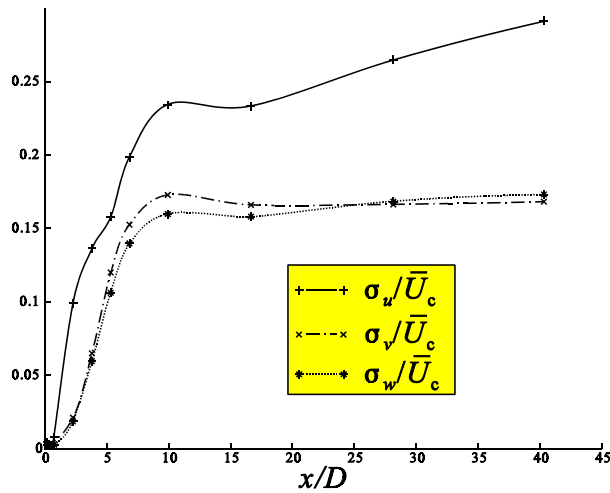


Figure 4.18 Centerline profiles of the relative velocity fluctuation intensities.

Figure 4.19 shows the measured turbulence intensity and that predicted by the present computational method based on the standard  $k-\epsilon$  model. The standard  $k-\epsilon$  model predicts a core

region in which the turbulence intensity remains small, whereas in the measurements an immediate increase of turbulence intensity is found after the nozzle exit. In the developed region, a good agreement is found between measured and predicted turbulence intensity.

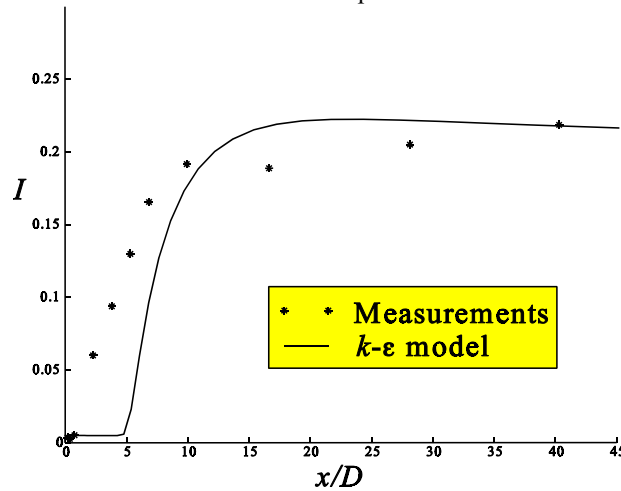


Figure 4.19 Measured and predicted turbulence intensity.

### 4.3 THERMOCOUPLE MEASUREMENTS IN A HEATED JET

The mixture fraction plays a very important role in combustion modelling. As an intermediate step to understand the mixing pattern during combustion, it is necessary to study the mixing pattern without chemical reaction. Therefore a test-rig has been built to simulate a combustion jet outlet making use of a heated jet as a counterpart of the fuel outlet surrounded by cold air, i.e. the oxidizer stream. By substitution of  $h = c_p T$  into Equation (2.44) and assuming a constant value for  $c_p$ , the differential equation for the temperature may be written as:

$$\frac{\partial}{\partial t} \rho T + \frac{\partial}{\partial x_k} \rho u_k T = \frac{\partial}{\partial x_k} \rho D \frac{\partial T}{\partial x_k} \quad (4.87)$$

This equation is similar to that for the mixture fraction. Therefore the mixture fraction  $Z$  may, under appropriate initial and boundary conditions, be evaluated from temperature measurements as a scaled 0/1 function of the temperature  $T$ ,

$$Z = \frac{T - T_{sec}}{T_{co} - T_{sec}} \quad (4.88)$$

where  $T_{co}$  is the outlet temperature at the centerline of the jet, and  $T_{sec}$  is the temperature of the secondary air.

There are several techniques to measure a temperature. One of the most commonly used techniques is the thermocouple. A thermocouple wire consists of two different metals. The principle is based on the physical phenomenon that a temperature difference causes a voltage difference over the wire.

The wires used in the present experiments are made of chromel/alumel (type K) with a wire

diameter of 12  $\mu\text{m}$ . With an air-stream velocity  $u$  of 20 m/s in the test-rig the measured response time of the thermocouple in air is  $t = 0.031\text{s}$ . This response time is however not low enough to be able to follow the smallest time scales of turbulence, which are of the order of milliseconds. Therefore only mean temperature profiles could be measured.

In the numerical simulations the time averaged density is calculated from Equation (3.49):

$$\bar{\rho} = \frac{P_c}{R\bar{T}} = \frac{P_c}{R[T_{\text{sec}} + \bar{Z}(T_{co} - T_{\text{sec}})]} \quad (4.89)$$

where  $R = R_0 \sum_{k=1}^N Y_k/W_k$  is constant and equal to 287.72 J/kg K.

The time averaged mixture fraction may be evaluated as:

$$\bar{Z} = \bar{\rho} \left( \frac{\bar{Z}}{\rho} \right) = \frac{\bar{Z} + (\omega - 1)[\bar{Z}^2 + \bar{Z}^{\prime 2}]}{1 + (\omega - 1)\bar{Z}} \quad (4.90)$$

where  $\omega$  is the density ratio  $\rho_{\text{sec}}/\rho_{co}$  with  $\rho_{co}$  the outlet density at the centerline of the jet, and  $\rho_{\text{sec}}$  the density of the secondary air.

#### 4.3.1 Results

Measurements have been carried out at the same mass flow as that for the isothermal measurements, i.e. the mass flow through the nozzle was adjusted by the Mass Flow Controller (MFC) to  $2.74 \cdot 10^{-3} \text{ kg/s}$ . Because the temperature increase of the jet was very small compared to that of the isothermal jet, the laminar viscosity was almost the same as that for the isothermal case and this leads to the same Reynolds number of 16500. The atmospheric pressure  $p$  was equal to  $1.031 \cdot 10^5 \text{ Pa}$ . The centerline temperature at the nozzle outlet  $T_{co}$  was kept constant at a temperature of  $38.4^\circ\text{C}$  while the temperature of the secondary air was equal to  $23.9^\circ\text{C}$ . The centerline density at the nozzle exit,  $\rho_{co}$ , may then be calculated to be equal to  $1.15 \text{ kg/m}^3$  while that of the secondary air,  $\rho_{\text{sec}}$ , is equal to  $1.21 \text{ kg/m}^3$ . The density ratio  $\rho_{\text{sec}}/\rho_{co}$  is thereby equal to 1.05. Because this density ratio is almost unity, the flowfield is assumed to be similar to that of the isothermal flow measured in the preceding section. The outlet velocity profile  $\bar{U}_o(r)$  of Figure 4.11 is multiplied by a factor  $\rho_{\text{sec}}/\bar{\rho}(r)$  in order to obtain the same massflow as that in the isothermal flow.

The radial distribution of the mixture fraction (and thereby the temperature) at the nozzle exit is given in Figure (4.20). Due to heat conduction at the wall, the outlet temperature decreases towards the wall. Also the temperature of the secondary air is seen to be slightly increased due to heat conduction. This effect may however be neglected in the numerical computations because of the low convection velocity in that region (Figure 4.11).

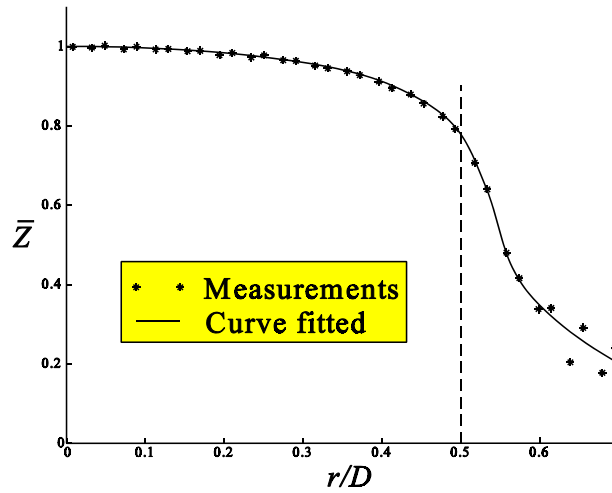


Figure 4.20 Mixture fraction profile close to the nozzle exit.

Figure (4.21) shows the centerline profile of the mixture fraction. In the result of the numerical simulation as well as in the result of the measurements, a core region in which the mixture fraction remains approximately constant is clearly present. The length of the core-region predicted by the present numerical method is too long. The mixture fraction decay constant  $K_Z$  varies between 0.20 upstream and 0.23 downstream in the experiment while it varies between 0.19 and 0.22 for the numerical solution. Pitts (1991) gives  $K_Z=0.2\pm 10\%$  which agrees reasonably well with the values found here.

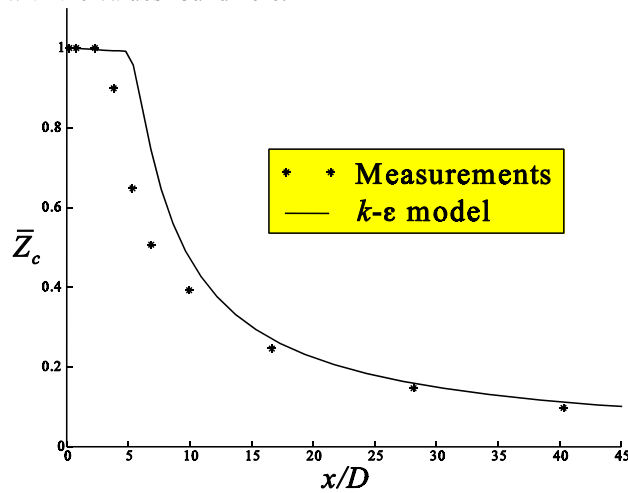


Figure 4.21 Centerline profile of the mixture fraction.

Figure 4.22 shows the half-width as a function of the axial distance. In the far field, the half-width spreading rate has been determined to be equal to 0.111. This value compares well with values found in literature (Table 4.2). From Figure 4.22 it can be seen that the virtual origin is

at an axial position of  $x=-a=-3.3D$ , which is further upstream of the nozzle exit than the virtual origin found for the velocity field (see page 62). The half-width spreading rate predicted by the  $k-\epsilon$  model agrees well with the experiment.

Author(s)	$S_{1/2}^Z$
Becker <i>et al.</i> (1976)	0.106
Birch <i>et al.</i> (1978)	0.097
Santoro <i>et al.</i> (1981)	0.097
Pitts <i>et al.</i> (1984)	0.104
Richards <i>et al.</i> (1993)	0.115
Present	0.111

Table 4.2 Measured halfwidth scalar spreading rates for round jets.

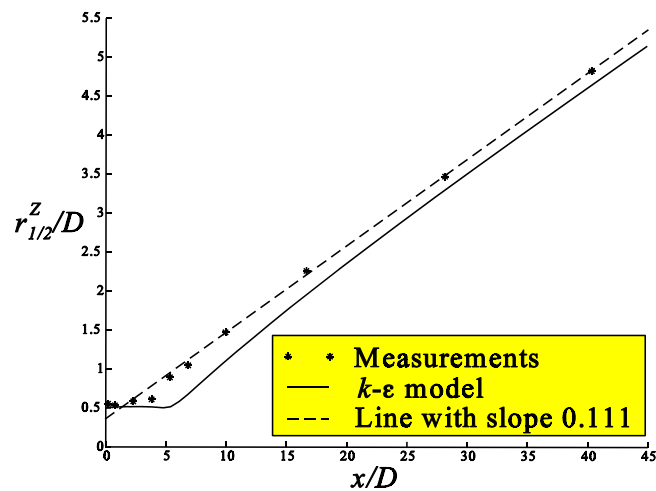


Figure 4.22 Variation of the half-width  $r_{1/2}^Z/D$  with axial distance.

Figure 4.23 shows the radial profile of the normalized mixture fraction  $\bar{Z}/\bar{Z}_c$  as a function of the normalized radial distance  $r/(x+a)$ . The distributions from the measurements satisfactorily collapse on one curve, indicating similarity in terms of  $r/(x+a)$ . Also shown is the analytical relation according to Equation (4.22). The value for  $\sigma_{t,Z}$  has been adjusted to 0.6 so that the two curves coincide at the half-value point  $r_{1/2}^Z=0.111(x+a)$ . Just as for the mean axial velocity component, also for the mixture fraction, the analytical solution predicts a too high value in the outer region.



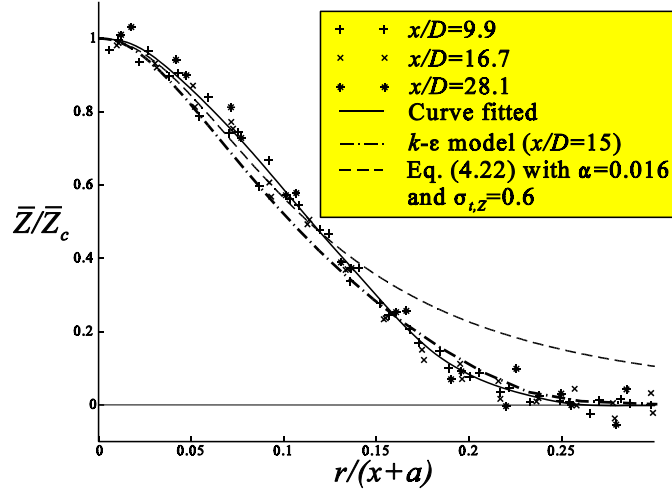


Figure 4.23 Radial profile of the normalized mixture fraction  $\bar{Z}/\bar{Z}_c$  as a function of the normalized radial distance  $r/(x+a)$ .

#### 4.4 MODIFICATIONS TO THE $k-\epsilon$ MODEL

In this section, some modifications to the standard  $k-\epsilon$  model will be considered. Because the standard  $k-\epsilon$  model constants do predict a too high spreading rate of momentum, Sanders (1994) suggested to set the  $C_\mu$  constant to 0.06 instead of the standard value of 0.09. However, such a modification would also make the core region longer. Such an effect is especially not desirable for the scalar mixing since the core region of the mixture fraction field is already predicted too long by the standard model. There is another important point with regard to the combustion problem to be treated in Chapter 6; changing the value for  $C_\mu$  will have influence on the predicted flame brush thickness. The reason for this is that the predicted flame brush thickness depends on the integral length scale which in turn depends on the mixing length  $l_m$  prescribed at the burner exit. Comparing Equation (3.19) with Equation (3.33) leads with  $C_\mu = 0.09$  to  $l_t = 1.22l_m$  and with  $C_\mu = 0.06$  to  $l_t = 1.65l_m$ . Changing the value of  $C_\mu$  from 0.09 to 0.06 would therefore enlarge the turbulent flame brush thickness by about 35%. A better modification would therefore be that recommended by Launder *et al.* (1972) based on the work of Rodi (1972):

$$\begin{aligned} C_\mu &= 0.09 - 0.04F \\ C_2 &= 1.92 - 0.0667F \end{aligned} \quad (4.91)$$

where

$$F = \left| \frac{r_{1/2}^u}{\tilde{u}_c - \tilde{u}_\infty} \left( \left| \frac{d\tilde{u}_c}{dx} \right| - \frac{d\tilde{u}_c}{dx} \right) \right|^{0.2} \quad (4.92)$$

This would result in a constant value of 0.09 for  $C_\mu$  in the core region and, according to the analytical model, a value of 0.06 in the developed region. However, because the scalar spreading rate was already predicted quite accurate by the standard model, also this modification will not

be used in the present study.

Another modification considered in this study is the so-called Renormalisation Group (RNG) model (Yakhot *et al.*, 1992). The RNG model differs from the standard  $k$ - $\epsilon$  model in the definition of its constants. The constants are given in Table 4.3.

$C_\mu$	$C_1$	$C_2$	$\sigma_k$	$\sigma_\epsilon$
0.085	$1.42 - \frac{\zeta(1-\zeta/\zeta_0)}{1+\beta\zeta^3}$ $\zeta_0=4.38$ and $\beta=0.015$	1.68	0.7179	0.7179

Table 4.3 Coefficients in the RNG model

The ‘constant’  $C_1$  is not really a constant anymore but depends on the local scaled strain rate  $\zeta$  given by

$$\zeta = S \frac{\tilde{k}}{\tilde{\epsilon}} \quad (4.93)$$

Here,  $S$  is the strain rate of the mean flow, defined by

$$S = \sqrt{2\overline{e_{ij}e_{ij}}} \quad (4.94)$$

in which  $e_{ij}$  is an element of the strain rate tensor,

$$e_{ij} = \frac{1}{2} \left( \frac{\partial u_i}{\partial x_j} + \frac{\partial u_j}{\partial x_i} \right) \quad (4.95)$$

Computational results show that the scaled strain rate is lower than  $\zeta_0$ . This implies a smaller  $C_1$  and therefore a lower dissipation rate. The higher  $\mu_t$  results in a much too high spreading rate and a too short core region.

The last model considered here is the so-called non-equal scales model (Sanders, 1994). The non-equal scales model consists essentially of new expressions for the eddy-diffusivity and scalar dissipation rate. The models discussed so far are based on the assumption of equal length and time scales for mechanical and scalar turbulence. This assumption is no longer used. Depending on the time scale ratio  $R$ ,

$$R = \frac{\tilde{k}/\tilde{\epsilon}}{\overline{Z'^2}/\overline{\epsilon Z'^2}} \quad (4.96)$$

the turbulent Schmidt number is calculated as

$$\sigma_{t,Z} = \begin{cases} \sigma_{t,Z_{equal}} \left( \frac{R}{2} \right)^2 & \text{for } R \geq 2 \\ \sigma_{t,Z_{equal}} & \text{for } R \leq 2 \end{cases} \quad (4.97)$$

where  $\sigma_{t,Z_{equal}} = 0.7$ .

The scalar dissipation rate is calculated as:

$$\varepsilon_{\tilde{Z}^{n2}} = \phi (\tilde{Z}^{n2})^{\lambda_1} \tilde{\varepsilon}^{\lambda_2} \quad (4.98)$$

The constant  $\phi$  is adjusted such that at the centerline position of maximum turbulence kinetic energy the scalar dissipation rate is equal to that predicted by the equal-scales model, i.e.

$$\left(\varepsilon_{\tilde{Z}^{n2}}\right)_{\max} = \phi \left(\tilde{Z}^{n2}\right)_{\max}^{\lambda_1} \tilde{\varepsilon}_{\max}^{\lambda_2} = 2 \frac{\tilde{\varepsilon}_{\max} \left(\tilde{Z}^{n2}\right)_{\max}}{\tilde{k}_{\max}} \quad (4.99)$$

and therefore

$$\phi = \frac{2 \left(\tilde{Z}^{n2}\right)_{\max}^{1-\lambda_1} \tilde{\varepsilon}_{\max}^{1-\lambda_2}}{\tilde{k}_{\max}} \quad (4.100)$$

Because the constant  $\phi$  is adjusted in this way, the predicted profiles are not too far from those predicted with the equal-scales model.

Figures 4.24 and 4.25 give a comparison between results obtained with the different turbulence models considered. These results indicate that the non-equal-scales model produces results that are almost identical to the results obtained with the standard equal-scales model. The RNG model gives results close to the experimental values for the region close to the nozzle exit, but further downstream the standard set of parameters performs better. Lowering  $C_\mu$  from 0.09 to 0.06 results in too high centerline values of velocity and mass fraction. Compared to the other turbulence models, the standard  $k$ - $\varepsilon$  gives relatively good results. Although the influence of large density fluctuations has not been considered in this chapter, the standard  $k$ - $\varepsilon$  model is also believed to be an appropriate model for simulating the combustion problems to be treated in the next chapters.

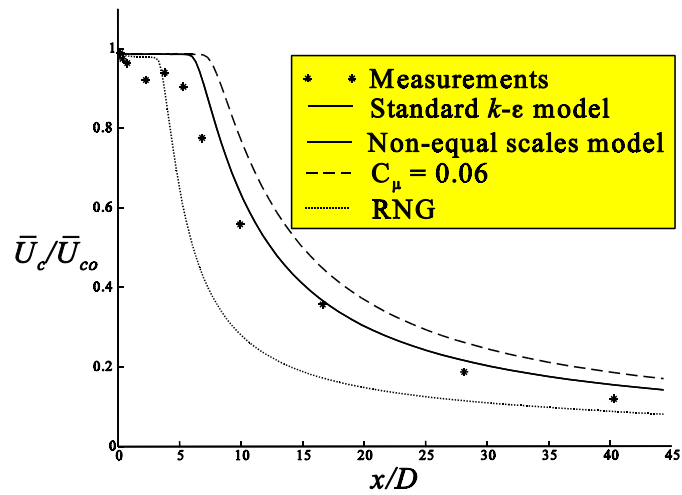


Figure 4.24 Centerline profiles of the normalized axial velocity predicted by different choices for the parameters in the  $k-\epsilon$  model.

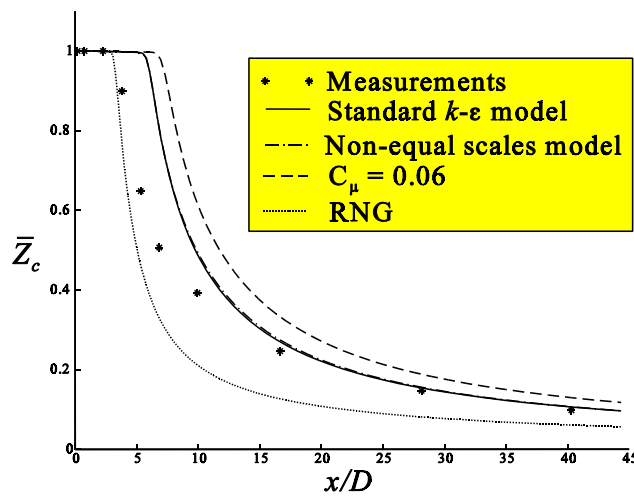


Figure 4.25 Centerline profile of the mixture fraction predicted by different choices for the parameters in the  $k-\epsilon$  model.

## 4.5 CONCLUSIONS

An axi-symmetrical turbulent jet has been studied, both theoretically as well as experimentally. In the mathematical model, the turbulent viscosity was assumed to be constant throughout the whole flow field and it was proportional to the square root of the momentum in axial direction. This assumption lead to a constant spreading rate in the analytical model which is also observed

experimentally. In the mathematical model, the empirical constant  $\alpha$  may be adjusted so as to obtain the same spreading rate as that found in experiments. Another important property of the mathematical model is that of similarity, i.e. the centerline value and the half-value distance alone were sufficient to describe the radial velocity and mixture fraction profile at any axial distance. Similarity was also found in the experiments after an axial distance from the nozzle outlet of about 10 nozzle diameters.

In the experiments, use has been made of the hot-wire anemometry method. A modified look-up inversion method has been developed. A set of X hot-wire response equations has been modified by including the influence of the binormal velocity component. In the limit of a zero binormal velocity component this new set of equations reduces to the commonly used X hot-wire equations. For a pure two-dimensional flow, this modified look-up inversion method still operates with very high accuracy.

For three-dimensional flows, the corrected X hot-wire response equations form an under-determined system of equations. To get a determined system of equations, the X hot-wire probe has to be used in two different attitudes. In the averaged equations, second and higher order velocity correlation terms have been modelled for the specific flow conditions found in a turbulent jet without swirl. The distribution for the axial and radial velocity components is assumed to be bivariate normal while the tangential velocity component is assumed to be statistically independent. The resulting set of six equations is solved by making use of the Newton method.

It was shown that neglecting the influence of the binormal velocity component leads to an over-prediction of the mean velocity and typically to an under-prediction of the measured velocity fluctuation intensities. Obviously, the influence of the binormal velocity component cannot be neglected if accurate flow measurements are required.

Mixture fraction profiles were obtained as a scaled function of the measured temperature. Temperatures were measured by making use of a thermocouple. Unfortunately, the response time of the thermocouple was not small enough to be able to measure the fluctuations in the mixture fraction.

The experimental results were compared to the mathematical model as well as to predictions obtained with the standard  $k-\epsilon$  turbulence model. It was found that with the standard  $k-\epsilon$  turbulence model, the spreading rate for the axial velocity component is over-predicted with about 8% while the spreading rate for the mixture fraction was in good agreement with that found in the measurements. Rather large differences between measurements and simulation were found near to the outlet of the nozzle. These differences may be caused by incorrect boundary conditions, especially in the co-flow where the radial velocity component was set to zero. Contrary to fully developed turbulent pipe flow, the radial velocity component was measured to be rather high at the nozzle outlet.

Several modifications to the standard  $k-\epsilon$  model have been considered. However, all models considered lead to either a too short or long core region or to an over- or under-prediction of the spreading rate. This lead to the decision to make use of the standard  $k-\epsilon$  model for simulation of the turbulent combustion problems to be treated in the next chapters.

## Chapter 5

### Turbulent diffusion flames

This chapter deals with the modelling of turbulent diffusion flames. If the conserved scalar approach of Section 2.4 is applied, the calculation of the state variables in a reacting flow is greatly simplified. Indeed if chemical equilibrium prevails, the solution for the conserved scalar  $Z$  and the static pressure  $p$  yields the entire state of the fluid. Different models have been developed for the case when equilibrium is not assumed, e.g. when use is made of finite-rate kinetics or the assumption is made that the chemical time scale is very short compared to the Kolmogorov time scale.

In this study, a laminar diffusion flamelet model will be used for modelling turbulent diffusion flames. Unlike the chemical equilibrium model, the laminar flamelet model makes it possible to represent chemical non-equilibrium effects like flame quenching. The use of a laminar diffusion flamelet model is based on the concept that within the turbulent flow field there do exist one-dimensional mixing layers. The one-dimensional structure of these mixing layers leads, under the influence of combustion, to the so-called flamelet equations. The species mass fractions and temperature calculated as function of the mixture fraction by the flamelet equations, depend on the shape of the scalar dissipation profile within the mixing layer. Because combustion takes mainly place under stoichiometric conditions, it is the scalar dissipation rate under stoichiometric conditions that has the largest influence on the outcome of the flamelet equations.

Other matters to be discussed in this chapter are the influence of premixing, the definition for the mixture fraction in the presence of multi-component diffusion, and the model used for obtaining the conditioned scalar dissipation rate which is used as the chemical non-equilibrium parameter. The model will be evaluated by simulating a stabilized natural gas flame.

#### 5.1 ONE-DIMENSIONAL SCALAR DISSIPATION LAYERS

Results obtained from detailed imaging measurements of conserved scalar fields  $Z(\underline{x},t)$  in nonreactive turbulent flows (Bish *et al.*, 1995) as well as direct numerical simulations (DNS) of passive scalar mixing in turbulent flows (Siggia, 1981) have shown that there do exist some coherent fine structures associated with the molecular mixing. The results show that the scalar dissipation field  $\chi(\underline{x},t)$  with  $\chi$  defined as

$$\chi = 2D \left( \frac{\partial Z}{\partial x_k} \right)^2 \quad (5.1)$$

consists entirely of thin strained laminar sheet-like diffusion layers. The internal structure of these scalar dissipation layers may be examined by considering the local velocity field in a translating and rotating coordinate frame moving with any chosen material point in the flow. This coordinate frame is aligned with the local instantaneous principal axes of the strain rate tensor. The local strain rate tensor may then be represented by its principal strain rates, i.e.

$$e = \begin{bmatrix} \frac{\partial u_1}{\partial x_1} & 0 & 0 \\ 0 & \frac{\partial u_2}{\partial x_2} & 0 \\ 0 & 0 & \frac{\partial u_3}{\partial x_3} \end{bmatrix} \quad (5.2)$$

For constant density, continuity requires  $e_{11} + e_{22} + e_{33} = 0$ . The strain rate tensor can then be written as:

$$e = a \begin{bmatrix} 1 & 0 & 0 \\ 0 & \sigma & 0 \\ 0 & 0 & -(1+\sigma) \end{bmatrix} \quad (5.3)$$

where  $\sigma = e_{22}/e_{11}$  is a single parameter describing the structure of the strain rate tensor, and  $a = e_{11}$  simply characterizes the magnitude of the principal strain rate component. If it is assumed that  $e_{11} \geq e_{22} \geq e_{33}$ , then the structure parameter  $\sigma$  is bounded by  $-1/2 \leq \sigma \leq 1$ . Two classes of local strain rate fields are possible, as shown in Figure 5.1. The first, namely  $\sigma > 0$ , corresponds to two extensional axes and one compressional strain axis. Deformations produced when  $\sigma > 0$  will distort any material volume towards a sheet-like topology, so that the local gradient  $\nabla Z$  will tend to align with the eigenvector for the most compressive principal strain rate  $e_{11}$ . Self-similar solutions (Buch *et al.*, 1996) show that, in the steady state limit, the scalar dissipation rate scales linearly with the strain rate  $a$ ;

$$\chi(Z; a, Z_r, Z_l) \sim \frac{a}{\pi} (Z_r - Z_l)^2 \exp \left\{ -2 \left[ \operatorname{erf}^{-1} \left( \frac{Z - \frac{1}{2}(Z_r + Z_l)}{\frac{1}{2}(Z_r - Z_l)} \right) \right]^2 \right\} \quad (5.4)$$

where  $\operatorname{erf}^{-1}(Z)$  is the inverse error function.  $Z_r$  and  $Z_l$  are the scalar boundary values for  $Z$ . In case of a jet of fuel, the subscripts  $r$  and  $l$  refer to the mixture fraction at the fuel-rich and fuel-lean side, respectively. Equation (5.4) reflects correctly that, at any strain rate  $a$ , the scalar dissipation can be large or small if the difference between  $Z_r$  and  $Z_l$  is large or small, respectively.  $Z_r$  and  $Z_l$  depend on the extent of premixing. Here it will be assumed that we are dealing with pure diffusion flames for which  $(Z_r, Z_l) = (1, 0)$ . The function  $\chi(Z, a)$  is shown in Figure 5.2 for  $(Z_r, Z_l) = (1, 0)$  and three different values of the strain rate  $a$ .

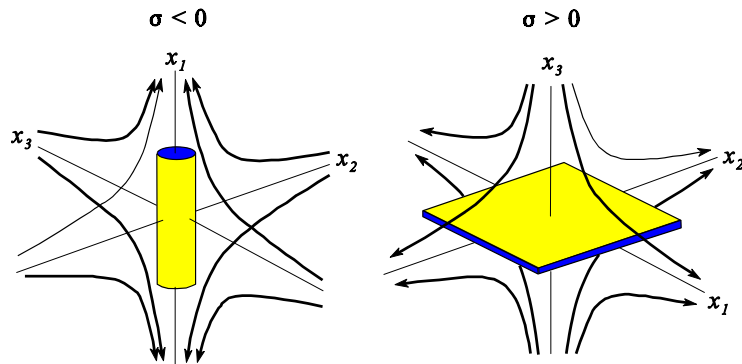


Figure 5.1 Local flow field structures for two different classes of the local strain rate structure.

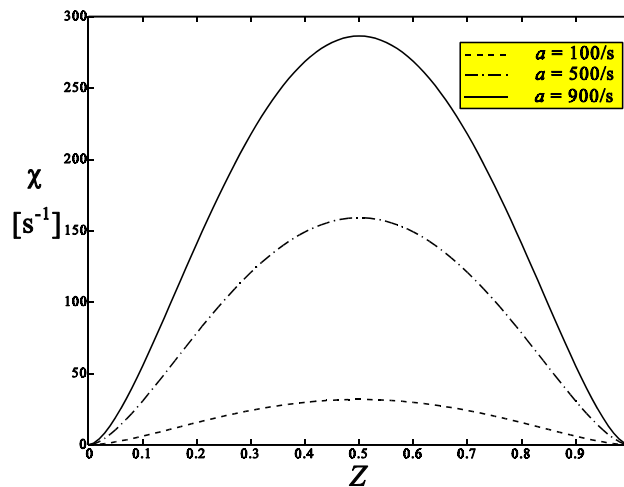


Figure 5.2 Scalar dissipation as a function of the mixture fraction at three different values of the strain rate  $a$ .

When  $\sigma < 0$  the local flow tends to deform a material volume into a line-like topology as indicated in Figure 5.1, with  $\nabla Z$  again tending to align with the most compressive principal strain rate axis. However, self-similar solutions (Buch *et al.*, 1996) show that line-like structures in the scalar dissipation field must decay exponentially in time. Therefore, no line-like structures can be sustained in the conserved scalar gradient field. Thus as the local  $\sigma(t)$  changes, the scalar dissipation dynamics allow only the sheet-like structures to be sustained.

The implications of this fundamentally layer-like structure of scalar mixing in turbulent flows are substantial, especially for turbulent combustion. This local one-dimensional layer-like structure must exist irrespective of the degree of chemical non-equilibrium to which the various constituent chemical species fields are subjected. The presence of the locally one-dimensional dissipation layers is independent of the chemical state of the flow. As a consequence, any model



relating the combustion chemistry in turbulent reactive flows to the underlying scalar mixing process must recover this layer-like dissipative structure in the mixture fraction. Therefore, this manifestly one-dimensional local structure of scalar dissipation fields in turbulent flows provides a starting point for a physically-based formulation for the chemical state of non-equilibrium combustion occurring in the flow. The insights provided by this analysis support the fluid dynamic foundations of certain sheet-like conceptual models of reacting flows, such as the flamelet model used in this study.

## 5.2 REGIMES DIAGRAM FOR NON-PREMIXED TURBULENT COMBUSTION

In order to construct a regimes diagram for non-premixed turbulent combustion, it is necessary to identify the relevant quantities that influence the flame structure. Since many chemical reactions with quite different rate constants occur in a real flame it is difficult to define a characteristic chemical time scale based on reaction kinetics. One way to resolve this is to consider the special case of a flamelet at extinction (see Section 5.3). The inverse of the strain rate  $a^{-1}$  represents the characteristic flow time. Therefore the inverse of the strain rate at extinction, i.e.  $a_q^{-1}$ , may be used to characterize the chemical time scale  $t_c$ , i.e.

$$t_c = a_q^{-1} \quad (5.5)$$

Let us consider the Damköhler number defined as the ratio of the Kolmogorov time  $t_\eta$  to the chemical time  $t_c$ :

$$Da = t_\eta/t_c \quad (5.6)$$

In the range  $Da < 1$ , turbulence is of fine scale; that is, the eddy size and mixing length are smaller than the flame-front thickness. The effect of these fine-scale eddies is to enhance the intensity of the transport processes within the combustion front, regions of intense mixing and reaction appear. We will call this regime the distributed reaction zones regime. If combustion is fast with respect to the Kolmogorov time, i.e. if  $Da > 1$ , the flow may be considered as quasi-steady. The turbulent eddies are of dimensions much larger than the laminar flame-front thickness. The large eddies distort the otherwise smooth "laminar" flame front, but there is a small influence of turbulence on the structure of the flame front (Figure 5.3). We call this the flamelet regime.

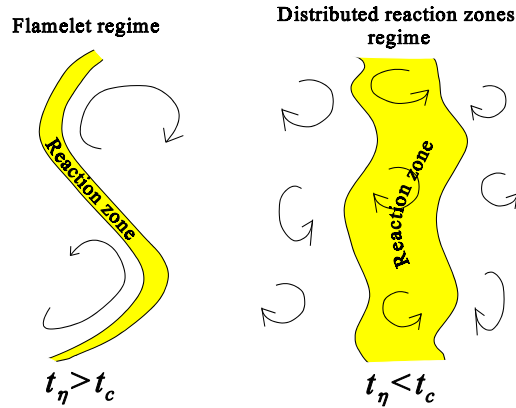


Figure 5.3 Effect of turbulence on the structure of the reaction zone.

Slow chemistry is not very often of practical interest: there are a few applications like combustion of highly diluted reactants in post-flame regions where chemistry is slow compared to convection and diffusion. On the other hand, reacting flows with fast chemistry occur in many applications. The reason is very simple: for combustion to be stable and complete it must be rapid and therefore the chemical time scales must be sufficiently short under all circumstances. For example a reciprocating engine is designed such that only at limiting conditions, that is at very high engine speeds, turbulent time scales may become comparable to chemical time scales. Therefore, the flamelet regime covers a wide range of applications.

Another important consideration in constructing the regimes diagram for non-premixed turbulent combustion is that of the flame thickness in mixture fraction space,  $(\Delta Z)_F$ . It may be defined as the thickness of the region in mixture fraction space where essentially all chemical activity occurs. In a non-homogeneous mixture field the reaction zone is attached to the high temperature region, close to stoichiometric mixture, and is convected and diffused with the mixture field. Reaction rates are high where the mean mixture fraction corresponds to the stoichiometric value. The shape of the surface at which the mixture fraction is equal to the stoichiometric value may be as depicted in the top of Figure 5.4. In this figure,  $\eta$  is the local layer-normal coordinate, i.e. normal to an iso-surface of the mixture fraction  $Z$ . The mixture fraction  $Z$  depends on  $\eta$  as depicted in the bottom of Figure 5.4. On both sides of the reaction layer the mixture fraction extends to the rich and lean value, i.e.  $Z_r$  and  $Z_l$ , respectively. Based on these values, a criterion can be formulated that distinguishes between the connected and separated reaction zones regimes. In case of hydrogen or hydrocarbon combustion in air, the stoichiometric mixture fraction is small and therefore heat loss is predominantly towards the oxidizer side. For hydrogen and hydrocarbon combustion the range  $0 \leq Z \leq (\Delta Z)_F$ , with typically  $(\Delta Z)_F = 2Z_{st}$ , essentially covers the region where all chemical activity occurs. Changing the boundary condition on the lean side is therefore expected to always have a rather large influence on the flamelet structure. However, changing the boundary condition on the fuel side is not expected to have a large influence on the flamelet structure as long as  $Z_r > (\Delta Z)_F$  (see Figure 5.5). This means that if the scalar dissipation rate under stoichiometric conditions ( $\chi_{st}$ ) is kept constant, changing the boundary condition of flamelet Equations (5.14) on the rich side to the

influence on the solution as long as  $Z_r > (\Delta Z)_F$ . The value for  $Z_r$  is decreased under the influence of premixing as indicated by the arrow in Figure 5.5. If  $Z_r$  is larger than  $(\Delta Z)_F$ , one has separated reaction zones, otherwise connected reaction zones. Also in the regimes diagram of Figure 5.6 an arrow has been drawn to indicate that under the influence of premixing a flame enters from the separated reaction zones regime into the connected reaction zones regime. Notice that laminar flamelet burning can still occur in the regime denoted by the connected reaction zones regime.

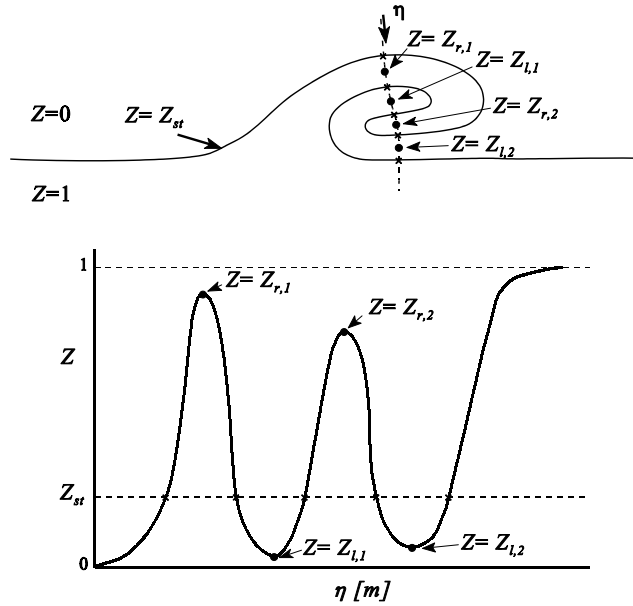


Figure 5.4 Mixture fraction extending to the rich and lean values.

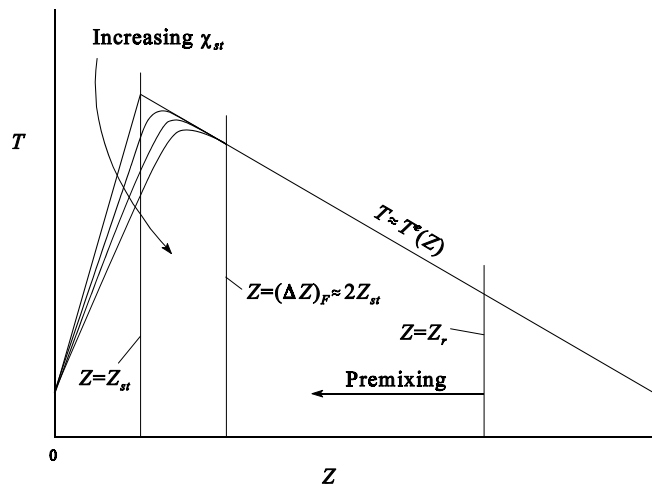


Figure 5.5 Flamelet profiles at different scalar dissipation rates under stoichiometric conditions.

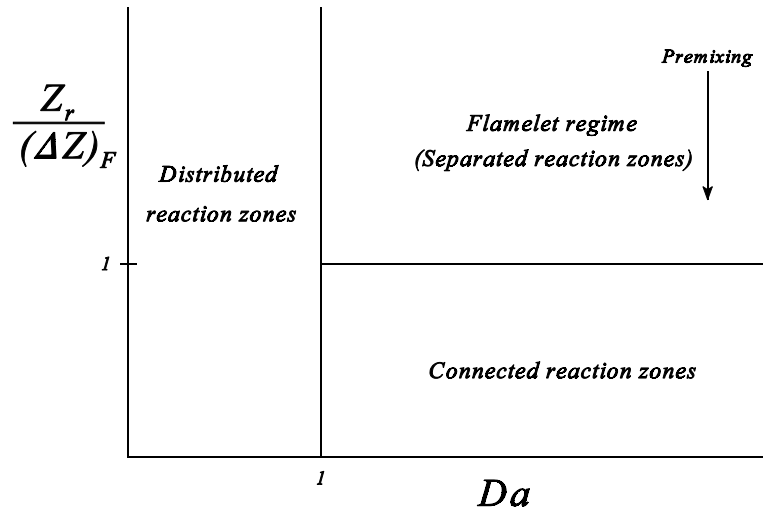


Figure 5.6 Regimes in non-premixed turbulent combustion.

### 5.3 LAMINAR DIFFUSION FLAMELET MODEL

In non-premixed combustion, the reactants are initially separated. When the different feeds of reactants are brought together, a reaction is possible. This reaction can only take place at the position where the reactants meet each other and a flammable composition of fuel and oxidizer exists, then a flame sheet will be formed. If the chemical reaction is very fast compared to the diffusion, this flame sheet will be very thin. In case of a laminar flowfield, a laminar diffusion flame will exist. In the laminar flamelet concept the turbulent flame is thought to be an ensemble of laminar flamelets. A flamelet is a very thin reaction layer embedded within the turbulent flow. Each flamelet has the structure of a laminar flame.

By introducing a coordinate transformation of the Crocco-type at the location of the laminar flame front and by making use of asymptotic expansions, Peters (1983) showed that the scalar flame structure to first order can be described as a function of two parameters, i.e. the mixture fraction  $Z$  and the scalar dissipation rate  $\chi$  under stoichiometric conditions, i.e.  $\chi_{st}$ . Under the assumption that gradients in the scalar quantities along surfaces of constant mixture fraction are negligible compared to the gradients perpendicular to these surfaces, locally, the concentration of any constituent can be expressed as a function of the mixture fraction, i.e.

$$Y_i = Y_i(Z) \quad (5.7)$$

In the limit of fast chemistry it can indeed be shown (Peters, 1983) that gradients along the surface of stoichiometric mixture fraction are smaller than the gradients perpendicular to that surface. Far away from the stoichiometric surface, the structure is to leading order equal to the equilibrium structure, which again depends on  $Z$  only.

By making use of the conservation equation of mass, the species conservation Equation (2.36) can then be written as:

$$\rho \frac{\partial Z}{\partial t} \frac{dY_i}{dZ} + \rho u_k \frac{\partial Z}{\partial x_k} \frac{dY_i}{dZ} = \frac{dY_i}{dZ} \frac{\partial}{\partial x_k} \rho D \frac{\partial Z}{\partial x_k} + \rho D \left( \frac{\partial Z}{\partial x_k} \right)^2 \frac{d^2 Y_i}{dZ^2} + \dot{w}_i \quad (5.8)$$

and by making use of the conservation equation for  $Z$  (2.40) this equation reduces to:

$$\frac{1}{2} \rho \chi \frac{d^2 Y_i}{dZ^2} + \dot{w}_i = 0 \quad (5.9)$$

Where  $\chi$  is the scalar dissipation rate defined as:

$$\chi = 2D \left( \frac{\partial Z}{\partial x_k} \right)^2 \quad (5.10)$$

In the same way, the conservation equation of energy (2.44) reduces to

$$\frac{d^2 h}{dZ^2} = 0 \quad (5.11)$$

By substitution of Equations (2.22) and (5.9) we get under the assumption that  $T=T(Z)$  (fast chemistry):

$$\begin{aligned} \frac{d^2 h}{dZ^2} &= c_p \frac{d^2 T}{dZ^2} + \sum_{i=1}^N h_i \frac{d^2 Y_i}{dZ^2} + \frac{dc_p}{dZ} \frac{dT}{dZ} + \sum_{i=1}^N \frac{dh_i}{dZ} \frac{dY_i}{dZ} \\ &= c_p \frac{d^2 T}{dZ^2} - \sum_{i=1}^N \frac{h_i \dot{w}_i}{\frac{1}{2} \rho \chi} + 2 \frac{dT}{dZ} \sum_{i=1}^N c_{p_i} \frac{dY_i}{dZ} + \left( \frac{dT}{dZ} \right)^2 \sum_{i=1}^N Y_i \frac{dc_{p_i}}{dT} \\ &= 0 \end{aligned} \quad (5.12)$$

So that the temperature equation can be written as:

$$\frac{1}{2} \rho \chi \frac{d^2 T}{dZ^2} - \sum_{i=1}^N \frac{h_i \dot{w}_i}{c_p} + \rho \chi \frac{dT}{dZ} \sum_{i=1}^N \frac{c_{p_i}}{c_p} \frac{dY_i}{dZ} + \frac{1}{2} \rho \chi \left( \frac{dT}{dZ} \right)^2 \sum_{i=1}^N \frac{Y_i}{c_p} \frac{dc_{p_i}}{dT} = 0 \quad (5.13)$$

So now we have a set of  $N+1$  one-dimensional equations in 'mixture-fraction-space',  $N$  for the mass fractions and one for the temperature:

$$\begin{aligned} \frac{1}{2} \rho \chi \frac{d^2 Y_i}{dZ^2} + \dot{w}_i &= 0 \quad (i=1, \dots, N) \\ \frac{1}{2} \rho \chi \frac{d^2 T}{dZ^2} - \sum_{i=1}^N \frac{h_i \dot{w}_i}{c_p} + \rho \chi \frac{dT}{dZ} \sum_{i=1}^N \frac{c_{p_i}}{c_p} \frac{dY_i}{dZ} + \frac{1}{2} \rho \chi \left( \frac{dT}{dZ} \right)^2 \sum_{i=1}^N \frac{Y_i}{c_p} \frac{dc_{p_i}}{dT} &= 0 \end{aligned} \quad (5.14)$$

The boundary conditions are:

-For  $Z=0$ ;  $Y_i=Y_i^0$  and  $T=T^0$

-For  $Z=1$ ;  $Y_i=Y_i^F$  and  $T=T^F$

Equations (5.14) can only be solved if all quantities involved are a function of the mass fractions and the temperature only, i.e. also a function of the mixture fraction only. Under the assumption that pressure fluctuations are negligible the density is related to the temperature and

the mass fractions by the equation of state (2.45), so that:

$$\rho = \rho(Y_1, \dots, Y_N, T) \quad (5.15)$$

According to Equation (2.30) then also the chemical source terms depend on the mass fractions and the temperature only:

$$\dot{w}_i = \dot{w}_i(Y_1, \dots, Y_N, T) \quad (5.16)$$

Further it holds that:

$$\begin{aligned} h_i &= h_i(T) \\ c_{p_i} &= c_{p_i}(T) \\ c_p &= c_p(Y_1, \dots, Y_N, T) \end{aligned} \quad (5.17)$$

Provided that the ' $\chi$ -profile'  $\chi = \chi(Z)$  is specified we are now able to solve the Equations (5.14) for that specific ' $\chi$ -profile'. In other words, for a specific  $\chi$ -profile we are able to map all scalar quantities (except for  $p$ ) into mixture fraction space by making use of Equations (5.14).

The problem now arises that we have to define a parametric description of all  $\chi$ -profiles appearing in a turbulent diffusion flame, and we have to find out how to calculate these parameters in the turbulent diffusion flame. The scalar flame structure may then be calculated a priori for a variety of these parameters. In turbulent diffusion flames, however, there is an infinite number of  $\chi$ -profiles belonging to the five different states of the flamelet:

1. The steady unreacted initial mixture.
2. The unsteady transition after ignition.
3. The quasi-steady burning state.
4. The unsteady transition after quenching.
5. The unsteady transition after re-ignition.

So we have to limit ourselves to the most frequently occurring  $\chi$ -profiles. Instead of using the constant density  $\chi$ -profiles of Equation (5.4), it is also possible to directly choose a laminar flame model to be representative for the flamelets in turbulent diffusion flames. Unsteady transition flamelets require the specification of initial conditions and depend therefore on a larger number of parameters. As they can be expected to occur less frequently than the steady states in turbulent diffusion flames, their contribution will be omitted and we will limit our attention to  $\chi$ -profiles of the steady-state flamelets. It seems appropriate to choose a laminar flow configuration that fulfils the following requirements:

1. It is a steady-state configuration that can be investigated theoretically or experimentally.
2. The  $Z$  dependence of the  $\chi$ -profile follows closely that of Equation (5.4).

Such a configuration is the counter-flow geometry or stagnation-point flow. It has the additional advantage that counter-flow diffusion flames have been studied theoretically and experimentally more often than any other diffusion flame configuration. The governing equations reduce via a similarity transformation to one-dimensional equations that can be solved with arbitrarily complicated transport properties and chemistry. For a counter-flow diffusion flame with strain rate  $a$  at the oxidizer side, the  $\chi$ -profile may be approximated by (Kim *et al.*, 1993)

$$\chi(Z) = \frac{(j+1)a}{4\pi} \frac{3\left(\sqrt{\rho_\infty/\rho(Z)}+1\right)^2}{2\sqrt{\rho_\infty/\rho(Z)}+1} \exp\{-2[\operatorname{erfc}^{-1}(2Z)]^2\} \quad (5.18)$$

where  $j=0$  applies for the planar configuration and  $j=1$  applies for the axi-symmetrical configuration. The density at the oxidizer side is given by  $\rho_\infty$  and  $\operatorname{erfc}^{-1}(Z)$  is the inverse of the complementary error function, i.e.  $\operatorname{erfc}(Z)=1-\operatorname{erf}(Z)$ .

In summary,  $\chi$ -profiles found in counter-flow diffusion flames are assumed to be predominant in turbulent diffusion flames. Therefore, it is possible to carry out calculations for a limited set of  $\chi$ -profiles a priori on a number of counter-flow diffusion flames. For each counter-flow diffusion flame all scalar quantities, except the pressure  $p$ , can then be calculated as a function of the strain rate  $a$  and the mixture fraction  $Z$  and stored in a so-called flamelet library.

If the mixture fraction field  $Z(\underline{x},t)$  has been solved then the scalar dissipation rate  $\chi(\underline{x},t)$  can be evaluated from Equation (5.10). The local chemical composition of the diffusion flame can then be determined from the pre-calculated flamelet with

$$\chi_{st} = \chi \frac{f(Z_{st})}{f(Z)} \quad (5.19)$$

where

$$f(Z) = \exp\{-2[\operatorname{erfc}^{-1}(2Z)]^2\} \quad (5.20)$$

The scalar dissipation under stoichiometric conditions, i.e. the scalar dissipation at the position  $Z=Z_{st}$ , is defined as:

$$\chi_{st} = 2D_{st} \left( \frac{\partial Z}{\partial x_k} \right)_{Z=Z_{st}}^2 \quad (5.21)$$

The choice of taking  $\chi_{st}$  as the parametric representation of the  $\chi$ -profile is motivated by the fact that in asymptotic analysis for large activation energies the variation of  $\chi$  around  $\chi_{st}$  is considered to be a higher-order effect (Peters, 1983). It has also been shown by Seshadri *et al.* (1988) that the exponential term has little influence on the flame structure, i.e. replacing  $\chi$  by  $\chi_{st}$  in Equations (5.14) leads to virtually the same results.

So, it can be summarized that the overall scalar flame structure (except for  $p$ ) can be described as a function of two parameters, i.e.  $Z$  and  $\chi_{st}$ :

$$\phi = \phi(Z, \chi_{st}) \quad (5.22)$$

The implementation of the flamelet concept is based on the development of a library of 'flamelet profiles', each of which is characterised by the scalar dissipation rate under stoichiometric conditions  $\chi_{st}$ . The structure of the flamelet is influenced by the turbulent flow. The flamelet can be stretched by the turbulent flowfield. The parameter  $\chi_{st}$  provides the interaction between the turbulent flowfield and the combustion.

A schematic representation of the flamelet model is given in Figure 5.7. The flamelet library depicted in the top of Figure 5.7 is constructed by determining the solution of laminar counterflow diffusion flames depicted in the lower left corner. The flamelet library contains a number of flamelet profiles at different conditioned scalar dissipation rates  $\chi_{st,i}$  ( $i=1..$ number of flamelets). In the turbulent flow depicted in the lower right corner, the scalar dissipation rate under stoichiometric conditions is computed from the local value of the mixture fraction and the

scalar dissipation rate. A flamelet profile with the same conditioned scalar dissipation rate is obtained from the flamelet library. Finally, the local mixture fraction is used to obtain the local values of the scalar variables from that flamelet solution.

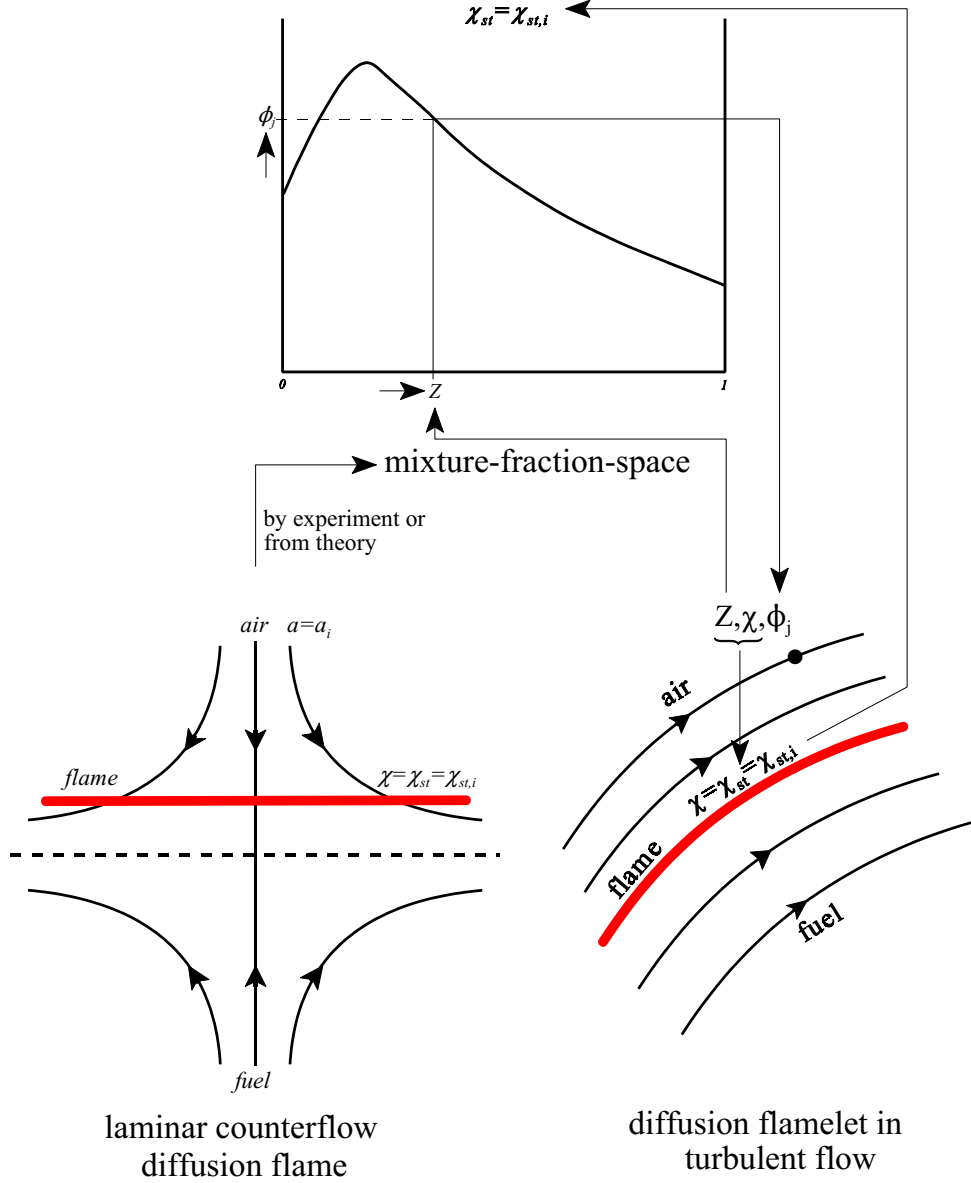


Figure 5.7 Schematic representation of the laminar flamelet model.



### Quenching

The structure of the flamelet is influenced by the turbulent flow field. Because of the velocity gradients present in a turbulent flow, the flamelet will be stretched. This stretching may result in extinction of the flamelet. When  $\chi_{st}$  becomes too large, the diffusion of heat away from the reaction zone is no longer balanced by the production of heat by chemical reaction. This results in a reduction of the temperature in the reaction zone. The decrease of temperature then results in a decrease of the chemical reaction rate, and so the flame will be quenched. This implies that there exists a critical value for  $\chi_{st}$ . For values of  $\chi_{st}$  larger than the critical value  $\chi_q$ , there is no burning state of the flamelet possible. For the laminar counter-flow diffusion flame, with the strain rate slightly smaller than the quenching strain rate, as the value of the scalar dissipation rate at  $Z=Z_{st}$ . A plot of  $T(Z_{st})$  as a function of  $\chi_{st}^{-1}$  is the well-known S-shaped curve of Figure 5.8.

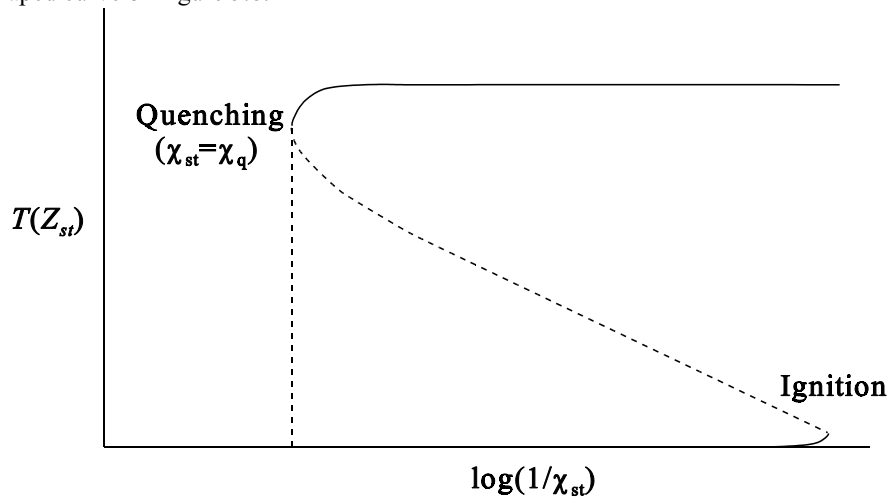


Figure 5.8 Response of a diffusion flame, i.e. the S-shaped curve.

## 5.4 ONE-DIMENSIONAL LAMINAR COUNTERFLOW DIFFUSION FLAMES

In this section the system of ordinary differential equations describing the laminar flamelets is derived. Consider a steady axisymmetrical counterflow configuration with the fuel originating from  $x=-\infty$  and the oxidizer from  $x=\infty$  (Figure 5.9). The velocity components are as defined in Section 3.4. A similarity solution is obtained by writing

$$\begin{aligned}
 u &= u(x) \\
 v &= rQ(x) \\
 Y_i &= Y_i(x) \\
 T &= T(x) \\
 p &= p(x,r)
 \end{aligned}
 \tag{5.23}$$

Thereby a set of one-dimensional equations in the x-direction is obtained.

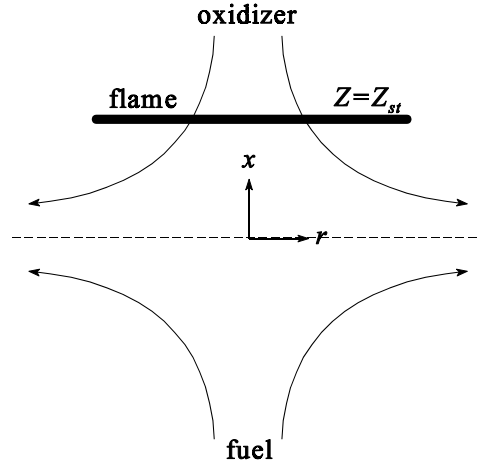


Figure 5.9 Laminar counterflow diffusion flame.

Continuity:

$$\frac{d(\rho u)}{dx} + (j+1)\rho Q = 0 \quad (5.24)$$

$r$ -component of momentum:

$$\rho u \frac{dQ}{dx} = -\rho Q^2 + P' + \frac{d}{dx} \left( \mu \frac{dQ}{dx} \right) \quad (5.25)$$

Species:

$$\rho u \frac{dY_i}{dx} = -\frac{dJ_i}{dx} + \dot{w}_i \quad (5.26)$$

Temperature:

$$\rho u c_p \frac{dT}{dx} = \frac{d}{dx} \left( \lambda \frac{dT}{dx} \right) - \sum_{i=1}^n h_i \dot{w}_i - \frac{dT}{dx} \sum_{i=1}^n c_{p_i} J_i - \frac{\partial q_R}{\partial x} \quad (5.27)$$

In Equation (5.24)  $j=0$  applies for the planar and  $j=1$  for the axisymmetrical configuration. In Equation (5.25),  $P'$  represents the pressure gradient term and is defined as:

$$P' = \rho_\infty a^2 \quad (5.28)$$

where  $a$  represents the strain rate, i.e. the velocity gradient in the oxidizer stream,

$$a = \left( \frac{\partial v}{\partial r} \right)_{x=\infty} \quad (5.29)$$

and is in general prescribed. The boundary conditions for  $Q$  are  $Q=a$  at  $x=+\infty$  and  $Q=(\rho_\infty/\rho_{-\infty})^{1/2}a$  at  $x=-\infty$ . The boundary condition for  $u$  follows from the continuity Equation (5.24). The system of equations is closed by the equation of state, i.e. Equation (2.18).

#### 5.4.1 Definition of the mixture fraction

The mixture fraction may be defined as a linear combination of element mass fractions  $Z_i$  such that it is 0 in the oxidizer stream and 1 in the fuel stream. In a two-feed system, the local mixture fraction represents the local mass fraction originating from the fuel stream. Therefore, the mixture fraction may be defined by:

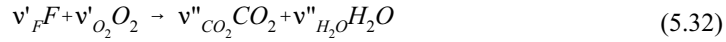
$$Y_{F,u} = Y_{F,1}Z \quad (5.30)$$

where  $Y_{F,u}$  is the local mass fraction of fuel in the unburnt mixture and  $Y_{F,1}$  denotes the mass fraction of fuel in the fuel stream. Similarly, since  $1-Z$  represents the mass fraction originating from the oxidizer stream, one obtains for the local mass fraction of oxygen in the unburnt mixture:

$$Y_{O_2,u} = Y_{O_2,2}(1-Z) \quad (5.31)$$

where  $Y_{O_2,2}$  represents the mass fraction of oxygen in the oxidizer stream.

The stoichiometric mixture fraction  $Z_{st}$  can be defined in terms of a global reaction equation. For instance for complete combustion of a hydrocarbon fuel  $F$ ,



the changes of mass fraction of oxygen and fuel are related by Equation (2.30):

$$\frac{dY_F}{dY_{O_2}} = \frac{\dot{w}_F}{\dot{w}_{O_2}} = \frac{W_F \nu'_F}{W_{O_2} \nu'_{O_2}} \quad (5.33)$$

where  $\nu'_F$  and  $\nu'_{O_2}$  are the stoichiometric coefficients of the fuel and oxygen, respectively, and  $W_F$  and  $W_{O_2}$  are the molecular weights of the fuel and oxygen, respectively. Equation (5.33) may be integrated to

$$\nu Y_F - Y_{O_2} = \nu Y_{F,u} - Y_{O_2,u} \quad (5.34)$$

where  $\nu = \nu'_{O_2} W_{O_2} / \nu'_F W_F$  is the stoichiometric oxidizer to fuel mass ratio. By substitution of Equations (5.30) and (5.31) into Equation (5.34) one obtains

$$Z = \frac{\nu Y_F - Y_{O_2} + Y_{O_2,2}}{\nu Y_{F,1} + Y_{O_2,2}} \quad (5.35)$$

For a stoichiometric mixture,  $Y_F$  and  $Y_{O_2}$  will both be zero and therefore

$$Z_{st} = \left[ 1 + \frac{\nu Y_{F,1}}{Y_{O_2,2}} \right]^{-1} \quad (5.36)$$

For methane-air combustion with 100%  $CH_4$  and  $Y_{O_2,2}=0.232$  the stoichiometric mixture fraction may be evaluated to be equal to 0.055. For hydrogen-air combustion it is equal to 0.028.

It must be noted here that the fuel mass fraction  $Y_F$  can only be defined if all diffusivities are equal. Because multi-component diffusion causes different elements to diffuse with different velocities, the definition of the mixture fraction is non-trivial. The fuel mass fraction must be expressed in terms of the element mass fractions.

Assume that

$$F = C_x H_y \quad (5.37)$$

$$\nu'_F = 1, \quad \nu'_{O_2} = x + \frac{1}{4}y, \quad \nu''_{CO_2} = x, \quad \nu''_{H_2O} = \frac{1}{2}y$$

The species mass fractions may be expressed in terms of the element mass fractions of  $C$  and  $H$  and the products mass fractions of  $H_2O$ :

$$\begin{aligned}
 Y_F = Y_{C,H,y} &= Z_C + Z_H - \frac{W_C}{W_{CO_2}} Y_{CO_2} - \frac{2W_H}{W_{H_2O}} Y_{H_2O} \\
 Y_{O_2} &= Z_O - \frac{2W_O}{W_{CO_2}} Y_{CO_2} - \frac{W_O}{W_{H_2O}} Y_{H_2O} \\
 Y_{CO_2} &= 2 \frac{x}{y} \frac{W_{CO_2}}{W_{H_2O}} Y_{H_2O}
 \end{aligned} \tag{5.38}$$

Substitution of Equations (5.37) and (5.38) into Equation (5.35) leads to:

$$Z = \frac{2Z_C/W_C + \frac{1}{2}Z_H/W_H + (Z_{O_2} - Z_O)/W_O}{2Z_{C,1}/W_C + \frac{1}{2}Z_{H,1}/W_H + Z_{O,2}/W_O} \tag{5.39}$$

The advantage of this definition for  $Z$  is that for  $Z$  equal to  $Z_{st}$ , the mixture is really stoichiometric in terms of the mixture fraction definition given by Equation (5.35).

#### 5.4.2 The relation between the strain rate and the scalar dissipation rate

Some results of a computation for a planar 100%  $CH_4$ -air flame performed by Peeters (1995) and results of a computation performed for a plane  $H_2$ -air flame by Sanders (1994) have been summarized in Appendix C. Figure 5.10 shows the calculated relation between the strain rate and the scalar dissipation rate at stoichiometric conditions in the planar  $CH_4$ -air flame. Obviously, the scalar dissipation rate increases linearly with the strain rate  $a$  as predicted by Equation (5.18). With  $Z_{st}=0.055$ ,  $\rho_{st}=0.66$  and  $\rho_\infty=1.18$  for the methane flame, Equation (5.18) predicts that  $d\chi_{st}/da \approx 2.8 \cdot 10^{-2}$  which is just slightly lower than the gradient of approximately  $3.2 \cdot 10^{-2}$  found from the calculations, i.e. from Equations (5.24-27).

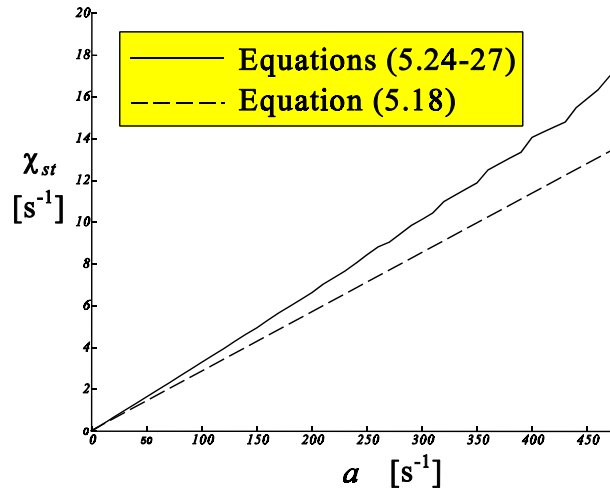


Figure 5.10 Relation between strain rate and scalar dissipation rate  $\chi_{st}$  in a planar 100%  $CH_4$ -air counterflow diffusion flame.

Because of the apparently linear relationship between the strain rate and the scalar dissipation rate in laminar counter flow diffusion flames, many researchers argue that the strain rate can be used as the chemical non-equilibrium parameter rather than the scalar dissipation rate. Here it is argued that such an approach may lead to very unrealistic results especially in cases where premixing plays an important role. In these cases the relation between  $\chi$  and  $a$  is very much influenced by the level of premixing (see Equation (5.4)). Consider the case of Figure 5.11 where a premixed flame heats up the mixture to the equilibrium temperature  $T=T^e(Z)$ . Physically, increasing the strain rate in the burnt mixture should not lead to a decreased temperature. However, if the strain rate would be used as the parameter indicating the state of non-equilibrium this would lead to the unrealistic result that the temperature is decreased by increasing the strain rate. Because the scalar dissipation rate equals zero in this case, the scalar dissipation rate would indeed lead to a temperature that remains close to the equilibrium temperature.

Another point clearly illustrating that the strain rate is not the proper parameter to be used as a chemical non-equilibrium parameter is that, with  $\chi_q$  being independent of the specific flow configuration, Equation (5.18) indicates that the quenching strain rate is flow configuration dependent. In numerical computations (e.g. Sanders, 1994) it has indeed been found that the quenching strain rate for planar counterflow diffusion flames is about twice as high as the quenching strain rate for the axi-symmetrical case. Nevertheless, in many studies, the uncertainty on the choice of the geometry of the laminar flamelets was transferred to an uncertainty in the choice of the mean strain rate coefficient. However, a consistent approach to the flamelet model should not very much depend on the choice of the laminar flame configuration used for building the flamelet library. Therefore the scalar dissipation rate is the appropriate parameter to be used as the parameter indicating the state of chemical non-equilibrium.

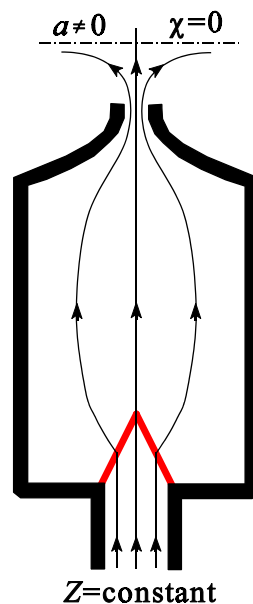


Figure 5.11 The effect of premixing.

## 5.5 AVERAGED SCALAR QUANTITIES

Favre-averaged scalar quantities are calculated by making use of a presumed PDF method. A Favre-averaged scalar quantity is calculated as

$$\bar{\phi} = \int_{\chi_{st}=0}^{\infty} \int_{Z=0}^1 \phi(Z, \chi_{st}) \tilde{P}(Z, \chi_{st}) dZ d\chi_{st} \quad (5.40)$$

$Z$  and  $\chi_{st}$  are assumed to be statistically independent and the PDF is described as the product of two separate PDF's;  $\tilde{P}(Z)$  and  $\tilde{P}(\chi_{st})$ . The variance in the conditioned Favre-averaged scalar dissipation rate  $\chi_{st}$  is assumed to be zero and therefore the PDF for  $\chi_{st}$  is given by a single delta function at  $\chi_{st} = \tilde{\chi}_{st}$ ,

$$\tilde{P}(\chi_{st}) = \delta(\chi_{st} - \tilde{\chi}_{st}) \quad (5.41)$$

Therefore, Favre averaged scalar quantities are obtained by integration over a flamelet profile with scalar dissipation rate  $\tilde{\chi}_{st}$ :

$$\bar{\phi} = \int_{Z=0}^1 \phi(Z | \tilde{\chi}_{st}) \tilde{P}(Z) dZ \quad (5.42)$$

The time-averaged density is obtained similar to Equation (3.73),

$$\bar{\rho} = \left[ \int_{Z=0}^1 \frac{\tilde{P}(Z)}{\rho(Z | \tilde{\chi}_{st})} dZ \right]^{-1} \quad (5.43)$$

The integrations in Equation (5.42) and Equation (5.43) are performed over a flamelet with scalar dissipation rate  $\tilde{\chi}_{st}$  at stoichiometric conditions. This average value  $\tilde{\chi}_{st}$  can be determined from Equation (5.19) as

$$\tilde{\chi}_{st} = \frac{\tilde{\chi}}{\int_0^1 \frac{f(Z)}{f(Z_{st})} \tilde{P}(Z) dZ} \quad (5.44)$$

where the mean scalar dissipation rate is modelled as (equal scales model):

$$\tilde{\chi} = 2D \left( \frac{\partial \tilde{Z}}{\partial x_k} \right)^2 + c_\chi \frac{\tilde{\epsilon}}{\tilde{k}} \quad (5.45)$$

with a modelling constant  $c_\chi = 2.0$ .

For the PDF over the mixture fraction a beta function PDF is assumed to be appropriate. Its shape is determined by the Favre-averaged mixture fraction and its variance. Therefore equations for the Favre-averaged mixture fraction  $\tilde{Z}$  and for the mixture fraction variance  $\tilde{Z}''^2$  are solved. In this way the mixture fraction variance serves as an additional parameter in the presumed PDF method to account for turbulence effects. Because the integration in Equations (5.42) and (5.43) is a very time-consuming process, these integrations are performed in advance and the outcome is tabulated in an adaptive way (Peeters, 1995). Making use of an adaptive tabulation algorithm for averaged quantities reduces the total CPU time by a factor of 10 or even more.

## 5.6 A STABILIZED NATURAL GAS FLAME

In this section, results of computations are compared to measurements published by Streb (1993) on natural-gas flames. The case considered is a stabilized methane-air flame with concentrations of 98.084%  $CH_4$ , 0.05%  $CO$ , 0.1%  $H_2O$  and 1.546%  $N_2$  by volume. A comparison between natural gas and pure methane (Peeters, 1995) shows that the differences between the properties of pure methane and those of natural gas are virtually negligible. Therefore predictions for this flame have been performed with the pure methane flamelets described in Appendix C.

The fuel issues from a nozzle with  $D=10\text{mm}$  with an average speed of 60.1 m/s into still air. The flame of approximately 1m ( $100D$ ) long is stabilized with two separate  $H_2$  and  $O_2$  streams. These streams have minimal effect on the downstream dynamics since their total momentum flux is only  $7 \times 10^{-4}$  N, while the fuel jet issues with a flux of 0.1744 N. The stabilizing mechanism can be explained by considering the quenching scalar dissipation rate. The quenching scalar dissipation rate increases when the oxygen mass fraction at the oxidizer boundary is increased. This makes the flamelets more resistant to strain. By also adding hydrogen through an outer annulus, the natural gas jet issues into an oxygen-rich hot mixture. The higher temperature also makes the flamelets more resistant to strain. Due to this second effect less oxygen has to be added and the influence of the stabilization gas is reduced. Because the stabilizing gas does not have a large influence on the flame, it is a good approximation in computational studies to completely neglect the stabilizing gas. To simulate the effect of the stabilizing gas, the value of the scalar dissipation rate as calculated by Equation (5.44) has been bounded by the quenching value for the scalar dissipation rate, i.e.  $\chi_{st} \leq \chi_q = 17.4/s$ .

The standard  $k-\varepsilon$  model has been used in combination with the equal-scales transport model. At the burner exit, a power-law velocity distribution for fully developed turbulent pipe flow was imposed (Nikuradse, 1932):

$$\frac{\tilde{u}_o}{\tilde{u}_{c,o}} = \left(1 - \frac{r}{R}\right)^{\frac{1}{n}} \quad (5.46)$$

where the subscript  $o$  indicates an outlet condition and  $c$  indicates the centerline condition. If the average burner outlet velocity  $\tilde{u}_{avg}$  is defined as

$$\tilde{u}_{avg} = \frac{1}{\pi R^2} \int_0^R \tilde{u}_o(r) 2\pi r dr \quad (5.47)$$

then, substitution of Equation (5.46) and integration over the outlet leads to:

$$\frac{\tilde{u}_{c,o}}{\tilde{u}_{avg}} = 1 + \frac{3n+1}{2n^2} \quad (5.48)$$

With an average outlet velocity equal to 60.1 m/s and  $n=10$  this leads to a maximum outlet centerline velocity of 69.3 m/s, equal to that found in the measurements.

The characteristic velocity fluctuation was adjusted to the value found in measurements of Laufer (1954):

$$\frac{v'}{\tilde{u}_{c,o}} = 0.028 + 0.13 \left(\frac{r}{D}\right)^2 \quad (5.49)$$

Therefore the turbulence kinetic energy at the burner exit is obtained from

$$\tilde{k} = \frac{3}{2}v'^2 \quad (5.50)$$

The dissipation rate of turbulence kinetic energy was obtained from a standard formula for fully-developed turbulent pipe flow (see Equation (3.33)),

$$\tilde{\epsilon} = C_\mu^{3/4} \frac{\tilde{k}^{3/2}}{l_m} \quad (5.51)$$

where the mixing length  $l_m$  was adjusted to the value found in measurements of Laufer (1954):

$$\frac{l_m}{R} = 0.14 - 0.08 \left( \frac{r}{R} \right)^2 - 0.06 \left( \frac{r}{R} \right)^4 \quad (5.52)$$

For  $r \rightarrow R$  this expression reduces to  $l_m = \kappa(R-r)$  with  $\kappa$  the von Kármán constant, equal to 0.40.

In Figure 5.12 the time scale ratio  $t_\eta/t_c$  has been plotted as a function of  $x/D$ . It can be seen that at the position where  $Z=Z_{st}$ , the flame is just inside the laminar flamelet regime of Figure 5.6. The degree of premixing may be evaluated by assuming that the mixture fraction fluctuates between  $Z=Z_r$  and  $Z=0$ , leading to  $Z_r \approx 2Z''$ . With  $(\Delta Z)_F \approx 2Z_{st}$  this leads to  $Z_r/(\Delta Z)_F \approx Z''/Z_{st}$ . From Figure 5.12 it is clear that the flame tip enters into the connected reaction zones regime of Figure 5.6. The applicability of the present flamelet model is questionable in that regime. However, mixture fraction gradients are small at the flame tip and therefore the measured as well as the predicted mixture composition will both be close to the equilibrium composition.

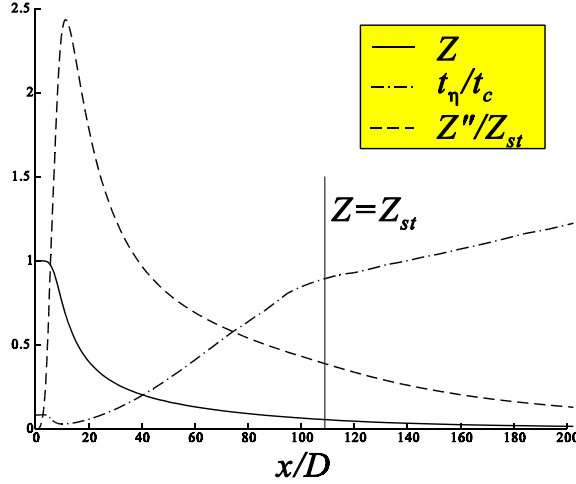


Figure 5.12 Comparing time scales and the premixing condition.

Figure 5.13 shows the predicted centerline profile of the mean temperature and its standard deviation. The predicted temperature without accounting for heat loss is seen to be much higher than that found experimentally by Streb (1993). Heat loss is mainly caused by thermal radiation of  $H_2O$ ,  $CO_2$  and soot particles. Crauford *et al.* (1985) artificially reduced the adiabatic temperature  $T_{ad}(Z)$  by the very crude assumption

$$T(Z) = T_{ad}(Z) \left[ 1 - \chi_r \left( \frac{T_{ad}}{T_{exp}} \right)^4 \right] \quad (5.53)$$



where  $T_{\text{exp}}$  is a ‘fitting’ temperature’ set to 2050 K and the constant  $\chi_r$  is set to 0.15 (Sanders, 1994). A disadvantage of this method is that the species concentrations, which are sensitive to the temperature, are not adjusted. A better way of implementing the effect of radiation would be by extending the equation for the flamelet temperature, i.e. Equation (5.27), with a radiative sink term (Sanders, 1994). However, this has not been pursued in the present study.

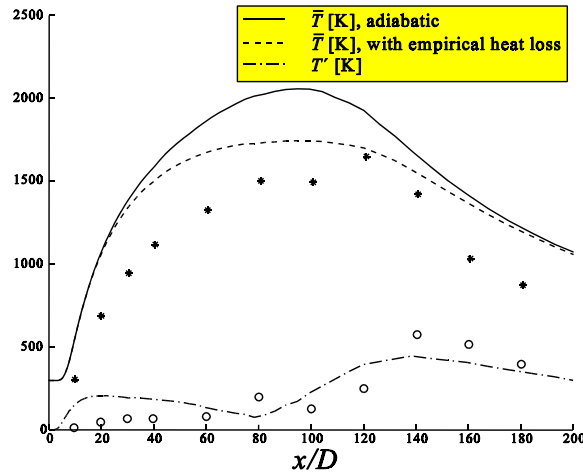


Figure 5.13 Predicted centerline profile of the mean temperature and its standard deviation. Experimental data are from Streb (1993);  $\bar{T}$  (\*) and  $T'$  (o).

Figure 5.14 illustrates that initially the predicted velocity decays faster than the measured velocity. This is probably due to laminarization in the experiment caused by the increase of molecular viscosity with temperature. The used  $k$ - $\epsilon$  turbulence model is not able to account for this effect. This is also a reason for the faster predicted temperature increase in Figure (5.13). The turbulence kinetic energy is predicted satisfactorily. The fast mixing in the predictions is also illustrated by the higher half-width spreading rates presented in Figure 5.15. The over-predicted temperature in the far field is probably caused by an over-predicted mixture fraction. Differences in the near field may be caused by the stabilizing  $H_2/O_2$  streams not accounted for in the simulation. The under-predicted  $CH_4$  mass fraction in the near field of Figure 5.16 is due to the over-predicted mixing in the near field. Measured  $CO$  mass fractions (not shown in a figure) are higher than those predicted with the laminar flamelet method using steady flamelets. The maximum centerline value of  $Y_{CO}$  in the experiment was 0.08 while the mass fractions of  $CO$  found in the steady flamelets show a maximum value of 0.06 (see Appendix C). According to Mauß *et al.* (1990) and also to Barlow *et al.* (1992), transient effects are the reason for this discrepancy. Along the jet axis, there is a strong decay of the scalar dissipation rate. The scalar dissipation rate influences the flamelet solution significantly and therefore a flamelet that is transported downstream has to undergo strong changes. Because a fast decrease of the scalar dissipation rate causes an overshoot of  $Y_{CO}$ , the  $CO$  mass fraction is under-predicted with the steady flamelets. Since  $CO$  is a fuel, the higher  $CO$  mass fraction can also explain part of the lower measured temperature.

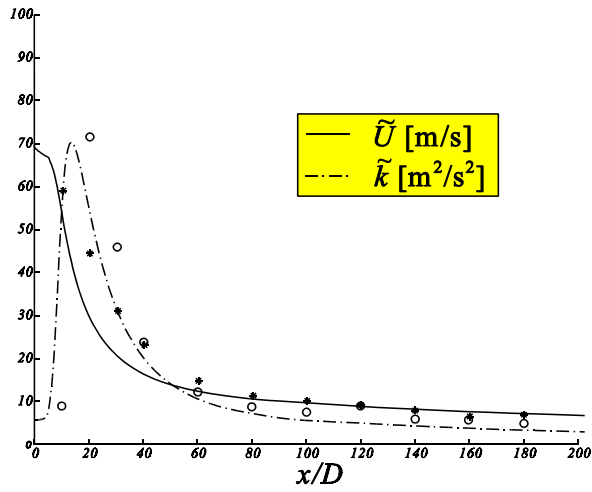


Figure 5.14 Predicted centerline profile of the mean axial velocity component and turbulence kinetic energy. Experimental data are from Streb (1993);  $\bar{u}$  (\*) and  $\bar{k}$  (○).

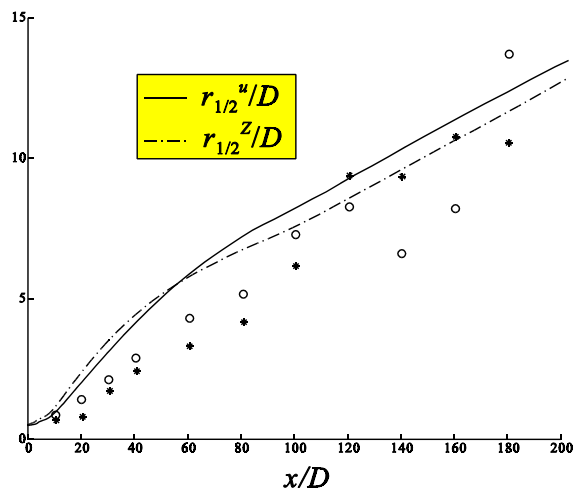


Figure 5.15 Predicted halfwidths for the velocity and the mixture fraction. Experimental data are from Streb (1993);  $r_{1/2}^u$  (\*) and  $r_{1/2}^Z$  (○).

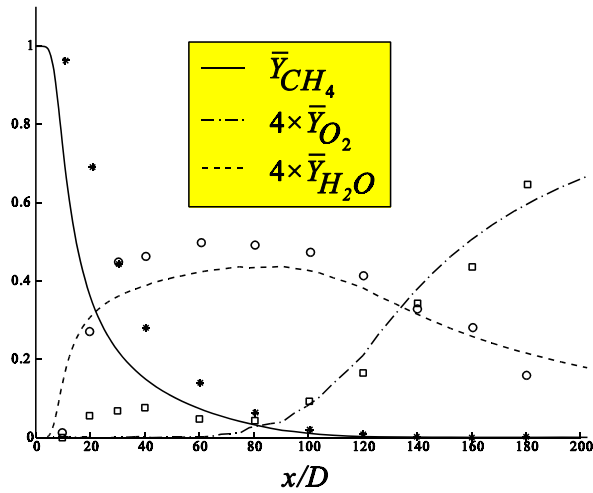


Figure 5.16 Predicted centerline profile of the mass fractions of  $CH_4$ ,  $O_2$  and  $H_2O$ . Experimental data are from Streb (1993);  $CH_4$  (\*),  $O_2$  ( $\square$ ) and  $H_2O$  ( $\circ$ ).

Radial profiles of the temperature and its standard deviation for  $x/D=120$ , i.e. just downstream of the flame, are shown in Figure 5.17. Again the inclusion of an empirical correction for radiation gives improved results. Figure 5.18 shows that the radial profile for the axial velocity component is in good agreement with the measurements. The predicted turbulence kinetic energy profile only shows a qualitative correspondence with the measurements. The reason for the apparent vertical shift between predictions and measurements is unknown.

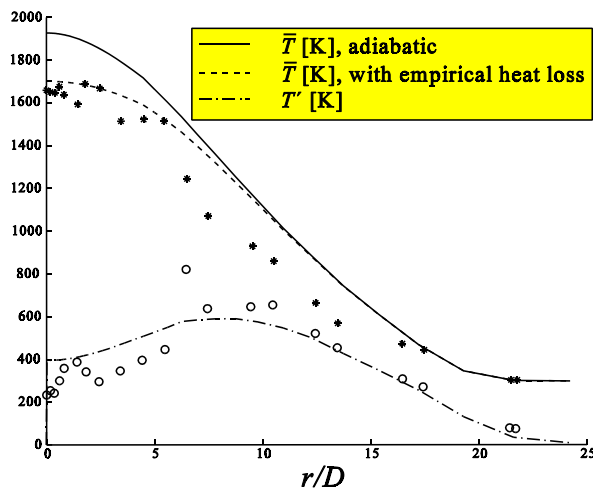


Figure 5.17 Predicted radial profile of the mean temperature and its standard deviation at  $x/D=120$ . Experimental data are from Streb (1993);  $\bar{T}$  (\*) and  $T'$  ( $\circ$ ).

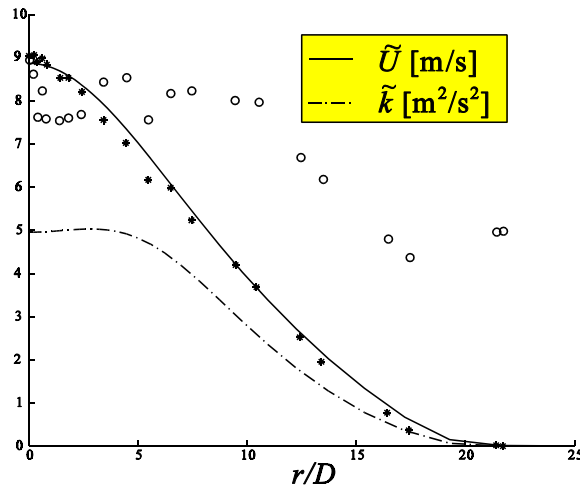


Figure 5.18 Predicted radial profile of the axial velocity component and the turbulence kinetic energy at  $x/D=120$ . Experimental data are from Streb (1993);  $\tilde{u}$  (\*) and  $\tilde{k}$  (○).

## 5.7 CONCLUSIONS

Turbulent flows show a fundamentally layer-like structure of scalar mixing. The one-dimensional local structure of the scalar dissipation fields in turbulent flows provides a starting point for formulating the chemical state of non-equilibrium combustion in the flow. In a one-dimensional set of flamelet equations, the scalar dissipation profile provides the relation between the flow field and the state of chemical non-equilibrium. The most frequently occurring  $\chi$ -profiles in a turbulent flow are those of the steady-state flamelets. Solutions to the flamelet equations may therefore also be obtained by analysing the counter-flow geometry for which the  $\chi$ -profile follows closely that of a frequently occurring steady-state flamelet in a turbulent flow. It is mainly the scalar dissipation rate under stoichiometric conditions that influences the outcome of the flamelet equations. Therefore, a flamelet library has been built with the scalar dissipation rate under stoichiometric conditions as the input parameter indicating the state of chemical non-equilibrium. In the numerical simulation, this conditioned scalar dissipation rate, which is needed as an input parameter for the flamelet library, is approximated by assuming a fixed shape for the scalar dissipation profile.

The accuracy of the flamelet model directly depends on the transport properties and chemistry used in the flamelet computations. The one-dimensional flamelet equations can be solved with arbitrarily complicated transport properties and chemistry. In the present numerical simulation of a stabilized natural gas flame (Streb, 1993), the absence of radiative heat transfer in the flamelet equations lead to a rather large difference between measured and calculated temperature. By implementing a relatively simple model for soot-related radiation, the difference between measured and calculated maximum mean temperature has been reduced by about 300K. Another source of error is that the predicted mixing rate close to the burner outlet is too large compared with values found from the experiments. This results in under-predicted velocity and mixture fraction values and over-predicted temperatures in this region.

Predicted *CO* mass fractions are lower than those measured by Streb (1993). Transient effects are thought to be responsible for the higher values in the experiments, i.e. the strong decrease of  $\chi_{st}$  as the flamelet is transported downstream causes an overshoot in the production of *CO*. However, all other predicted mass fractions show a reasonably good agreement with the experimental data. Also other features such as spreading rates, velocity and turbulence intensities are predicted satisfactorily.

## Chapter 6

### Turbulent premixed flames

In this chapter, a flamelet model for turbulent premixed flames will be considered and evaluated. The approach to the premixed flamelet model followed in this chapter is quite different from that followed in the diffusion flamelet model of Chapter 5. There is however a certain analogy with the diffusion flamelet model: chemistry is considered to be fast compared to the characteristic time scales of turbulence and therefore combustion tends to occur in locally laminar premixed flames embedded in the turbulent flow field. Like for the diffusion flamelets, the reaction zone in the premixed flamelets is also very thin. The preheat zone thickness of the premixed flamelet, which is determined by the ratio of the thermal diffusivity and the laminar burning velocity, is also considered to be very thin compared to the turbulent length scales. Therefore, different from the diffusion flamelet approach, the internal structure of the premixed flamelets remains unresolved. The propagation of an infinitesimally thin premixed flame is described by a kinematic equation.

Averaging techniques lead to a kinematic equation for the turbulent flame brush, an expression for the turbulent burning velocity and an expression for the turbulent flame brush thickness. A solution to the kinematic equation is found by making use of a so-called level-set algorithm. It will be shown how the premixed flamelet model may be used in combination with the diffusion flamelet model.

To evaluate the model, a numerical simulation of a turbulent premixed Bunsen flame will be carried out. Turbulent mixing is of minor importance in the used test case, it therefore presents a good way of evaluating the used expression for the turbulent burning velocity in a homogeneous mixture fraction field. The effect of mixture fraction fluctuations on the turbulent burning velocity will be treated in the next chapter.

#### 6.1 REGIMES DIAGRAM FOR PREMIXED TURBULENT COMBUSTION

The turbulent length, time and velocity scales that play an important role in the classification of premixed turbulent combustion will be considered here.

##### Turbulent length scales

The turbulent premixed flame brush thickness  $l_{F,t}$  is of the same order of magnitude as the integral length scale  $l_t$ . It may be defined as two times the r.m.s. value of the distance of the premixed flame to its average position:

$$l_{F,t} = 2\sqrt{\overline{G^2}} = 2\sqrt{\int_{-\infty}^{\infty} (G-\overline{G})^2 P(G) dG} \quad (6.1)$$

Where  $G(\underline{x},t)$  is defined as the instantaneous distance from location  $\underline{x}$  to the premixed flame front and  $\overline{G}$  as the average distance to the premixed flame front.  $P(G)$  is the so-called probability density function of  $G$ . The form of this PDF is “pre-assumed” and its local shape may be determined by two parameters; the mean and the variance of  $G$ .

In many practical applications of turbulent combustion the smallest length scale is the reaction zone thickness of a premixed flame,  $l_\delta$ . The thickness  $l_\delta$  of the inner layer in which the chemical reactions take place is typically one tenth of the preheat zone thickness. The laminar flame thickness,  $l_F$ , represents the thickness of this preheat zone. On dimensional grounds, and the assumption of a chemically inert preheat zone, its thickness may be calculated from:

$$l_F = \frac{D}{s_L^0} \quad (6.2)$$

where, for a Lewis number equal to one,  $D=D^T$  is the thermal diffusivity of the unburnt mixture,  $D^T=(\lambda/\rho c_p)_u$ , and  $s_L^0$  is the laminar burning velocity of a flat flame. For fuel lean mixtures, the ratio of thermal conductivity to specific heat at constant pressure may be evaluated from (Smooke, 1991):

$$\left( \frac{\lambda}{c_p} \right)_u = 2.58 \cdot 10^{-5} \frac{kg}{m \cdot s} \left( \frac{T_u}{298K} \right)^{0.7} \quad (6.3)$$

For example for a hydrogen flame, with  $T_u$  equal to 298K,  $\rho_u$  approximately equal to 1.2kg/m<sup>3</sup> and a laminar burning velocity of approximately 2m/s, the preheat zone thickness is of the order of 0.01 mm.

#### Turbulent velocity scales

An important velocity scale is given by the laminar burning velocity. It is defined as the velocity at which the laminar premixed flame propagates relative to the unburnt mixture. Or in other words, it may be defined as the normal component of the velocity of the unburnt mixture relative to the laminar premixed flame front. In the same way the turbulent burning velocity  $s_T$  is defined as the normal component of the mean velocity of the unburnt mixture relative to the surface of the average flame position, i.e. the surface  $\bar{G}=0$ . This turbulent burning velocity depends on both the characteristic velocity fluctuation as well as on the laminar burning velocity. Damköhler (1940) was the first to present theoretical expressions for the turbulent burning velocity. He identified two different regimes which he called the large-scale and small-scale-turbulence regime. For the large-scale-turbulence regime he assumed that the turbulent burning velocity is proportional to the surface area of the turbulent flame, which is in turn proportional to the characteristic velocity fluctuation  $v'$ . Experimental data for fully developed flames (Abdel-Gayed *et al.*, 1981) suggest that the turbulent burning velocity is approximately

$$s_T = 2.0v' \quad \text{for} \quad v' \gg s_L \quad (6.4)$$

in the large-scale-turbulence limit. However, there is a deficiency in this expression: when  $v'$  approaches zero,  $s_T$  tends to zero. Actually  $s_T$  should be close to  $s_L$  when  $v'$  tends to zero. In order to avoid this anomaly, Equation (6.4) may be replaced by

$$\frac{s_T}{s_L} = 1 + 2.0 \frac{v'}{s_L} \quad (6.5)$$

For large-scale turbulence, the turbulent burning velocity is therefore assumed to be independent of chemical processes. Sufficiently large-scale turbulence merely wrinkles a premixed laminar flame without significantly modifying its internal structure. Although Equation (6.4) predicts that  $s_T/s_L$  increases linearly with  $v'/s_L$  this is not observed in measurements for very large values of  $v'/s_L$ . For large turbulence intensities an increased value for  $v'/s_L$  gives rise to a smaller than

linear increase of the turbulent burning velocity (e.g. Abdel-Gayed *et al.*, 1987). This deviation from the straight line of the large-scale-turbulence limit is called the ‘bending of the turbulent burning velocity’, also known as ‘the bending effect’. This ‘bending effect’ cannot be explained from Damköhler’s analysis, which is solely based on geometrical arguments.

For small-scale turbulence Damköhler argued that turbulence modifies the transport in the preheat zone. Sufficiently small-scale turbulence alters the effective transport coefficients in the flame without significantly wrinkling the flame front. Damköhler used the scaling relation for the laminar burning velocity,

$$s_L = \sqrt{D/t_c} \quad (6.6)$$

where  $t_c$  is the chemical time scale. He replaced the laminar diffusivity  $D$  by a turbulent diffusivity  $D_t$  to obtain

$$s_T = \sqrt{D_t/t_c} \quad (6.7)$$

where for a turbulent Schmidt number  $Sc_t = \mu_t/(\rho D_t) = 0.7$  the turbulent diffusivity is given by  $D_t = 0.78 \nu' l_t$  (for definitions of  $\nu'$  and  $l_t$  see Section 3.1). If it is assumed that the chemical time scale is not affected by turbulence, then combining Equation (6.6) with Equation (6.7) leads to

$$\frac{s_T}{s_L} = \sqrt{\frac{D_t}{D}} = \sqrt{0.78 \frac{\nu' l_t}{s_L l_F}} \quad (6.8)$$

For the same reason that Equation (6.4) was replaced by Equation (6.5), Equation (6.8) may be replaced by:

$$\frac{s_T}{s_L} = 1 + \sqrt{0.78 \frac{\nu' l_t}{s_L l_F}} \quad (6.9)$$

showing that in the small-scale-turbulence regime the ratio of the turbulent to the laminar burning velocity not only depends on the velocity ratio  $\nu'/s_L$  but also on the length scale ratio  $l_t/l_F$ .

In the past, many attempts have been made trying to modify Damköhler’s analysis and to derive expressions that would reproduce the large amount of experimental data on turbulent burning velocities. However, many of these expressions fail because of the existence of the two different regimes that were already recognized by Damköhler in 1940. Recently Peters (1997) derived an expression that indeed covers both regimes in premixed turbulent combustion;

$$\frac{s_T}{s_L^0} = 1 + \bar{\sigma} \left( 1 - 1.3 \frac{\mathcal{Q}}{l_t} \frac{\nu'}{s_L^0} \right) \quad (6.10)$$

where  $\bar{\sigma}$  is called the flame surface area ratio which, for the case of a fully developed turbulent flame, may be approximated by (see Appendix E):

$$\bar{\sigma} = -\frac{0.39}{2} \frac{l_t}{l_F} + \sqrt{\left( \frac{0.39}{2} \frac{l_t}{l_F} \right)^2 + 0.78 \frac{\nu' l_t}{s_L^0 l_F}} \quad (6.11)$$

and  $s_L^0$  is the burning velocity of the unstretched flame. In Equation (6.10), the Markstein length  $\mathcal{Q}$  accounts for effects of flame curvature and flame stretch on the laminar burning velocity (see Equation (6.23)). Equation (6.10) has been derived by considering a turbulent flame which is time-averaged stationary and one-dimensional as in Figure 6.1. The variable  $G$  has here been defined as the distance in  $x$ -direction to the premixed flame front.



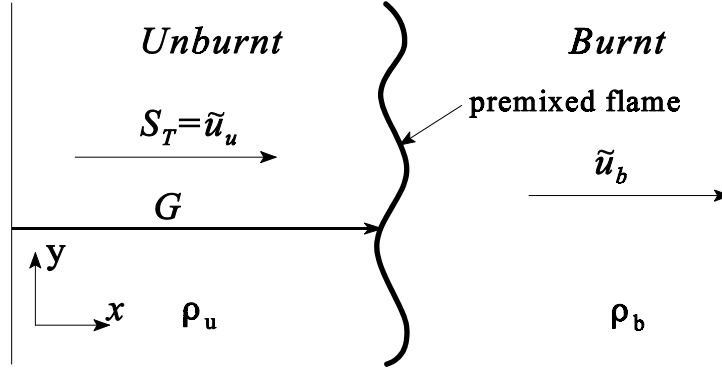


Figure 6.1 Time-averaged stationary and one-dimensional premixed flame.

Averaging of the kinematic equation for  $G$  (6.28) with substitution of Equation (6.23) leads to

$$\bar{u}_k \frac{\partial \bar{G}}{\partial x_k} + u'_k \frac{\partial \bar{G}'}{\partial x_k} = s_L^0 \bar{\sigma} - s_L^0 \mathcal{L} \bar{\kappa} \bar{\sigma} + \mathcal{L} \bar{\underline{n}} \cdot (\nabla \underline{u}) \cdot \bar{\underline{n}} \sigma \quad (6.12)$$

Where  $\sigma = |\nabla G|$ . Comparing this equation to the kinematic equation for  $\bar{G}$ , i.e.

$$\bar{u}_k \frac{\partial \bar{G}}{\partial x_k} = s_T |\nabla \bar{G}| \quad (6.13)$$

leads to

$$s_T |\nabla \bar{G}| = s_L^0 \bar{\sigma} - s_L^0 \mathcal{L} \bar{\kappa} \bar{\sigma} + \mathcal{L} \bar{\underline{n}} \cdot (\nabla \underline{u}) \cdot \bar{\underline{n}} \sigma - u'_k \frac{\partial \bar{G}'}{\partial x_k} \quad (6.14)$$

The last three terms in this equation are unclosed and should be modelled. Since diffusion is not present in the instantaneous  $G$ -equation, it cannot appear in the equation for  $\bar{G}$ . The curvature term is therefore combined with the turbulent transport term as:

$$-s_L^0 \mathcal{L} \bar{\kappa} \bar{\sigma} - u'_k \frac{\partial \bar{G}'}{\partial x_k} = -(s_L^0 \mathcal{L} + D) \bar{\kappa}(\bar{G}) |\nabla \bar{G}| \quad (6.15)$$

In this model, these terms may therefore be neglected in case of a flat flame ( $\bar{\kappa}(\bar{G})=0$ ). Numerical simulations by Ashurst (1997) have shown that the strain is statistically independent of  $\sigma$  and that the mean strain  $\bar{\underline{n}} \cdot (\nabla \underline{u}) \cdot \bar{\underline{n}}$  on the flame surface is always negative. The mean strain has been modelled as

$$\bar{\underline{n}} \cdot (\nabla \underline{u}) \cdot \bar{\underline{n}} = -1.3 \frac{v'}{l_t} \quad (6.16)$$

With  $|\nabla \bar{G}|=1$ , Equation (6.14) may then be written as Equation (6.10) except for the defect correction for the case of  $\bar{\sigma}=0$ .

The derivation of Equation (6.11) is given in Appendix E, based on a transport equation for  $\sigma$  given by Peters (1997). Here it is only mentioned that in the limit  $l/l_F \rightarrow \infty$  Equation (6.11) reduces to:

$$\begin{aligned}
\lim_{l_t/l_F \rightarrow \infty} \bar{\sigma} &= \lim_{x \rightarrow \infty} \left\{ -x + x \sqrt{1 + \frac{4v'/s_L^0}{x}} \right\} \\
&= \lim_{x \rightarrow \infty} \left\{ -x + x \left[ 1 + \frac{2v'/s_L^0}{x} + O\left(\frac{1}{x^2}\right) \right] \right\} = 2 \frac{v'}{s_L^0}
\end{aligned} \tag{6.17}$$

and for  $\mathcal{L}=0$  Equation(6.10) then becomes identical to Equation (6.5). This regime of  $l_t/l_F \rightarrow \infty$  is what Peters called the corrugated-flamelet regime.

In the limit  $l_t/l_F \rightarrow 0$  Equation (6.11) reduces to  $\bar{\sigma} = \sqrt{D_t/D}$  and for  $\mathcal{L}=0$  Equation(6.10) then becomes identical to Equation(6.9). This regime of  $l_t/l_F \rightarrow 0$  is what Peters called the thin-reaction-zones regime. In this small-scale-turbulence regime, Damköhler assumed that the chemical time scale is not affected by turbulence. The physical picture behind this is that, in the thin-reaction-zones regime, turbulent eddies that enter into the chemically inert preheat zone do not enter the reaction zone. Therefore they affect the chemical reactions only indirectly by controlling the diffusion processes in that zone.

Also the “bending effect” is described by Equation (6.10). For a constant length scale ratio  $l_t/l_F$ , which is typical for experiments at constant pressure and with a fixed geometry, Equation (6.10) shows a deviation from the straight line  $s_T = s_L^0 + 2.0v'$  and leads to smaller values of  $s_T/s_L^0$  for small length scale ratios. This is illustrated in Figure 6.2 for  $\mathcal{L}=0$ .

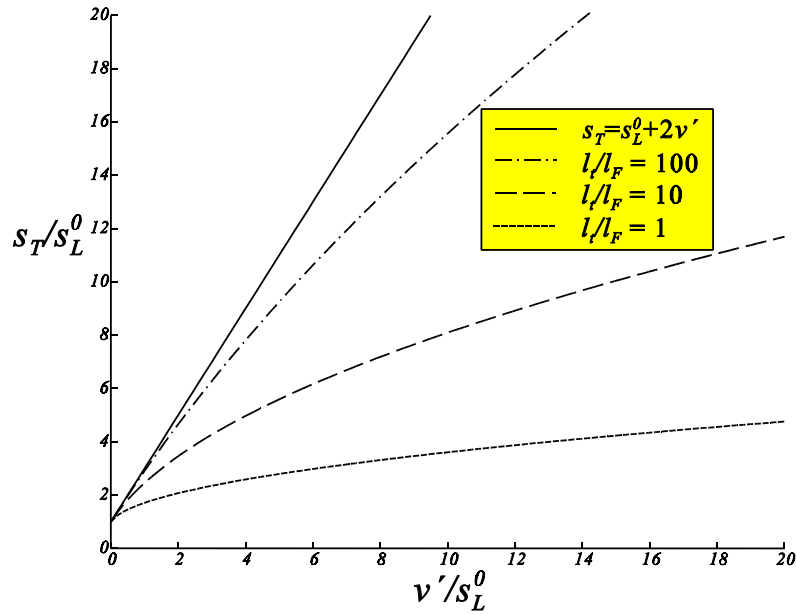


Figure 6.2  $s_T/s_L^0$  as a function of  $v'/s_L^0$  for different length scale ratios.

Figure 6.3 shows the regimes diagram for premixed turbulent combustion resulting from the analysis given above. Along the horizontal axis is the length scale ratio  $l_t/l_F$  where  $l_t$  is the integral length scale of turbulence and  $l_F$  is the laminar flame thickness. Along the vertical axis is the velocity scale ratio  $v'/s_L$  where  $v'$  is a characteristic velocity fluctuation and  $s_L$  is the laminar burning velocity. The turbulence Reynolds number  $Re_t$  may be defined as:

$$Re_t = \frac{v'l_t}{(\mu/\rho)_u} = \frac{1}{\sigma} \frac{v'l_t}{D} = \frac{1}{\sigma} \frac{v'l_t}{s_L l_F} \quad (6.18)$$

where  $\sigma$  is the Schmidt number of order unity. The line of  $Re_t=1$  separates the laminar-flame regime, which is situated in the lower left corner, from the turbulent-flame regimes. In the turbulent-flame regimes the line  $v'/s_L=1$  separates the wrinkled and corrugated flamelets. Both regimes are in the flamelet regime characterized by the Karlovitz number ( $Ka$ ) being smaller than 1 (fast chemistry). The Karlovitz number is defined here as:

$$Ka = \left( \frac{l_F}{\eta} \right)^2 \quad (6.19)$$

The boundary to the thin-reaction-zones regime is given by  $Ka=1$ , which is equivalent to the condition that the laminar flame thickness  $l_F$  is equal to the Kolmogorov scale  $\eta$ . The thickness  $l_\delta$  of the inner layer in which the chemical reactions take place is typically one tenth of the preheat zone thickness. The boundary between the thin-reaction-zones regime and the broken-reaction-zones regime is given by  $Ka_\delta=(l_F/l_\delta)^2=1$ , which is equivalent to the condition that the inner layer thickness  $l_\delta$  is equal to the Kolmogorov scale  $\eta$ . A more detailed discussion of the various regimes has been given by Peters (1997).

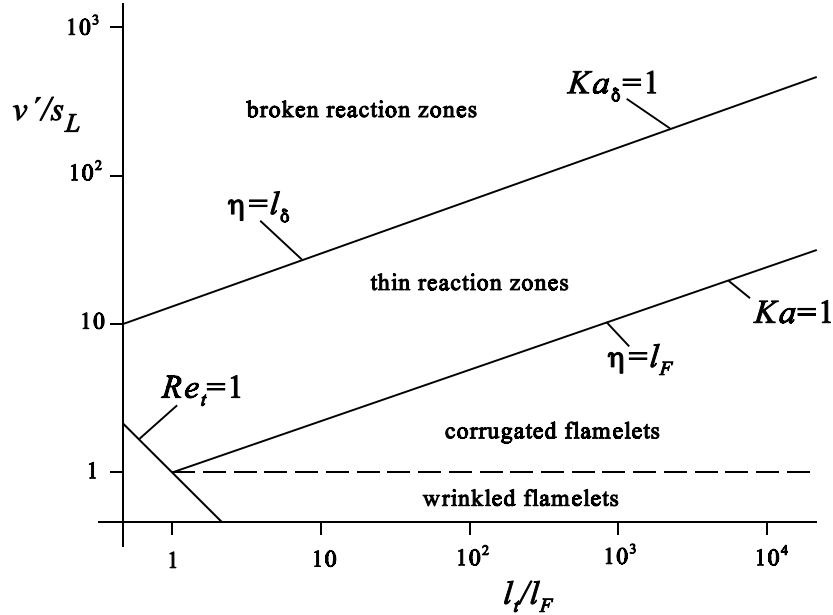


Figure 6.3 Regimes for premixed turbulent combustion.

## 6.2 FLAMELET MODELLING

If chemistry is fast compared to convection and diffusion, both the premixed flame as well as the diffusion flame may be regarded as locally laminar flames embedded in a turbulent flow field. A partially premixed turbulent diffusion flame may then be treated as an ensemble of laminar premixed flamelets and laminar diffusion flamelets (see Figure 6.4).

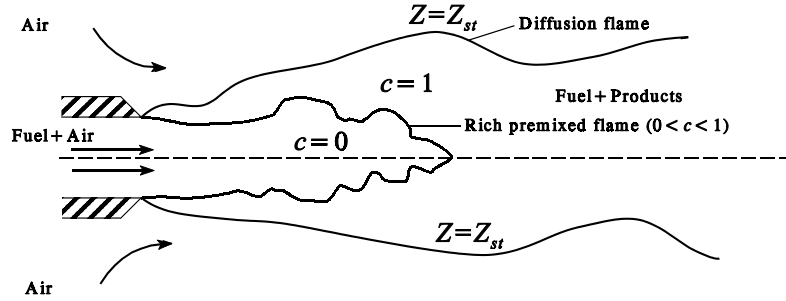


Figure 6.4 Turbulent flame as an ensemble of laminar premixed and laminar diffusion flamelets.

The premixed flame is described by a progress variable  $c$ . This progress variable may be interpreted as a non-dimensional product mass fraction,

$$c = \frac{Y_{fu} - Y_{fu_u}}{Y_{fu_b} - Y_{fu_u}} \quad (6.20)$$

in which  $Y_{fu}$  is the local mass fraction of the fuel. Because the premixed flame front is very thin, its internal structure is left unresolved and the flame front is treated as a discontinuity. The progress variable may then be interpreted as a step function that separates the unburnt mixture and the burnt gas in the given flow field. By definition  $c$  equals 0 in the unburnt mixture and  $c$  equals 1 in the burnt gas. The time dependent position of the premixed flame is described by the kinematic equation

$$\frac{Dc}{Dt} = \frac{\partial c}{\partial t} + (\mathbf{v}_f \cdot \nabla) c = 0 \quad (6.21)$$

in which  $\mathbf{v}_f$  is the velocity of the flame surface. This flame surface velocity is the sum of the local flow velocity at the unburnt side of the flame and the laminar burning velocity normal and relative to the unburnt side of the flame (Figure 6.5),

$$\mathbf{v}_f = \mathbf{u} + s_L \mathbf{n} \quad (6.22)$$

in which  $\mathbf{n}$  is the normal vector on the flame surface pointing towards the unburnt mixture. The laminar burning velocity is known as a function of flame curvature and flame stretch (Clavin, 1985),

$$s_L = s_L^0 - s_L^0 \mathcal{L} \kappa + \mathcal{L} \mathbf{n} \cdot (\nabla \mathbf{u}) \cdot \mathbf{n} \quad (6.23)$$

Here  $s_L^0$  is the burning velocity of the unstretched flame,  $\kappa$  is the flame front curvature and  $\mathcal{L}$  is the Markstein length. The Markstein length accounts for flame curvature and flame stretch effects on the laminar burning velocity. It may be derived on the basis of flamelet calculations (Peters, 1994) or measurements (Searby *et al.*, 1990 and Karpov *et al.*, 1997).

A numerical problem now arises; how to track this evolving interface? An attractive way is making use of a so-called level-set method (Sethian, 1996). The main idea of the level-set methodology is to embed the propagating interface as the zero level set of a higher dimensional function  $G$ .  $G$  may for example be defined as a signed-distance function where  $G$  is positive at the burnt side of the flame front and negative at the unburnt side of the flame front (Figure 6.5).

The level-set method divides the domain into grid points that hold approximations to the values of the level-set function  $G$ . The normal  $\underline{n}$  to the flame front may then be evaluated as

$$\underline{n} = -\frac{\nabla G}{|\nabla G|} \quad (6.24)$$

and the curvature  $\kappa$  as

$$\kappa = \nabla \cdot \underline{n} = -\nabla \cdot \left( \frac{\nabla G}{|\nabla G|} \right) \quad (6.25)$$

where  $\nabla G$  may be approximated by some appropriate finite-difference operator, i.e.  $\nabla G \approx \nabla_{ij} G_{ij}$ . The flame position is then found as the zero level set of  $G$  by interpolation.

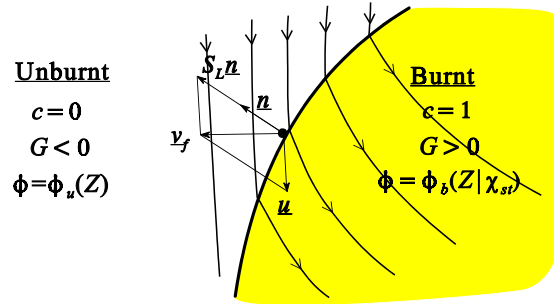


Figure 6.5 Burnt and unburnt gas regions separated by a thin flame surface at  $G=0$ .

For  $G$  equal to zero it should satisfy the same kinematic equation as that for  $c$ , i.e. Equation (6.21). In combination with Equation (6.22) and Equation (6.24) this leads, after some manipulations, to the level-set equation for  $G$ :

$$\frac{\partial G}{\partial t} + F|\nabla G| = 0 \quad (6.26)$$

where  $F$  is the so-called speed function,

$$F = -(\underline{u} \cdot \underline{n} + s_L) \quad (6.27)$$

which provides the speed of the flame front surface in the direction opposite to the direction of the normal on the flame front. Equation (6.26) was first formulated by Markstein (1964) and independently by Williams (1985a) in a slightly different way, i.e. as

$$\frac{\partial G}{\partial t} + u_k \frac{\partial G}{\partial x_k} = s_L |\nabla G| \quad (6.28)$$

Numerical solutions of Equation (6.28) in a fluctuating flow field have been obtained for the first time by Kerstein *et al.* (1988).

If the level-set equation for  $G$  is solved then the solution for the progress variable  $c$  may be found by  $c=H(G)$ , where  $H$  is the Heaviside function which equals 0 for  $G<0$  and 1 for  $G>0$ . Scalar quantities may then be calculated as:

$$\phi = (1-c) \phi_u(Z) + c \phi_b(Z|\chi_{st}) \quad (6.29)$$

where  $\phi_u$  is the unburnt scalar quantity which is determined by an inert mixing process and

thereby, if the diffusivities of all species are assumed to be equal, solely by the mixture fraction  $Z$ . The burnt scalar quantity  $\phi_b$  is calculated by making use of the flamelet model described in Chapter 5.

### 6.3 ONE-DIMENSIONAL LAMINAR PREMIXED FLAMES

Solutions for premixed flames in a counterflow configuration may be obtained with the same set of equations as those given for the laminar counterflow diffusion flames in Section 5.4. Boundary conditions have to be set as shown in Figure 6.6, i.e. premixed gases with the same composition at both boundaries  $x = -\infty$  and  $x = \infty$ . Therefore, the mixture fraction is constant through the whole domain. Because of symmetry, boundary conditions on one side may be replaced by zero gradient conditions at the symmetry position, except for the velocity  $u$ , which takes the value  $u=0$ .

The laminar burning velocity  $s_L^u$  may be identified as a minimum point in the velocity profile ahead of the premixed flame. The velocity gradient ahead of it is equal to the imposed strain rate  $a$  (times two for the axi-symmetrical case). Linear extrapolation of  $s_L^u(a)$  to  $a=0$  yields a value which should closely approximate the stretch-free burning velocity  $s_L^0$ .

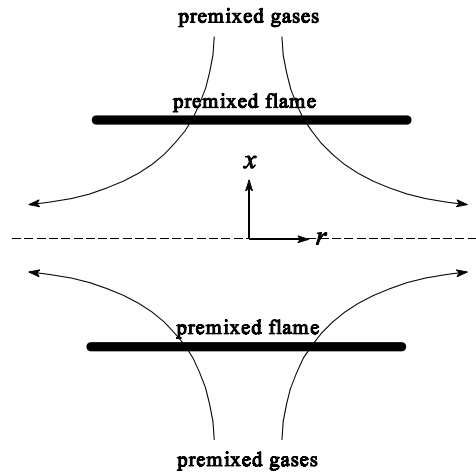


Figure 6.6 Counterflow premixed flames.

Another way of obtaining the stretch-free burning velocity  $s_L^0$  is by solving the equations for the planar steady flame configuration normal to the  $x$ -direction with the unburnt mixture at  $x \rightarrow -\infty$ , and the burnt gas at  $x \rightarrow \infty$ . The equations are as follows.

Continuity:

$$\frac{d(\rho u)}{dx} = 0 \quad (6.30)$$

Species:

$$\rho u \frac{dY_i}{dx} = -\frac{dJ_i}{dx} + \dot{w}_i \quad (6.31)$$

Temperature:

$$\rho u c_p \frac{dT}{dx} = \frac{d}{dx} \left( \lambda \frac{dT}{dx} \right) - \sum_{i=1}^n h_i \dot{w}_i - \frac{dT}{dx} \sum_{i=1}^n c_{p_i} J_i - \frac{\partial q_R}{\partial x} \quad (6.32)$$

The continuity equation may be integrated to yield  $\rho u = \rho_u s_L^u$ , where the index  $u$  denotes conditions of the unburnt mixture. The burning velocity  $s_L^u$  is an eigenvalue, which must be determined as part of the solution. The pressure is taken as constant, and the system of equations is closed by the equation of state, i.e. Equation (2.45). Some numerical as well as experimental results on methane and hydrogen flames, obtained by different authors, have been summarized in Appendix D.

## 6.4 AVERAGED EQUATIONS

The mean premixed flame position is found as the zero level set of the level-set function  $\bar{G}$  (see Figure 6.7). At some initial time  $t=0$ ,  $\bar{G}$  is set equal to a signed-distance function that obeys

$$|\nabla \bar{G}| = 1 \quad (6.33)$$

After this initialization the propagation of the zero level set is found by solving the level-set equation,

$$\frac{\partial \bar{G}}{\partial t} + F |\nabla \bar{G}| = 0 \quad (6.34)$$

where for the zero level set the speed function  $F$  is now given by

$$F = -(\tilde{u}^c \underline{n} + s_T) \quad (6.35)$$

with  $s_T$  the turbulent burning velocity. For steady mean flow situations the turbulent burning velocity is defined as the component of the mean velocity ahead of the turbulent flame brush normal to the surface of the average flame position. Obviously, the steady-state solution of Equation (6.34), i.e.  $F=0$ , obeys this definition for the turbulent burning velocity. Müller *et al.* (1994a) evaluated the conditioned velocity  $\tilde{u}^c$  under the assumption that the mass flux through the turbulent flame is constant and therefore that  $\tilde{u}^c \approx \bar{\rho} \tilde{u} / \rho_u$  where  $\rho_u = \rho_u(\tilde{Z})$  is the density in the unburnt mixture. This is however only true for steady one-dimensional flames and may lead to large errors in the case of strongly curved flames. Keller (1996) evaluated the conditioned velocity  $\tilde{u}^c$  at the unburnt side of the turbulent flame brush by making use of a search algorithm. In the present study the conditioned velocity  $\tilde{u}^c$  is evaluated at the unburnt side of the turbulent flame brush, i.e. at  $\bar{G} = -0.5l_{F,t}$  by interpolation from the mean velocity field solved in the  $k$ - $\epsilon$  model, and found elsewhere by solving

$$\frac{\partial \tilde{u}^c}{\partial \eta} = 0 \quad (6.36)$$

with the  $\eta$  coordinate normal to an iso-surface of  $\bar{G}$ , so that

$$\frac{\partial \cdot}{\partial \eta} = \frac{\partial \bar{G} / \partial x_i}{|\nabla \bar{G}|} \frac{\partial \cdot}{\partial x_i} \quad (6.37)$$

The boundary condition for Equation (6.36) is given by  $\tilde{u}^c = \tilde{u}$  at  $\bar{G} = -0.5l_{F,t}$ . Also the turbulent burning velocity  $s_T$  is evaluated at the unburnt side of the turbulent flame brush and a similar procedure is followed.

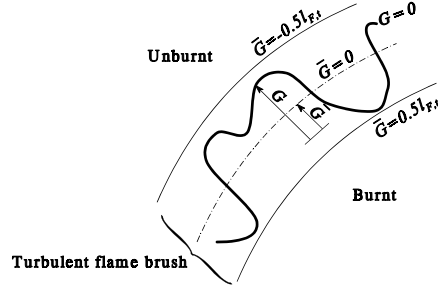


Figure 6.7  $G$  as the distance to the premixed flame, and  $\bar{G}$  as the distance to the mean flame position.

The level-set equation may be discretized with a forward difference scheme in time, like

$$\frac{\bar{G}^{n+1} - \bar{G}^n}{\Delta t} + F^n |\nabla \bar{G}^n| = 0 \quad (6.38)$$

So that:

$$\bar{G}^{n+1} = \bar{G}^n - F^n |\nabla \bar{G}^n| \Delta t \quad (6.39)$$

and therefore

$$\begin{aligned} |\nabla \bar{G}^{n+1}|^2 &= |\nabla \bar{G}^n - \nabla F^n |\nabla \bar{G}^n| \Delta t - F^n \nabla (|\nabla \bar{G}^n|) \Delta t|^2 \\ &\approx |\nabla \bar{G}^n - \nabla F^n |\nabla \bar{G}^n| \Delta t|^2 \\ &= |\nabla \bar{G}^n|^2 - 2 |\nabla \bar{G}^n| \Delta t \frac{\partial \bar{G}^n}{\partial x_i} \frac{\partial F^n}{\partial x_i} + |\nabla \bar{G}^n|^2 \Delta t^2 \left( \frac{\partial F^n}{\partial x_i} \right)^2 \end{aligned} \quad (6.40)$$

In many level-set methods, the speed function is taken to be constant in  $\eta$  direction (Ovink *et al.*, 1998), i.e.  $\partial F / \partial \eta = 0$ . However, if such an approach is used, this leads to the necessity of making use of a re-initialization algorithm. This is explained as follows. If at time level  $n$  the level-set function  $\bar{G}^n$  is equal to the signed-distance function then, by solving Equation (6.38), this would lead at time level  $n+1$  to

$$|\nabla \bar{G}^{n+1}| = \sqrt{1 + \left[ \left( \frac{\partial F^n}{\partial \xi} \right)^2 + \left( \frac{\partial F^n}{\partial \zeta} \right)^2 \right] \Delta t^2} \quad (6.41)$$

where  $\xi$  and  $\zeta$  are perpendicular coordinates along an isosurface of  $\bar{G}^n$ . So gradients in the level-set function are getting steeper after every time step. To ensure that the level-set function stays well-behaved the level-set calculation has to be stopped periodically and the level-set function has to be re-initialized by solving the discretized version of Equation (6.33) (Ovink *et al.*, 1998). The net effect is to straighten out the level sets on either side of the zero level set and to produce a  $\bar{G}$  function with  $|\nabla \bar{G}| = 1$  corresponding to the signed-distance function. For turbulent flame calculations in three dimensions, Keller (1996) used a re-initialization algorithm devised by Sussman (1994) in which the solution of Equation (6.33) is found as the steady-state solution of a time-dependent equation. Here another procedure is followed which makes the use of a reinitialization algorithm redundant. If it is assumed that at time level  $n+1$  the magnitude of the gradient in  $\bar{G}$  is equal to 1 then Equation (6.40) simply leads to the following approximate



differential equation which the speed function  $F^n$  should satisfy in order to keep the gradient in  $\bar{G}$  equal to 1:

$$\frac{\partial \bar{G}^n}{\partial x_i} \frac{\partial F^n}{\partial x_i} = \frac{|\nabla \bar{G}^n|^2 - 1}{2|\nabla \bar{G}^n| \Delta t} \approx \frac{|\nabla \bar{G}^n| - 1}{\Delta t} \quad (6.42)$$

The boundary condition for  $F^n$  is given by Equation (6.35) in grid nodes where  $\bar{G}$  is positive and one of the neighbouring grid nodes has a negative value for  $\bar{G}$ .

The spatial discretization is such that gradients are evaluated in an ‘upwind’ manner, for example

$$\frac{\partial \phi}{\partial x} = \frac{\phi_{i,j} - \phi_{k,j}}{x_i - x_k} \quad (6.43)$$

In which  $k$  equals  $i-1$  or  $i+1$  so that it fulfills

$$\begin{cases} \bar{G}_{k,j}^n = \max(\bar{G}_{i-1,j}^n, \bar{G}_{i+1,j}^n) & \text{if } \bar{G}_{i,j}^n < 0 \\ \bar{G}_{k,j}^n = \min(\bar{G}_{i-1,j}^n, \bar{G}_{i+1,j}^n) & \text{if } \bar{G}_{i,j}^n > 0 \end{cases} \quad (6.44)$$

The turbulent burning velocity which appears in the expression for the speed function still has to be specified. The expression for the turbulent burning velocity given in Equation (6.10) has been used. A curvature term  $\bar{\kappa}(\bar{G})$  has been added which arises from the effect of turbulent transport and Markstein diffusion, i.e. from the closure of Equation (6.15),

$$s_T = s_L^0 + s_L^0 \sigma \left( 1 - 1.3 \frac{\mathcal{L}}{l_t} \frac{v'}{s_L^0} \right) - (s_L^0 \mathcal{L} + D_t) \bar{\kappa}(\bar{G}) \quad (6.45)$$

where  $\bar{\kappa}(\bar{G})$  is defined as in Equation (6.25) but with  $\bar{G}$  instead of  $G$ . The inclusion of this term avoids the formation of cusps in the mean flame front. In general,  $s_L^0 \mathcal{L} + D_t$  is positive because of a large turbulent diffusion coefficient. Therefore, an increased curvature of the mean turbulent flame front gives rise to a decreased turbulent burning velocity tending to decrease the curvature again. In mathematical terms; the solution of the level-set equation becomes total-variation diminishing (Sethian, 1996).

The expression for the curvature in cylindrical coordinates is given by

$$\begin{aligned} \bar{\kappa}(\bar{G}) &= -\nabla \cdot \left( \frac{\nabla \bar{G}}{|\nabla \bar{G}|} \right) = -\frac{\partial}{\partial x} \left( \frac{\bar{G}_x}{\sqrt{\bar{G}_x^2 + \bar{G}_r^2}} \right) - \frac{1}{r} \frac{\partial}{\partial r} \left( r \frac{\bar{G}_r}{\sqrt{\bar{G}_x^2 + \bar{G}_r^2}} \right) = \\ &= \frac{\bar{G}_{xx} \bar{G}_r^2 - 2\bar{G}_r \bar{G}_x \bar{G}_{xr} + \bar{G}_{rr} \bar{G}_x^2 + \frac{1}{r} (\bar{G}_x^2 + \bar{G}_r^2) \bar{G}_r}{(\bar{G}_x^2 + \bar{G}_r^2)^{3/2}} \end{aligned} \quad (6.46)$$

second order derivatives are discretized like

$$\bar{G}_{xx} = \frac{\frac{\bar{G}_{i+1,j} - \bar{G}_{i,j}}{x_{i+1} - x_i} - \frac{\bar{G}_{i,j} - \bar{G}_{i-1,j}}{x_i - x_{i-1}}}{\frac{1}{2}(x_{i+1} - x_{i-1})} \quad (6.47)$$

Strictly speaking Equation (6.45) is only valid in premixed systems with zero mixture fraction

gradients. How the effect of mixture fraction fluctuations on the turbulent burning velocity can be taken into account will be discussed in Chapter 7.

Because the spatial displacement of the flamelet from its mean position is typically near Gaussian (Wirth *et al.*, 1992) the PDF for  $G$  should be close to a Gaussian distribution. In the present study the Probability Density Function (PDF) for  $G$  is taken as

$$P(G) = \frac{1}{l_{F,t}} \left[ 1 + \cos \left( \frac{2\pi(G-\bar{G})}{l_{F,t}} \right) \right] \quad (6.48)$$

where  $l_{F,t}$  is the turbulent flame brush thickness. Because of

$$\sqrt{G'^2} = \overline{(G-\bar{G})^2} = \int_{\bar{G}-0.5l_{F,t}}^{\bar{G}+0.5l_{F,t}} (G-\bar{G})^2 P(G) dG \quad (6.49)$$

it can be deduced from Equation (6.48) that

$$l_{F,t} = \sqrt{\frac{12\pi^2}{\pi^2-6}} \sqrt{G'^2} \approx 5.53 \sqrt{G'^2} \quad (6.50)$$

Furthermore,  $\sqrt{G'^2}$  is taken to be proportional to the integral length scale  $l_t$  (Peters, 1997),

$$\sqrt{G'^2} = b_2 l_t \quad (6.51)$$

with a modelling constant  $b_2=1.78$ . It is a steady-state solution of the transport equation for  $\overline{G'^2}$  (See Appendix F). Therefore, the turbulent flame brush thickness is proportional to the integral length scale with a constant of proportionality equal to 9.84. Also other definitions for the turbulent flame brush thickness have been used in the literature, e.g.  $l_{F,t}=2\sqrt{G'^2}$  (Bray *et al.*, 1994), or  $l_{F,t}=\sqrt{G'^2}$  (Peters, 1997). These definitions would obviously reduce the constant of proportionality between the turbulent flame brush thickness and the integral length scale but they would by no means alter the present model.

The probability of burning  $P_b$  may be evaluated as the probability that  $G$  is larger than zero:

$$P_b = \int_{G=0}^{\bar{G}+0.5l_{F,t}} P(G) dG = \frac{\bar{G}+0.5l_{F,t}}{l_{F,t}} + \frac{1}{2\pi} \sin \left( \frac{2\pi\bar{G}}{l_{F,t}} \right) \quad (6.52)$$

Because the layer within which chemical conversion of reactants to products takes place is assumed to be infinitesimally thin, the PDF for  $c$  is dominated by delta functions at  $c=0$  and  $c=1$ ,

$$P(c) = (1-P_b)\delta(c-0) + P_b\delta(c-1) \quad (6.53)$$

Therefore the time-averaged value of  $c$  is equal to the probability of burning.

Favre-averaged scalar quantities are calculated from the flamelet libraries by making use of a presumed PDF method. A Favre-averaged scalar quantity is calculated as

$$\bar{\phi} = \int_{c=0}^1 \int_{\chi_{st}=0}^{\infty} \int_{Z=0}^1 \phi(Z, \chi_{st}, c) \tilde{P}(Z, \chi_{st}, c) dZ d\chi_{st} dc \quad (6.54)$$

$Z$ ,  $\chi_{st}$  and  $c$  are assumed to be statistically independent and the PDF is described by the product of three PDF's;  $\tilde{P}(Z)$ ,  $\tilde{P}(\chi_{st})$  and  $\tilde{P}(c)$ . The Favre PDF for  $c$  is given by

$$\tilde{P}(c) = (1-\tilde{c})\delta(c-0) + \tilde{c}\delta(c-1) \quad (6.55)$$

The variance in the conditioned Favre-averaged scalar dissipation rate  $\chi_{st}$  is assumed to be zero and therefore the PDF for  $\chi_{st}$  is given by a single delta function at  $\chi_{st} = \tilde{\chi}_{st}$ ,

$$\tilde{P}(\chi_{st}) = \delta(\chi_{st} - \tilde{\chi}_{st}) \quad (6.56)$$

Substituting Equation (6.29) into Equation (6.54) and evaluating the partial integration over  $c$  and  $\chi_{st}$  gives:

$$\tilde{\Phi} = (1 - \tilde{c}) \int_{Z=0}^1 \phi_u(Z) \tilde{P}(Z) dZ + \tilde{c} \int_{Z=0}^1 \phi_b(Z | \tilde{\chi}_{st}) \tilde{P}(Z) dZ \quad (6.57)$$

The Favre-averaged progress variable is obtainable from

$$\tilde{c} = \frac{\overline{\rho c}}{\bar{\rho}} = \frac{\bar{\rho}_b P_b}{\bar{\rho}} \quad (6.58)$$

where  $\bar{\rho}_b$  is the average density in the burnt gas,

$$\bar{\rho}_b = \left[ \int_{Z=0}^1 \frac{1}{\rho_b(Z | \tilde{\chi}_{st})} \tilde{P}(Z) dZ \right]^{-1} \quad (6.59)$$

In the same way the average density  $\bar{\rho}_u$  in the unburnt gas can be calculated from a quenched flamelet. The mean density is then determined from

$$\bar{\rho} = (1 - P_b) \bar{\rho}_u + P_b \bar{\rho}_b \quad (6.60)$$

The integrations in Equation (6.57) and Equation (6.59) are performed over a flamelet with scalar dissipation rate  $\tilde{\chi}_{st}$  at stoichiometric conditions. This average value  $\tilde{\chi}_{st}$  can be determined from Equation (5.44).

#### Boundary conditions

At the boundary of the calculation domain, the boundary condition for the level-set function is given by Equation (6.33). At the symmetry axis, the boundary condition for  $\bar{G}$  is given by  $\partial \bar{G} / \partial r = 0$ . At the burner wall, the gradient of  $\bar{G}$  in normal direction is set equal to zero. In this way diffusion of products towards the wall is zero. With the present model, a problem occurs near to the burner wall. In practice, near the wall, not only the mixture velocity is reduced by friction, but also the burning velocity near the wall is reduced for example by cooling of a cold burner wall. This effect is not modelled by Equation (6.45). A gradient theory, similar to that of Lewis *et al.* (1943) for laminar flames, might be useful to improve the present model on this stabilization mechanism. At present, the speed function is simply set equal to zero in the first grid node at the burner wall. In this way, the flame is prevented from moving along the wall, or from detaching from the wall. Unrealistic results might be obtained near the burner wall. However, this effect is assumed to have a negligible effect on the downstream dynamics of the flame. Boundary conditions have been implemented as indicated in Figure 6.8.

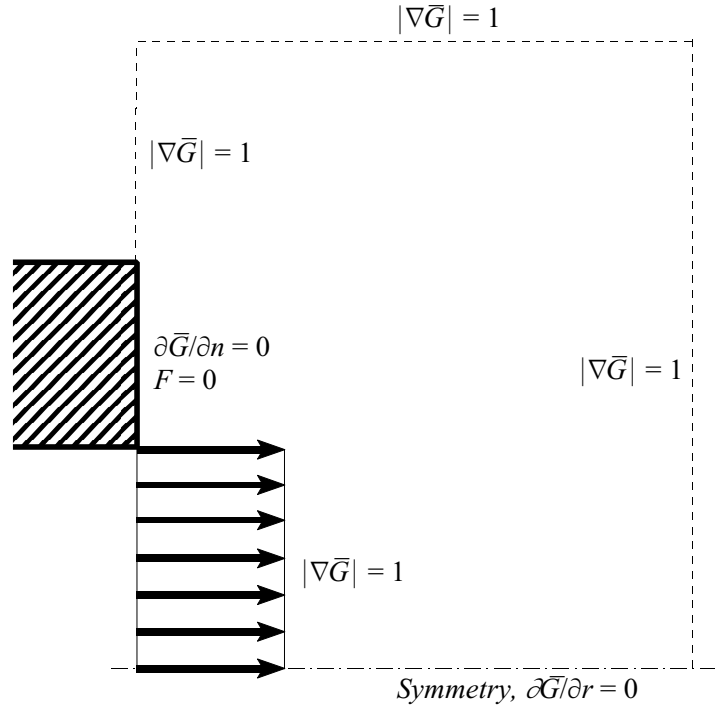


Figure 6.8 Boundary conditions for the level-set function.

## 6.5 RESULTS

To evaluate the model, a high Reynolds number turbulent premixed hydrogen/air flame has been simulated numerically and results have been compared to experimental data given by Wu *et al.* (1990). A coaxial model geometry of a round jet burner was used. The diameter of the burner was 11 mm with a wall thickness of 1 mm. A 1/7 power-law velocity distribution for fully developed turbulent pipe flow was imposed at the burner exit, i.e. Equation (5.46) with  $n$  equal to 7. Boundary conditions for  $\tilde{k}$  and  $\tilde{\epsilon}$  have been treated in the same way as described in Section 5.6.

Test cases are as summarized in Table 6.1. The length scale ratio  $l_t/l_F$  and velocity scale ratio  $v'/s_L^0$  have been evaluated at the centerline of the jet burner. For each test case, the laminar burning velocity has been obtained from data given in Appendix D. The laminar flame thickness may be evaluated from Equation (6.2). At atmospheric pressure and a temperature of 293 K the density in the unburnt mixture is approximately equal to 1.20 kg/m<sup>3</sup>. With Equation (6.3) the thermal diffusivity  $D^T$  may then be evaluated to be approximately equal to  $2.13 \cdot 10^{-5}$  m<sup>2</sup>/s. According to Table 6.1, the length scale ratio is approximately equal to 100 and the velocity scale ratio is smaller than 2.1 for all flames. Therefore, all premixed flames are well within the wrinkled and corrugated-flamelet regimes of Figure 6.3. This justifies to make use of the flamelet model.

Case	$\phi$	$Re$	$\tilde{u}_{avg}$ [m/s]	$s_L^0$ [m/s]	$M$	$(l/l_F)_{c,o}$	$(v'/s_L^0)_{c,o}$
1	1.0	7000	13.3	2.3	-14.27	101	0.20
2	1.0	20000	37.9	2.3	-14.27	101	0.56
3	1.0	40000	75.8	2.3	-14.27	101	1.12
4	1.8	7000	15.7	3.3	5.64	145	0.16
5	1.8	20000	45.0	3.3	5.64	145	0.46
6	1.8	40000	90.0	3.3	5.64	145	0.93
7	3.57	7000	20.4	1.9	5.71	83	0.37
8	3.57	20000	58.3	1.9	5.71	83	1.04
9	3.57	40000	116.4	1.9	5.71	83	2.08

Table 6.1 Important parameters evaluated for the different test cases, i.e. equivalence ratio  $\phi$ , Reynolds number  $Re$ , average burner exit velocity  $\tilde{u}_{avg}$ , the laminar burning velocity  $s_L^0$  and the Markstein number  $M$ . The length scale ratio  $l/l_F$  and velocity scale ratio  $v'/s_L^0$  have been evaluated at the centerline of the burner exit.

In the numerical simulation, the turbulent burning velocity is obtained from Equation (6.45). Because the premixed flame is in the core region of the jet, the laminar burning velocity  $s_L^0$  and Markstein number  $M$  are assumed to be constant for each test case as given in Table 6.1. The Markstein length is obtained from data given in Appendix D.

Calculations have been performed on a rectangular grid consisting of  $150 \times 65$  nodes in axial and radial direction, respectively. The total length of the calculation domain is  $17D$  in axial direction and  $14D$  in radial direction. Figure 6.9 shows the solution for the level-set function for test case 5, i.e. a calculation at an average burner exit velocity of 45 m/s and an equivalence ratio of 1.8. The zero level set represents the averaged premixed flame position. Figure 6.10 shows the solution for the average progress variable for the same test case. Also shown in this figure are the streamlines (contour lines of the streamfunction). Streamlines diverge while crossing the premixed flame due to thermal expansion. The contour line  $\bar{c}=0.5$  coincides with the contour line  $\bar{G}=0$  in Figure 6.9.

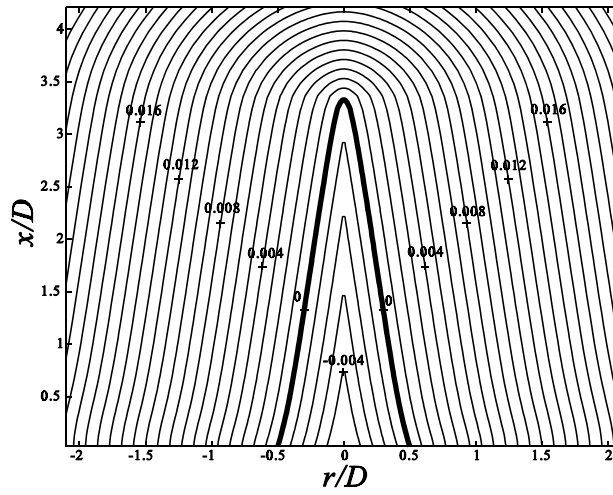


Figure 6.9 Contour lines of the level-set function  $\bar{G}$  [m] predicted for test case 5.

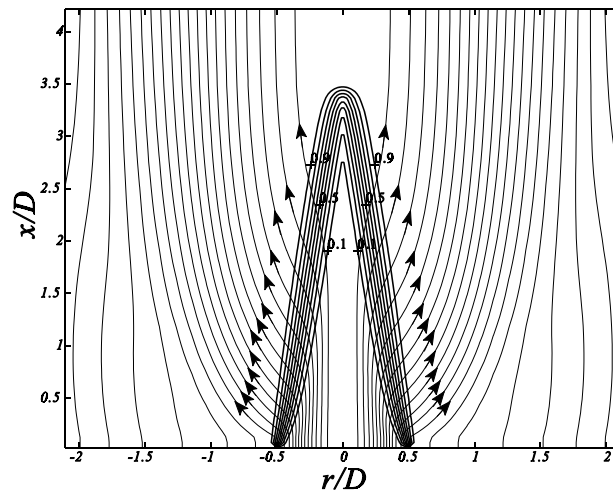


Figure 6.10 Contour lines of the progress variable  $\bar{c}$  and streamlines predicted for test case 5.

Figure 6.11 clearly illustrates that the temperature depends on both the progress variable and the mixture fraction. Mixing turns out to take place mainly downstream of the premixed flame. This is also the reason why a constant laminar burning velocity  $s_L^0$  was used for calculating the turbulent burning velocity without taking the effect of mixture fraction fluctuations into account. It was also observed by Wu *et al.* (1990) that varying the equivalence ratio of the outer burner flame had no significant influence on the flow and combustion properties within the inner

premixed flame. Therefore, the equivalence ratio of the outer burner was kept near to the flammability limit ( $\Phi=0.3$ ).

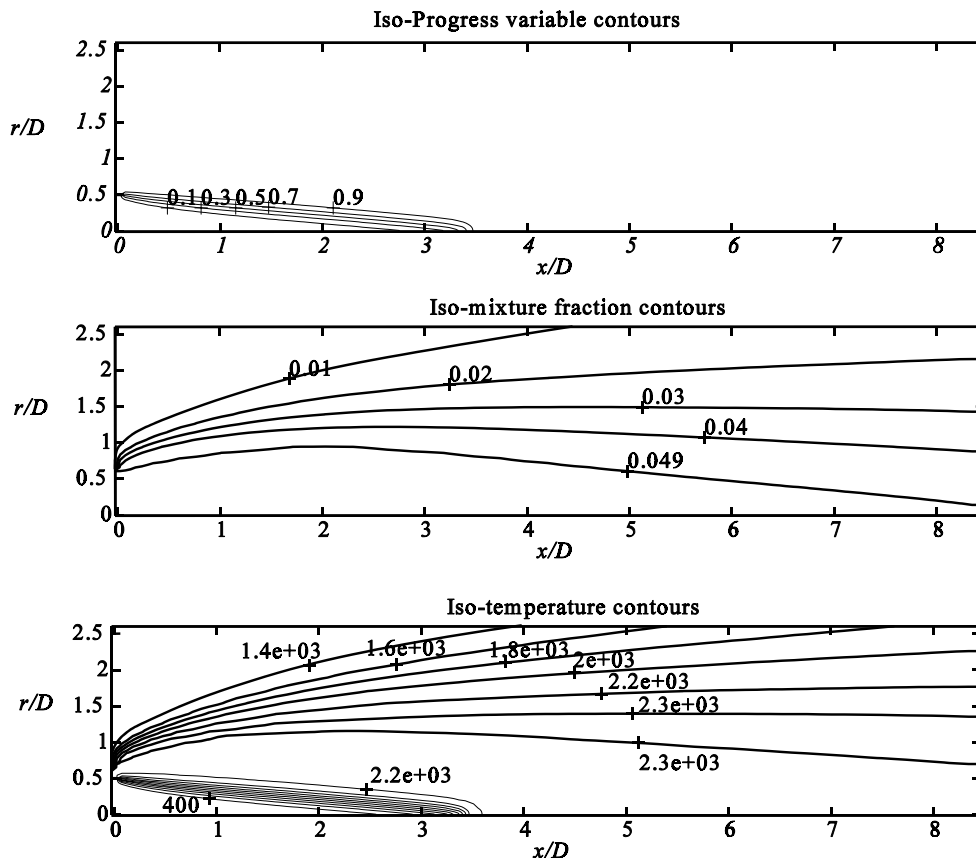


Figure 6.11 Calculated iso-contours of the time-averaged progress variable, Favre-averaged mixture fraction and the Favre-averaged temperature predicted for test case 5.

Figure 6.12 shows the measured (Wu *et al.*, 1990) and predicted time-averaged unreactedness along the centerline. The unreactedness is simply defined as  $1-c$ . A significant trend is that the flame length increases with increasing Reynolds number for all values of the equivalence ratio. The length of the premixed flame is defined as the distance from the nozzle to the centerline position where  $c=0.5$ . The turbulent flame brush thickness at the tip of the flame is under-predicted. Especially towards the tip of the flame, a too fast decrease in the progress variable is predicted. This may be caused by the prescribed boundary condition for the characteristic velocity fluctuation which will turn out later to be slightly too low at the centerline. Also anisotropic effects might play an important role in the modelling of the flame tip whereas, according to the used  $k-\epsilon$  model, predicted fluctuations are equal in all directions.

Figure 6.13 shows the premixed flame length as a function of the average burner exit velocity. It is shown that the flame length is shortest for the flames with equivalence ratio 1.8. This may be explained from the fact that at this equivalence ratio, the laminar burning velocity reaches its maximum value (see Figure D.3 in Appendix D). However, especially for the large Reynolds

numbers, the flame length of the stoichiometric flame is not much shorter than that of the flame with equivalence ratio 1.8. This is caused by the Markstein length changing from negative for the stoichiometric flame to positive for the flame with equivalence ratio 1.8. A negative Markstein length is acting to increase wrinkling of the flame surface so that the required area to complete reaction can be achieved in a shorter flame length. For the flame with equivalence ratio 3.57, on the other hand, the Markstein length remains almost the same as that for the flame with equivalence ratio 1.8. Therefore, although the laminar burning velocity of the flame with equivalence ratio 3.57 is not much lower than that for the stoichiometric flame, the flame length of the flame with equivalence ratio 3.57 is much larger than that of the stoichiometric flame. However, this effect is more pronounced in the measurements.

Figure 6.13 also shows that for large Reynolds numbers, an increased burner exit velocity gives rise to a smaller increase of the flame length. This is caused by the fact that at the high Reynolds numbers, where the laminar flame speed becomes relatively small in comparison to the characteristic velocity fluctuation, the turbulent burning velocity increases nearly proportional to the characteristic velocity fluctuation. Since the characteristic velocity fluctuation is proportional to the average burner exit velocity, the turbulent burning velocity becomes proportional to the average burner exit velocity, and an increased turbulent burning velocity nearly compensates for the increased burner exit velocity. Therefore, at the high Reynolds numbers, the flame length tends to become independent of the average burner exit velocity.

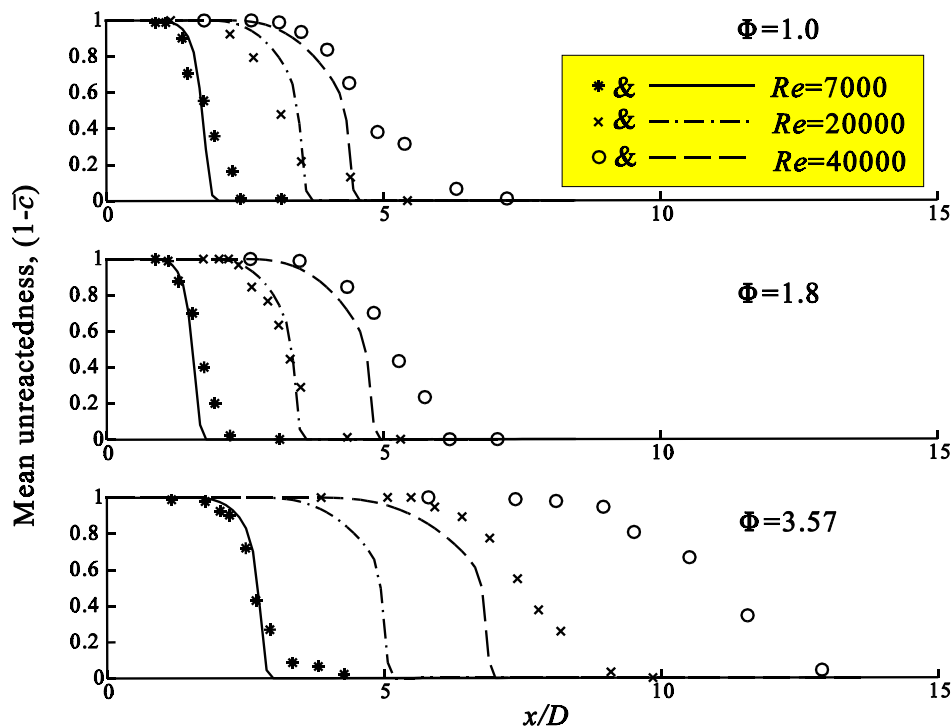


Figure 6.12 Mean unreactedness along the centerline. Symbols are measurements of Wu *et al.* (1990).



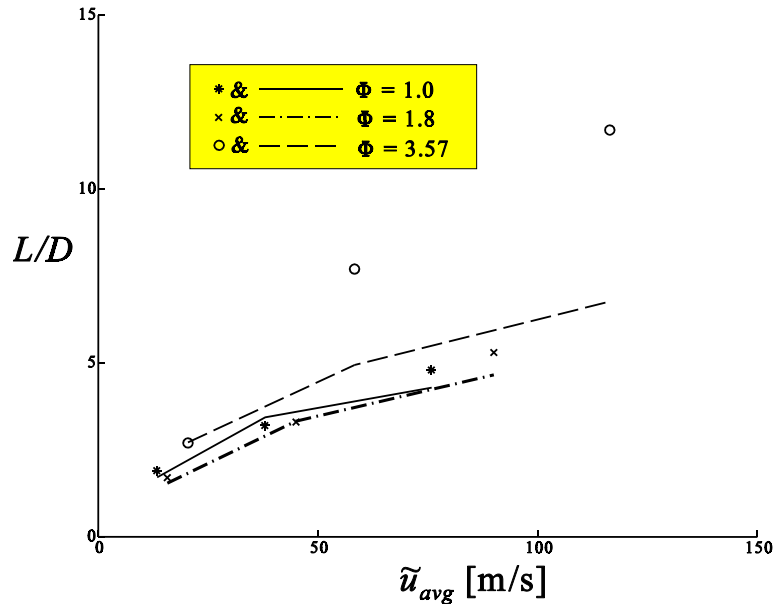


Figure 6.13 Flame length as a function of the average burner exit velocity. Symbols are measurements of Wu *et al.* (1990).

In Figure 6.14, the measured and predicted radial variation of unreactedness are illustrated for  $\Phi=1.8$  and  $3.57$  and  $Re=40000$ . The other test cases revealed similar results. The shape of the mean flame position in a plane through its axis is roughly triangular for all predicted flames (see Figure 6.9). Because all flames have the same base dimension, they all have roughly the same width at equal fractions of their height. However, the measured flames turn out to have a less triangular shape than the predicted flames, the predicted flames are located more towards the centerline of the jet. The turbulent burning velocity is over-predicted close to the burner wall. The reason for this may be found in the prescribed boundary conditions, especially that for the characteristic velocity fluctuation, i.e. Equation (5.49), that does not tend to zero close to the burner wall. If the characteristic velocity fluctuation is over-predicted, then also the turbulent burning velocity will be over-predicted. Another reason for the over-predicted turbulent burning velocity may be given by the fact that in the measurements the laminar burning velocity is lower because of heat-release to the burner wall.

At an axial position of one half of the flame length, the turbulent flame brush thickness is predicted rather well. Also, the increase of the progress variable over the turbulent flame brush is seen to be very similar to that of the measurements. Again, at the flame tip, the turbulent flame brush thickness is under-predicted.

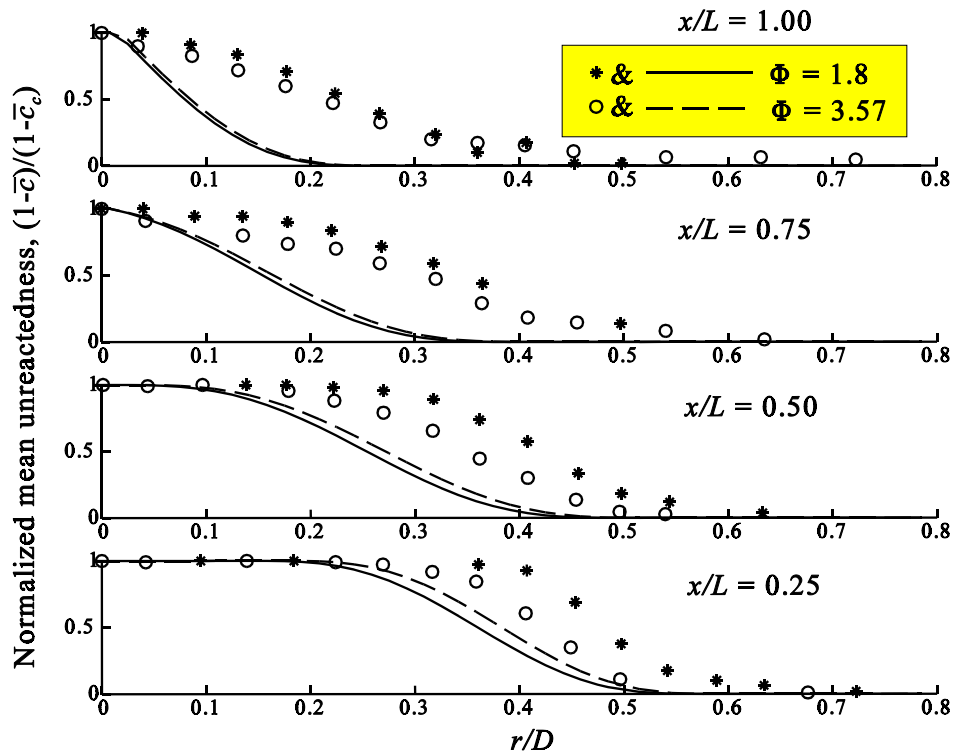


Figure 6.14 Radial profiles of normalized mean unreactedness for  $Re=40000$ . Symbols are measurements of Wu *et al.* (1990).

In Figure 6.15, the predicted and measured centerline profiles of the mean normalized axial velocity component are given. Results are given for  $\Phi=1.0, 1.8$  and  $3.57$  at  $Re=7000$  and  $40000$ . Because the predicted flames are located more towards the centerline than in the experiment, there is a rather large influence of the flame on the centerline velocity. The thermal expansion within the premixed flame results in a convergence of the streamline near the centerline, resulting in an increased velocity. A larger velocity increase is observed when the flame length is shorter. The increased centerline velocity was not observed in the measurements by Wu *et al.* (1990). They assumed that, everywhere in front of the premixed flame, the mean axial velocity component was the same as at the burner exit. Unfortunately, just a few measurements have been done within the interesting region of the premixed flame. Further downstream, the velocity decreases due to mixing with the surrounding flow.

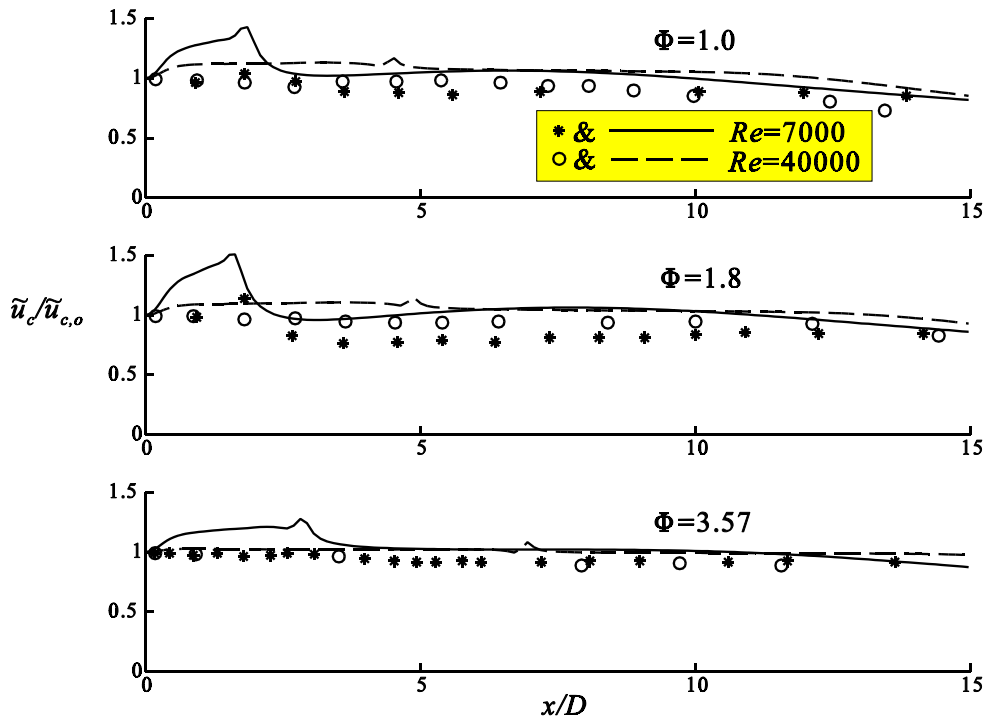


Figure 6.15 Centerline profile of the mean normalized axial velocity. Symbols are measurements of Wu *et al.* (1990).

In Figure 6.16, the predicted characteristic velocity fluctuation is compared to the measured characteristic velocity fluctuation. As found for the mean axial velocity component, also the characteristic velocity fluctuation increases the most for the shortest flames. This result is also found in the measurements. Due to the density ratio of the flames, velocity increases normal to the flames. Flame intermittency causes the velocity to fluctuate. Although, for most predicted flames, the characteristic velocity fluctuation decreases again downstream of the premixed flame, this effect is not as strong as in the measurements. This suggests that the dissipation of turbulence kinetic energy is under-predicted. An adaptation of the constants like in Equation (4.91) with a lower value for  $C_2$  might therefore be useful.

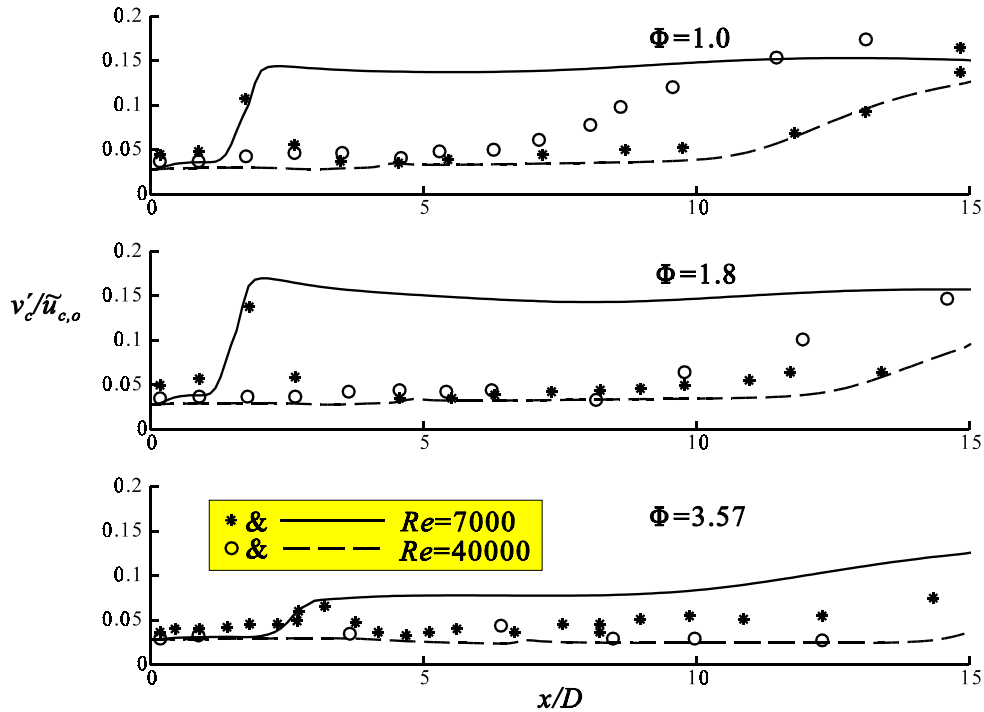


Figure 6.16 Centerline profile of the normalized velocity fluctuation. Symbols are measurements of Wu *et al.* (1990).

## 6.6 CONCLUSIONS

Use has been made of a premixed flamelet model based on a level-set equation for the scalar  $\bar{G}$ . The expression for the turbulent burning velocity, used in this kinematic equation, covers the corrugated-flamelet regime as well as the thin-reaction-zones regime. In the corrugated-flamelet regime, the expression for the turbulent burning velocity reduces to the expression given by Damköhler (1940) for what he called the large-scale-turbulence regime. In the thin-reaction-zones regime, the expression for the turbulent burning velocity reduces to the expression given by Damköhler (1940) for what he called the small-scale-turbulence regime.

An expression given by Clavin (1985) for the laminar burning velocity has been used to model the kinematic equation for the level-set function  $\bar{G}$ . In the expression for the laminar burning velocity, the Markstein length  $\mathcal{L}$  accounts for flame curvature and flame stretch effects on the laminar burning velocity. Also in the equation for  $\bar{G}$ , the influence of mean curvature has been incorporated into the expression for the turbulent burning velocity by means of the Markstein length and the turbulent diffusivity. Because of a large turbulent diffusion coefficient, the solution for the level-set function  $\bar{G}$  becomes total-variation diminishing, even if the laminar flame is unstable because of a negative Markstein length.

The level-set function  $G$  is defined as a signed-distance function, and the PDF for  $G$  is approximated by a cosine relation. Because the premixed flame is assumed to be infinitesimally thin, a solution for the mean progress variable  $\bar{c}$  may be obtained from the solution for  $\bar{G}$  and

an expression given for the turbulent flame brush thickness. The turbulent flame brush thickness is taken to be proportional to the integral length scale.

The condition that  $\bar{G}$  should satisfy the level-set equation as well as the condition that  $\bar{G}$  should remain a signed-distance function leads to an additional equation for the speed function  $F$ . By introduction of this additional equation for the speed function  $F$ , the commonly used procedure in which the re-initialisation algorithm alternates with the level-set equation, i.e. two equations for one unknown, has been made redundant. Therefore it may be concluded that the introduction of this additional equation for the speed function  $F$  leads to a more consistent approach to the level-set algorithm with two equations for two unknowns.

Results of a numerical simulation have been compared to measurements of Wu *et al.* (1990). Test cases have been done for equivalence ratios  $\Phi=1.0$ , 1.8 and 3.57 and Reynolds numbers of 7000, 20000 and 40000. Numerical results as well as measurements revealed a clear influence of the Markstein number. While for test cases with an equivalence ratio  $\Phi$  of 1.8 the laminar burning velocity was highest, the flame length for the stoichiometric flames was not much longer because of the negative Markstein number. The flame length for the stoichiometric flames was even slightly shorter at the highest Reynolds number. A negative Markstein length makes the laminar flame unstable which leads to an increased flame surface and thereby an increased turbulent burning velocity. Longest flame lengths were found for the rich flames with an equivalence ratio  $\Phi$  of 3.57 for which the laminar burning velocity was lowest and the Markstein length was positive having a stabilizing effect on the premixed flame. However, these effects were more pronounced in the measurements. The Markstein length for the flames with  $\Phi=3.57$  is almost the same as that for the flames with  $\Phi=1.8$ . Therefore, the increased flame length for the flames with  $\Phi=3.57$  is probably caused by a decreased laminar burning velocity. The difference between measurements and numerical simulation for the very rich flames with  $\Phi=3.57$  might be caused by an inaccuracy in the laminar burning velocity or an inaccuracy in the equivalence ratio. Because the test case with  $\Phi=3.57$  and  $Re=40000$  was closest to the thin-reaction-zones regime, also the model constant 0.78 in Equation (6.8) might be too high.

The shape of the flame seems to differ from that found experimentally in the sense that the simulated flame has a more triangular shape. Close to the burner wall, the turbulent burning velocity seems to be over-predicted. Therefore, radial profiles of the mean unreactedness are located a bit more towards the centerline. A good comparison has been found for the turbulent flame brush thickness at one half of the turbulent flame length. At the flame tip, an under-predicted turbulence kinetic energy seems to be the reason for the difference between calculated and measured centerline and radial profiles of the mean progress variable. Also anisotropic effects might play an important role in the modelling of the flame tip. However, with the used  $k$ - $\epsilon$  turbulence model, it is impossible to model anisotropic effects.

Centerline profiles of the mean velocity show a velocity increase in front of the premixed flame. This velocity increase is due to a contraction of the flow on the centerline caused by an expansion of the flow within the premixed flame. Because in the simulation the premixed flame is located more towards the centerline, this effect is more pronounced. Also this effect is the largest for the shortest flames. Similar results have been obtained for the characteristic velocity fluctuation. However, the used turbulence model turns out to be incapable of predicting the rather fast turbulence decrease behind the premixed flame. An adaptation of the constants like in Equation (4.91) might be useful.



Vanquickenborne and van Tiggelen (1966) suggest that flame stabilization occurs on the contour of mean stoichiometric mixture at the position where the axial mean velocity equals the turbulent burning velocity for entirely premixed conditions. However, Peters and Williams (1983) have argued that in a non-premixed flow field, flame propagation will proceed along instantaneous surfaces of stoichiometric mixtures up to the position where too many flamelets are quenched, so that flame propagation of the turbulent flame towards the nozzle cannot proceed further. In addition, Müller *et al.* (1994a) combine flamelet formulations for premixed and nonpremixed combustion in order to treat partially premixed combustion in the fast chemistry limit, and suggest that flame stabilization occurs via so-called triple flames.

Also in this study, triple flames are considered to be the key element in the stabilization mechanism. As indicated in Figure 7.1, a premixed flame will propagate fastest along the surface of stoichiometric mixture. The leading edge of the flame, called the triple point, propagates along the surface of stoichiometric mixture. On the lean side of that surface there is a lean premixed flame branch and on the rich side there is a rich premixed flame branch, both propagating with a lower burning velocity. Downstream of the triple point, on the surface of stoichiometric mixture, a diffusion flame develops where the unburnt fuel from the rich premixed flame branch reacts with the remaining oxygen from the lean premixed flame branch.

The burning velocity on the two premixed flame branches should to first approximation depend on the local mixture fraction. However, numerical simulations (Plessing *et al.*, 1998) show that the maximum of the mass burning rate normal to the flame front evaluated from two-dimensional simulations is significantly lower than the mass burning rate through a one-dimensional flame in a homogeneous mixture. The lowering of the burning velocity may in part be attributed to the local mixture fraction gradient. An ad-hoc expression that models this effect was proposed earlier by Müller *et al.* (1994):

$$s_L(Z, \chi_{st}) = s_L^0(Z) \left( 1 - \alpha \frac{\chi_{st}}{\chi_q} \right) \quad (7.1)$$

The burning velocity  $s_L$  is expected to decrease with increasing  $\chi_{st}$  and to vanish at a scalar dissipation rate close to the quenching scalar dissipation rate  $\chi_q$ . Therefore, the parameter  $\alpha$  is close to unity and it is set equal to 0.96, a value which was found for diluted methane flames (Peters, 1997).

## 7.2 TURBULENT BURNING VELOCITY IN A NON-HOMOGENEOUS MIXTURE FRACTION FIELD

In this section an expression is derived for the turbulent burning velocity in a non-homogeneous mixture fraction field. The turbulent burning velocity is expected to be highest in regions where the probability of finding a stoichiometric mixture is highest. This corresponds to regions where the mean mixture fraction is in the vicinity of the stoichiometric value. The expression used for the turbulent burning velocity is essentially the same as that used in homogeneous mixture fraction fields, i.e. Equation (6.45) with the laminar burning velocity replaced by an average value:

$$s_T = \overline{s_L + s_L \sigma} \left( 1 - 1.3 \frac{\overline{\mathcal{Q}}}{l_t} \frac{v'}{s_L} \right) - (\overline{s_L \mathcal{Q}} + D_t) \overline{\kappa}(\overline{G}) \quad (7.2)$$

The average laminar burning velocity is obtained from

$$\overline{s_L} = \int_{\chi_{st}=0}^{\infty} \int_{Z=0}^1 s_L(Z, \chi_{st}) \tilde{P}(Z) \tilde{P}(\chi_{st}) dZ d\chi_{st} \quad (7.3)$$

Substitution of Equation (7.1) and using a single Dirac PDF for  $\chi_{st}$ , i.e. Equation (6.56), leads to:

$$\overline{s_L} = \left( 1 - \alpha \frac{\tilde{\chi}_{st}}{\chi_q} \right) \int_{Z=0}^1 s_L^0(Z) \tilde{P}(Z) dZ \quad (7.4)$$

Where  $\tilde{\chi}_{st}$  can be determined from Equation (5.44). A convenient representation of the integral in Equation (7.4) is

$$\int_{Z=0}^1 s_L^0(Z) \tilde{P}(Z) dZ = s_L^0(Z_{st}) P(Z_{st}) (\Delta Z)_{s_L} \quad (7.5)$$

which defines the width  $(\Delta Z)_{s_L}$ . Because  $s_L^0(Z)$  has a strong peak in the vicinity of  $Z_{st}$  and decreases rapidly towards the lean and rich side,  $(\Delta Z)_{s_L}$  has an almost constant value of 0.06 for methane flames. The average laminar burning velocity in Equation (7.2) is now given by

$$\overline{s_L} = \underbrace{s_L^0(Z_{st}) P(Z_{st}) (\Delta Z)_{s_L}}_{\text{partial premixing}} \underbrace{\left( 1 - \alpha \frac{\tilde{\chi}_{st}}{\chi_q} \right)}_{\text{flamelet quenching}} \quad (7.6)$$

This formulation of the average laminar burning velocity contains two contributions:

1. A term due to partial premixing which restricts flame propagation to regions where the probability for stoichiometric conditions is large.
2. A factor accounting for flamelet quenching. The laminar burning velocity decreases if the mean scalar dissipation rate increases, indicating that laminar triple flames are less able to propagate due to increased local mixture fraction gradients.

### 7.3 RESULTS

The turbulent burning velocity model of Equation (7.2) was used to simulate flame stabilization in a turbulent methane jet diffusion flame. Numerical results have been compared to measurement data obtained by Schefer *et al.* (1998). The burner consists of a 5.4 mm diameter fuel jet located in the center of a plate. Methane was injected through the central fuel tube into surrounding still air. Measurements from Schefer *et al.* (1998) were obtained at jet exit velocities of 21, 37 and 60 m/s, corresponding to jet exit Reynolds numbers of 7000, 12000 and 19500, respectively. These jet exit velocities are well below the flame blow-off velocity of about 90 m/s.

Calculations have been performed on a rectangular grid consisting of 70×50 nodes in axial and radial direction, respectively. The total length of the calculation domain is 31D in axial direction



and  $13D$  in radial direction. To start with, an isothermal jet of methane is calculated. Upon obtaining a converged solution for the isothermal jet, combustion is initiated by setting the  $\bar{G}$ -field equal to that for a spherical flame front with radius  $2D$  and its centre in the so-called ignition-node  $(I_i, J_i)$ :

$$\bar{G}(I_i, J_i) = 2D - \sqrt{[X(I_i) - X(J_i)]^2 + [Y(I_i) - Y(J_i)]^2} \quad (7.7)$$

The position of the ignition-node  $(I_i, J_i)$  should be chosen such that the local burning velocity is high enough to prevent direct blow-off of the flame. Therefore, the ignition-node is chosen at the end of the calculation domain as a node in which the mixture fraction is close to stoichiometric. With such an ignition-node, the flame should be able to propagate towards the burner. Notice that there is also a threshold to the chosen radius of the spherical flame front; a radius too small (curvature too large) will decrease the laminar burning velocity to such an extent that the flame will also blow off directly.

When the unsteady flame front propagation towards the burner exit reaches a steady state, the lift-off height can be determined. Figure 7.2 depicts the steady-state solution obtained for the level set function at an average burner exit velocity of 37 m/s which corresponds to a Reynolds number of 12000. Figure 7.3 shows the solution for the average progress variable for the same test case. Also shown in this figure are the predicted streamlines. Figure 7.4 depicts the axial velocity profile along an axial line through the flame base for different Reynolds numbers. For the  $Re=12000$  case, this line has been indicated in Figure 7.3 as a dashed line. It can be seen that the axial velocity component in front of the flame base decreases to a local minimum at the flame base, and then accelerates across the flame due to volume expansion. It is found that the downstream value of the axial velocity component increases with increasing Reynolds number. Although no quantitative data on the mean axial velocity component is available from the measurements by Schefer *et al.* (1998), they also observed the same trend from the instantaneous velocity profiles measured along an axial line through the instantaneous flame base.

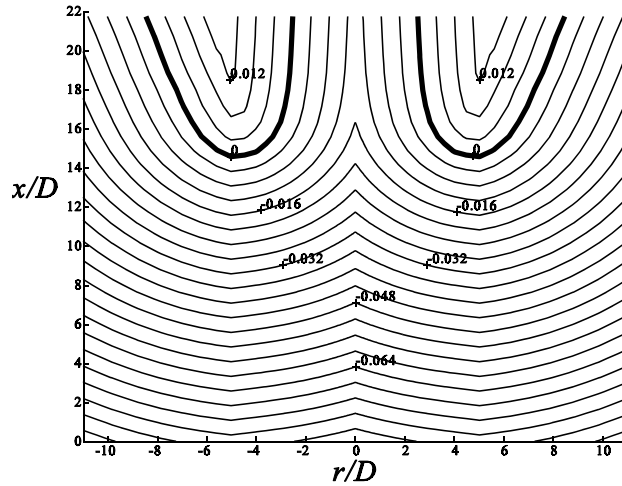


Figure 7.2 Contour lines of the level set function  $\bar{G}$  [m] in the stabilization region of a lifted turbulent jet diffusion flame. Exit velocity is 37 m/s ( $Re=12000$ ).

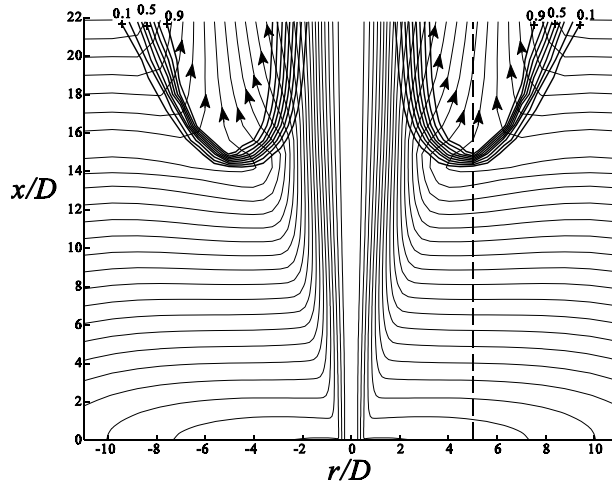


Figure 7.3 Contour lines of the progress variable  $\bar{c}$  and streamlines predicted in the stabilization region of a lifted turbulent jet diffusion flame. Exit velocity is 37 m/s ( $Re=12000$ ).

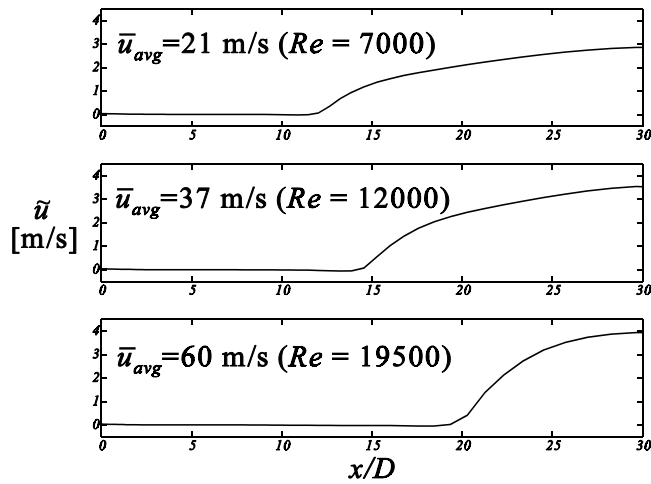


Figure 7.4 Axial mean velocity profiles at different Reynolds numbers. Profiles are along an axial line through the flame base as indicated in Figure 7.3 for  $Re=12000$ .

Figure 7.5 shows the iso-contour lines of the Favre-averaged mixture fraction. Also indicated is the zero level set of  $\bar{G}$  and the contour line of  $\tilde{\chi}$  equal to the quenching scalar dissipation rate  $\chi_q=17.4/s$ . If the stabilization height would be determined by  $\tilde{\chi}=\chi_q$ , as by the flamelet quenching criterion, the lift-off height would be under-predicted. At the lift-off height, the value of  $\tilde{\chi}/\chi_q$  is approximately equal to 0.03. Therefore, in the numerical simulation, the contribution of diffusion flamelet quenching to the stabilization mechanism is small. The deflection of the mixture fraction iso-contours at the flame base is caused by the local deflection of the streamlines

at the flame base which in turn is caused by expansion in the flame.

Figure 7.6 shows the measured and calculated lift-off height  $H$  as a function of the average burner exit velocity. At low burner exit velocities, the lift-off height is over-predicted which is probably caused by an under-predicted turbulent burning velocity. Decreasing the applied value for  $\alpha$  is expected to have just a small influence on the predicted lift-off height since the value of  $\tilde{\chi}/\chi_q$  is small at the lift-off height. Furthermore, at high exit velocities, the lift-off height is under-predicted and an increased value for  $\alpha$  would be desirable.

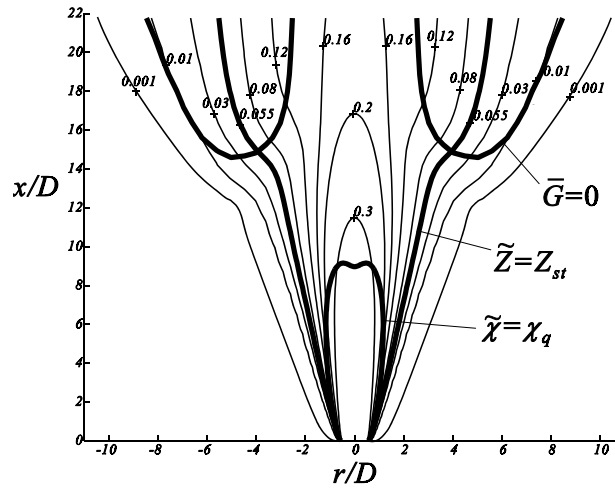


Figure 7.5 Contour lines of the mixture fraction, the zero level set of  $\bar{G}$  and the contour line  $\tilde{\chi}=\chi_q$  in the stabilization region of a lifted turbulent jet diffusion flame.

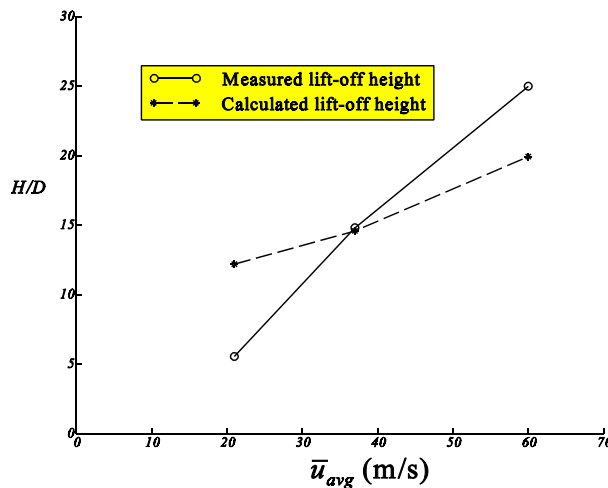


Figure 7.6 Measured and calculated lift-off heights as a function of the average burner exit velocity.

## 7.4 CONCLUSIONS

The applicability of triple-flame concepts to lifted flame stabilization has been evaluated. In this triple-flame concept, both effects, premixed flame propagation and flamelet quenching add to the stabilization mechanism. Both effects have been included in the used expression for the turbulent burning velocity. At the lift-off height, the value of  $\chi/\chi_q$  turned out to be small, i.e. about 0.03. Therefore, in the present study, the influence of flamelet quenching on the predicted turbulent burning velocity turned out to be small. Although the influence of flamelet quenching may be increased by increasing the applied value for  $\alpha$ , this is not expected to improve the predicted lift-off height as a function of the burner exit velocity. However, the lift-off height is predicted rather well by making use of the triple-flame concept.

As a final remark it is mentioned here that, at the moment, it is not at all certain whether or not the triple flame concept provides a good description of what happens in reality. Although experiments indeed show a downstream propagating diffusion flame that is anchored by a leading-edge flame, which is similar to a triple flame, it is also clear that turbulence causes considerable distortion of the local velocity field and significant differences from the laminar case, which makes application of Equation (7.1) uncertain. Calculations of Veynante *et al.* (1994) show that interactions between triple flames and even a single vortex can cause considerable distortion of the flame structure. Furthermore, experiments (e.g. Muller *et al.*, 1994) appear to show a transport of the flame by large structures at the edge of the jet. Local propagation velocities are influenced by three-dimensional structures moving sometimes in spirals around the axis of symmetry. Therefore, there remains a substantial difference between the very crude turbulence modelling based on the  $k$ - $\epsilon$  model and the large-scale dynamics in a jet. Modelling of these features is beyond the scope of this thesis.



## Chapter 8

### Concluding discussion

In this thesis, flamelet modelling has been used for the modelling of partially premixed turbulent jet diffusion flames. Modelling of partially premixed turbulent jet diffusion flames was facilitated by first dealing with the problem of turbulent mixing (in Chapter 4). The chemical aspects were considered first for the case of non-premixed systems (in Chapter 5) and subsequently for the case of premixed systems (in Chapter 6).

For performing measurements in a turbulent jet, a new method for treating X hot-wire signals has been developed. This method enables taking into account the effect of the fluctuating binormal velocity component. Measured velocity and temperature profiles have been compared to simulations performed employing the standard  $k$ - $\epsilon$  model.

In the diffusion flamelet model for non-premixed systems, the scalar dissipation rate was proposed as the appropriate chemical non-equilibrium parameter. The present diffusion flamelet model for non-premixed systems has been evaluated by considering a stabilized natural-gas flame.

In the flamelet model for premixed systems, use was made of the level-set equation for the distance function  $\bar{G}$ . An additional equation for the speed function  $F$  was introduced that leads to a more consistent approach to the level-set algorithm in which the use of a re-initialisation algorithm is redundant. In the level-set equation, an expression was used for the turbulent burning velocity  $s_T$  that can be applied in both the corrugated-flamelet regime as well as in the thin-reaction-zones regime. Also the bending effect is described by the used expression for  $s_T$ . The premixed flamelet model was evaluated by considering a turbulent premixed hydrogen/air flame. Finally (in Chapter 7) a combination of all models discussed was used for the modelling of lifted flames in which partial premixing plays an important role.

In the present Chapter, concluding remarks will be provided on each subject separately and suggestions will be given for future research in turbulent combustion.

### 8.1 TURBULENCE MEASUREMENTS AND MODELLING

Scalar transport and mixing in turbulent flows is of particular interest in combustion modelling. Predicted scalar quantities depend on the predicted mixture fraction. Unfortunately, the predicted mixture fraction, in turn, strongly depends on the used turbulence model (see Chapter 4). In the downstream region of the jet, where chemical equilibrium prevails, errors in the predicted scalar quantities are directly related to the error in the predicted mixture fraction. Also close to the burner exit, there is a strong relation between the calculated mixture fraction and the calculated scalar quantities, as can be seen from the used flamelet data in Appendix C. Large differences in calculated scalar quantities can therefore be introduced by large differences found in the calculated mixture fraction from numerical simulations performed with different turbulence models.

In the measurement, mixture fraction profiles were obtained as a scaled function of the measured temperature in a heated jet. Velocity distributions in an isothermal jet were obtained by making use of X hot-wire anemometry in combination with a look-up inversion method. A correction method has been developed that accounts for the influence of the fluctuating binormal

velocity component. Experimental results were compared to predictions obtained with different turbulence models. Predictions obtained with the standard  $k$ - $\epsilon$  turbulence model agreed reasonably well with values found experimentally. Therefore, the standard  $k$ - $\epsilon$  turbulence model offers an adequate way of simulating turbulent jets.

In experiments, the flow at the burner exit is often that of a fully developed turbulent pipe flow. In the numerical simulation this provides a well-known description for the boundary conditions at the burner exit (see Section 5.6). However, sometimes the flow at the nozzle exit is not equal to that of a fully developed turbulent pipe flow, e.g. for the flow studied in Chapter 4. When the boundary conditions at the inlet plane of the computational domain are not known exactly, it might be useful to extend the computational domain by also taking into account part of the nozzle geometry. Such an approach would however require a more complex method of grid generation than that used in the present study. Also the implementation of boundary conditions would become more complex.

## 8.2 TURBULENT COMBUSTION MODELLING

### Diffusion flames

In the region close to the burner exit, besides the modelling of turbulent mixing, the modelling of chemical non-equilibrium effects plays an important role. Chemical non-equilibrium is caused by strong gradients in the mixture fraction field, i.e. by a high value for the scalar dissipation rate. The scalar dissipation rate is highest near the burner exit and it plays an important role in the stabilization mechanism of turbulent jet diffusion flames.

In many other studies (e.g. Sanders, 1994), the strain rate has been used as the chemical non-equilibrium parameter. However, the quenching strain rate depends on the considered flow configuration and on the level of premixing. Contrary to the quenching strain rate, the quenching scalar dissipation rate is independent of the specific flow configuration and, to a certain degree, independent of the level of premixing. Therefore, in this study, the scalar dissipation rate was used as the chemical non-equilibrium parameter.

Because of multi-component diffusion, the definition of the mixture fraction is non-trivial. An appropriate definition of the mixture fraction is based on a scaled combination of element mass fractions (see Section 5.4.1) which reproduces the correct stoichiometric value, regardless the strength of the differential diffusion effects.

Close to the nozzle exit, mixture fraction values on the rich and lean side of the flamelet extend to 1 and 0, respectively. These values correspond to the boundary conditions used in the flamelet calculations. Effects like increased temperature levels at the lean side of stoichiometric, caused by differential diffusion, are taken into account correctly. In the downstream region of jet flames, however, mixture fraction values on the rich and lean side of the flamelet do not extend to those imposed in the flamelet calculations and calculated results are questionable. Especially for diluted hydrogen flames, results of flamelet modelling in the downstream region of jet flames predict too high temperature levels at the lean side of stoichiometric (e.g. Sanders, 1994). Surely the absence of differential diffusion effects in the measured temperature field (e.g. Meier *et al.* 1996), far downstream in jet flames, indicates the local inapplicability of the present flamelet model. In these regions, a better prediction would be obtained by assuming chemical equilibrium or by using equal diffusivities in the flamelet calculations. Nevertheless, for studying the stabilization mechanism close to the burner exit ( $x/D \leq 30$ ), the present flamelet model provides an accurate description of the diffusion flames.

An analytic expression for the conditioned scalar dissipation rate was used that has been derived with the assumption of the mixture fraction extending from pure air to pure fuel. However, in turbulent diffusion flames, premixed fuel is originating from the axis of symmetry. Therefore, a better representation of the mixture fraction profile is given by the relation for an infinite mixing layer with partially premixed boundary conditions on the fuel side. A correct value for the local conditioned scalar dissipation rate can also be obtained by using the value for the scalar dissipation rate at the radial position where the mixture fraction is equal to the stoichiometric value. This last method requires the use of some kind of search algorithm or the solution of an additional equation similar to Equation (6.36) used for the conditioned velocities. However, close to the burner exit, where the prescribed scalar dissipation profile is used to study the stabilization and quenching mechanism, the non-premixed scalar dissipation profiles are assumed to be accurate enough.

Although the laminar flamelet model in non-premixed combustion has been successfully applied for the prediction of mean values of temperature and species concentration, some aspects of laminar flamelet modelling in turbulent combustion are still unclear, as, for instance, the modelling of transient effects. When transient effects play an important role, like for the prediction of  $CO$  mass fractions (see Section 5.6), use has to be made of a flamelet model with unsteady flamelets. The temporal development of the scalar dissipation rate in the flamelet has to be known. This temporal development of the scalar dissipation rate, however, depends on the considered flow configuration. Therefore, this would lead to an interactive flamelet approach in which the used flamelet library has to be adjusted to the specific flow configuration.

#### Premixed flames

For modelling of the turbulent premixed flame brush, use has been made of a level-set algorithm for the scalar  $\bar{G}$  in which  $\bar{G}$  is defined as the distance to the mean premixed flame front position. The solution for  $\bar{G}$  was found as the steady-state solution of a time-dependent equation, i.e. the level-set equation. The instantaneous value for  $G$  is defined as the distance to the instantaneous premixed flame front in the direction perpendicular to the zero level-set of  $\bar{G}$ . By using this definition for  $G$ ,  $|\nabla\bar{G}|$  is equal to 1. However, with this definition, the time-dependent  $|\nabla G|$  is by no means equal to 1 at all time. The mean value for  $|\nabla G|$  is called the flame surface area ratio and it increases with increasing turbulence intensity (see Appendix E).

An additional equation was introduced for the speed function  $F$ . By simultaneously solving this equation for  $F$  with the level-set equation, the magnitude of the gradient in  $\bar{G}$  is kept equal to 1. Unlike the boundary conditions for other scalar quantities, the boundary conditions for  $F$  and  $\bar{G}$  are not given at the boundary of the computational domain but at the zero level set of  $\bar{G}$ . At the zero level set of  $\bar{G}$ , the speed function  $F$  is prescribed by the conditioned flow velocities and local laminar burning velocity. Values for  $F$  and  $\bar{G}$  at the boundary of the computational domain are given by the fact that  $|\nabla\bar{G}|$  should remain equal to 1.

For the turbulent burning velocity, a model expression given by Peters (1997) was used. This expression covers the small-scale and large-scale turbulence regime already recognized by Damköhler (1940). Numerical results as well as measurement data given by Wu *et al.* (1990) revealed a clear influence of the Markstein number. Compared to measurement data given by Wu *et al.* (1990) a reasonably good correspondence was found for the predicted flame brush thickness and flame length.



### Lifted flames

In Chapter 7, triple flames were considered to be the key element in the stabilization mechanism of lifted flames. A triple flame is a combination of a premixed flame and a diffusion flame. The flamelet formulations for premixed combustion and non-premixed combustion were used in combination with the standard  $k-\varepsilon$  turbulence model for calculating a lifted flame. The influence of a non-homogenous mixture fraction field was incorporated into the used expression for the turbulent burning velocity. Predicted lift-off heights compared quite well to measurement data given by Schefer *et al.* (1998).

The boundary conditions for the diffusion flame within the triple flame are different from those applied in the diffusion flamelet computations, i.e. the mixture fraction does not extend from pure air to pure fuel. Also, at the triple point, there is a strong deviation from one-dimensional behaviour. Therefore, the use of one-dimensional diffusion flamelets for describing the triple flamelet structure is not really justified. However, for the lift-off height predictions of Chapter 7, the propagation velocity of the premixed flame front is most important and therefore the used expression for the turbulent burning velocity has the largest influence on the predicted lift-off height.

Downstream of the triple-point, there will be a point where the lean premixed flame branch reaches its lean burning limit. At this point, the equation for the progress variable reduces to a source free transport equation similar to that for the mixture fraction. Therefore, downstream of this point, the use of the  $G$ -equation model is not needed. However, in the present study, a decomposition of the calculation domain into a domain where use is made of the  $G$ -equation model and a domain where a solution for  $c$  is directly obtained from its source free transport equation has not been used, because attention has been limited to the stabilization region only.

Since the phenomenon of turbulent combustion is non-linear, dependent on initial conditions there is often more than one solution to the equations. For example, a burning and non-burning solution may both coexist at the same Reynolds number. There may also be a regime in which a stabilized and a non-stabilized flame solution coexist. In Chapter 5, the stabilized solution was forced by a pilot flame, however, also a lifted-flame solution like that obtained in Chapter 7 might coexist.

## **8.3 FUTURE DIRECTIONS**

Computational fluid dynamics employing two-equation ( $k-\varepsilon$ ) and Reynolds-stress closure modelling is an important tool in the design of many flow machines, from pumps to aeroplanes. However, a universal solution to the turbulence closure problem still seems a long way off. One-point closure models such as the  $k-\varepsilon$  model are applicable to a fairly wide range of flows, while other flows will need two-point closure models and the remainder will need a Large Eddy Simulation (LES). Also in the stabilization mechanism of lifted turbulent jet diffusion flames, large-scale dynamics seem to play an important role. LES with subgrid-scale (SGS) modelling for the fine scales of the flame front may be a possible approach for modelling these features in future research.

More experiments and direct numerical simulations (DNS) are needed to clarify the modelling issues of for example the lifted flame stabilisation mechanism. From these experiments and simulations it may then be possible to extract the relevant parameters to be used as input to a detailed kinetic calculation. Experts in the field of experiments, DNS and turbulent combustion modelling need to debate on the design of (numerical or physical) experiments needed for

turbulent combustion research. Often, experts in DNS have little experience in turbulent combustion and are unlikely to choose the most interesting cases to be simulated. Another problem is that still too many of the existing data bases are accessible only to those that generated them and the few that can afford to expend a large amount of time to unravel the highly specialized form in which they are stored. It is important that the existing data bases, and the new ones generated, be made available to any interested combustion scientist in a form in which they can be readily post-processed. The internet is becoming more and more important in providing us an efficient way for distributing these data bases.



## References

- Abdel-Gayed, R.G., Bradley, D. (1981). A two-eddy theory of premixed turbulent flame propagation. *Phil. Trans. R. Soc. Lond.*, Vol. A301, No. 1457, pp. 1-25.
- Abdel-Gayed, R.G., Bradley, D. and Lawes, M. (1987) Turbulent burning velocities: a general correlation in terms of straining rates. *Proc. R. Soc. Lond. A* 414, pp. 389-413.
- Abdel-Gayed, R.G., Bradley, D. and Lau, A.K.C. (1988). The straining of premixed turbulent flames. 22-nd Symposium (International) on Combustion, pp. 731-738.
- Acharya, Y.V.G. (1954). Momentum transfer and heat diffusion in the mixing of coaxial turbulent jets surrounded by a pipe. Ph.D. Thesis, Delft University of Technology.
- Aldredge, R.C. (1995). The scalar-field front propagation equation and its applications Cited in: *Modeling in combustion science*. Editors: Buckmaster, J.D. and Takeno, T. *Lecture Notes In Physics*, Vol. 449, Springer-Verlag, Berlin, pp. 23-35.
- Ashurst, Wm. T. (1997). Cited in: *Four Lectures on Turbulent Combustion*. Editor: Peters, N. ERCOFTAC Summer School, Aachen, Germany.
- Balakrishnan, G., Smooke, M.D., Williams, F.A. (1995). A numerical investigation of extinction and ignition limits in laminar nonpremixed counterflowing hydrogen-air streams for both elementary and reduced chemistry. *Combustion and Flame*, Vol. 102, pp. 231-237.
- Barlow, R.S. and Chen, J.-Y. (1992). On transient flamelets and their relationship to turbulent methane-air jet flames. 24-th Symposium on Combustion, pp. 231-237.
- Batchelor, G.K., Bondi, H. (1956). *The theory of homogeneous turbulence*. Cambridge, at the University Press.
- Baz, A. el, Craft, T.J., Ince, N.Z. and Launder, B.E. (1993). On the adequacy of the thin-shear-flow equations for computing turbulent jets in stagnant surroundings. *Int. J. Heat and Fluid Flow*, Vol. 14, No. 2, pp. 164-169.
- Becker, H.A., Hottel, H.C. and Williams, G.C. (1976). The nozzle-fluid concentration field of the round, turbulent, free jet. *J. Fluid Mech.* 30, pp. 285-303.
- Beguier, C., Dekeyser, I. And Launder, B.E. (1978). Ratio of scalar and velocity dissipation time scales in shear flow turbulence. *Phys. Fluids* 21:307-310.
- Berkenbosch, A.C. (1995). Capturing detonation waves for the reactive Euler equations. Ph.D. Thesis, Eindhoven University of Technology.
- Bilger, R.W. (1994). Future directions in turbulent combustion research. *Combust. Sci. And Techn.*, Vol. 98, pp. 223-228.
- Birch, A.D., Brown, D.R., Dodson, M.G., Thomas, J.R. (1978). The turbulent concentration field of a methane jet. *J. Fluid Mech.* 88, pp. 431-449.
- Bird, R.B., Stewart, W.E. and Lightfoot, E.N. (1960). *Transport Phenomena*. John Wiley & Sons, Inc., London.
- Bish, Eric S., Dahm, Werner J.A. (1995). Strained dissipation and reaction layer analyses of nonequilibrium chemistry in turbulent reacting flows. *Combust. Flame*, Vol. 100, pp. 457-464.
- Boll, R.H.H.F. (1997). Experimental analyses of a turbulent jet surrounded by a co-flow. Thesis, Eindhoven University of Technology.
- Boll, R.H.H.F., Ovink, R., Lamers, A. (1997) Experimental study of mixing of two co-axial confined jets in a cold model furnace. *Proceedings of Eurotherm seminar No. 54 on Compact Fired Heating Units*, Leuven, Belgium.

- Bourlioux, A. (1995). A coupled level-set volume of fluid algorithm for tracking material interfaces. Sixth International Symposium on Computational Fluid Dynamics, Lake Tahoe
- Bradley, D. (1992). How fast can we burn? Twenty-Fourth Symposium (International) on Combustion/The Combustion Institute, pp. 247-262.
- Bradley, D., Gaskell, P.H. and Gu, X.J. (1994). Application of a Reynolds stress, stretched flamelet, mathematical model to computations of turbulent burning velocities and comparison with experiments. *Combustion and Flame*, Vol. 96, pp. 221-248.
- Bray, K.N.C. (1990). Studies of turbulent burning velocity. *Proc. R. Soc. Lond. A* 431, pp. 315-335.
- Bray, K.N.C., Champion, M. and Libby, P.A. (1991). Premixed flames in stagnating turbulence: Part I. The general formulation for counterflowing streams and gradient models for turbulent transport. *Combustion and Flame*, Vol. 84, pp. 391-410.
- Bray, K.N.C., Peters, N. (1994a). Laminar flamelets in turbulent flames. In: *Turbulent Reactive Flows*. Editors: Libby, P.A. and Williams, F.A. Academic Press, New York, pp. 63-113.
- Bray, K.N.C. and Libby, P.A. (1994b). Recent developments in the BML model of premixed turbulent combustion. In: *Turbulent Reactive Flows*. Editors: Libby, P.A. and Williams, F.A. Academic Press, New York, pp. 115-151.
- Bremhorst, K. (1985). Effect of fluid temperature on hot-wire anemometers and an improved method of temperature compensation and linearisation without use of small signal sensitivities. *J. Phys. E: Sci. Instrum.*, Vol. 18.
- Bremhorst, Klaus (1993). Some past contributions to hot/cold-wire anemometry measurements in heated flows: where to from here? FED-Vol. 167, *Thermal Anemometry - 1993 ASME* 1993.
- Browne, L.W.B., Antonia, R.A. and Chua, L.P. (1989). Calibration of X-probes for turbulent flow measurements. *Exp. In Fluids*, Vol. 7, pp. 201-208.
- Bruun, H.H., Nabhani, N., Fardad, A.A., Al-Kayiem, H.H. (1990). Velocity component measurements by X hot-wire anemometry. *Meas. Sci. Technol.*, Vol. 1, pp. 1314-1321.
- Bruun, H.H. (1995). *Hot-wire anemometry, principles and signal analysis*. Oxford University Press, Oxford.
- Buch, K.A. and Dahm, W.J.A. (1996). Experimental study of the fine-scale structure of conserved scalar mixing in turbulent shear flows. Part 1. *Scv1. J. Fluid Mech.*, Vol. 317, pp. 21-71.
- Buckmaster, J.D. (1985). *The mathematics of combustion*. SIAM, Philadelphia.
- Buckmaster, J.D., Peters, N. (1986). The infinite candle and its stability-a paradigm for flickering diffusion flames. Twenty-First Symposium (International) on Combustion/The Combustion Institute, pp. 1829-1836.
- Buresti, G., Talamelli, A. and Petagna, P. (1994). Experimental characterization of the velocity field of a coaxial jet configuration. *Experimental Thermal and Fluid Science*, Vol. 9, pp. 135-146.
- Burke, S.P. and Schumann, T.E.W. (1928). Diffusion flames. *Industrial and Engineering Chemistry*, Vol. 20, pp. 998-1004.
- Cant, R.S., Pope, S.B. and Bray, K.N.C. (1990). Modelling of flamelet surface-to-volume ratio in turbulent premixed combustion. 23<sup>rd</sup> Symp. (Int.) on Combustion, pp. 809-815. The Combustion Institute, Pittsburgh.
- Capp, S.P., Hussein, H.J. and George, W.K. (1990). Velocity measurements in a high Reynolds number momentum conserving axisymmetric turbulent jet. Tech. Rep. 123, Turbulence Research Laboratory Univ. at Buffalo SUNY.

- Cenedese, A., Doglia, G., Romano, G.P., De Michele, G. and Tanzini, G. (1994). LDA and PIV velocity measurements in free jets. *Experimental Thermal and Fluid Science*, Vol. 9, pp. 125-134.
- Champagne F.H., Sleicher C.A. and Wehrmann O.H. (1982). Turbulence measurements with inclined hot-wires. *J. Fluid Mech.*, Vol. 119, pp. 155-172.
- Chan, S.H., Pan, X.C., Abou-Ellail, M.M.M. (1995). Flamelet structure of radiating CH<sub>4</sub>-air flames. *Combustion and Flame*, Vol. 102, pp. 438-446.
- Chang, F. and Dhir, V.K. (1994). Turbulent flow field in tangentially injected swirl flows in tubes. *Int. J. Heat and Fluid Flow*, Vol. 15, No. 5, pp. 346-356
- Cheesewright, R. (1972). The application of digital techniques to hot-wire anemometry in highly turbulent flows. *Proc. Conf. on Fluid Dynamic Measurements in the Industrial and Medical Environment*, pp. 145-151, Leicester University.
- Chen, Yung-Cheng, Peters, N., Schneemann, G.A., Wruck, N., Renz, U., Mansour, M.S. (1996). The detailed flame structure of highly stretched turbulent premixed methane-air flames. *Combustion and flame*, Vol. 107, pp. 223-244.
- Clavin, P. and Williams, F.A. (1982). Effects of molecular diffusion and of thermal expansion on the structure and dynamics of premixed flames in turbulent flows of large scale and low intensity. *J. Fluid Mech.*, Vol. 116
- Clavin, P. (1985). Dynamic Behaviour of Premixed Flame Fronts in Laminar and Turbulent Flows, *Prog. Energy Combust. Sci.*, Vol. 11.
- Crauford, N.L., Liew, S.K. and Moss, J.B. (1985). Experimental and numerical simulation of a buoyant fire. *Combust. Flame*, Vol. 61, pp. 63-77.
- Damköhler, G. (1940). *Z. Elektrochem.*, Vol. 46, pp. 601-652. English translation: NACA Techn. Memo., No. 1112 (1947).
- Davis, M.R. and Rekrshanandana, P. (1994). Integral scales and mixing lengths in turbulent mixing and combustion. *Experimental Thermal and Fluid Science*, Vol. 8, pp. 239-244.
- Dixon-Lewis, G., David, T., Gaskell, P.H., Fukutani, S., Jinno, H., Miller, J.A., Kee, R.J., Smooke, M.D., Peters, N., Effelsberg, E., Warnatz, J., Behrendt, F. (1984). Calculation of the structure and extinction limit of a methane-air counterflow diffusion flame in the forward stagnation region of a porous cylinder. 20-th Symposium on Combustion, pp. 1893-1904.
- Doormaal, J.P. van and Raithby, G.D. (1984). Enhancements of the Simple method for predicting incompressible fluid flows. *Numerical Heat Transfer*, Vol. 7, pp. 147-163
- Dryden, H.L., Schubauer, G.B., Mock, W.C. Jr., and Skramstad, H.K. (1937). *Natl. Advisory Comm. Aeronaut. Tech. Repts. No. 581.*
- Duclos, J.M. and Veynante, D. (1993). A comparison of flamelet models for premixed turbulent combustion. *Combustion and flame*, Vol. 95, pp. 101-117.
- Echekki, T., Chen, J.H. (1996). Unsteady strain rate and curvature effects in turbulent premixed methane-air flames. *Combustion and flame*, Vol. 106, pp. 184-202.
- Embid, Pedro F., Majda, Andrew J., Souganidis, Panagiotis E. (1995). Comparison of turbulent flame speeds from complete averaging and the  $G$ -equation. *Phys. Fluids* 7 (8), pp. 2052-2060.
- Everest, David A., Driscoll, James F., Dahm, J.A., Feikema, Douglas A. (1995). Images of the two-dimensional field and temperature gradients to quantify mixing rates within a non-premixed turbulent jet flame. *Combustion and Flame*, Vol. 101, pp. 58-68, 1995.
- Favre, A.J., Gaviglio, J.J., and Dumas, R. (1957). Space-time double correlations and spectra in a turbulent boundary layer. *J. Fluid Mech.*, Vol. 2, pp. 313-342.

- Fedotov, S.P. (1996). Stochastic description of premixed turbulent combustion in terms of a coarse-grained flame surface density. *Combustion and Flame*, Vol. 106, pp. 369-376.
- Fedotov, S.P. (1997). *G*-equation, stochastic control theory and relativistic mechanics of a particle moving in a random field. *Combust. Theory Modelling*, Vol. 1, L1-L6.
- Furukawa, J., Maruta, K. And Hirano, T. (1998). Flame front configuration of turbulent premixed flames. *Combustion and flame*, Vol. 112, pp. 293-301.
- Galen, R.A.M.L. (1994). Design of a modular multichannel hot-wire anemometer system. Thesis, Eindhoven University of Technology.
- George, W.K. and Capp, S.P. (1988). A study of the turbulent axisymmetric jet. *J. Eng. Sci. King Saud Univ.*, Vol. 14, pp. 85-93.
- Germano, M. (1996). The statistical meaning of the Boussinesq approximation in terms of the Favre averages. *ERCOFTAC Bulletin*, Vol. 28, pp. 59-60.
- Girimaji, S.S. (1991). Assumed  $\beta$ -pdf model for turbulent mixing: validation and extension to multiple scalar mixing. *Combust. Sci. and Technol.*, Vol. 78, pp. 177-196.
- Glassman, I. (1987). *Combustion*. Academic Press, Inc., San Diego, California.
- Graham, L.J.W. and Bremhorst, K. (1990). A linear compensation technique for inclined hot-wire anemometers subjected to fluid temperature changes. *Meas. Sci. Technol.*, Vol. 1, pp. 1322-1325.
- Graham, L.J.W. and Bremhorst, K. (1991). Instantaneous time-constant adjustment of cold-wires acting as resistance thermometers when using multi-wire anemometer probes. *Meas. Sci. Technol.*, Vol. 2, pp. 238-241.
- Habib, M.A. and Whitelaw, J.H. (1979). Velocity characteristics of a confined coaxial jet. *Journal of Fluids Engineering*, Vol. 101, pp. 521-529.
- Habib, M.A. and Whitelaw, J.H. (1980). Velocity characteristics of confined coaxial jets with and without swirl. *Journal of Fluids Engineering*, Vol. 102, pp. 47-53.
- Hanjalic, K., Launder, B.E. (1972). A Reynolds stress model and its applications to thin shear flow. *J. Fluid Mech.*, Vol. 52, pp. 609-638.
- Hanjalic, K. (1994). Advanced turbulence closure models: a view of current status and future prospects. *Int. J. Heat and Fluid Flow*, Vol. 15, No. 3, pp. 178-203.
- Hernandez, J., Crespo, A., Duijm, N.J. (1995). Numerical modeling of turbulent jet diffusion flames in the atmospheric surface layer. *Combustion and Flame*, Vol. 101, pp. 113-131.
- Hinze, J.O. (1959). *Turbulence: an introduction to its mechanism and theory*. McGraw-Hill, New York.
- Im, H.G., Bechtold, J.K. and Law, C.K. (1995). Counterflow diffusion flames with unsteady strain rates. *Combust. Sci. and Tech.*, Vol. 106, pp. 345-361.
- Inage, S.-I. and Ohtsuka, M. (1996). A proposal for a new turbulent premixed combustion model and its evaluation (development of the model). *JSME International Journal, Series B*, Vol. 39, No. 3.
- Johnson, F.D. and Eckelmann, H. (1984). A variable angle method of calibration for X-probes applied to wall-bounded turbulent shear flow. *Exp. In Fluids*, Vol. 2, pp. 121-130.
- Jones, W.P., Launder, B.E. (1972). The prediction of laminarisation with a two-equation turbulence model. *Int. J. Heat Mass Transfer*, Vol. 15, pp. 301-314.
- Jörgenson F.E. (1971). Directional sensitivity of wire and fibre film probes. *DISA Info* 11.
- Karpov, V.P., Lipatnikov, A.N., Wolanski, P. (1997). Finding the Markstein Number Using the Measurements of Expanding Spherical Laminar Flames. *Combust. Flame*, Vol. 109, pp. 436-448.

- Keagy, W.R. and Weller, A.E. (1950). A study of freely expanding inhomogeneous jets. Proc. Heat Transf. Fluid Mech. Inst. 1-3, pp. 89-98.
- Keller, P. (1996). Berechnungen der Turbulenten Flammenausbreitung bei der Ottomotorischen Verbrennung mit einem Flamelet-Modell. Ph. D. Thesis, Technischen Hochschule Aachen, Germany.
- Kennedy, I.M. and Kent, J.H. (1979). Measurements of a conserved scalar in turbulent jet diffusion flames. 17-th Symposium on Combustion, pp. 279-287.
- Kennedy, I.M. and Kent, J.H. (1981). Scalar measurements in a co-flowing turbulent diffusion flame. Combust. Sci. and Techn., Vol. 25, pp. 109-119.
- Kennedy, L.A. (1978). Turbulent combustion : selected technical papers. Progress in astronautics and aeronautics, Vol. 58. American Institute of Aeronautics and Astronautics.
- Kent, J.H. and Bilger, R.W. (1973). Turbulent diffusion flames. 14-th Symposium on Combustion, pp. 615-625.
- Kent, J.H. and Bilger, R.W. (1977). The prediction of turbulent diffusion flame fields and nitric oxide formation. 16-th Symposium on Combustion, pp. 1643-1656.
- Kerstein, A.R., Ashurst, W.T., Williams, F.A. (1988). Field Equation for Interface Propagation in an Unsteady Homogeneous Flow Field. Physical Review A, Vol. 37, No. 7, pp. 2728-2731.
- Khalil, K.H., El-Mahallawy, F.M. and Khalil, E.E (1978). Flow, mixing and heat transfer in furnaces : selection from papers presented at the 1st conference on mechanical power engineering, Cairo. MHT-the science and applications of heat and mass transfer, Vol. 2. Pergamon Press, Oxford.
- Kim, J.S., Williams, F.A. (1993). Structures of Flow and Mixture-Fraction Fields for Counterflow Diffusion Flames with Small Stoichiometric Mixture Fractions. SIAM J. Appl. Math., Vol. 53, pp. 1551-1556.
- Kuo, K.K.-Y. (1986). Principles of combustion. Wiley-Interscience, Chichester.
- Lamers, A.P.G.G. and Sanders, J.P.H. (1990a). Tijds gemiddelde behoudsvergelijkingen en het  $k-\epsilon$  model. Eindhoven University of Technology.
- Lamers, A.P.G.G. and Sanders, J.P.H. (1990b). Waarschijnlijkheidsdichtheidsfunctie in de vorm van 2 Delta-Dirac functies. Eindhoven University of Technology.
- Lasher, W.C. and Taulbee, D.B. (1992). On the computation of turbulent backstep flow. Int. J. Heat and Fluid Flow, Vol. 13, No. 1, pp. 30-40.
- Lasher, W.C. and Taulbee, D.B. (1994). Reynolds stress model assessment using round jet experimental data. Int. J. Heat and Fluid Flow, Vol. 15, No. 5, pp. 357-363.
- Laufer, J. (1954). Cited in Hinze, J.O. (1975), Turbulence, McGraw-Hill, New York, 2<sup>nd</sup> edition, pp. 520-524.
- Launder, B.E., Morse, A., Rodi, W. and Spalding, D.B. (1972). The prediction of free shear flows -A comparison of the performance of six turbulence models. Proceedings of NASA Conference on Free Shear Flows, Langley (Also Imperial College Mechanical Engineering Department Report TM/TN/A/19).
- Law, C.K., Cho, P., Mizomoto, M. and Yoshida, H. (1986). Flame curvature and preferential diffusion in the burning intensity of bunsen flames. Twenty-first Symposium (International) on Combustion/The Combustion Institute, pp. 1903-1809.
- Law, C.K. (1993). A compilation of recent experimental data of premixed laminar flames. In: Reduced kinetic mechanisms for applications in combustion systems. Editors: Peters, N. and Rogg, B.



- Lee, T.-W., Shankland, R. and Fenton, M. (1995). Flame curvature statistics in axisymmetric turbulent jet flames. *Combust. Sci. and Tech.*, Vol. 108, pp. 31-46.
- Lehmann, B. and Mante, J. (1994). A two-component Laser-Doppler scanning technique for the analysis of unsteady flow fields and turbulent structures. *Experimental Thermal and Fluid Science*, Vol. 9, pp. 111-118.
- Lewis, B., Elbe, G.v. (1943) Stability and structure of burner flames, *J. Chem. Phys.*, Vol. 11, pp. 75-97
- Lesieur, M. (1990). *Turbulence in Fluids*. Kluwer Academic Publishers, Dordrecht.
- Libby, P.A. (1996). *Introduction to turbulence*. Taylor & Francis, Washington, D.C.
- Libby, P.A. and Economos, C. (1963). A flame zone model for chemical reaction in a laminar boundary layer with application to the injection of hydrogen-oxygen mixtures. *Int. J. Heat Mass Transfer*, Vol. 6, pp. 113-128.
- Libby, P.A. and Williams, F.A. (1980). *Turbulent reacting flows*. Topics in applied physics, Vol. 44. Springer, Berlin.
- Libby, P.A. and Williams, F.A. (1987). Premixed laminar flames with general rates of strain. *Combust. Sci. And Tech.*, Vol. 54, pp. 237-273.
- Libby, P.A. and Williams, F.A. (1994). *Turbulent reacting flows (Combustion treatise)*. Academic Press, London.
- Libby, P.A. (1996). *Introduction to turbulence*. Taylor and Francis, Washington D.C.
- Libby, P.A., Bray, K.N.C. and Moss, J.B. (1979). Effects of finite reaction rate and molecular transport in premixed turbulent combustion. *Combustion and Flame*, Vol. 34, pp. 285-301.
- Linan, A. and Williams, F.A. (1993). *Fundamental aspects of combustion*. The Oxford engineering science series, Vol. 33. Oxford University Press, Oxford.
- Lockwood, F.C. and Moneib, H.A. (1980). Fluctuating temperature measurements in a heated round free jet. *Combustion Science and Technology*, Vol. 22, pp. 63-81.
- Louch, D.S. (1995). A different physical interpretation of flame sheet surface density. *Combust. Sci. and Techn.*, Vol. 108, pp. 81-90.
- Lueptow, R.M., Breuer, K.S. and Haritonidis, J.H. (1988). Computer-aided calibration of X-probes using a look-up table. *Exp. in fluids*, Vol. 6, pp. 115-118.
- Mansour, M.S., Chen, Y-C. and Peters, N. (1992). The reaction zone structure of turbulent premixed methane-helium-air flames near extinction. *Twenty-Fourth Symposium (International) on Combustion/The Combustion Institute*, pp. 461-468.
- Markstein, G.H. (1964). *Nonsteady flame propagation*. Pergamon Press, London.
- Maury, F.A., Libby, P.A. (1995). Nonpremixed flames in stagnating turbulence part I- the  $k-\epsilon$  theory with equilibrium chemistry for the methane-air system. *Combustion and Flame*, Vol. 102, pp. 341-356.
- Mauß, F., Keller, D. and Peters, N. (1990). A lagrangian simulation of flamelet extinction and re-ignition in turbulent jet diffusion flames. *23-rd Symposium on Combustion*, pp. 693-698.
- Mauß, F. and Peters, N. (1993). Reduced kinetic mechanisms for premixed methane-air flames In: *Reduced kinetic mechanisms for applications in combustion systems*. Editors: Peters, N. and Rogg, B.
- McComb W.D. (1990) *The physics of fluid turbulence*. Clarendon Press, Oxford.
- Mehta, R.V. (1985). *Experimental study of turbulent mixing and selectivity of competing reactions*. Thesis, Pennsylvania State University.

- Meier, W., Prucker, S., Cao, M.-H. and Stricker, W. (1996) Characterization of turbulent  $H_2/N_2$ /air jet diffusion flames by single-pulse spontaneous Raman scattering. *Combust. Sci. and Techn.*, Vol. 118, pp. 293-312.
- Mell, W.E., Nilsen, V., Kosály, G., Riley, J.J. (1994). Investigation of closure models for nonpremixed turbulent reacting flows. *Phys. Fluids*, Vol. 6, No. 3.
- Muñiz, L. and Mungal, M.G. (1997). Instantaneous flame-stabilization velocities in lifted-jet diffusion flames. *Combustion and flame*, Vol. 111, pp. 16-31.
- Müller, C.M., Breitbach, H., Peters, N. (1994a). Partially Premixed Turbulent Flame Propagation in Jet Flames. Twenty-Fifth Symposium (International) on Combustion, pp. 1099-1106. The Combustion Institute, Pittsburgh.
- Müller, C.M. (1994b). Numerische simulation instationärer, turbulenter freistrahldiffusionsflammen mit dem flamelet-modell. Ph.D. Thesis, Technische Hochschule Aachen.
- Müller, U.R. (1982). On the accuracy of turbulence measurements with inclined hot wires. *J. Fluid Mech.*, Vol. 119, pp. 155-172.
- Murthy, S.N.B. (1975). Turbulent mixing in nonreactive and reactive flows. Project SQUID workshop, West Lafayette, Ind. proceedings by Project SQUID. Plenum Press, New York.
- Nagago, Y. and Tsuji, T. (1994). Recent developments in hot- and cold-wire techniques for measurements in turbulent shear flows near walls. *Experimental thermal and fluid science*, Vol. 9, pp. 94-110.
- Naus, I.M.M.M.C. (1998) Application of hot-wire anemometry in a free turbulent jet. Thesis, Eindhoven University of Technology.
- Nho, E. Le Huu and Béguier, C. (1995). Velocity measurements in 3D turbulent flows by means of a rotating X-wire probe. *Meas. Sci. Technol.*, Vol. 6, pp. 843-850.
- Nikuradse, J. (1932). Cited in Schlichting, H. and Gersten, K. (1997), *Grenzschicht-Theorie*, Springer-Verlag, Berlin Heidelberg, 9nd edition, pp. 15.
- Nilsen, P.J. and Andersson, H.I. (1994). Developing turbulent flow in a rotating channel. *Int. J. Heat and Fluid Flow*, Vol. 15, No. 2, pp. 100-103.
- Ovink, R. and Lamers, A. (1998). Modelling and calculation of a partially premixed turbulent flame. Submitted to *Combustion Science and Technology*.
- Panchapakesan, N.R. and Lumley, J.L. (1993). Turbulence measurements in axisymmetric jets of air and helium. Part 1. Air jet. *J. Fluid Mech.*, Vol. 246, pp. 197-223.
- Parchen, R.R. (1993). Decay of swirl in turbulent pipe flows. Ph.D. Thesis, Eindhoven University of Technology.
- Patankar, S.V. (1980). Numerical heat transfer and fluid flow. Series in computational and physical processes in mechanics and thermal. Hemisphere, London.
- Payne, F.R. and Lumley, J.L. (1966). One dimensional spectra derived from an airborne hot-wire anemometer. *Q. J. Roy. Met. Soc.*, Vol. 92, pp. 397-401.
- Peeters, T.W.J. (1995). Numerical modeling of turbulent natural-gas diffusion flames. Ph.D. Thesis, Delft University of Technology.
- Perry, A.E. (1982). Hot-wire anemometry. Clarendon Press, Oxford.
- Peters, N. (1979). Premixed burning in diffusion flames -the flame zone model of libby and ekonomos. *Int. J. Heat Mass Transfer*, Vol. 22, pp.691-703.
- Peters, N. and Williams, F.A. (1983). *AIAA J.*, Vol. 21, pp. 423-429.
- Peters, N. (1983). Local quenching due to flame stretch and non-premixed turbulent combustion *Combustion Science and Technology*, Vol. 30, pp. 1-17.

- Peters, N. (1984a). Laminar diffusion flamelet models in non-premixed turbulent combustion. *Prog. Energy Combust. Sci.*, Vol. 10, pp. 319-339.
- Peters, N. (1984b). Partially premixed diffusion flamelets in non-premixed turbulent combustion. 20-th Symposium on Combustion, pp. 353-360.
- Peters, N. (1986). Laminar flamelet concepts in turbulent combustion. 21-th Symposium on Combustion, pp. 1231-1250.
- Peters, N. (1992). A spectral closure for premixed turbulent combustion in the flamelet regime. *J. Fluid Mech.*, Vol. 242, pp. 611-629.
- Peters, N. and Rogg, B. (1993). Reduced kinetic mechanisms for applications in combustion systems. Springer-Verlag, Berlin Heidelberg.
- Peters, N. (1994). Turbulente Brenngeschwindigkeit. DFG-Abschlußbericht zum Forschungs vorhaben Pe 241/9-2.
- Peters, N. (1997). Four Lectures on Turbulent Combustion. ERCOFTAC Summer School, Aachen, Germany.
- Pirumov, U.G. and Roslyakov, G.S. (1986). Gas flow in nozzles. Springer Series in Chemical Physics, Vol. 29. Springer-Verlag, Berlin Heidelberg.
- Pitts, W.M. and Kashiwagi, T. (1984). The application of laser-induced Rayleigh light scattering to the study of turbulent mixing. *J. Fluid Mech.*, Vol. 141, pp. 391-429.
- Pitts, W.M. (1988). Assessment of theories for the behavior and blowout of lifted turbulent jet diffusion flames. Twenty-Second Symposium (International) on Combustion, pp. 809-816. The Combustion Institute, Pittsburgh.
- Pitts, W.M. (1991). Effects of global density ratio on the centerline mixing behaviour of axisymmetric jets. *Exp. Fluids*, Vol. 11, pp. 125-134.
- Plessing, T., Terhoeven, P., Peters, N. and Mansour, M.S. (1998). An experimental and numerical study on a laminar triple flame. *Combustion and Flame*, Vol. 115, pp. 335-353.
- Pollard, A. and Siu, A.L.-W. (1982). The calculation of some laminar flows using various discretisation schemes. *Computer methods in applied mechanics and engineering*, Vol. 35, pp. 293-313.
- Prandtl, L. (1925). Über die ausgebildete turbulenz. *ZAMM*, Vol. 5, pp. 136-139.
- Press, W.H., Teukolsky, S.A., Vetterling, W.T. and Flannery, B.P. (1992). *Numerical Recipes in Fortran*. Cambridge University Press, Cambridge.
- Razinsky, E. and Brighton, J.A. (1971). Confined jet mixing for nonseparating conditions. *Journal of Basic Engineering*, pp. 333-335
- Reader-Harris, M.J. (1994). The decay of swirl in a pipe. *Int. J. Heat and Fluid Flow*, Vol. 15, No. 3, pp. 212-217.
- Reynolds, O. (1883). An experimental determination of the circumstances which determine whether the motion of water shall be direct or sinuous, and of the law of resistance on parallel channels. *Phil. Trans. R. Soc.* A175, pp. 935.
- Reynolds, O. (1895). On incompressible viscous flow and the determination of the criterion. *Phil. Trans. R. Soc.* A186, pp. 123.
- Richards, B.E. (1977). Measurement of unsteady fluid dynamic phenomena. Series in thermal and fluids engineering. Hemisphere Publ. Corp., McGraw-Hill.
- Richards, C.D. and Pitts, W.M. (1993). Global density effects on the self-preservation behaviour of turbulent free jets. *J. Fluid Mech.*, Vol. 254, pp. 417-435.
- Ricou, F.P. and Spalding, D.B. (1961). Measurement of Entrainment by axi-symmetrical turbulent jets. *J. Fluid Mechanics*, Vol. 11, pp. 21-32.

- Rodi, W. (1972). The predictions of free turbulent boundary layers by use of a 2-equation model of turbulence. Ph.D. Thesis, University of London.
- Rodi, W. (1975). A new method of analysing hot-wire signals in highly turbulent flow and its evaluation in a round jet. DISA Information, Vol. 17.
- Roekaerts, D. and van der Meer, Th. H. (1996). Statistical Properties of turbulent gaseous flames. ERCOFTAC Bulletin, Vol. 28, pp. 55-56.
- Rogg, B., Behrendt, F., Warnatz, J. (1986). Turbulent non-premixed combustion in partially premixed diffusion flamelets with detailed chemistry. 21-th Symposium on Combustion, pp. 1533-1541.
- Roshko, A. (1976). Structure of turbulent shear flows: a new look. AIAA Paper No. 76-78.
- Sampers, W.F.J. (1991). Experimental analysis of the swirling flow in a model of a tangentially fire furnace. Thesis, Eindhoven University of Technology.
- Sampers, W.F.J., Lamers, A.P.G.G. and Steenhoven, A.A.v. (1993). Analysis of experimental and numerical results of a turbulent swirling flow in a tube. Chem. Eng. Comm., Vol. 125, pp. 187-196.
- Sanders, J.P.H. en Lamers, A.P.G.G. (1990). Favre middeling en de modellering van een turbulente diffusievlam. Eindhoven University of Technology.
- Sanders, J.P.H. and Lamers, A.P.G.G. (1992). Scalar transport in a turbulent jet. Int. Comm. Heat Mass Transfer, Vol. 19, pp. 851-858.
- Sanders, J.P.H. (1994). Scalar transport and flamelet modelling in turbulent jet diffusion flames. Ph.D. Thesis, Eindhoven University of Technology.
- Santoro, R.J., Semerjian, H.G., Emmerman, P.J. and Goulard, R. (1981). Optical Tomography for flow field diagnostics. Int. J. Heat Mass Transfer, Vol. 24, pp. 1139-1150.
- Schefer, R.W., Namazian, M. and Kelly, J. (1990). CH, OH and CH<sub>4</sub> concentration measurements in a lifted turbulent-jet flame. SANDIA report SAND89-8806.
- Schefer, R.W. and Goix, P.J. (1998). Mechanism of flame stabilization in turbulent, lifted-jet flames. Combustion and Flame, Vol. 112, pp. 559-574.
- Schewe, J. And Ronneberger, D. (1990). Error-tolerant calibration of dual sensor probes used in a turbulent wall boundary layer. Exp. In Fluids, Vol. 9, pp. 285-289.
- Schlichting, H. (1965). Grenzschicht-Theorie - 5. erw. und neubearb. Aufl. (Wissenschaftliche Buecherei). Braun, Karlsruhe.
- Schlichting, H. and Gersten, K. (1997). Grenzschicht-Theorie, 9nd edition. Springer-Verlag, Berlin Heidelberg.
- Searby, G., Quinard, J. (1990). Direct and Indirect Measurements of Markstein Numbers of Premixed Flames. Combust. Flame, Vol. 82, pp. 298-311.
- Seshadri, K. and Peters, N. (1988). Asymptotic Structure and Extinction of Methane-Air Diffusion Flames. Combust. Flame, Vol. 73, pp. 23-44.
- Sethian, J.A. (1985). Curvature and the evolution of fronts. Commun. Math Phys., Vol. 101, pp. 487-499.
- Sethian, J.A. (1996). Level set methods. Evolving interfaces in geometry, fluid mechanics, computer vision, and materials science. Cambridge University Press, New York.
- Sheih, C.M., Tennekes, H., and Lumley, J.L. (1971). Airborne hot-wire measurements of the small-scale structure of atmospheric turbulence. Phys. Fluids, Vol. 14, pp. 201-215.
- Siggia, E.D. (1981). Numerical study of small-scale intermittency in three-dimensional turbulence. J. Fluid Mech., Vol. 107, pp. 375-406.

- Smallwood, G.J., Gülder, Ö.L., Snelling, D.R., Deschamps, B.M. and Gökalp, I. (1995). Characterization of flame front surfaces in turbulent premixed methane/air combustion. *Combustion and Flame*, Vol. 101, pp. 461-470.
- Smals, A.H.L. (1991). TEACH-T: een computerprogramma voor twee-dimensionale, turbulente, recirculerende stromingen. Eindhoven University of Technology.
- Smooke, M.D., Giovangigli, V. (1991) Formulation of the premixed and nonpremixed test problems. In: *Reduced kinetic mechanisms and asymptotic approximations for methane-air flames*. Editor: Smooke, M.D. Springer, Berlin, pp. 1-28.
- Spalding, D.B. (1971). Mixing and chemical reaction in steady confined turbulent flames. 13<sup>th</sup> Symposium (International) on Combustion, pp. 649-657. The Combustion Institute, Pittsburgh.
- Spalding, D.B. (1979). *Combustion and mass transfer : a textbook with multiple-choice exercises for engineering students*. Pergamon Press, Oxford.
- Stårner, S.H., Kelman, J.B., Masri, A.R. and Bilger, R.W. (1994). Multispecies measurements and mixture fraction imaging in turbulent diffusion flames. *Experimental thermal and fluid science*, Vol. 9, pp. 119-124.
- Stårner, S.H., Bilger, R.W., Long, M.B. (1995). A method for contour-aligned smoothing of joint 2D scalar images in turbulent flames. *Combust. Sci. and Tech.*, Vol. 107, pp. 195-203.
- Streb, H. (1993). *Untersuchungen zum Einfluß des Auftriebs auf die Mischung und Reaktion in turbulenten Freistrahldiffusionsflammen*. Ph.D. thesis, Universität Karlsruhe, Germany.
- Sun, C.J., Sung, C.J. and Law, C.K. (1997). Stretch effects in counterflow and propagating spherical flames. AIAA 97-0901, Reno.
- Sussman, M., Smereka, P., Osher, S. (1994). A Level Set Approach for Computing Solutions to Incompressible Two-Phase Flows. *Journ. Of Comp. Phys.*, Vol. 114, pp. 146-159.
- Swaminathan, M.K., Rankin, G.W. and Sridhar, K. (1986). Evaluation of the basic system of equations for turbulence measurements using the Monte Carlo technique. *J. Fluid Mech.*, Vol. 170, pp. 1-19.
- Takagi, Toshimi, Shin, Hyun-Dong, and Ishio, Akira (1981). Properties of turbulence in turbulent diffusion flames. *Combustion and Flame*, Vol. 40, pp. 121-140.
- Taylor, S.C. (1991). Ph.D. thesis, University of Leeds.
- Tseng, L.-K., Ismail, M.A., Faeth, G.M. (1993). Laminar burning velocities and Markstein numbers of hydrocarbon-air flames. *Combustion and Flame*, Vol. 95, pp. 410-426.
- Tutu, Narinder K. and Chevray, Rene (1975). Cross-wire anemometry in high intensity turbulence. *J. Fluid Mech.*, Vol. 71, No. 4, pp. 785-800.
- Vanquickenborne, L. and van Tiggelen, A. (1966). *Combust. Flame*, Vol. 10, pp. 59-69.
- Veynante, D., Verisch, L., Poinso, T., Liñán, A. and Ruetsch, G. (1994). Studying turbulence using numerical databases (V.P. Moin and W.C. Reynolds, Eds.). Center for turbulence Research, Stanford University, pp. 55-73.
- Videto, B.D. and Santavicca, D.A. (1990). Flame-turbulence interactions in a freely-propagating, premixed flame. *Combust. Sci. And Tech.*, Vol. 70, pp. 47-73.
- Vos, J.B. (1987). The calculation of turbulent reacting flows with a combustion model based on finite chemical kinetics. Ph.D. Thesis, Delft University of Technology.
- Wagner, T.C. and Kent, J.C. (1988). On the directional sensitivity of hot-wires: a new look at an old phenomenon. *Experiments in Fluids*, Vol. 6, pp. 553-560.
- Walker, D.A., Ng, W.F., Walker, M.D. (1989). Experimental comparison of two hot-wire techniques in supersonic flow. *AIAA Journal*, Vol. 27, No. 8, pp. 1074-1080.

- Warnatz, J. (1981). The structure of laminar alkane-, alkene-, and acetylene flames. Eighteenth Symposium (International) on Combustion, pp. 369-384.
- Warnatz, J., Maas, U., Dibble, R.W. (1996). Combustion. Springer-Verlag, Berlin.
- Westbrook, C.K. and Dryer, F.L. (1984). Chemical kinetic modeling of hydrocarbon combustion. Prog. Energy Combust. Sci., Vol. 10, pp. 1-57.
- Wick, D.P., Glauser, M.N. and Ukeiley, L.S. (1994). Investigation of Turbulent Flows via Pseudo Flow Visualisation Part I: Axisymmetric Jet Mixing Layer. Experimental Thermal and Fluid Science, Vol. 9, pp. 391-404.
- Williams, F.A. (1965). Combustion theory. Addison-Wesley Publishing Co., Amsterdam.
- Williams, F.A. (1985a). In: The Mathematics of Combustion, pp. 97-131. Editor: Buckmaster, J. SIAM, Philadelphia.
- Williams, F.A. (1985b). Combustion theory, second Edition. The Benjamin/Cummings Publishing Company, Inc., California.
- Willmarth, W.W. and Bogar, T.J. (1977). Survey and new measurements of turbulent structure near the wall. Phys. Fluids, Vol. 20, S9-S21.
- Wilson, R.A.M. and Danckwerts, P.V. (1964). Studies in turbulent mixing-II. A hot-air jet. Chemical Engineering Science, Vol. 19, pp. 885-895.
- Wirth, M., Peters, N. (1992). Turbulent Premixed Combustion: a Flamelet Formulation and Spectral Analysis in Theory and IC-Engine Experiments. Twenty-Fourth Symposium (International) on Combustion, pp. 493-501. The Combustion Institute, Pittsburgh.
- Wittmer, V. (1980). Geschwindigkeit und Temperatur in einer turbulenten Freistrahldiffusionsflammen. Ph.D. Thesis, Universität Karlsruhe, Germany.
- Wu, M.S., Kwon, S., Driscoll, J.F., Faeth, G.M. (1990). Turbulent Premixed Hydrogen/Air Flames at High Reynolds Numbers. Combust. Sci. And Tech., Vol. 73, pp. 327-250.
- Wynanski, I. and Fiedler, H. (1969). Some measurements in the self-preserving jet. J. Fluid Mech., Vol. 38, pp. 577-612.
- Yakhot, V., Orszag, S.A., Thangam, S., Gatski, T.B. and Speziale, C.G. (1992). Development of turbulence models for shear flows by a double expansion technique. Phys. Fluids A4, pp. 1510-1520.
- Yoshizawa, A. (1982). A statistically-derived subgrid model for the large-eddy simulation of turbulence. Phys. Fluids, Vol. 25, No. 9, pp. 1532-1538.
- Yoshizawa, A. (1984). Statistical analysis of the deviation of the Reynolds stress from its eddy-viscosity representation. Phys. Fluids, Vol. 27, No. 6, pp. 1377-1387.
- Yule, A.J., Damou, M. and Kostopoulos, D. (1993). Modeling confined jet flow. Int. J. Heat and Fluid Flow, Vol. 14, No. 1, pp. 10-17.
- Zijlema, M. (1996). Computational modeling of turbulent flow in general domains. Ph.D. Thesis, Delft University of Technology.
- Zilberman, M. (1981). On the interaction of transitional spots and generation of a synthetic turbulent boundary layer Ph.D. Thesis, Tel-Aviv University, Israel.



## Appendix A

### Measured mean velocity and temperature distributions in a turbulent jet

In this appendix, some more results are presented of measurements done in the high Reynolds number turbulent air jet discussed in Section 4.2.7. Figure A.1 shows the measured profiles of the axial mean velocity component at several axial distances from the nozzle exit. The spreading of the jet is clearly evident.

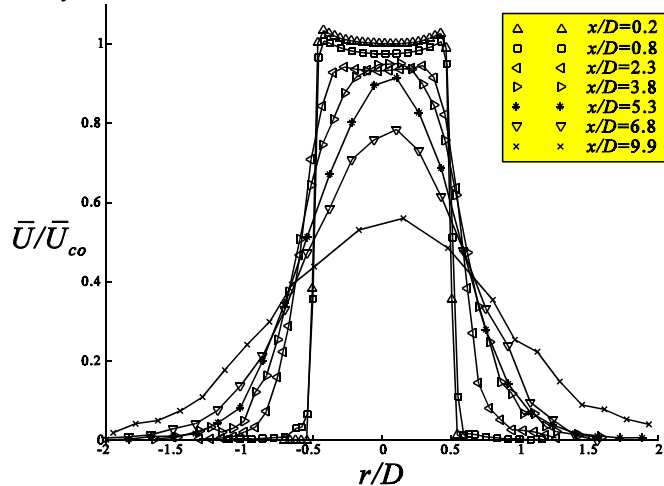


Figure A.1 Mean axial velocity profiles at various axial positions.

Figure A.2 shows the measured profiles of the radial mean velocity component at several axial distances. This figure shows a lot more scatter because the radial velocity component is very small compared to the axial velocity component. Therefore, a very small error in the probe angle adjustment results in a relative large error in the radial velocity component. With an axial velocity component of 20 m/s and a radial velocity component of 1 m/s, an error in the probe angle adjustment of only  $0.1^\circ$  would already lead to an error in the measured radial velocity component of 3.5%. That is also the reason why measurement results on the radial velocity component are not very often reported in literature. Nevertheless, Figure A.2 has been given here to demonstrate the accuracy of the present measurement method and to demonstrate the possibility of measuring the radial velocity component. A maximum value of 1.4 m/s was observed for  $\bar{V}$  at an axial position of 2.3 times the nozzle diameter. Also negative values for  $\bar{V}$  were observed in the outer flow region. These negative values are caused by the mass entrainment of the jet. Also in this plot, the spreading of the jet is clearly evident.



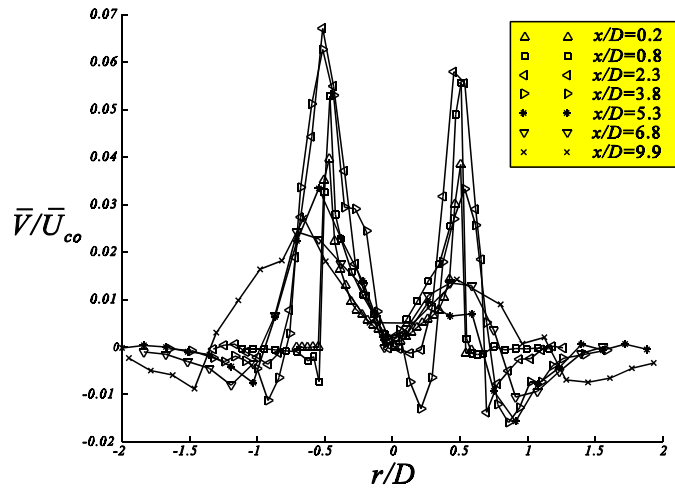


Figure A.2 Mean radial velocity component at various axial positions.

Figure A.3 shows the measured mean mixture fraction profiles at several axial stations. The mixture fraction is defined as a scaled function of the measured temperature (see Section 4.3). Figure A.3 shows the evolution of the radial distribution with distance from the nozzle exit. In downstream direction the centerline temperature drops and the radial distribution spreads out conform the spreading of the jet found in Figure A.1. Clearly the temperature distribution extends further in radial direction than the axial velocity distribution.

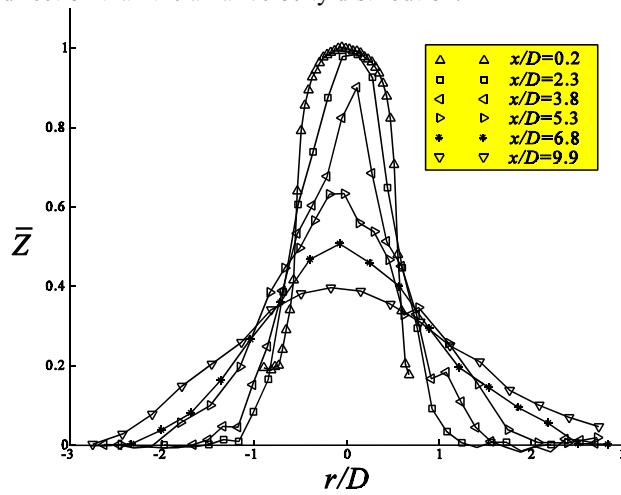


Figure A.3 Mean mixture fraction profiles at various axial positions.

## Appendix B

### Reaction mechanism

Number	Reaction	B [mole, cm <sup>-3</sup> , s]	$\alpha$	E [kJ/mole]
<b>H<sub>2</sub>-O<sub>2</sub> chain reactions</b>				
1	H+O <sub>2</sub> -OH+O	2.000E+14	0.00	70.300
2	OH+O-H+O <sub>2</sub>	1.568E+13	0.00	3.520
3	H <sub>2</sub> +O-OH+H	5.060E+4	2.67	26.300
4	OH+H-H <sub>2</sub> +O	2.222E+4	2.67	18.290
5	H <sub>2</sub> +OH-H <sub>2</sub> O+H	1.000E+8	1.60	13.080
6	H <sub>2</sub> O+H-H <sub>2</sub> +OH	4.312E+8	1.60	76.460
7	OH+OH-H <sub>2</sub> O+O	1.500E+9	1.14	0.420
8	H <sub>2</sub> O+O-OH+OH	1.473E+10	1.14	71.090
<b>HO<sub>2</sub> formation and consumption</b>				
9	H+O <sub>2</sub> +M'-HO <sub>2</sub> +M'	2.300E+18	-0.80	0.000
10	HO <sub>2</sub> +M'-H+O <sub>2</sub> +M'	3.190E+18	-0.80	195.390
11	HO <sub>2</sub> +H-OH+OH	1.500E+14	0.00	4.200
12	HO <sub>2</sub> +H-H <sub>2</sub> +O <sub>2</sub>	2.500E+13	0.00	2.900
13	HO <sub>2</sub> +OH-H <sub>2</sub> O+O <sub>2</sub>	6.000E+13	0.00	0.000
14	HO <sub>2</sub> +H-H <sub>2</sub> O+O	3.000E+13	0.00	7.200
15	H <sub>2</sub> O+O-OH+O <sub>2</sub>	1.800E+13	0.00	-1.700
<b>H<sub>2</sub>O<sub>2</sub> formation and consumption</b>				
16	HO <sub>2</sub> +HO <sub>2</sub> -H <sub>2</sub> O <sub>2</sub> +O <sub>2</sub>	2.500E+11	0.00	-5.200
17	OH+OH+M'-H <sub>2</sub> O <sub>2</sub> +M'	3.250E+22	-2.00	0.000
18	H <sub>2</sub> O <sub>2</sub> +M'-OH+OH+M'	1.692E+24	-2.00	202.29
19	H <sub>2</sub> O <sub>2</sub> +H-H <sub>2</sub> O+OH	1.000E+13	0.00	15.000
20	H <sub>2</sub> O <sub>2</sub> +OH-H <sub>2</sub> O+HO <sub>2</sub>	5.400E+12	0.00	4.200
21	H <sub>2</sub> O+HO <sub>2</sub> -H <sub>2</sub> O <sub>2</sub> +OH	1.802E+13	0.00	134.750
<b>Radical recombination</b>				
22	H+H+M'-H <sub>2</sub> +M'	1.800E+18	-1.00	0.000
23	OH+H+M'-H <sub>2</sub> O+M'	2.200E+22	-2.00	0.000
24	O+O+M'-O <sub>2</sub> +M'	2.900E+17	-1.00	0.000
<b>NO Production</b>				
25	N <sub>2</sub> +O-NO+N	1.900E+14	0.00	319.300
26	NO+N-N <sub>2</sub> +O	4.22047E+13	0.00	4.253
27	NO+H-N+OH	1.300E+14	0.00	205.850
28	N+OH-NO+H	4.80384E+13	0.00	5.270
29	NO+O-N+O <sub>2</sub>	2.400E+9	1.00	161.670
30	N+O <sub>2</sub> -NO+O	1.13052E+10	1.00	27.838

Table B.1: The hydrogen reaction mechanism, including the NO scheme, used in the flamelet calculations by Sanders (1994).

Number	Reaction	B [mole <sub>e</sub> .cm <sup>-3</sup> .s]	$\alpha$	E [kJ/mole]
CO-CO <sub>2</sub> reactions				
31	CO+OH- CO <sub>2</sub> +H	4.400E+6	1.50	-3.100
32	CO <sub>2</sub> +H- CO+OH	4.956E+8	1.50	89.760
CH consumption				
33	CH+O <sub>2</sub> -HCO+O	3.000E+13	0.00	0.000
34	CH+CO <sub>2</sub> -HCO+CO	3.400E+12	0.00	2.900
HCO consumption				
35	HCO+H- CO+H <sub>2</sub>	2.000E+14	0.00	0.000
36	HCO+OH- O+H <sub>2</sub> O	1.000E+14	0.00	0.000
37	HCO+O <sub>2</sub> - CO+HO <sub>2</sub>	3.000E+12	0.00	0.000
38	HCO+M'- CO+H+M'	7.100E+14	0.00	70.300
39	CO+H+M'- HCO+M'	1.136E+15	0.00	9.970
CH <sub>2</sub> consumption				
40	CH <sub>2</sub> +H- CH+H <sub>2</sub>	8.400E+9	1.50	1.400
41	CH+H <sub>2</sub> - CH <sub>2</sub> +H	5.830E+9	1.50	13.800
42	CH <sub>2</sub> +O- CO+H+H	8.000E+13	0.00	0.000
43	CH <sub>2</sub> +O <sub>2</sub> - CO+OH+H	6.500E+12	0.00	6.300
44	CH <sub>2</sub> +O <sub>2</sub> - CO <sub>2</sub> +H+H	6.500E+12	0.00	6.300
CH <sub>2</sub> O consumption				
45	CH <sub>2</sub> O+H- HCO+H <sub>2</sub>	2.500E+13	0.00	16.700
46	CH <sub>2</sub> O+O- HCO+OH	3.500E+13	0.00	14.600
47	CH <sub>2</sub> O+OH- HCO+H <sub>2</sub> O	3.000E+13	0.00	5.000
48	CH <sub>2</sub> O+M'- HCO+H+M'	1.400E+17	0.00	320.00
CH <sub>3</sub> consumption				
49	CH <sub>3</sub> +H- CH <sub>2</sub> +H <sub>2</sub>	1.800E+14	0.00	63.000
50	CH <sub>2</sub> +H <sub>2</sub> - CH <sub>3</sub> +H	3.680E+13	0.00	44.300
51	CH <sub>3</sub> +H- CH <sub>4</sub>	3.050E+34	-6.5	32.010
52	CH <sub>3</sub> +O- CH <sub>2</sub> O+H	7.000E+13	0.00	0.000
53	CH <sub>3</sub> +CH <sub>3</sub> - C <sub>2</sub> H <sub>6</sub>	5.730E+51	-11.6	75.660
54	CH <sub>3</sub> +O <sub>2</sub> - CH <sub>2</sub> O+OH	3.400E+11	0.00	37.400
55	CH <sub>4</sub> +H- CH <sub>3</sub> +H <sub>2</sub>	2.200E+4	3.00	36.600
56	CH <sub>3</sub> +H <sub>2</sub> - CH <sub>4</sub> +H	8.391E+2	3.00	34.560
57	CH <sub>4</sub> +O- CH <sub>3</sub> +OH	1.200E+7	2.10	31.900
58	CH <sub>4</sub> +OH- CH <sub>3</sub> +H <sub>2</sub> O	1.600E+6	2.10	10.300
59	CH <sub>3</sub> +H <sub>2</sub> O- CH <sub>4</sub> +OH	2.631E+5	2.10	70.920

Table B.2: The C1 mechanism used in the flamelet calculations by Sanders (1994).

H <sub>2</sub> O	6.5
CO	0.75
CO <sub>2</sub>	1.5
CH <sub>4</sub>	6.5
O <sub>2</sub>	0.4
N <sub>2</sub>	0.4

Table B.3: Third body efficiencies used in the flamelet calculations by Sanders (1994).



## Appendix C

### Diffusion flamelet results

Figure C.2 shows the result of computations performed on a plane  $H_2$ -air flame by Sanders (1994) at different strain rates. The calculations have been performed with the mechanism of Table B.1 including 11 species and 30 reactions. Increasing the strain rate causes a temperature decrease. A quenching value of  $a_q=14260/s$  was found corresponding to a quenching scalar dissipation rate  $\chi_q$  of 2877/s.

Figure C.1 shows the mass fraction profiles. The oxygen leak through the reaction zone (at  $Z=Z_{st}=0.028$ ) increases as the strain rate increases.

Figure C.3 shows the result of computations on a plane 100%  $CH_4$ -air flame performed by Peeters (1995) at different strain rates. Calculations have been performed with a C1 mechanism. Increasing the strain rate causes a temperature decrease. A quenching value of  $a_q=485/s$  was found corresponding to a quenching scalar dissipation rate  $\chi_q$  of 17.4/s.

Figure C.4 shows the mass fraction profiles. As the strain rate increases the following can be observed:

- the oxygen leak through the reaction zone (at  $Z=Z_{st}=0.055$ ) increases.
- $Y_{CO}$  increases as expected in a flame near extinction, while  $Y_{CO_2}$  decreases. A flame near quenching is not able to burn the fuel completely which leads to a higher  $CO$  level, while correspondingly less  $CO_2$  is produced.

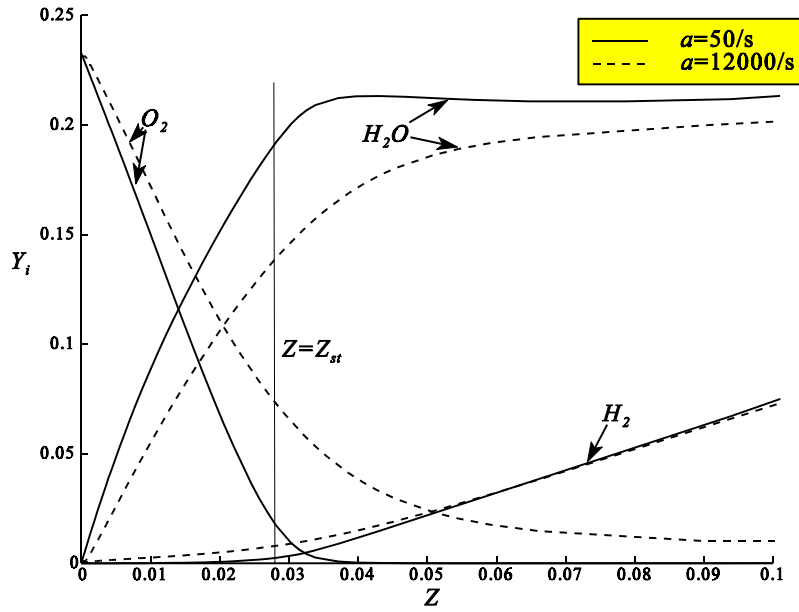


Figure C.1 Mass fraction profiles for laminar counterflow hydrogen-air flames at strain rates 50/s and 12000/s (after Sanders, 1994).

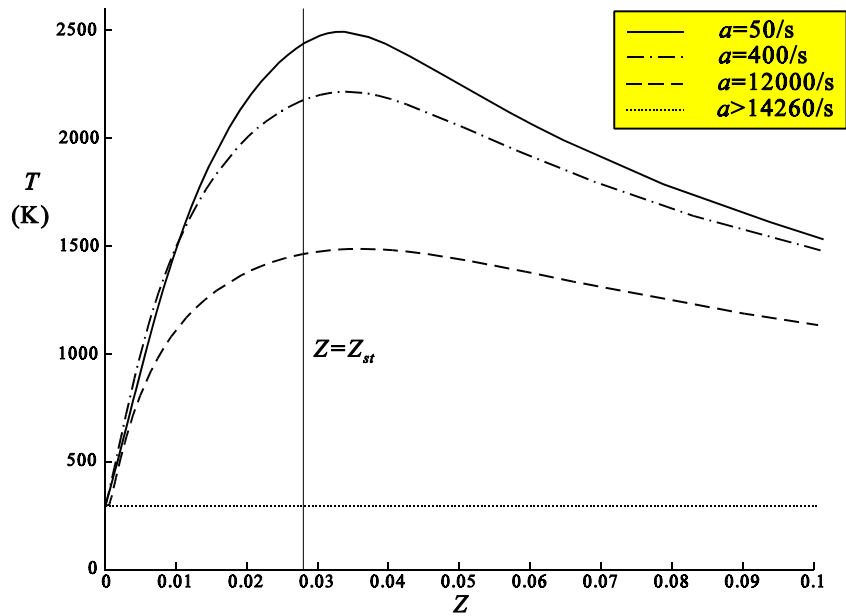


Figure C.2 Temperature profiles for laminar counterflow hydrogen-air diffusion flames at different strain rates (after Sanders, 1994).

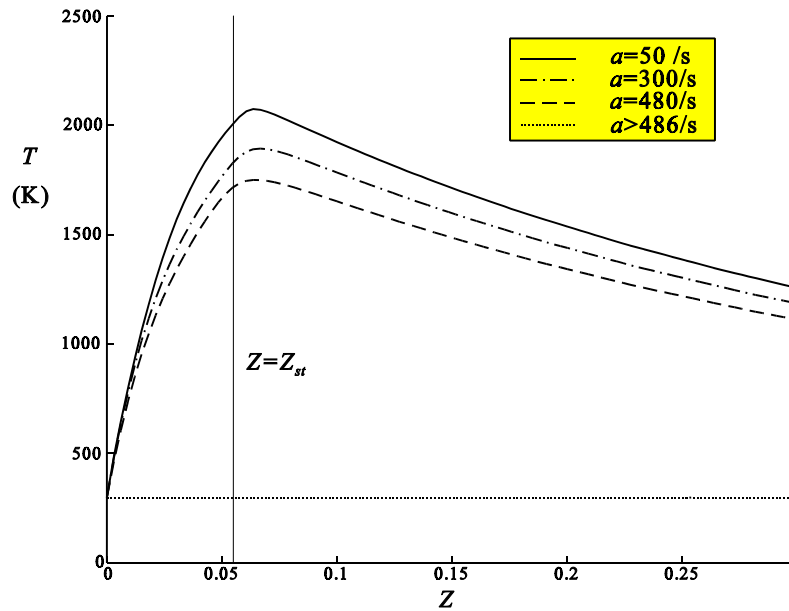


Figure C.3 Temperature profiles for laminar counter-flow methane-air diffusion flames at different strain rates (after Peeters, 1995).

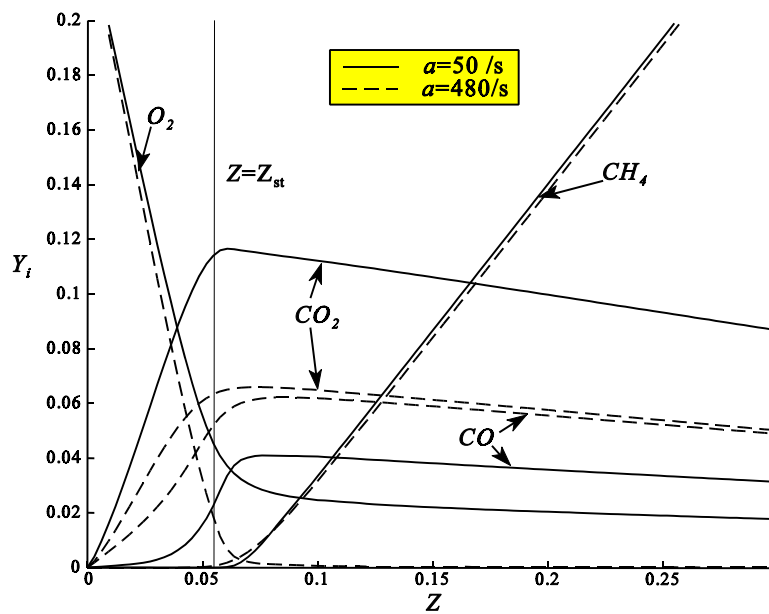


Figure C.4 Mass fraction profiles for laminar counter-flow methane-air diffusion flames at strain rates of 50/s and 480/s (after Peeters, 1995).





## Appendix D

### Premixed flamelet results

Figure D.1 shows some results of calculations by Mauß *et al.* (1993) for a methane-air flame by making use of the  $C_1$ -mechanism of Appendix B. Also shown are some results of experiments compiled by Warnatz (1981) and results of experiments by Law (1993). Plotted along the horizontal axis is the equivalence ratio,  $\Phi$ , which is related to the mixture fraction as:

$$\Phi = \frac{Z}{1-Z} \frac{1-Z_{st}}{Z_{st}} \quad (D.1)$$

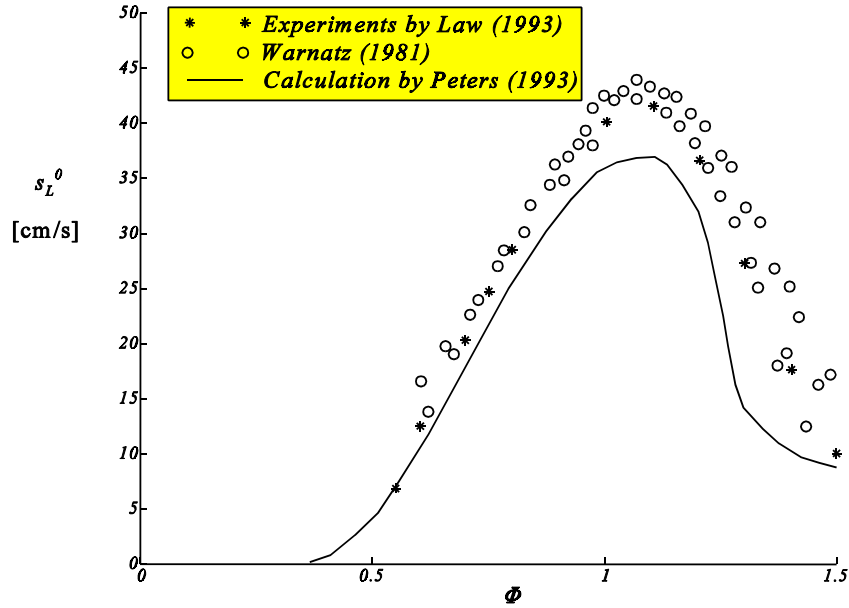


Figure D.1 Burning velocities of an unstretched laminar methane flame at atmospheric pressure and a temperature of  $T_u=298\text{K}$ .

The influence of flame stretch and curvature on the laminar burning velocity is represented by the Markstein length  $\mathcal{L}$  in Equation (6.23). It may be derived from an asymptotic analysis for weakly stretched flames (Clavin *et al.*, 1982), with the result

$$M = \frac{\mathcal{L}}{l_F} = \frac{1}{\gamma} \ln \frac{1}{1-\gamma} + \frac{\beta(Le-1)}{2} \frac{1-\gamma}{\gamma} \int_0^{\gamma/(1-\gamma)} \frac{\ln(1+x)}{x} dx \quad (D.2)$$

where  $M$  is the so-called Markstein number. The quantity  $\gamma$  is the reduced gas expansion factor:

$$\gamma = \frac{T_b - T_u}{T_b} \quad (D.3)$$

The constant  $\beta$  is the Zel'dovich number which is the product of  $\gamma$  with the nondimensional

activation energy  $E/(R_0T_b)$ , i.e.

$$\beta = \frac{E(T_b - T_u)}{R_0T_b^2} \quad (\text{D.4})$$

and  $Le$  is the Lewis number of the unburnt mixture. The Markstein number is generally a positive quantity except for lean hydrogen flames where the Lewis number may be sufficient small to result in negative values of  $M$ . The Markstein number can in principle be determined directly from Equation (6.23) by making measurements of the local burning velocity, radius of curvature, and local flow gradients imposed on a stretched flame. However, such direct methods often have an error tolerance of about 100%. Experimental findings of the Markstein number are very sensitive to the used experimental method (Searby *et al.*, 1990). Figure D.2 shows some experimental results for an atmospheric methane-air flame as obtained by Searby (1990), Tseng (1993) and Taylor (1991). Also shown are some results calculated by Peters (1993) from Equation (D.2). Obviously, the Markstein number decreases for lean mixtures. For very lean mixtures, the Markstein number even becomes negative. A negative Markstein number means that the burning velocity increases under increased curvature, leading to an unstable flame. The negative Markstein numbers are caused by the fact that the Lewis number is slightly smaller than one, i.e. being equal to 0.91.

Figure D.3 and Figure D.4 show the same results for an atmospheric hydrogen-air flame. Also for hydrogen flames, the Markstein number becomes negative for lean mixtures. Even at stoichiometric mixture ( $\phi=1$ ), the Markstein number is negative and therefore the flame is unstable. Only for very rich mixtures, the hydrogen flame becomes stable. The fact that the Markstein numbers for hydrogen flames are negative in a large regime is caused by the fact that the Lewis number for hydrogen is significantly smaller than one, i.e.  $Le=0.3$ .

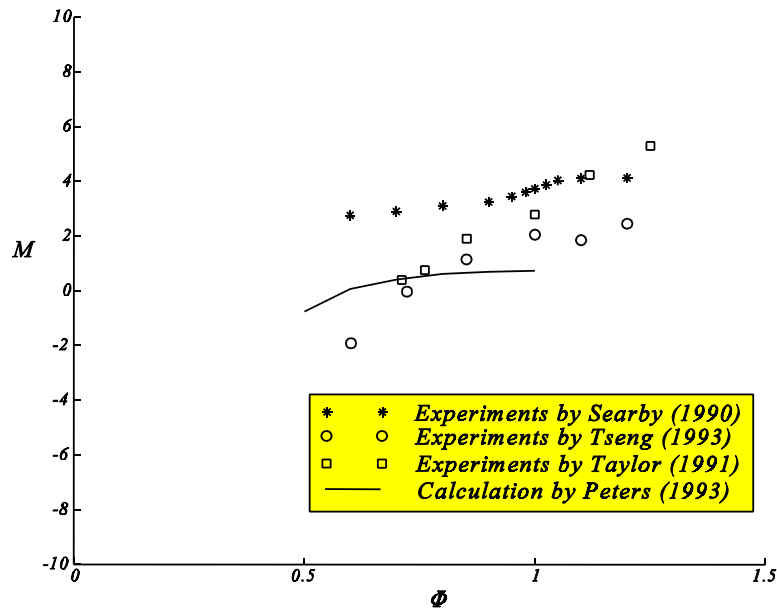


Figure D.2 Markstein numbers of a methane flame at atmospheric pressure and  $T_u=298\text{K}$ .

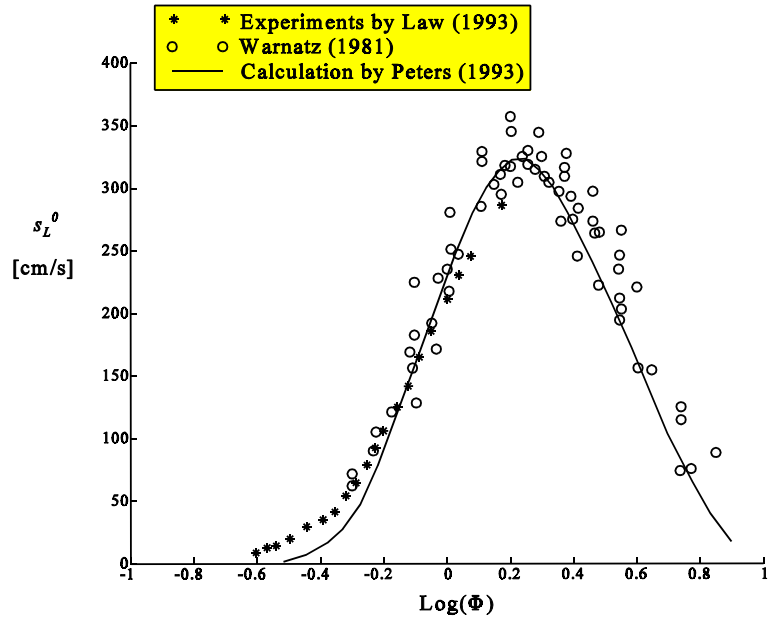


Figure D.3 Burning velocities of an unstretched laminar hydrogen flame at atmospheric pressure and a temperature of  $T_u=298\text{K}$ .

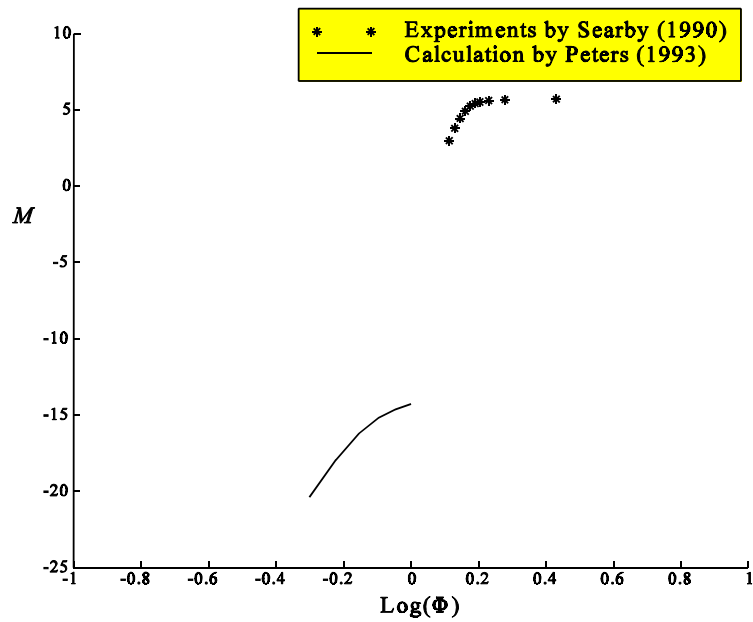


Figure D.4 Markstein numbers of a hydrogen-air flame at atmospheric pressure and  $T_u=298\text{K}$ .



## Appendix E

### Equation for the flame surface area ratio

A model equation for the flame surface area ratio  $\bar{\sigma} = |\nabla G|$  has been obtained by Peters (1997):

$$\frac{\partial \bar{\sigma}}{\partial t} + \bar{u}_k \frac{\partial \bar{\sigma}}{\partial x_k} = -D \bar{\kappa}(\bar{\sigma}) |\nabla \bar{\sigma}| + c_0 \frac{-\bar{u}'_\alpha \bar{u}'_\beta}{\bar{k}} \frac{\partial \bar{u}_\alpha}{\partial x_\beta} + c_1 \frac{D_t (\nabla \bar{G})^2}{G^2} \bar{\sigma} - c_2 \frac{s_L^0 \bar{\sigma}^2}{\sqrt{G'^2}} - c_3 \frac{D \bar{\sigma}^3}{G^2} \quad (\text{E.1})$$

The terms on the left hand side represent the unsteady change and convection of  $\bar{\sigma}$  by the mean velocity field. The first term on the right hand side describes the turbulent transport of  $\bar{\sigma}$  which was modelled as a curvature term. Here,  $\kappa(\bar{\sigma})$  is defined as in Equation (6.25) but with  $\bar{\sigma}$  instead of  $G$ . The second term represents the production of the flame surface area ratio by mean velocity gradients and the third term by local turbulent fluctuations. The fourth and last terms on the right hand side are the kinematic restoration term and the scalar dissipation term of the flame surface area ratio, respectively.

For the case of fully developed turbulence and a fully developed turbulent flame in the limit of large times, turbulent production of flame surface area ratio equals kinematic restoration and scalar dissipation in Equation (E.1):

$$c_1 \frac{D_t \bar{\sigma}}{G^2} - c_2 \frac{s_L^0 \bar{\sigma}^2}{\sqrt{G'^2}} - c_3 \frac{D \bar{\sigma}^3}{G^2} = 0 \quad (\text{E.2})$$

where  $|\nabla \bar{G}|$  has been set equal to unity. In the limit of large times, it holds that  $\sqrt{G'^2} = b_2 l_t$  (see Appendix F). With  $D_t = 0.78 v l_t$  (for a turbulent Schmidt number of 0.7) and  $D = s_L^0 l_F$ , Equation (E.2) may then be written as

$$\bar{\sigma}^2 + \frac{c_2 b_2 l_t}{c_3 l_F} \bar{\sigma} - \frac{c_1 0.78 v l_t}{c_3 s_L^0 l_F} = 0 \quad (\text{E.3})$$

with the solution

$$\bar{\sigma} = -\frac{c_2 b_2 l_t}{c_3 l_F} + \sqrt{\left(\frac{c_2 b_2 l_t}{c_3 l_F}\right)^2 + 4 \frac{c_1 0.78 v l_t}{c_3 s_L^0 l_F}} \quad (\text{E.4})$$

Constants are adapted such as to retrieve Damköhlers relations for the small scale and large scale turbulence regime (see Section 6.1), i.e.

$$\begin{aligned} c_2 b_2 &= 0.39 c_1 \\ c_3 &= c_1 \end{aligned} \quad (\text{E.5})$$

Leading to

$$\bar{\sigma} = -\frac{0.39 l_t}{2 l_F} + \sqrt{\left(\frac{0.39 l_t}{2 l_F}\right)^2 + 0.78 \frac{v l_t}{s_L^0 l_F}} \quad (\text{E.6})$$



## Appendix F

### Equation for the variance in $G$

A model equation for the variance in  $G$ , i.e.  $\overline{G'^2}$  has been obtained by Peters (1997):

$$\frac{\partial \overline{G'^2}}{\partial t} + \overline{u}_k \frac{\partial \overline{G'^2}}{\partial x_k} = -(s_L^0 \mathcal{L} + D_t) \overline{\kappa(G'^2)} |\nabla \overline{G'^2}| + 2D_t (\nabla \overline{G'})^2 - c_s \frac{\overline{\varepsilon}}{\overline{k}} \overline{G'^2} \quad (\text{F.1})$$

The terms on the left hand side represent the unsteady change and convection of  $\overline{G'^2}$  by the mean velocity field. The first term on the right hand side describes the effect of Markstein diffusion and turbulent transport of  $\overline{G'^2}$  which was modelled as a curvature term. Here,  $\overline{\kappa(G'^2)}$  is defined as in Equation (6.25) but with  $\overline{G'^2}$  instead of  $G$ . The second term represents the production of  $\overline{G'^2}$  by local turbulent fluctuations. The last term on the right hand side is the scalar dissipation term with  $c_s = 2.0$ .

Consider a planar flame for which the curvature term vanishes. In interpreting  $\overline{G}$  as a distance function for the turbulent flame,  $|\nabla \overline{G}|$  is equal to unity in the production term. With  $D_t = 0.78 \nu' l_t$  (for a turbulent Schmidt number of 0.7) and replacing  $\overline{\varepsilon}/\overline{k}$  by

$$\frac{\overline{\varepsilon}}{\overline{k}} = 0.247 \frac{\nu'}{l_t} \quad (\text{F.2})$$

the variance equation may be written as:

$$\frac{\partial \overline{G'^2}}{\partial (t/\tau)} = 6.32 l_t^2 - 2 \overline{G'^2} \quad (\text{F.3})$$

with  $\tau = \overline{k}/\overline{\varepsilon}$  as the integral time scale. The solution of Equation (F.3) is given by

$$\overline{G'^2} = b_2^2 l_t^2 [1 - \exp(-2t/\tau)] + \overline{G_0'^2} \exp(-2t/\tau) \quad (\text{F.4})$$

where  $b_2 = \sqrt{6.32/2} = 1.78$ . Therefore, in the limit of large times, it holds that

$$\sqrt{\overline{G'^2}} = b_2 l_t \quad (\text{F.5})$$





## Summary

In this thesis, a model for numerically simulating a partially premixed turbulent flame is presented. The used model is based on the flamelet concept, i.e. the assumption that laminar flames are embedded in the turbulent flow field. In many cases of practical interest, chemistry is fast compared to convective and diffusive processes. In these cases the Kolmogorov time  $t_\eta$ , which is the turnover time of the smallest eddies, is much larger than the chemical time scale  $t_c$ . The turbulent eddies are of dimensions much larger than the thickness of the laminar flame. In this high Damköhler number ‘flamelet regime’ the partially premixed turbulent diffusion flame may be treated as an ensemble of laminar premixed flamelets and laminar diffusion flamelets.

In the flamelet regime, the diffusion flame is mapped instantaneously into ‘mixture fraction space’ as a function of two parameters; the mixture fraction  $Z$  and the scalar dissipation rate  $\chi$ . The iso-surface at which the mixture fraction  $Z$  equals the stoichiometric mixture fraction defines the location of the diffusion flame. By calculating the conditioned scalar dissipation rate  $\chi_{st}$ , the local chemical composition of the diffusion flame is determined from the pre-calculated flamelet-libraries. Laminar counterflow diffusion flames are chosen to be the most representative for building these diffusion-flamelet libraries.

For many turbulent flames partial premixing is relevant. The mixed reactants can ignite and burn in a premixed fashion. The premixed flame is described by a progress variable  $c$ . Because the premixed flame front is very thin, its internal structure remains unresolved and it is treated as a discontinuity. The motion of the premixed flame is described by a kinematic equation in which the laminar burning velocity is known as a function of flame curvature and flame stretch. For the representation of the location of the premixed flame front a field equation for the scalar  $G$  may be used.  $G$  is defined as the distance to the premixed flame, and the level set  $G=0$  defines the location of the premixed flame front.

To treat the turbulence closure problem, use has been made of the standard  $k$ - $\epsilon$  model. Favre-averaged scalar quantities have been calculated from the flamelet libraries by making use of a presumed Probability Density Function (PDF) method. The mean flame position is found as the zero level set of the level-set function  $\overline{G}$ . This zero level-set is found by solving the level-set equation for  $\overline{G}$  in which  $\overline{G}$  is equal to a signed distance function. The Favre-averaged progress variable is found as a function of  $\overline{G}$ .

Numerical simulations have been performed for a burner-stabilised turbulent methane diffusion flame, for a premixed turbulent hydrogen/air flame and for a lifted turbulent methane diffusion flame. From the simulated diffusion flame it is clear that besides radiation, also time-dependent effects should be taken into account in order to obtain a good comparison between simulation and measurement data from literature. For the premixed flame, a good agreement has been found on the location of the premixed flame as well as on the turbulent flame brush thickness. Also for the lifted turbulent methane diffusion flame a rather good agreement has been found between calculated average lift-off height of the flame above the burner and values for the average lift-off height found in literature.

Besides the work done on the modelling of partially premixed turbulent jet diffusion flames, measurements have been carried out on an axi-symmetric turbulent jet. The aim here was to test the applicability of the  $k$ - $\epsilon$  model to the flow problem considered. The hot-wire anemometry method has been used in combination with a look-up inversion method for  $X$  hot-wires. A correction method has been applied to account for the effect of the fluctuating binormal velocity component. Second and higher-order velocity correlation terms have been modelled by assuming

a bivariate normal distribution for the axial and radial velocity components, while the tangential velocity component is assumed to be statistically independent from the other velocity components. An additional equation for the variance in the tangential velocity component is obtained from a measurement at which the prong plane is rotated over 90 degrees. The resulting set of six algebraic equations is solved by making use of Newton's iteration method. Measured axial and radial velocity components and their fluctuations in a turbulent jet agreed well with other experimental data from literature. The measured centerline velocity decay as well as the half-width spreading rate also agreed well with values found from the  $k$ - $\epsilon$  model prediction.

## Samenvatting

In dit proefschrift wordt een model gepresenteerd voor het uitvoeren van berekeningen aan een gedeeltelijk voorgemengde turbulente jet diffusievlam. Het gebruikte model is gebaseerd op het flamelet concept, d.w.z. de aanname dat laminaire vlammen zijn ingebed in het turbulente stromingsveld. In veel gevallen die van praktisch belang zijn is de chemie snel in vergelijking tot convectieve en diffusieve processen. In deze gevallen is de Kolmogorov tijdschaal  $t_\eta$ , die overeenkomt met de omwentelingstijd van de kleinste werveltjes, een stuk langer dan de chemische tijdschaal  $t_c$ . De ruimtelijke dimensie van de turbulente wervels is veel groter dan de dikte van de laminaire vlam. In dit ‘flamelet regime’ van hoge Damköhler getallen mag de gedeeltelijk voorgemengde turbulente diffusievlam worden behandeld als een compositie van laminaire voorgemengde vlammen en laminaire diffusievlammen.

In het flamelet regime kan de diffusievlam instantaan worden afgebeeld op de ‘mengfractie ruimte’, dit als functie van twee parameters; de mengfractie  $Z$  en de scalaire dissipatie snelheid  $\chi$ . Het oppervlak waarop de mengfractie  $Z$  gelijk is aan de stoichiometrische mengfractie  $Z_{st}$  legt de locatie van de diffusievlam vast. Door het bepalen van de geconditioneerde scalaire dissipatie snelheid  $\chi_{st}$  wordt de lokale chemische samenstelling in de diffusievlam vastgelegd m.b.v. een vooraf opgestelde flamelet bibliotheek. Laminaire tegenstroom diffusievlammen zijn gekozen als meest geschikte vlammen voor het opbouwen van deze flamelet bibliotheek.

Voor veel turbulente vlammen is gedeeltelijke voormenging relevant. De voorgemengde reactanten kunnen ontbranden en een voorgemengde vlam vormen. De voorgemengde vlam wordt beschreven door de voortgangsvariabele  $c$ . Omdat de voorgemengde vlam erg dun is wordt de interne structuur van de vlam niet beschouwd maar wordt deze behandeld als discontinuïteit. De beweging van de voorgemengde vlam wordt beschreven door een kinematische vergelijking waarin de laminaire verbrandingssnelheid gegeven is als functie van de lokale vlamkromming en vlamstrekking. Voor het vinden van de locatie van de voorgemengde vlam wordt gebruik gemaakt van de scalaire grootheid  $G$ . De scalaire grootheid  $G$  is gedefinieerd als de afstand tot de voorgemengde vlam en het nul-niveau  $G=0$  definieert dan de locatie van het voorgemengde vlamfront.

Voor behandeling van het turbulente sluitingsprobleem is gebruik gemaakt van het standaard  $k-\epsilon$  model. Favre-gemiddelde scalaire grootheden worden berekend uit de flamelet bibliotheek door gebruikmaking van een aangenomen vorm voor de kansdichtheidsverdeling. De gemiddelde positie van het vlamfront wordt gevonden als het nul-niveau van de niveau-functie  $\bar{G}$ . Dit nul-niveau wordt gevonden door het oplossen van de niveau-plaatsings vergelijking voor  $\bar{G}$  waarin  $\bar{G}$  gelijk is aan de afstandsfunctie met een positief of negatief teken. De Favre-gemiddelde voortgangsvariabele wordt gevonden als functie van  $\bar{G}$ .

Numerieke simulaties zijn uitgevoerd voor een brander-gestabiliseerde turbulente methaan diffusievlam, een voorgemengde turbulente waterstof/lucht vlam en voor een van de brander losgekomen (‘lifted’) turbulente methaan diffusievlam. Uit de gesimuleerde diffusievlam blijkt dat naast straling ook tijdafhankelijke effecten mee zouden moeten worden genomen om tot een goede overeenkomst tussen simulatie en metingen uit de literatuur te komen. Voor de voorgemengde vlam is een goede overeenkomst gevonden voor de locatie van de voorgemengde vlam, als ook voor de dikte van het turbulente vlamgebied. Ook voor de van de brander losgekomen turbulente methaan diffusievlam is een redelijke overeenkomst gevonden tussen berekende gemiddelde ‘lift-off’ hoogte van de vlam boven de brander en waarden voor de gemiddelde ‘lift-off’ hoogte gevonden in de literatuur.

Naast het werk aan de modellering van gedeeltelijk voorgemengde turbulente jet diffusievlammen zijn metingen uitgevoerd aan een axiaal-symmetrische turbulente jet. Doel hiervan was te testen of het  $k$ - $\epsilon$  model toepasbaar is voor de onderzochte stromingsconfiguratie. Daartoe is de hittedraad-anemometrie methode gebruikt in combinatie met een opzoek-inversie methode voor kruis-hittedraden. Een correctie methode is toegepast om voor het effect van de fluctuerende binormale snelheidscomponent te corrigeren. Tweede- en hogere-orde snelheids-correlatie termen zijn gemodelleerd onder de aanname van een bivariante normale verdeling voor de axiale en radiale snelheidscomponenten terwijl de tangentiële snelheidscomponent statistisch onafhankelijk is aangenomen van de andere snelheidscomponenten. Een extra vergelijking voor de variantie in de tangentiële snelheidscomponent wordt verkregen uit een meting waarbij het vlak van de hittedraden is gerooteerd over 90 graden. Het resulterende stelsel van zes algebraïsche vergelijkingen wordt opgelost door gebruik te maken van Newton's iteratie methode. Gemeten axiale en radiale snelheidscomponenten en hun fluctuaties in een turbulente jet komen goed overeen met gegevens uit de literatuur. Het gemeten hartlijn snelheidsverval en de halfwaarde spreidingssnelheid komen ook goed overeen met waarden gevonden uit numerieke simulaties met het  $k$ - $\epsilon$  model.

## Nawoord

Deze studie is uitgevoerd aan de faculteit werktuigbouwkunde, sectie energie technologie. Aan dit onderzoek hebben meerdere personen hun bijdrage geleverd, waarvoor ik hen hartelijk wil bedanken. Ir. Antoon P.G.G. Lamers, prof.dr.ir. Harry W.M. Hoeijmakers en prof.dr.ir. Anton A. van Steenhoven wil ik bedanken voor het kritisch lezen van mijn proefschrift en het geven van zinvolle suggesties. Mede dankzij hen werd dit onderzoek in goede banen geleid. Ook de overige leden van de kerncommissie, prof.dr. D.J.E.M. Roekaerts en prof.dr.ir. M.E.H. van Dongen, wil ik bedanken voor het proeflezen en voor hun suggesties.

Voor het helpen opbouwen van de meetopstelling ben ik dank verschuldigd aan de volgende studenten/afgestudeerden. Maurice van Gils, voor het ontwerpen en bouwen van de meetopstelling. Ferry van der Hijden, voor het verder perfectioneren hiervan. Richard Boll, voor het ontwerpen en bouwen van de callibratieopstelling en het schrijven van de bijbehorende software. Roger Mateijssen en Jürgen Benischek voor het verder ontwikkelen van deze callibratieopstelling. Tot slot, Ingrid Naus, voor het testen/valideren van de gebruikte correctie methode voor de invloed van de binormale snelheidscomponent.

Dr.ir. Tim W.J. Peeters wil ik bedanken voor het ter beschikking stellen van de door hem ontwikkelde software voor de adaptieve tabulatie van flamelet gemiddelde scalaire grootheden.

Vooraf ook dankzij mijn kamergenoten Roel Luppens en Ton Gielen heb ik mijn werk aan de TU Eindhoven altijd met plezier kunnen uitvoeren. Als het nodig was, dan waren zij altijd bereid een helpende hand te bieden, hiervoor wil ik hen hartelijk bedanken.

Tot slot wil ik mijn familie en vrienden bedanken voor alle steun die ik van hen gekregen heb.

## Curriculum Vitae

- 19 mei 1970 Geboren te Hengelo (Overijssel).
- 1982 - 1987 HAVO, Christelijke Scholengemeenschap, Aalten.
- 1987 - 1988 Propaedeuse Vliegtuigbouwkunde aan de Hogeschool Haarlem.
- 1988 - 1994 Luchtvaart- en Ruimtevaarttechniek aan de Technische Universiteit Delft. Afgestudeerd in de vakgroep Theoretische Aërodynamica met als afstudeeropdracht "A perturbation method applied to shock wave annihilation by magnetohydrodynamic action in supersonic flow" onder begeleiding van ir. G. Schouten en prof.dr.ir. H.W.M. Hoeijmakers.
- 1994 - 1999 Promotieonderzoek aan de Technische Universiteit Eindhoven, faculteit Werktuigbouwkunde, sectie Energietechnologie.
- 1 november 1999 Werkzaam als Software Development Engineer bij de MacNeal Schwendler Corporation (MSC) te Gouda ([www.macsch.com](http://www.macsch.com)).

# Stellingen

behorende bij het proefschrift

## Flamelet Modelling for Partially Premixed Turbulent Jet Diffusion Flames

Roy Ovink

1. Onder de aanname van gelijke diffusiecoëfficiënten voor alle stoffen is de definitie van de mengfractie te kiezen als een willekeurige lineaire combinatie van massafracties van elementen. Als echter niet alle diffusiecoëfficiënten gelijk zijn kan de mengfractie het beste worden gedefinieerd als de massafractie brandstof in het onverbrande gas. *Hoofdstuk 2 respectievelijk hoofdstuk 5 van dit proefschrift.*
2. Het voorschrijven van de kansdichtheidsverdeling in termen van Favre-gemiddelde grootheden leidt niet alleen tot een mathematische vereenvoudiging, maar ook tot een betere beschrijving van de realiteit. *Kennedy et al. (1979)<sup>1</sup> en hoofdstuk 3 van dit proefschrift.*
3. Het verwaarlozen van de invloed van de binormale snelheidscomponent in de verwerking van de signalen van hittedraad anemometrie leidt bij hoge turbulentie intensiteit tot grote fouten in de bepaalde waarden voor de Reynoldsspanningen. *Hoofdstuk 4 van dit proefschrift.*
4. Als parameter die de toestand van niet-chemisch evenwicht aangeeft dient bij voorkeur toch gebruik te worden gemaakt van de scalaire dissipatie snelheid en niet van de ‘strain rate’ zoals wordt gepropageerd door Sanders (1994)<sup>2</sup>. *Hoofdstuk 5 van dit proefschrift.*
5. De turbulente verbrandingssnelheid wordt zowel beïnvloed door lokale snelheidsfluctuaties in het turbulente stromingsveld als ook door de lokale chemische samenstelling. *Hoofdstuk 6 van dit proefschrift.*
6. ‘Triple-flames’ spelen een belangrijke rol in het stabilisatie-mechanisme van ‘lifted’ (van de brander losgekomen) diffusievlammen. *Hoofdstuk 7 van dit proefschrift.*
7. Dit proefschrift is ‘millennium-proof’.
8. Naarmate een studie fundamenteeler van aard is, is deze moeilijker in een maatschappelijke context te plaatsen.

---

<sup>1</sup> Kennedy, I.M. and Kent, J.H. (1979). Measurements of a conserved scalar in turbulent jet diffusion flames. 17-th Symposium on Combustion, pp. 279-287.

<sup>2</sup> Sanders, J.P.H. (1994). Scalar transport and flamelet modelling in turbulent jet diffusion flames. Ph.D. Thesis, Eindhoven University of Technology.



9. Bij het aangeven van de richting 'Centrum' op verkeersborden zou men ook de afstand moeten vermelden. Dit om eindeloos heen en weer rijden te voorkomen in het geval dat het centrum niet voldoet aan de verwachting.
10. In de sport zal winnen of verliezen steeds meer gaan afhangen van steeds kleinere prestatieverbeteringen. Om te komen tot een eerlijke prestatievergelijking zal naast het opstellen van richtlijnen betreffende prestatiebevorderende voedingssupplementen (doping), in veel takken van sport ook het opstellen van nauwgezette aërodynamische richtlijnen steeds belangrijker worden.
11. Het grote aantal files op de digitale snelweg zorgt nogal eens voor te veel afleiding. Het is dan beter om de windows te sluiten.
12. Een theorie 'begrijpen' betekent vaak het in staat zijn aan te kunnen geven waarom die theorie een beperkte geldigheid heeft.